Optical development for second- and third-generation gravitational-wave detectors: stable recycling cavities for advanced virgo and higher-order Laguerre-Gauss modes

Massimo Granata

Université Paris Diderot (Paris 7)
Ecole Doctorale 517: Particules, Noyaux et Cosmos

Università degli Studi di Roma Tor Vergata

DOCTORAT
Physique: champs, particules, matières

DOTTORATO IN FISICA

Massimo Granata

Optical Development for Second- and Third-Generation Gravitational-Wave Detectors: Stable Recycling Cavities for Advanced Virgo and Higher-Order Laguerre-Gauss Modes

Thèse soutenue le 29·09·2011 au Laboratoire AstroParticule et Cosmologie (APC)

Jury

M.	P. Binétruy,	Président
M.	M. Barsuglia,	Directeur de thèse
M.me	V. Fafone,	Directeur de thèse
M.	G. Losurdo,	Examinateur
M.	D. Shoemaker,	Rapporteur
M.me	E. Tournefier,	Rapporteur

To Donatella

"There are more things in heaven and earth, Horatio,
Than are dreamt of in your philosophy."

"In our sky there is no limits
And masters we have none"

Acknowledgements

I first want to thank Fulvio Ricci and Yves Charon, who, by different ways, made this thesis concretely possible. Then I sincerely thank Matteo for having supervised my thesis, and for his trust in me: I thank him for what he taught me, for his support, for being always present. Thanks to him, I will always keep a good memory of this thesis. Thanks to Viviana, Alessio and all the group of Tor Vergata for the work together and the good time I spent in Rome, and thanks to Alessandra and to IDAPP for this opportunity. Thanks to Christelle, who shared with me most of my time at the laboratory: I really enjoyed working with her, as well as her company beyond the work. Thanks to Eric, for his company, his advices and our discussions. Thanks to Robert, for his precious help, and thanks equally to Hiro Yamamoto, Jérôme Degallaix and Fabien Reversat and Stéphane Tisserand of Silios Technologies. Thanks to Eden, Olivier, Pierre, Bérengère and Alain, for their help and friendship.

I acknowledge Pierre Binétruy and Yannick Giraud-Héraud, as well as all the people of the group Cosmologie et Gravitation and of the administration staff, for their warm welcome and their support. It has been a great pleasure to work with all of them, I really loved my time at APC. Then, since they really made this time unforgettable, I want to thank all of my friends at the lab: Silvia, Michela, Lorenzo, Alejandro, George, Florian, Alex, Giulio, Margherita, Héloïse, Fabio, Dana, Mariana, Marie-Anne, Gael, Sébastien, Romain, Alexandre, Josquin, Guillaume and Matthieu. Finally, a special mention is for Mario. Sincerely, thank you all.

Un ringraziamento molto speciale è per Filippo, mio padre, e per Marina, mia madre, per essermi stati sempre vicini: nei momenti più belli, e in quelli più difficili. Voglio infine ricordare Piero e Valentina, i miei nonni, che purtroppo non hanno potuto condividere con me la gioia di veder realizzato questo lavoro. Questa tesi è dedicata anche a loro.

Contents

Introduction

The existence of gravitational radiation, known as *gravitational waves*, is one of the most important predictions of the General Theory of Relativity. Gravitational waves are ripples in the metric of space-time that propagate at the speed of light, emitted by accelerating massive bodies. This radiation has never been directly detected so far, but the discovery of the binary pulsar PSR1913+16 in 1974 provided the indirect evidence that gravitational waves do exist. The waves emitted by nearby astrophysical sources, such as neutron star binaries, are expected to be detectable on Earth.

The very weak space-time strain of a gravitational wave might be detected as a phase shift between two laser beams propagating in the arms of a Michelson interferometer. Thereby a basic interferometric detector is composed of a laser, mirrors and a photodiode: the detection is performed by counting the photons of the laser beam interference fringe at the interferometer output. In order to increase the sensitivity of the detector, Fabry-Perot cavities are usually implemented in the interferometer.

During the last two decades, several interferometric detectors have been built and are now operating: LIGO, Virgo and GEO600 form a worldwide network of gravitational wave interferometers. These first-generation instruments approximately reached their design sensitivities, successfully demonstrating the technical feasibility of the detection principle, and completed several observational runs. No detections have been reported so far, but the data collected over the last years have been used to put constraints (either in terms of amplitude of emitted gravitational radiation or as event rates) on several astrophysical sources in the nearby universe, such as binary systems, known pulsars and burst sources. Also the amplitude of the stochastic gravitational-wave background of cosmological origin has been constrained, in a limited region of its spectrum.

Advanced Virgo and Advanced LIGO are planned to increase the sensitivity of the initial detectors by an order of magnitude. The Large-scale Cryogenic Gravitational-wave Telescope (LCGT) will attain a similar sensitivity, and will test for the first time the use of cryogenics and a new substrate material on a km-scale detector, in an underground site. These *second-generation* detectors will allow the first direct detection of gravitational waves. The construction of Advanced Virgo and advanced LIGO has already started, and their first joint scientific run is planned around 2016.

In the meanwhile, the project of a European detector of third generation, named Einstein Telescope, is presently in a phase of design study. The aim of this detector, which should be one hundred times more sensitive than initial interferometers, is to initiate in the 2020 decade the era of *precision* gravitational wave astronomy.

The sensitivity of future gravitational-wave interferometers of second and third generation will be limited by mirror thermal noise in the central part of the detection band. The exigence of solving this issue led to spend a great effort in the design of future detectors, and triggered the investigation of new technical solutions.

In advanced detectors the increase of the beam radius on the arm cavity mirrors will be necessary to reduce mirror thermal noise, and this will increase mode degeneracy in the recycling cavities. As already pointed out by the past experience with initial detectors, mode degeneracy can considerably affect the operation of gravitational-wave interferometers. To solve this issue, Advanced LIGO adopted non-degenerate recycling cavities as first, then initially Advanced Virgo embraced this solution too. Non-degenerate cavities should make the interferometer more robust against figure errors or thermal deformations of its mirrors.

The first part of this thesis concerns the optical design of non-degenerate recycling cavities for Advanced Virgo. We worked on this subject since fall 2008 to spring 2011. In the beginning we studied the general properties of non-degenerate cavities and how to adapt this solution to the requirements and constraints of the project. Then we developed a general design procedure to draw the optical layout of the cavities, and several layouts have been proposed and analyzed. We finally chose a configuration with the required optical features, the *vertical layout*, which might be implemented in Advanced Virgo.

Mirror thermal noise might be reduced using non-Gaussian beams. Initially *mesa* and *conical* beams have been proposed, but they have the relevant drawback of requiring resonators with non-spherical mirrors. Higher-order *Laguerre-Gauss modes* have been proposed in 2006 in alternative, since they should provide a comparable noise reduction but are eigenmodes of spherical resonators. Laguerre-Gauss modes have never been used for applications in gravitational-wave detection. No technique has been developed so far to generate these beams with reasonable purity and efficiency, and with the capability of handling high-power laser beams that will be used in future gravitational wave detectors. Moreover, and most important, the behavior of higher-order Laguerre-Gauss modes in Fabry-Perot interferometers is not known at present.

The second part of the thesis concerns the reduction of mirror thermal noise in future detectors through the use of higher-order Laguerre-Gauss modes. We assembled a table-top experimental setup where we tested the generation of Laguerre-Gauss beams using a diffractive plate of fused silica and a Fabry-Perot mode-cleaner cavity. Subsequently we used these beams inside a Michelson interferometer, to start the analysis of their optical performances in a basic optical system.

Outline of the Thesis

- **Chapters 1, 2** and **3** are of introductory nature. Chapter 1 will describe the basis of the theory of General Relativity and of gravitational waves and their astrophysical sources. Chapter 2 will treat the fundamental principles of interferometric detection of gravitational waves, introducing the Michelson interferometer, the Fabry-Perot cavities and illustrating the fundamental sources of noise that affect the instrument. In Chapter 3 we describe the network of gravitational wave detectors of first generation, with a review of the observational results achieved so far. We then introduce second- and third-generation detectors, with a particular focus on the sensitivity and the science case of Advanced Virgo.

PART II - Optical Design of the Non-Degenerate Recycling Cavities of Advanced Virgo

- **Chapter 4** will describe the Advanced Virgo project, focusing mostly on the optical layout, the thermal compensation system and the suspensions of mirrors.

- **Chapter 5** is dedicated to the design of the recycling cavities of Advanced Virgo. After a brief introduction about laser modes, optical resonators and mode degeneracy, we will describe the motivations supporting the choice of non-degenerate recycling cavities. Therefore we will illustrate how to design a non-degenerate cavity, and the particular design constraints of Advanced Virgo.
- In **Chapter 6** we will describe the design procedure and the optical simulations that we developed to design the layout of non-degenerate recycling cavities for Advanced Virgo. We will present and discuss the various cavity layouts studied, and the one which has been retained.

PART III - Use of Higher-Order Laguerre-Gauss Modes in Future Detectors

- In **Chapter 7** we will describe the available techniques to decrease mirror thermal noise in future detectors, and we will show the sensitivity gain achievable using higher-order Laguerre-Gauss modes.
- **Chapter 8** will illustrate the design and the assembly of a table-top experiment to test generation and interferometry of LG_3^3 beams, together with the results achieved.

Chapter 1

Gravitational Waves

The theory of General Relativity is the geometric theory of gravitation published by Albert Einstein in 1916 [1]. In General Relativity, the gravitational interaction is described as a geometric effect of curvature of space-time, which is determined by the energy-matter distribution of a system of bodies. In this theoretical frame, gravitational waves are local deformations of space-time which propagate with a finite velocity, being emitted by massive accelerated bodies. Since the coupling between gravitational radiation and matter is predicted to be extremely small, only astrophysical sources which are particularly massive and compact and move at relativistic speed are expected to emit gravitational waves of detectable amplitude. Thus the aim of gravitational wave detectors is to observe on Earth the gravitational waves emitted by astrophysical sources in space.

In this chapter we will introduce the fundamental concepts of the theory of General Relativity, and we will show that the prediction of the existence of gravitational waves is a natural consequence of the theory. Subsequently, we will describe the astrophysical sources of gravitational waves detectable on Earth. The last part of the chapter will introduce the indirect measurement of gravitational wave emission through the observation of the orbital period decay of pulsars in binary systems.

1.1 The Metric Tensor and the Geodesic Equation

In General Relativity, the line element ds which defines the distance between two points in space-time in an arbitrary reference frame of coordinates x^α ($\alpha = 0, 1, 2, 3$) is

$$ds^2 = g_{\mu\nu} dx^\mu dx^\nu \ , \tag{1.1}$$

where $g_{\mu\nu}$ is the *metric tensor* which describe the space-time geometry ($\mu, \nu = 0, 1, 2, 3$). The equation of motion of a particle which is only subject to the influence of gravity is the geodesic equation

$$\frac{d^2 x^\alpha}{d\tau^2} + \Gamma^\alpha_{\mu\nu} \frac{dx^\mu}{d\tau} \frac{dx^\nu}{d\tau} = 0 \ , \tag{1.2}$$

where τ is the proper time in the frame where the particle moves and $\Gamma^\alpha_{\mu\nu}$ are the affine connections (also referred to as Christoffel symbols), defined through the derivatives of the metric tensor:

$$\Gamma^\alpha_{\mu\nu} = \frac{1}{2} g^{\gamma\alpha} \Big(\frac{\partial g_{\nu\gamma}}{\partial x^\mu} + \frac{\partial g_{\mu\gamma}}{\partial x^\nu} - \frac{\partial g_{\mu\nu}}{\partial x^\gamma} \Big) \ . \tag{1.3}$$

Eqs.(1.2) and (1.3) are of fundamental importance, since they establish a relation between the geometrical properties of space-time and the physical properties of the gravitational field. The effect of the gravitational field can be interpreted as a curvature of space-time, forcing the bodies of a system to move along lines called *geodesics*. In analogy with the law of universal gravitation of Newton, the metric tensor $g_{\mu\nu}$ can be considered as the generalization of the gravitational potential, as well as the affine connections can be considered as the generalization of the gravitational field associated to the potential.

According to the Equivalence Principle, it is always possible to define a local inertial frame where the effect of gravity is canceled by the choice of the frame coordinates. In the local inertial frame of coordinates ξ^α, the line element ds simplifies to the usual Euclidean distance of the flat Minkowsky space-time metric,

$$ds^2 = \eta_{\mu\nu} dx^\mu dx^\nu \ , \tag{1.4}$$

where

$$\eta_{\mu\nu} = \begin{pmatrix} 1 & 0 & 0 & 0 \\ 0 & -1 & 0 & 0 \\ 0 & 0 & -1 & 0 \\ 0 & 0 & 0 & -1 \end{pmatrix} \ , \tag{1.5}$$

and the relation between the metric tensor and the flat space-time metric writes

$$g_{\mu\nu} = \frac{\partial \xi^\alpha}{\partial x^\mu} \frac{\partial \xi^\beta}{\partial x^\nu} \eta_{\alpha\beta} \ , \tag{1.6}$$

where $\partial\xi^\alpha/\partial x^\mu$ and $\partial\xi^\beta/\partial x^\nu$ are the matrices which describe the change of coordinates between the arbitrary frame and the local inertial frame. In the local inertial frame the affine connections are equal to

$$\Gamma^\alpha_{\mu\nu} = \frac{\partial x^\alpha}{\partial \xi^\lambda} \frac{\partial^2 \xi^\lambda}{\partial x^\mu x^\nu} \ , \tag{1.7}$$

and the geodesic equation simplifies to

$$\frac{\partial^2 \xi^\alpha}{d\tau^2} = 0 \ . \tag{1.8}$$

Eq.(1.8) is analogous to the second law of motion of Newton, $\vec{F} = m d^2\vec{x}/dt^2$, for a particle in a system where forces are in equilibrium ($\vec{F} = 0$). In other words, with a particular choice of the reference frame, the effect of gravity can be canceled so that the physics of the system is governed by the laws of Special Relativity.

1.2 The Einstein Equations and the Wave Solution

The curvature of space-time (and therefore the gravitational field) is determined by the energy-matter distribution through the Einstein equations

$$G_{\mu\nu} = R_{\mu\nu} - \frac{1}{2} g_{\mu\nu} R = \frac{8\pi G}{c^4} T_{\mu\nu} \ , \tag{1.9}$$

where c is the speed of light and G is the constant of gravitation from the law of universal gravitation of Newton. $G_{\mu\nu}$ is the Einstein tensor which describes the space-time geometry, defined as the sum

of two symmetric tensors: the Ricci tensor $R_{\mu\nu}$ and the metric tensor $g_{\mu\nu}$. The Ricci tensor derives from the contraction of the *curvature tensor* (also called the Riemann tensor) $R^{\alpha}_{\beta\mu\nu}$ with the metric tensor, according to the relation

$$R_{\mu\nu} = g^{k\alpha} R_{k\mu\alpha\nu} = R^{\alpha}_{\mu\alpha\nu} \ . \tag{1.10}$$

The curvature tensor is obtained from the first and the second derivatives of the metric tensor, through the affine connections:

$$R^{\alpha}_{\beta\mu\nu} = \Gamma^{\alpha}_{\beta\nu,\mu} - \Gamma^{\alpha}_{\beta\mu,\nu} + \Gamma^{\alpha}_{\sigma\mu}\Gamma^{\sigma}_{\beta\nu} - \Gamma^{\alpha}_{\sigma\nu}\Gamma^{\sigma}_{\beta\mu} \ . \tag{1.11}$$

$R^{\alpha}_{\beta\mu\nu}$ contains the information of how much a vector changes when it is parallel transported around a loop in a curved space-time, thereby it is said to contain the information about the curvature of space-time.

$T_{\mu\nu}$ is the *stress-energy tensor* which describes the sources of the gravitational field: matter and energy. In the simple case of a system of n non-interacting particles, each one with position ξ^{α}_{n} and four-momentum p^{α}_{n}, the T_{00} component of the tensor is the energy density of the system, the T_{0i}/c components are momentum densities, the T_{ik} are the currents of momentum of the i-th component through the unitary surface element orthogonal to the k-th axis. The stress-energy tensor is a symmetric tensor.

The Einstein equations form a set of 10 non-linear partial differential equations, whose solution is in general a complex problem. A simple solution may be obtained by applying a perturbative approach in the limit of weak gravitational field in vacuum, where the metric can be written as

$$g_{\mu\nu} = \eta_{\mu\nu} + h_{\mu\nu} \tag{1.12}$$

and $h_{\mu\nu} << 1$ is the small gravitational perturbation. Within this approximation, the Einstein equations are linear to first order with respect to $h_{\mu\nu}$ and it is possible to demonstrate that the perturbation solution propagates in space-time like a **gravitational wave**. In fact, the freedom in the choice of the coordinate system allows to impose a gauge where $h_{\mu\nu}$ is transverse and traceless (TT gauge), and eqs.(1.9) simplify to

$$\left(\nabla^2 - \frac{1}{c^2}\frac{\partial^2}{\partial t^2}\right) h_{\mu\nu} = 0 \ , \tag{1.13}$$

describing the propagation of waves at speed c. The solutions of eq.(1.13) can be written as plane waves,

$$h_{\mu\nu} = \epsilon_{\mu\nu} \exp[i(\Omega_{\rm GW} t - \vec{k}_{\rm GW} \cdot \vec{x})] \ , \tag{1.14}$$

where $\Omega_{\rm GW}$ is the angular frequency of the waves, $\vec{k}_{\rm GW}$ is the wave vector and $\epsilon_{\mu\nu}$ is the polarization tensor. In the TT gauge, the polarization tensor of a wave propagating along the z axis writes

$$\epsilon_{\mu\nu} = h_{+}\epsilon^{+}_{\mu\nu} + h_{\times}\epsilon^{\times}_{\mu\nu} \ , \tag{1.15}$$

with $\epsilon^{+}_{\mu\nu}$ and $\epsilon^{\times}_{\mu\nu}$ being the basis tensors defined as

$$\epsilon^{+}_{\mu\nu} = \begin{pmatrix} 0 & 0 & 0 & 0 \\ 0 & 1 & 0 & 0 \\ 0 & 0 & -1 & 0 \\ 0 & 0 & 0 & 0 \end{pmatrix}$$

$$\epsilon^{\times}_{\mu\nu} = \begin{pmatrix} 0 & 0 & 0 & 0 \\ 0 & 0 & 1 & 0 \\ 0 & 1 & 0 & 0 \\ 0 & 0 & 0 & 0 \end{pmatrix} .$$

Thus gravitational waves have only two possible polarization states, which are + (*plus*) and × (*cross*), both shown on fig.2.1. The important result that follows from eq.(1.15) is that the effect of a gravitational wave on the space-time metric has an intrinsic differential nature. The distance between two nearby test masses in the metric perturbed by a gravitational wave is modulated at the wave frequency with opposite sign in the plane transverse to the direction of propagation, as shown on fig.2.1.

1.3 Emission of Gravitational Waves

Gravitational waves are emitted by accelerated masses, as well as electromagnetic waves are emitted by accelerated charges. However, due to the conservation of total momentum of isolated systems, the gravitational dipole is null and gravitational waves have a quadrupolar nature. Thereby the emission of gravitational radiation is associated to the variation of the quadrupolar moment tensor of mass distribution, defined as

$$Q_{ij}(t, \vec{x}) = \frac{1}{c^2} \int_V T_{00}(t, \vec{x}) x_i x_j dV \ , \tag{1.16}$$

where $T_{00}(t, \vec{x})$ is the time component of the time-dependent stress-energy tensor. From eq.(1.16) it is clear that systems with spherically symmetric mass distribution, which do not have a quadrupole moment, cannot emit gravitational waves. In the far field and slow motion approximation (i. e. far from the source and when the typical velocities of the physical processes of the source are much smaller than light speed), the amplitude of the wave due to the quadrupolar moment tensor is

$$h_{ij} = \frac{2}{r} \frac{G}{c^4} \frac{\partial^2}{\partial t^2} Q_{ij}(t - r/c, \vec{x}) \ , \tag{1.17}$$

where r is the distance between the source and the point of observation, $t - r/c$ is the retarded time representing the delay between the wave emission and the moment when it reaches the observer. Thus the wave amplitude measured by an observer is inversely proportional to the distance traveled by the wave from the source.

The factor $G/c^4 \simeq 8 \cdot 10^{-45}$ s^2/kg m in eq.(1.17) is extremely small, yielding a very weak amplitude of the emitted wave. Starting from eq.(1.17), it can be demonstrated [2] that the generation of gravitational waves in laboratory with a controlled source is impossible. Consider for example a system of two masses of 1 tonne each, at either ends of a rod 2 m long, spinning about an axis orthogonal to the rod with an angular frequency of 1 kHz. The amplitude of the gravitational wave generated by such a machine would be

$$h \sim 10^{-33} \cdot \frac{1}{r} \ ,$$

which is of many orders of magnitude fainter than the amplitude measurable ($h \sim 10^{-21} - 10^{-23}$) by any present ground-based detector, as we will see in the next chapter. It is for this reason that the experimental study of gravitational waves is directed towards astrophysical sources.

The luminosity of the gravitational wave, that is the gravitational energy emitted by the source per unit time, writes

$$\mathcal{L} = \frac{G}{5c^5}\Big\langle \sum_{i,j=1}^{3} \dddot{Q}_{ij}\Big(t - \frac{r}{c}\Big)\ddot{Q}_{ij}\Big(t - \frac{r}{c}\Big)\Big\rangle \ , \tag{1.18}$$

where the average is performed over several wavelenghts since in General Relativity the energy of the gravitational field cannot be defined locally. Eq.(1.18) can be used to estimate with some approximation the luminosity of an astrophysical source of mass M and characteristic radius R. Let T be the characteristic time scale for the time evolution of the source, and let ϵ be a factor measuring the degree of asymmetry in the spatial mass distribution. Thus the quadrupole moment of the source is approximately equal to $Q \sim \epsilon M R^2$. The gravitational wave luminosity is then

$$\mathcal{L} = \epsilon \frac{G}{c^5}\frac{M^2R^4}{T^6} \ . \tag{1.19}$$

By introducing the Schwarzschild radius $R_S = 2GM/c^2$, which is a length scale which measures the compactness of the source, and the characteristic speed $v = R/T$, eq.(1.19) can be rewritten as

$$\mathcal{L} = \epsilon \frac{c^5}{G}\left(\frac{R_S}{R}\right)^2\left(\frac{v}{c}\right)^6 \ . \tag{1.20}$$

Eq.(1.20) indicates that the more the source is compact ($R \sim R_S$), has an asymmetric mass distribution ($\epsilon \sim 1$) and moves or evolves with a relativistic speed ($v \sim c$), the larger is the gravitational wave energy emitted per unit time.

1.4 Sources of Gravitational Waves

The sources of gravitational waves can be classified depending on the time evolution of the signal they generate:

- periodic and quasi periodic sources emitting a signal of superposed sinusoidal components, whose frequencies are more or less constant over a time interval longer than the observational time. Pulsars (pulsating neutron stars) and in general spinning neutron stars are expected to be sources of periodic gravitational wave signals, as well as coalescing binary systems of neutron stars or black holes during the early phase of their orbital motion

- transient and impulsive sources (bursts), if the expected time duration of their signal is shorter than the typical time of observation. This kind of signal is related to phenomena which involve a violent gravitational collapse, like Supernovae, magnetars or coalescing systems at the merging point

- stochastic background, if the signal is expected to fluctuate statistically and last for a time duration much longer than the typical observational time. This background can have an astrophysical or a cosmological origin.

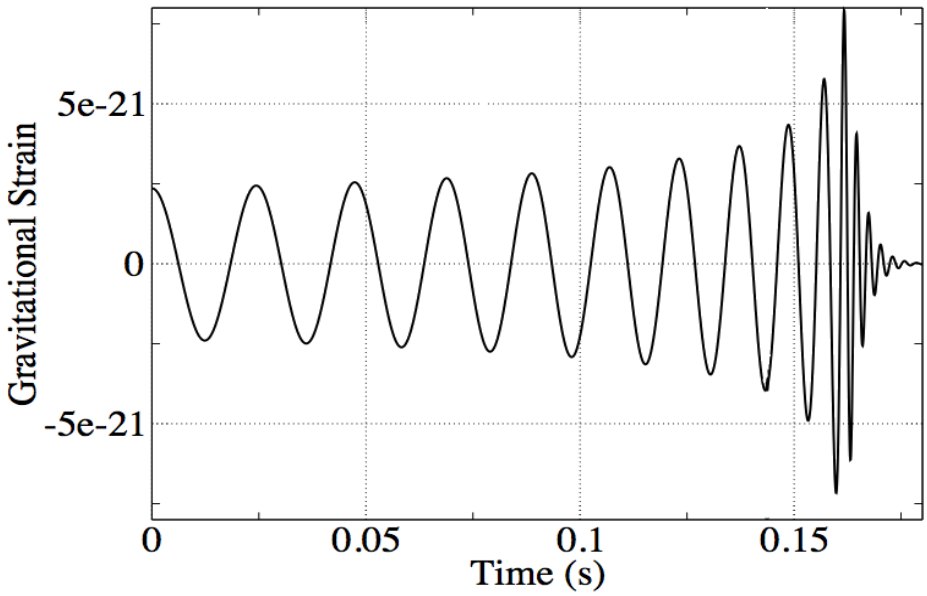

Figure 1.1: Typical *chirp* waveform emitted during the coalescence of a black-hole binary system, from [56].

1.4.1 Coalescing Binaries

A large fraction of the stellar objects presently known are binary systems. If in such a system the two stars are compact bodies, like two neutron stars, two black holes or a neutron star and a black hole, the system is expected to lose a considerable amount of energy by emission of detectable gravitational radiation. The frequency of the emitted wave is the double of the orbital one.

In the early phase of the orbital motion the emission is small, and the emitted radiation is a periodic signal with frequency of the order of mHz, too slow to be measured at Earth (in this band ground-based detectors are blinded by seismic noise due to ground vibrations). However, when the emission of gravitational radiation increases, the orbital energy decreases together with the period and the two bodies start spiralling around each other, in a phase named *coalescence*. The expected signal emitted in this phase of shrinking of the orbit has a characteristic shape called *chirp*, shown on fig.1.1, where the amplitude and frequency increase with time. By supposing that the system has a circular orbit of radius R and a total mass $M = m_1 + m_2$, the time scale of the inspiralling phase is [3]

$$t_{chirp} = \frac{5}{96}\frac{M}{\nu}\left(\frac{M}{R}\right)^{-4}, \tag{1.21}$$

where $\nu = \mu/M$ and $\mu = m_1 m_2/(m_1 + m_2)$ is the reduced mass. It is clear from eq.(1.21) that systems with large mass ratios between the bodies can spend a long time in relativistic orbits, whereas equal-mass binaries are expected to merge after only a few orbits in the relativistic regime.

The inspiral phase ends either when the bodies begin to interact and merge or when the distance between the stars is roughly equal to the last stable orbit allowed. During this period the gravitational signal is expected to be burst-like, with frequencies around 1 kHz for systems composed of two neutron stars. The characteristic amplitude of the emitted waves (for a system on a circular

source	coalescence rate $\mathcal{R}$ [$\mathrm{Myr}^{-1}\mathrm{MWEG}^{-1}$]
NS-NS	100
NS-BH	3
BH-BH	0.4

Table 1.1: Predicted compact binary coalescence rates for systems of neutron stars (NS-NS), black holes (BH-BH) and black hole-neutron star (NS-BH), from [5].

orbit) at a distance r from the source is [3]

$$h \sim \frac{1}{r}\mathcal{M}^{5/3}\Omega^{5/3} \ , \tag{1.22}$$

with

$$\mathcal{M} \equiv \mu^{3/5}M^{2/5} \tag{1.23}$$

being the *chirp mass* of the system, and Ω being the angular velocity of the orbit. For example, for a system of neutron stars at $r = 10$ Mpc with $m1 = m2 = 1.4$ solar masses and initial orbital frequency 10 Hz, the amplitude of the emitted gravitational wave is $h \sim 2 \cdot 10^{-22}$.

A compact binary coalescence is the best known among the expected gravitational wave sources. The detection of signals emitted in the inspiral phase of binary neutron-star systems would be a direct validation of the theory of General Relativity. Furthermore, a direct observation of black hole coalescences would be a test of General Relativity in a strong field regime.

The black hole-neutron star or neutron star-neutron star collisions have the potential to shine a light on the equation of state of neutron stars. In these events the neutron star is expected to be disrupted by the tidal forces due the black hole field, and the emitted gravitational wave should carry the information about the internal structure of the star. Moreover, neutron star coalescences are one of the proposed mechanisms for producing the violent shocks that would generate γ-ray burst events [4], which are flashes of gamma rays associated with extremely energetic explosions that have been observed in distant galaxies. The detection of a gravitational wave in coincidence with a γ-ray burst would be a fundamental test of the physical mechanism behind these events.

There are basically two methods to predict the number of binary neutron-star coalescence events. The empirical method, based on a few observations of compact binary systems which will coalesce on a timescale comparable with the age of the Universe, and the theoretical method, based on models of binary star formation and evolution. For black hole-neutron star and black hole-black hole events instead, it is only possible to use the same population synthesis models applied to the neutron star systems. In any case, the coalescence rates vary over about two orders of magnitude because of the large uncertainties of the observations or the assumptions of the theoretical models. The average values of coalescence rates that can be found in the literature [5] are reported in table 1.1. Rates are reported in units of number per Myr per MWEG, where MWEG stands for *Milky Way equivalent galaxy.*

1.4.2 Pulsars

Pulsars are neutron stars in rapid rotation which emit periodic pulses of electromagnetic radiation, and the period of the pulse sequence is equal to the rotation period of the star. Most of the known

pulsars emit in the radio frequency domain, but few cases of emission in the visible frequency range or at higher frequencies are also reported (the Crab pulsar, for example). Presently more than 1500 radio pulsars are known, whose period varies from 10^{-3} s up to few seconds. The period can be used to classify the pulsars into two classes of objects: the millisecond pulsars with period $P < 20$ ms, which are presumably more aged objects, and pulsars with larger period of more recent formation.

If a mass asymmetry is present at the surface of a pulsar, the star can emit gravitational radiation at twice the rotation frequency. The star can be modeled as an ellipsoid of semiaxes (a, b, c), and its quadrupole moment can be expressed in terms of a dimensionless parameter ϵ, the *ellipticity* (or oblateness), which measures the deviation from axisymmetry. If c is oriented along the rotation axis, the ellipticity is

$$\epsilon \equiv \frac{2(a-b)}{a+b} \ . \tag{1.24}$$

The emitted wave is expected to have the following characteristic amplitude:

$$h_c = 4.2 \cdot 10^{-24} \left(\frac{1 \text{ ms}}{P}\right)^2 \left(\frac{\text{kpc}}{r}\right) \left(\frac{I_3}{10^{38} \text{ kgm}^2}\right) \left(\frac{\epsilon}{10^{-6}}\right) \ , \tag{1.25}$$

where P is the rotation period and I_3 is the moment of inertia along the rotation axis. Theoretical predictions of ϵ are affected by large uncertainties and can range from 10^{-7} up to 10^{-4} [3]. By assuming that the typical radius of a pulsar is $R = 10$ km, an ellipticity of 10^{-7} corresponds to a mass asymmetry of $\epsilon R = 1$ mm. Despite the weakness of the signal expected from pulsars, their almost-periodic nature makes possible to integrate over a long period of time T to improve the signal-to-noise ratio, which increases as $\sqrt{T}$.

As for binary systems, the detection of continuous gravitational wave signals from galactic pulsars would be a fundamental test of General Relativity. Moreover, since the strength of the signal is proportional to the ellipticity parameter ϵ, the relationship between the gravitational wave emission frequency and the rate of electromagnetic pulses would help discriminating among competing mechanisms generating the axial asymmetry.

1.4.3 Supernovae

The general class of stellar collapse includes a rather wide variety of astrophysical objects, which might be roughly classified in two distinct categories on the basis of the dynamics of their formation. According to the current accepted model, Supernovae of type I originate from the gravitational collapse of a white dwarf star in a binary system. The white dwarf accretes matter from the companion until it exceeds the Chandrasekhar mass limit of 1.44 solar masses, undergoing a gravitational collapse. Following the collapse, the central core of the star reaches a temperature sufficient to trigger the combustion of heavy elements like Carbon, and the the energy released in the reaction induces a violent explosion. In most cases, the explosion causes the destruction of the star. On the other hand, Supernovae of type II should originate from the gravitational collapse of a massive aged star, in the process which leads to the formation of a neutron star.

The emission of gravitational wave radiation from a Supernova explosion happens in the phase of gravitational collapse of the star, and the amount of the emitted radiation strongly depends on the degree of asymmetry of the collapse. A collapse which is perfectly spherically symmetric would

not generate gravitational waves, whereas a highly asymmetric collapse might generate an intense emission of waves.

It is hard to estimate the expected detection rate of gravitational waves emitted during the gravitational core collapse of massive stars. While the Supernovae rate in our Galaxy and the local group of galaxies (i. e. up to distances of the order of 300 kpc) is rather low and probably less than 1 event per two decades (the last observed event was the famous Supernova 1987a), there might be one Supernova occurring about every 2 years between $3-5$ Mpc from Earth [6]. A typical Supernova explosion event should generate a gravitational wave signal in the 10^2-10^3 Hz frequency band, with a characteristic amplitude that depends on the total amount of energy released under the form of gravitational waves (ΔE_{GW}, expressed in unit of solar masses $M_\odot$) and is given by [7]

$$h_c \sim 2.7 \cdot 10^{-20} \left(\frac{\Delta E_{GW}}{M_\odot c^2}\right)^{1/2} \cdot \left(\frac{1kHz}{f_c}\right)^{1/2} \cdot \left(\frac{10Mpc}{r_0}\right) \ . \tag{1.26}$$

Recent estimates have shown that the gravitational wave energy emitted by such events might be as low as $\leq 10^{-8} M_\odot c^2$ [6].

Although there is presently very little doubt that stellar collapse might generate gravitational waves, since the modelling of these events is almost unknown it is difficult to accurately estimate the features of the signal produced. The expected signal is taken to be burst-like, with a duration of few milliseconds. The waveforms of gravitational wave signals from Supernovae are currently investigated through numerical simulations [6], with results of increasing confidence as well as the models of gravitational core collapse are constrained by observations and theoretical developments.

1.4.4 Magnetars

Magnetars are thought to be isolated neutron stars featuring extreme magnetic fields, of the order of $\sim 10^{15}$ G. The magnetar model can explain the observed properties of two classes of rare objects, the soft gamma repeaters and the anomalous X-ray pulsars. These objects are compact sources of X-rays which sporadically emit short bursts of soft gamma rays of the duration of ~ 0.1 s. Less than 20 objects with these properties are presently known.

Magnetars are likely to emit bursts of gravitational radiation through the damped pulsation of stellar non-radial vibrational modes, excited by the repeated sudden energy flares released by these stars. Depending on the different type of vibrational mode excited, magnetars may emit gravitational radiation with frequency within the $10-2000$ Hz band, i. e. in the detection band of ground-based detectors. However, due to lack of theoretical understanding of the mechanisms triggering the excitation of vibrational modes, quantitative predictions on the amplitude of gravitational-wave emission associated with magnetar bursts are quite uncertain [8].

1.4.5 Stochastic Background

A stochastic background of gravitational waves might have a twofold origin. The incoherent superposition of gravitational waves emitted by sources which are too faint or distant to be resolved individually is expected to generate an astrophysical background. Sources of this background can be divided into galactic sources, concentrated in the plane of our Galaxy, and extragalactic sources.

On the other hand, current cosmological models predict the existence of a relic stochastic background, generated during the early phase of the Universe history [9]. Such a cosmological

background is expected to be isotropic, stationary and unpolarized. Its spectrum is expected to feature the imprinting of early cosmology, carrying the information about the state of the Universe at time scales $t \sim 10^{-20} - 10^{-26}$ s, or equivalently at temperature scales $T \sim 10^7 - 10^{10}$ GeV.

The intensity of the gravitational wave background is usually characterized through the dimensionless quantity

$$\Omega_{\rm GW}(f) = \frac{1}{\rho_c}\frac{d\rho_{\rm GW}}{d(\log f)} \ , \tag{1.27}$$

which represent the normalized energy density of the gravitational radiation in the Universe per logarithmic interval of frequency. $\rho_{\rm GW}$ is the energy density of the background, f is the spectrum frequency and ρ_c is the critical energy density value for a closed Universe. The critical density is defined as

$$\rho_c = \frac{3H_0^2}{8\pi G} \ , \tag{1.28}$$

H_0 being the present value of the Hubble constant, parametrized as $H_0 = h_0 \cdot 100$ km/s/Mpc.

The estimates for the background intensity are affected by large uncertainties. The strictest limits on the $\Omega_{\rm GW}$ spectrum (for the cosmological background only) come from Big Bang nucleosynthesis model and observations [9],

$$\Omega_{\rm GW} = \textstyle\int_0^\infty h_0^2\Omega_{\rm GW}(f)d(\log f) < 5.6 \cdot 10^{-6}(N_\nu - 3) \ , \tag{1.29}$$

where N_ν is the effective number of neutrino species at the time of nucleosynthesis, and from the observation of the cosmic microwave background anisotropies (CMB) measured by COBE [9]:

$$h_0^2\Omega_{\rm GW}(f) < 7 \cdot 10^{-11}\big(H_0/f\big)^2 \ , \quad 3 \cdot 10^{-18}{\rm Hz} < f < 10^{-16}{\rm Hz} \ . \tag{1.30}$$

We will see in chapter 3 that at higher frequencies, in the detection band of the ground-based gravitational-wave detectors of first generation (ranging from about 10 Hz to about 1 kHz), this limits (taking a flat energy density spectrum) have now been beaten by LIGO measurements [10].

1.4.6 Multimessenger Astrophysics

A source of gravitational waves is reasonably likely to radiate in other ways too, and a detectable gravitational wave source should release a large amount of energy and/or be relatively close. *Multimessenger astrophysics* is the observation of the same astrophysical event or system made by different (electromagnetic, particle, gravitational-wave) observatories. Electromagnetic or particle signals may provide more information about the gravitational wave source sky position, host galaxy type, distance, emission characteristics and related astrophysical processes. On the other hand, additional coincident observations would increase the confidence in a putative gravitational wave detection candidate. Furthermore, external triggers would allow the coincidence search for weaker gravitational wave signals of lower signal-to-noise ratio in the detector data.

A typical event that would be likely better understood through the complementary observation of a gravitational wave signal are γ-ray bursts. Long γ-ray bursts (or at least those with a softer γ spectrum) might be associated with core-collapse Supernovae [11], whereas short bursts could be related with coalescing binary neutron-star or neutron star-black hole systems [4].

If observed by a network of gravitational-wave detectors, a compact binary coalescence might allow to reconstruct the distance of the source (from the observed waveform amplitude) and the

masses of the objects of the systems (from the time evolution of the waveform). If the event could be associated with an astrophysical object, for example through a complementary electromagnetic follow-up survey, it would serve as distance calibration, thus potentially competing with other observational methods for determining the cosmological Hubble constant $H(t)$. As Supernovae of type Ia are used as standard candles to determine the luminosity distance of the host galaxies, the coalescence of binary systems might be used as *standard sirens* to estimate the distance of astrophysical objects [12].

1.5 Indirect Measurement of Gravitational Radiation

Although so far gravitational waves remains undetected, the discovery and the observation in 1974 of the pulsar binary system PSR1913+16 by R. Hulse and J. Taylor [13] provided for the first time the indirect evidence of the existence of gravitational radiation. The system is formed by a pulsar and a dark companion, bound in an orbit of period $P = 7^{\mathrm{h}}\ 45^{\mathrm{m}}$.

General Relativity predicts such a system to lose energy and angular momentum via emission of gravitational waves. This loss turns into a decrease of the orbital period of the pulsar, $dP/dt < 0$, which has been measured by Hulse and Taylor and compared to the value predicted by the theory. The agreement between the measurement and the theory demonstrated indirectly the existence of gravitational waves, and for this discovery Hulse and Taylor were granted the Nobel Prize in 1993.

The shift of the orbital period of PSR1913+16 has been measured since the system discovery for more than 30 years, and is now known with great accuracy [14]:

$$\frac{dP}{dt} = -(2.4184 +/- 0.0009) \cdot 10^{-12} \tag{1.31}$$

The measured curve of the cumulated shift against time is shown on fig.1.2, together with the theoretical curve predicted by General Relativity.

Since the discovery of PSR1913+16, other pulsars in binary systems of neutron stars have been detected and observed [15]. Some of these binaries are PSR B1534+12 [16], PSR J1756-2251 [17] and PSR J0737-3039A/B [18], which is formed by two pulsars orbiting around each other. All of these binaries are relativistic systems which show a decrease of their orbital period, like the one observed for 1913+16.

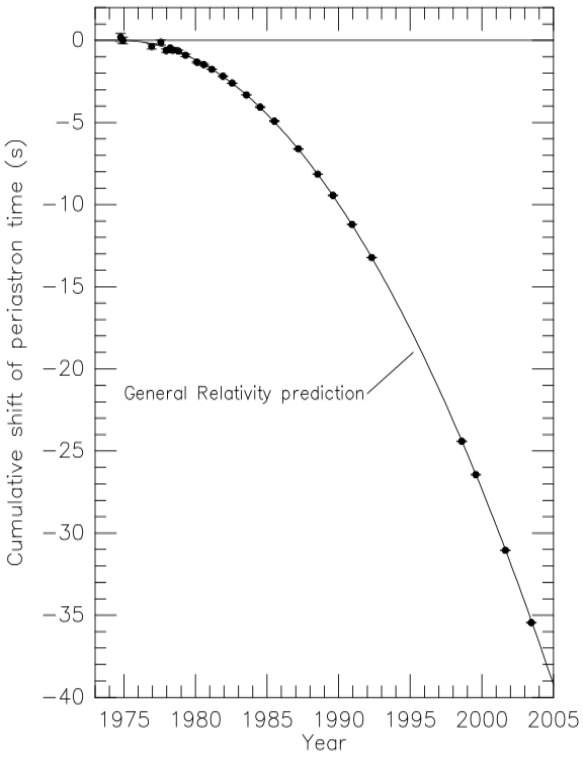

Figure 1.2: Orbital decay of PSR B1913+16, from [14]. The data points indicate the observed change in the epoch of periastron with date while the parabola illustrates the theoretically expected change in epoch for a system emitting gravitational radiation, according to General Relativity.

Chapter 2

Interferometric Detectors of Gravitational Waves

This chapter introduces the fundamental principles of interferometric detection of gravitational waves, with the aim of describing all the main components of a typical gravitational-wave interferometer. To explain the choice of interferometry as the basic principle of detection, we will show in section 2.1 the effect of the passage of a gravitational wave on a set of free-falling test particles, stressing the effect of the resulting differential strain of space-time. The Michelson interferometer with suspended mirrors, described in section 2.2, is the most appropriate instrument to measure this strain, since it has the optimal optical configuration to detect differential effects in its arms.

We will see in section 2.3 that mirrors must be suspended for a twofold reason: the suspended mirrors of the interferometer can be considered (with a reasonable approximation) free-falling test masses, furthermore they have to be isolated from seismic noise. Vibrations are a fundamental noise which affects gravitational-wave interferometers, as well as thermal noise (due to the thermal excitation of the particles in the mirror and in the suspensions) and photon counting noise. Together with technical noises of the laser, fundamental noises limit the smallest signal detectable by the interferometer. All these noise sources are described in section 2.4.

To increase the sensitivity of the interferometer, optical resonators can be used. Since the strain sensitivity of the interferometer is directly proportional to the optical path length in its arms, kilometer-scale Fabry-Perot arm cavities are used to increase the effective length traveled by the laser light. In order to decrease the photon noise, the power stored in the detector can be increased with a power recycling cavity coupled to the rest of the interferometer. The laser noise at the interferometer input can be filtered with an input mode-cleaner cavity, whereas the contrast at the detector output can be increased by using an output mode-cleaner cavity. The basic working principle of optical resonators will be illustrated in section 2.6.

2.1 Geodesic Deviation

From the theory of General Relativity we know that the motion of a single probe particle is not affected by the field perturbation of a gravitational wave. To detect a gravitational wave, a system of at least two test particles must be used. If δx^λ is the distance between the two particles ($\lambda = 0, 1, 2, 3$), the effect of the passage of a gravitational wave on such a system is described by the

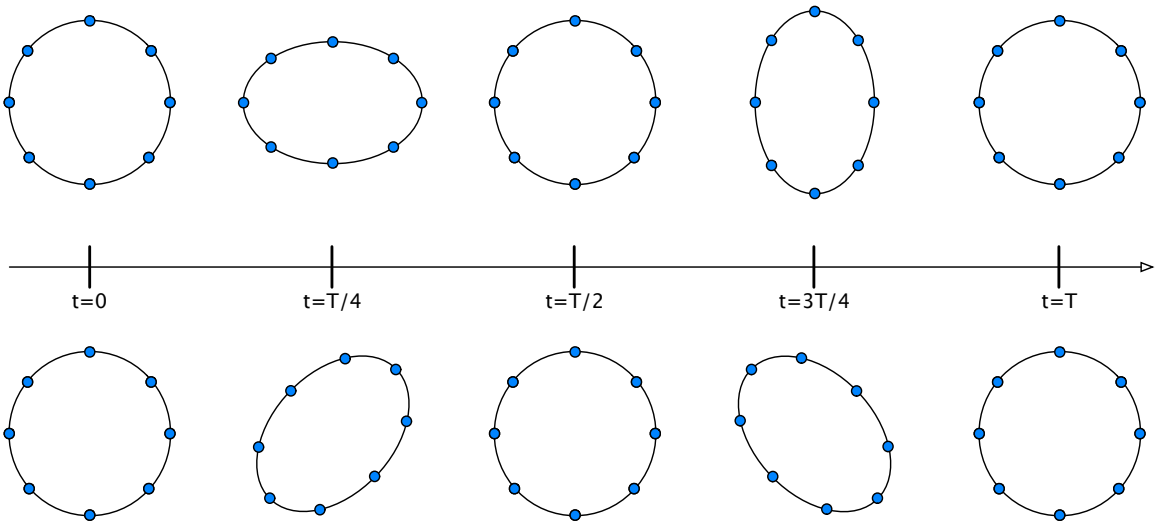

Figure 2.1: Effect of + (top row) and × (bottom row) polarized gravitational waves propagating along the z axis on a ring of free falling masses in the $x-y$ plane. The strain is shown every quarter of wave period T.

equation of geodesic deviation,

$$\frac{d^2\delta x^\lambda}{d\tau^2} = R^\lambda_{\nu\beta\mu}\frac{dx^\beta}{d\tau}\frac{dx^\nu}{d\tau}\delta x^\mu \ , \tag{2.1}$$

which shows that the relative acceleration $d^2\delta x^\lambda/d\tau^2$ of particles moving along nearby geodesics depends on the curvature tensor $R^\lambda_{\nu\beta\mu}$. It can be demonstrated that if the gravitational wave $h_{\mu\nu}$ perturbs a flat space-time metric, i. e. the metric tensor can be written as $g_{\mu\nu} = \eta_{\mu\nu} + h_{\mu\nu}$, eq.(2.1) simplifies to

$$\frac{d^2}{dt^2}\delta x^\lambda = \frac{1}{2}\eta^{\lambda i}\frac{\partial^2 h_{im}}{\partial t^2}\delta x^m \ , \tag{2.2}$$

where $h_{\mu\nu}$ is the wave perturbation in the TT gauge ($i, m = 1, 2, 3$). The solution to this equation is

$$\delta x^\lambda = \delta x^\lambda_0 + \frac{1}{2}\eta^{\lambda i}h_{ik}\delta x^k_0 \ , \tag{2.3}$$

which is the sum of an unperturbed term δx^λ_0 and a term which depends on the perturbation of the gravitational wave, $\eta^{\lambda i}h_{ik}\delta x^k_0/2$. Thus the relative distance of the two particles varies in time according to the oscillatory perturbation of the wave.

The result of eq.(2.3) can be generalized to more complex systems of bodies. For example, fig.2.1 shows the effect of a polarized gravitational wave passing through a system of particles arranged on a circumference. It is very clear from this figure the differential effect of the wave perturbation in the (x, y) plane perpendicular to the propagation axis of the wave. This effect is the key principle at the basis of gravitational wave detection with interferometers based on the Michelson configuration.

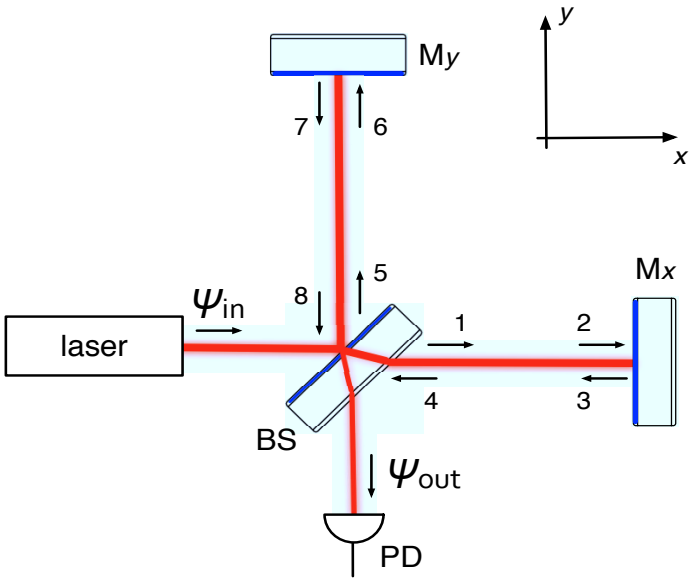

Figure 2.2: Optical scheme of the Michelson interferometer: the laser, the beamsplitter (BS), the arm mirrors (M_x and M_y), the photodiode (PD) and the field notation (ψ_i) are shown.

2.2 The Michelson Inteferometer

The basic optical configuration of all interferometric gravitational wave detectors is the Michelson interferometer [19, 20]. In its simplest form – depicted in fig.2.2 – the Michelson interferometer consists of a source of light, a partially reflecting mirror called beamsplitter, and two end mirrors located at a distance l from the beamsplitter along two orthogonal directions, forming two arms. The light coming from the source (which is usually a laser) propagates to the beamsplitter, where it is divided in two beams. One beam is transmitted through the beamsplitter, one is reflected. Both beams propagate in the arms towards the end mirrors, where they are reflected backwards to recombine at the beamsplitter. A photodiode, placed at the output of the interferometer, converts the light of the interference fringe in a current signal.

The function of the Michelson interferometer is to compare the amount of time the light beams take to complete their paths in the two arms, or equivalently, to measure the phase difference acquired by the light beams in their round trip in the arms. By computing the electromagnetic fields inside the interferometer, it is possible to demonstrate that the output signal depends on the phase difference of the two light beams interfering at the beamsplitter. Let ψ_{in} be the input electromagnetic field, which for simplicity will be a plane wave. Each mirror is characterized by an amplitude reflectivity r_i and an amplitude transmissivity t_i $(i = 1, 2)$, defined by the ratio of reflected electric field to the incident field at the surface. For the propagation in the instrument, the following conventions are used:

- the field propagated over a distance L is $\psi = \psi_{in} e^{-ikL}$
- the field reflected by a mirror of reflectivity r is $\psi = -r\psi_{in}$

- the field transmitted by a mirror of transmissivity t is $\psi = t\psi_{in}$
- the total energy is conserved: $r^2 + t^2 + L_{opt} = R + T + L_{opt} = 1$,

where λ is the light wavelength, $k = 2\pi/\lambda$ is the wave number, L_{opt} is the amplitude loss coefficient of mirrors. The electromagnetic fields inside the interferometer are:

$$\begin{array}{ll} \psi_1 = t_{BS}\psi_{in} & \psi_5 = -r_{BS}\psi_{in} \\ \psi_2 = \exp(-ikL_1)\psi_1 & \psi_6 = \exp(-ikL_2)\psi_5 \\ \psi_3 = -r_1\psi_2 & \psi_7 = -r_2\psi_6 \\ \psi_4 = \exp(-ikL_1)\psi_3 & \psi_8 = \exp(-ikL_2)\psi_7 \ , \end{array}$$

where r_i and t_i are the reflectivity and the transmissivity of the i-th mirror, respectively. At the output, the field is

$$\begin{array}{rcl} \psi_{OUT} & = & -r_{BS}\psi_4 + t_{BS}\psi_8 \ = \\ & = & r_{BS}t_{BS}\psi_{in}(r_1 e^{-i2\omega L_1/c} + r_2 e^{-i2\omega L_2/c}) \ , \end{array} \tag{2.4}$$

where L_1 and L_2 are the lengths of the two arms, $\omega/2\pi$ is the frequency of the monochromatic light source (which is usually a laser), c is the speed of light. Thus the amplitude of the light leaving the interferometer depends on the difference in phase $\phi = 2\omega(L_2 - L_1)/c$ cumulated by the light beams traveling in the two arms. The power on the output photodiode is

$$P_{OUT} = P_{IN}R_{BS}T_{BS}(R_1 + R_2 + 2r_1 r_2 \cos\phi) \ , \tag{2.5}$$

with $P_{IN} = |\psi_{IN}|^2$ and $P_{OUT} = |\psi_{OUT}|^2$. The maximum output power of the interferometer is $P_{MAX} = P_{OUT}(\phi = 0)$, whereas the minimum output power is $P_{min} = P_{OUT}(\phi = \pi)$. The output power can thus be rewritten as

$$P_{OUT} = P_{IN}R_{BS}T_{BS}(R_1 + R_2)(1 + C\cos\phi) \ , \tag{2.6}$$

where

$$C = \frac{P_{MAX} - P_{min}}{P_{MAX} + P_{min}} = \frac{2r_1 r_2}{R_1 + R_2} \tag{2.7}$$

is the contrast of the interferometer. From eq.(2.6) it is clear that any change in the lengths l_1 and l_2 causes a change in the photodiode output current, so the Michelson interferometer acts as a transducer from travel time difference to output optical power.

Assuming that the mirrors of the interferometer behave approximately like free-falling test masses (we will see how in the next section), the detector can be used to measure the phase change of light induced by the passage of a gravitational wave. The wave will change the optical path length traveled by the light in the interferometer arms. Because of the differential nature of the strain induced by a gravitational wave, shown on fig.2.1, the optical path variation will have opposite sign in the two arms of the interferometer. Thereby the passage of the wave will modulate in time the interference fringe at the output of the detector.

The phase shift due to an incident gravitational wave can be computed by making some simple assumptions. Let the interferometer arms be equally long and oriented along the x and y axis, with a symmetric beamsplitter ($R_{BS} = T_{BS}$) at the origin. Then, since the paths taken by light in each arm will have only either dx or dy different from zero, we will consider only the 11 and

22 components of the metric. The light beam traveling in the x arm obeys the condition of null geodesic (i. e. the interval between two neighboring space-time events linked by a light beam is always null),

$$\begin{aligned} ds^2 &\equiv g_{\mu\nu}dx^\mu dx^\nu \\ &= (\eta_{\mu\nu} + h_{\mu\nu})dx^\mu dx^\nu \\ &= -c^2dt^2 + \Big(1 + h_{11}\exp[i(\Omega_{\rm GW}t - \vec{k}_{\rm GW}\cdot\vec{x})]\Big)dx^2 = 0 \ , \end{aligned} \tag{2.8}$$

where $\Omega_{\rm GW}/2\pi$ is the wave frequency and $\vec{k}_{\rm GW}$ is the wave vector. The time the light takes to travel from the beamsplitter to the x end mirror at a distance L is

$$\tau_1 = \int_0^{\tau_1} dt = \frac{1}{c}\int_0^L \sqrt{1+h_{11}}\ dx \simeq \frac{1}{c}\int_0^L \Big(1 + \frac{1}{2}h_{11}\exp[i(\Omega_{\rm GW}t - \vec{k}_{\rm GW}\cdot\vec{x})]\Big)dx \ , \tag{2.9}$$

and for the return trip a similar equation holds:

$$\tau_2 = \int_{\tau_1}^{\tau_2} dt = -\frac{1}{c}\int_L^0 \Big(1 + \frac{1}{2}h_{11}\exp[i(\Omega_{\rm GW}t - \vec{k}_{\rm GW}\cdot\vec{x})\Big)]dx \ . \tag{2.10}$$

Thereby the total round trip time in the x arm is

$$\Delta\tau_x = \frac{2L}{c} + \frac{1}{2c}\int_0^L h_{11}\exp[i(\Omega_{\rm GW}t - \vec{k}_{\rm GW}\cdot\vec{x})]dx - \frac{1}{2c}\int_L^0 h_{11}\exp[i(\Omega_{\rm GW}t - \vec{k}_{\rm GW}\cdot\vec{x})]dx \ , \tag{2.11}$$

and an analogous expression can be written for the light round-trip time $\Delta\tau_y$ in the y arm (recalling that $h_{22} = -h_{11}$):

$$\Delta\tau_y = \frac{2L}{c} - \frac{1}{2c}\int_0^L h_{11}\exp[i(\Omega_{\rm GW}t - \vec{k}_{\rm GW}\cdot\vec{x})]dy + \frac{1}{2c}\int_L^0 h_{11}\exp[i(\Omega_{\rm GW}t - \vec{k}_{\rm GW}\cdot\vec{x})]dy \ . \tag{2.12}$$

Thus, due to the quadrupolar nature of gravitational of the impinging gravitational wave, there will be equal and opposite perturbations to the light travel time in the two arms. For sake of simplicity, consider a plane wave propagating along the direction z perpendicular to the plane z_0 of the interferometer, and let the wave be + polarized with amplitude $h_+ \equiv h$. Then eq.(2.11) and (2.12) yield the total time difference

$$\Delta\tau(\Omega_{\rm GW}) = \Delta\tau_x - \Delta\tau_y = \frac{h}{i\Omega_{\rm GW}}\Big[e^{i2\Omega_{\rm GW}L/c} - 1\Big] = h\frac{2L}{c}\frac{\sin\left(\frac{\Omega_{\rm GW}L}{c}\right)}{\frac{\Omega_{\rm GW}L}{c}}e^{i\Omega_{\rm GW}L/c} \ , \tag{2.13}$$

corresponding to the phase difference

$$\Delta\phi(\Omega_{\rm GW}) = \frac{2\pi c}{\lambda}\Delta\tau(\Omega_{\rm GW}) \tag{2.14}$$

of the output field. Eq.(2.14) represents the *frequency response* of the interferometer, and its modulus is shown in fig.2.3. This figure puts in evidence the $1/f$ decay of the response for frequencies $\Omega_{\rm GW}/2\pi$ greater than $c/2L$, and the existence of frequencies for which no phase change is generated. This happens when $\Omega_{\rm GW}/2\pi = nc/2L$ with $n \in \mathbb{N}$, i.e. when the phase variation period of the gravitational wave is equal to the round trip time of light in the arms.

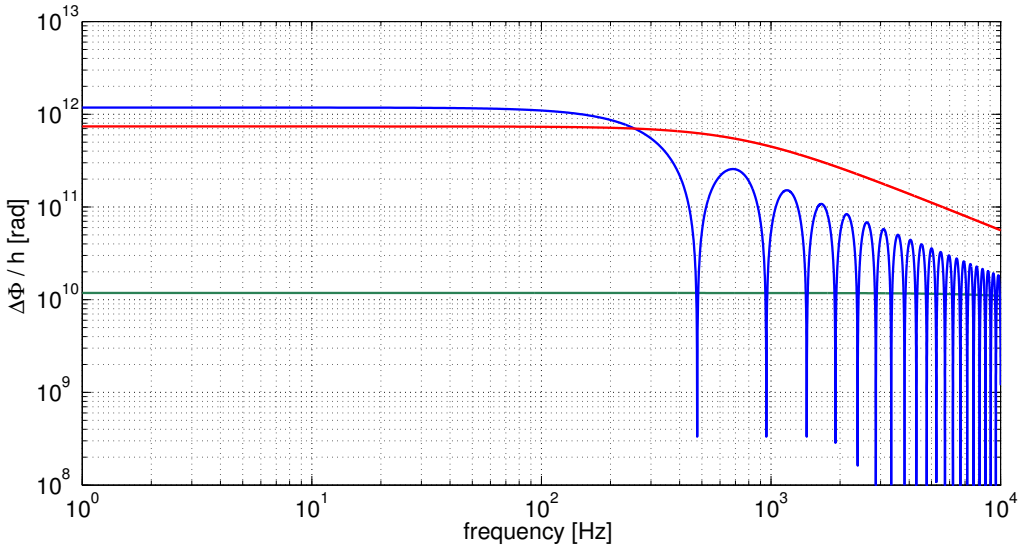

Figure 2.3: Magnitude of the frequency response of a Michelson interferometer with 1-km long arms (green curve) and 100-km long arms (blue curve), compared to that of a Michelson interferometer with 1-km long Fabry-Perot cavities in the arms (mirror reflectivities: $R_1 = 88\%$ and $R_2 = 1$, red curve).

The response of the instrument is optimal when the frequency of the incident wave is smaller than $c/2L$, that is

$$\frac{\Omega_{\rm GW}}{2\pi} << \frac{c}{2L} \ . \tag{2.15}$$

When this condition is verified, the phase of the incident wave can be considered approximately constant during the time any given wavefront is traveling in the interferometer, and the phase difference of the light at the beamsplitter simplifies to

$$\Delta\phi = \frac{4\pi}{\lambda} hL \ . \tag{2.16}$$

Eq.(2.16) clearly indicates that the response of the interferometer is directly proportional to the length of its arms. For gravitational waves of given amplitude, the sensitivity of the interferometer is higher as the arms are longer.

In the case the wave has both polarizations and its arrival direction is not perpendicular to the plane of the interferometer, the response of the detector can be generalized to [2]

$$\Delta\phi = h \ \frac{4\pi L}{\lambda} \left(\frac{1}{2}(1+\cos^2\Theta)\cos 2\Phi \cos 2\Psi - \cos\Theta \sin 2\Phi \sin 2\Psi \right) \ , \tag{2.17}$$

where (Θ, Φ, Ψ) are the angles between the wave vector and the frame containing the detector. Eq.(2.17) shows that the response, or *antenna pattern*, is function of the arrival angle. The pattern, shown on fig.2.4, is non-directional with nulls along the bisector of the arm axes. In these directions the arm length changes are always equal in the two arms, yielding no response.

On one hand the broad angular response is an advantage, since the detector can survey almost the whole sky. On the other hand, it is a disadvantage since such a response forbids the identification

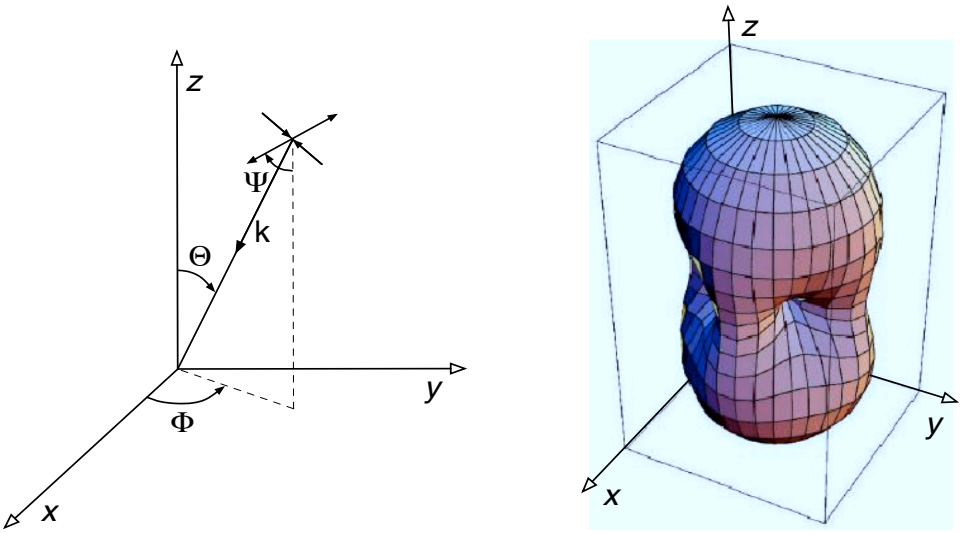

Figure 2.4: Antenna pattern of an interferometric gravitational wave detector. The arms of the interferometer are oriented along the x and y axes.

of the wave arrival direction, preventing the pointing of an electromagnetic receiver to collect any potential complementary signal from the source. As we will see in chapter 3, the arrival direction might be reconstructed by using the signal of the wave recorded by a network of detectors.

2.3 Free-falling Mirrors

The mirrors of a gravitational wave interferometer must be suspended like pendulums, for two fundamental reasons: (i) suspended mirrors behave like free-falling masses in the frequency range above the pendulum resonance, and (ii) as it will be shown in section 2.4, the suspension isolates the optics from ground vibrations which are cause of noise.

Let us consider a mirror of mass m suspended to a massless wire of length l, moving with small oscillation amplitude and with no dissipation of energy. If we indicate by $x(t)$ the mirror position, by $x_0(t)$ the position of the suspension point and by $F(t)$ any force acting on the mirror, the equation of motion is

$$F(t) - m\omega_0^2[x(t) - x_0(t)] = m\frac{d^2\ x(t)}{dt^2}\ , \tag{2.18}$$

with ω_0^2 being the resonant angular frequency. In the angular frequency domain, the solution to eq.(2.18) writes

$$x(\omega) = \frac{\omega_0^2 x_0(\omega) + F(\omega)/m}{\omega_0^2 - \omega^2}\ . \tag{2.19}$$

From eq.(2.19) one can easily compute the transfer function

$$G(\omega) = \frac{x(\omega)}{x_0(\omega)}\ , \tag{2.20}$$

which relates the input function $x_0(\omega)$ of the system to the output function $x(\omega)$. In absence of external forces, $F(\omega) = 0$, the transfer function is

$$G(\omega) = \frac{\omega_0^2}{\omega_0^2 - \omega^2} \ , \tag{2.21}$$

meaning that

- below the resonance ($\omega << \omega_0$) the motion of the suspension point (due for example to ground vibrations) is entirely transmitted to the mirror: $x(\omega) \approx x_0(\omega)$
- above the resonance ($\omega >> \omega_0$) the displacement of the mirror is attenuated like

$$G(\omega) \approx \frac{\omega_0^2}{\omega^2} \ . \tag{2.22}$$

From eq.(2.19) we can see that the motion of the mirror for frequencies $\omega >> \omega_0$ is described by

$$m\omega^2 x(\omega) + F(\omega) \approx 0 \ , \tag{2.23}$$

which is the equation of motion of a free mass. Under this condition, the effect of the gravitational wave impinging on the detector is effectively described by eq.(2.8).

2.4 Sensitivity and Noise Sources

The output signal of a gravitational wave interferometer is affected by noise, which consists in random fluctuations of the measured output power. These fluctuations are associated to perturbations of the mirror position and to noise sources that affect the optical read-out system (composed by the laser and the photodiode). The fundamental noise sources that affect the detector are

- the fluctuation of the number of photons impinging on the detection photodiode (*shot noise*)
- the fluctuation of the laser radiation pressure on the mirrors
- the seismic excitation of the ground
- the stochastic fluctuations of the gravitational field around the detector, which couple directly to the mirrors
- the thermal excitation of the mirrors and the suspension wires.

The technical noise sources, instead, are

- the amplitude, frequency and position (*jitter*) fluctuations of the laser beam
- fluctuations of the refraction index along the optical path of the laser
- parasite diffused light that couples into the main laser beam generating phase noise
- electronic noise in the main interferometer read-out and control systems

The common effect of these noise sources is the generation of a random time-dependent phase shift $\delta\phi(t)$ which mimics the effect of an incident gravitational wave and limits the detection of astrophysical signals.

The noise of the detector can be characterized by means of its power spectral density

$$S(f) = \lim_{T\to\infty} \frac{2}{T} \left| \int_{-T}^{T} A(t) e^{-2i\pi f t} dt \right|^2 , \tag{2.24}$$

where $A(t)$ represents the time evolution of the measured physical quantity. Form eq.(2.24) one can compute the linear spectral density

$$\tilde{s}(f) = \sqrt{S(f)} , \tag{2.25}$$

measured in $[A]/\sqrt{\text{Hz}}$, and the mean amplitude of noise fluctuations

$$A_{rms} = \sqrt{\int_0^\infty S(f) df} . \tag{2.26}$$

In order to quantify the noise in terms of the measurable gravitational wave amplitude, we can impose $A(t) \equiv h(t)$ so that we introduce the equivalent strain noise spectral density $\tilde{h}(f)$ (defined only for positive frequencies). For example, if $\tilde{x}(f)$ is the linear spectral density of mirror displacement noise, the equivalent-strain noise is

$$\tilde{h}(f) = \frac{\tilde{x}}{L} , \tag{2.27}$$

with L being the interferometer arm length. In the following we will describe in detail the noise sources mentioned above, giving for each of these the corresponding equivalent-strain noise $\tilde{h}(f)$.

2.4.1 Shot Noise

The shot noise is a fundamental noise due to the quantum nature of light. Measuring the optical power at the output of the detector is equivalent to determining the number of photons impinging on the photodiode during the measurement interval, which follows a Poisson distribution. Let us recall the expression of the output power from eq.(2.6):

$$P_{OUT} = P_0(1 + C\cos\phi) . \tag{2.28}$$

Thus the average number of photons of energy $\hbar\omega$ detected in the time Δt is

$$\bar{N} = \frac{\eta P_0 \Delta t}{\hbar\omega}(1 + C\cos\phi) , \tag{2.29}$$

where η is the photodiode quantum efficiency. The power fluctuation associated to the variance $\sigma_{\bar{N}}$ of the number of photons is

$$\delta P_{shot} = \sqrt{\frac{\eta P_0 \hbar\omega}{\Delta t}(1 + C\cos\phi)} . \tag{2.30}$$

The passage of a gravitational wave yields an output power (to first order approximation) equal to

$$P_{OUT}(\phi + \delta\phi_{\rm GW}) \simeq P_{OUT}(\phi) + \frac{dP}{d\phi}\delta\phi_{\rm GW} = P_{OUT}(\phi) + \delta P_{\rm GW} \ , \tag{2.31}$$

where $\delta\phi_{\rm GW}$ is the phase perturbation and

$$\delta P_{\rm GW} = -\frac{P_0}{2} C \delta\phi_{\rm GW} \sin\phi \tag{2.32}$$

is the power change due to the passage of the wave. Eq.(2.32) shows that the slope $dP/d\phi$ is maximum when $\sin\phi = 1$, in the *mid-fringe* condition. If, however, we consider the signal to noise ratio due to the presence of shot noise,

$$\frac{S}{N} = \frac{|\delta P_{\rm GW}|}{\delta P_{shot}} = \sqrt{\frac{\eta P_0 \Delta t}{\hbar\omega}} \frac{C\sin\phi}{\sqrt{(1 + C\cos\phi)}} \delta\phi_{\rm GW} \ , \tag{2.33}$$

this ratio is maximum when

$$\cos\phi = \frac{-1 + \sqrt{1 - C^2}}{C} \ , \tag{2.34}$$

close to the *dark fringe* condition (destructive interference). We will see in section 2.6 that the the dark fringe condition is also necessary to realize the recycling of the power circulating in the detector. On the dark fringe, assuming $C \simeq 1$, the minimum detectable phase shift ($S/N = 1$) due to shot noise is

$$\delta\phi_{shot} = \sqrt{\frac{\hbar\omega}{\eta P_0 \Delta t}} \ , \tag{2.35}$$

which corresponds to an equivalent noise spectral density limit of

$$\tilde{h}_{shot} = \frac{\lambda}{2\pi L}\sqrt{\frac{\hbar\omega}{\eta P_0}} \ [1/\sqrt{\rm Hz}] \ . \tag{2.36}$$

The shot noise spectrum is flat, i. e. there is no preferred frequency scale for this noise: the arrival of each photon is independent of the arrival of each of the others. For $L = 1$ km, $\lambda = 1.064$ μm and $P_0 = 10$ W the shot noise equivalent-strain is

$$\tilde{h}_{shot} \sim 10^{-20} \ [1/\sqrt{\rm Hz}] \ . \tag{2.37}$$

In a detector with Fabry-Perot arm cavities, as described in section 2.6, the spectrum of shot noise is flat only below the frequency cut-off of the cavity. Eq.(2.36) indicates that shot noise could be lowered by increasing the interferometer arm length, together with the laser power.

2.4.2 Radiation Pressure Noise and Quantum Limit

The power fluctuations associated to the quantum nature of light generate a radiation pressure noise, which make the mirrors of mass m move with a frequency spectrum [2]

$$\tilde{x}(f) = \frac{1}{mf^2}\sqrt{\frac{\hbar P_0}{8\pi^3 c\lambda}} \ . \tag{2.38}$$

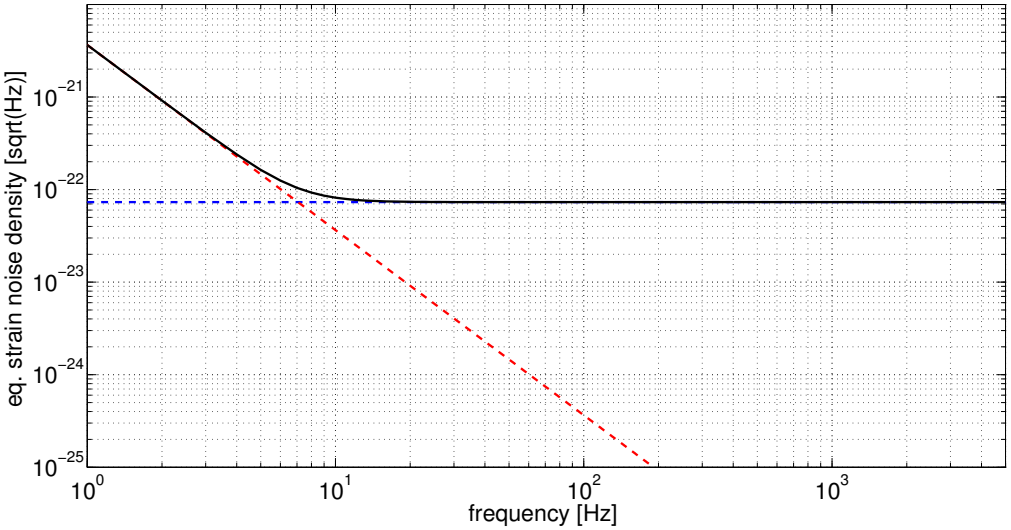

Figure 2.5: Equivalent strain spectral density of read-out noise (black curve), shot noise (blue curve) and radiation pressure noise (red curve) for $L = 1$ km, $m = 20$ kg, $P_0 = 1$ MW.

The corresponding equivalent strain noise spectrum is

$$\tilde{h}_{rp} = \frac{1}{mLf^2}\sqrt{\frac{\hbar P_0}{2\pi^3 c\lambda}} \ , \tag{2.39}$$

which shows that radiation pressure noise increases as the power in the detector increases and is proportional to $1/f^2$. Thus radiation pressure noise and shot noise can be considered as two aspects of a unique optical readout noise, given (in the interferometer configuration under discussion) by the quadrature sum

$$\tilde{h}_{or}(f) = \sqrt{\tilde{h}^2_{shot} + \tilde{h}^2_{rp}} \ . \tag{2.40}$$

At low frequencies the radiation pressure term will dominate, whereas at high frequencies the shot noise is more important, as shown by fig.2.5. We could improve the high frequency sensitivity by increasing P_0, at the expense of increased noise at low frequency. At any given frequency f, there is a minimum noise spectral density: this occurs when the power P_0 is chosen to have the value the optimal value that yields $\tilde{h}_{shot} = \tilde{h}_{rp}$. This optimal power is

$$P_{opt} = \pi c\lambda m f^2 \ , \tag{2.41}$$

which is typically quite large. For a set of parameters with $m = 20$ kg, $\lambda = 1.064$ μm and $f = 100$ Hz, the optimal power is 200 MW. This value is far higher than the power stored in present detectors, which is of the order of 30 kW. Second and third generation detectors are expected to store from about 1 to few megawatts, respectively.

In analogy to to the Heisenberg uncertainty principle, we can state that shot and radiation pressure noise set a *quantum limit* to the sensitivity of the interferometer. Shot noise represents the minimum uncertainty related to the measurement of mirror position, while radiation pressure noise causes the mirrors move in a random way. In this sense, these two sources of noise are

conjugate phenomena. We can compute the quantum limit by replacing eq.(2.41) into eq.(2.40), yielding

$$\tilde{h}_{QL} = \frac{1}{\pi f L}\sqrt{\frac{\hbar}{m}} \ , \tag{2.42}$$

which is the locus of the minima of $\tilde{h}_{or}(f)$ at any given frequency. This limit does not depend on P_0 or any feature of the optical readout scheme.

2.4.3 Seismic Noise

Seismic noise is due to the vibrations of the ground, which couple to the mirrors via the suspension system. There is no universal law describing this noise. Ground vibrations are caused by seismic and ocean activity, wind, human activity. Thus seismic noise intensity can vary of orders of magnitude from place to place, and in the same place from day to day. A general $1/f^2$ behavior has been observed worldwide in the 10 mHz−10 kHz region, following the empirical law [21]

$$\tilde{x}_s(f) = 10^{-7} \text{ m Hz}^{-1/2} \left(\frac{1\text{Hz}}{f}\right)^2 \ , \tag{2.43}$$

which corresponds to an equivalent strain noise spectrum of $\tilde{x}_s(f)/L$. To get rid of seismic noise, mirrors have to be isolated through a suspension system of suitable filters. For example, if N pendulums were cascaded in a single chain, the transfer function of the system would be (recalling eq.(2.20))

$$\frac{x(\omega)}{x_0(\omega)} = \prod_{k=1}^{N} \frac{\omega_k^2}{\omega_k^2 - \omega^2} \ , \tag{2.44}$$

where $\omega_k^2/2\pi$ are the N resonant frequencies of the system. For $\omega >> \omega_k \ \forall k$, the attenuation is given by

$$\frac{x(\omega)}{x_0(\omega)} \simeq \prod_{k=1}^{N} \frac{\omega_k^2}{\omega^2} \ , \tag{2.45}$$

which shows that in principle an arbitrarily steep low pass filter for ground vibrations might be built, by cascading a large number of oscillators. The filter cut-off frequency depends on the resonant frequencies ω_k of the system. The lower the frequencies, the wider the range where vibrations are attenuated. Nevertheless, due to technical limitations (for example, the number of pendulums and their length are limited by the space available for suspension), seismic noise below ~ 1 Hz cannot be attenuated and remains one of the main limitations to the sensitivity of ground based detectors.

2.4.4 Gravity Gradient Noise

Gravity gradient noise (also called Newtonian noise) is caused by fluctuations of the local gravitational field. These fluctuations are induced by the time variation of mass density distribution around the mirrors, because of seismic waves in the ground [22] and sound waves and temperature perturbations in air [23]. For instance, the equivalent noise strain due to seismic gravity gradient noise is [24]

$$\tilde{h}_{GG}(f) \sim 1.2 \cdot 10^{-11} \frac{\tilde{x}_s(f)}{f^2} \ , \tag{2.46}$$

where $\tilde{x}_s(f)$ is the local seismic noise spectrum. The amplitude of noise due to atmospheric fluctuation is estimated to be of similar size to the seismic ground motion [23]. Gravity gradient noise is a fundamental limitation for the sensitivity of ground-based detectors at frequencies below ~ 10 Hz, since gravity field fluctuations bypass the suspension system and couple directly to the mirrors.

A suitable solution to decrease this noise might be the identification of a quiet site for the installation of the detector, like an underground site where atmospheric perturbations are relatively far from the mirrors, the environmental conditions are stable and seismic waves are attenuated [25]. Another option to mitigate gravity gradient noise might be the subtraction of the estimated noise contribution itself, from the detector output [26, 25]. Since this noise cannot be measured directly with the required precision, except than with a gravitational-wave detector, the noise contribution should be predicted by monitoring the seismic field around the mirrors and feeding the data to a model of the sources. Both methods of mitigation might be implemented in third-generation detectors, which will be presented in chapter 3.

2.4.5 Thermal Noise

Thermal noise consists in random fluctuations of a physical variable of a system which is in thermal equilibrium with its surrounding. In gravitational-wave interferometers, thermal noise shows up as fluctuations of the position of mirrors. According to the fluctuation-dissipation theorem, the amplitude of these fluctuations is related to the dissipative mechanisms of the system, which drive the irreversible dissipation of energy into heat [27]. The power spectral density of mirror thermal displacement can be calculated starting from the knowledge of the admittance $Y(f)$ of the system, which characterizes the irreversible response of the system to applied forces:

$$S_{TN}(f,T) = \frac{k_B T}{\pi^2 f^2} \mathfrak{Re}\Big[Y(f)\Big] \ , \tag{2.47}$$

where κ_B is the Boltzmann constant and T is temperature of the system. This is equivalent to say that the system is subject to a generalized thermal force with power spectrum

$$|F_{TN}(f,T)|^2 = 4k_B T \mathfrak{Re}\Big[Z(f)\Big] \ , \tag{2.48}$$

with $Z(f) \equiv Y^{-1}(f)$ being the generalized impedance of the system.

Since dissipations take place in mirrors and in their suspension wires, the global spectral density of thermal noise is given by the sum of the spectral densities of mirror thermal noise and suspension thermal noise. Suspension thermal noise is in turn given by the sum of pendulum thermal noise, associated to the pendular suspension of mirrors, and of the thermal noise related to the transverse vibrational modes of wires. Mirror thermal noise is given by the sum of substrate thermal noise and coating thermal noise as well.

As we will see hereafter and later on, thermal noise is the dominant source of noise in the central region of the detection band of present interferometers, and is expected to severely affect the sensitivity of future detectors. To give a global picture of all thermal noise contributions, we will introduce hereafter the power spectral densities of suspension and mirror thermal noise. To follow the notation used in the literature, we will introduce *displacement power* spectral densities $S(f)$ instead of usual *linear strain* spectral densities $\tilde{h}(f)$. If L is the length of the interferometer arms, the relation between the two is given by

$$\tilde{h}(f) = \sqrt{S(f)}/L = \tilde{x}(f)/L \ . \tag{2.49}$$

Suspension thermal noise

Two main contributions of thermal noise originate in the suspension system. The first is pendulum thermal noise, where thermally induced motion associated with the pendulum mode of the suspension directly affects the displacement of the test mass. In order to calculate the thermal displacement due to pendular suspensions, the system can be treated as a damped harmonic oscillator with a frequency-dependent damping factor $\Phi(f)$. If m is the mirror mass and k is the elastic constant of the suspension, according to eq.(2.47) the pendulum thermal noise spectral density is [28]

$$S(f,T) = \frac{k_B T}{2\pi^3 m f} \frac{f_0^2 \Phi(f,T)}{\left[(f^2 - f_0^2)^2 + f^4 \Phi^2(f,T)\right]} \ . \tag{2.50}$$

The pendulum damping factor is [28]

$$\Phi(f,T) = \sqrt{\frac{nYI}{mgL^2}} \phi(f,T) \ , \tag{2.51}$$

where $\phi(f,T)$ is the loss of the suspension material, Y is its Young modulus, I is the cross-sectional moment of inertia of wires, L is the wire length, n is the number of wires of the suspension. The loss term itself consists of three main contributions:

$$\phi(f,T) = \phi_{bulk} + \phi_{TE}(f,T) + \phi_S \ . \tag{2.52}$$

The bulk loss ϕ_{bulk} is the internal intrinsic loss of the material, $\phi_{TE}(f,T)$ is the thermo-elastic contribution, ϕ_S is a surface loss term. The thermo-elastic loss is due to the coupling between the temperature field and the local strain of the suspension wires through the linear expansion coefficient $\alpha(T)$. Because of the strain field, compressed region becomes hotter and extended region becomes cooler. Energy is dissipated when irreversible heat flow driven by the induced temperature gradient occurs, resulting in thermo-elastic damping. The frequency dependence of $\phi_{TE}(f,T)$ is [29]

$$\phi_{TE}(f,T) = \frac{Y\alpha^2 T}{C} \frac{2\pi f \tau_d}{1 + (2\pi f \tau_d)^2} \ , \tag{2.53}$$

where C is the heat capacity per unit volume and τ_d is the thermal diffusion characteristic time in the material. The surface loss ϕ_S depends on the surface-to-volume ratio of the suspension, according to the equation [30]

$$\phi_S = \mu \frac{S}{V} l_S \ , \tag{2.54}$$

where μ is a geometrical factor of the wire and l_S is the typical loss length of the material.

The second type of suspension thermal noise arises from the transverse vibrational modes ψ_n of the suspension wires under a tension mg, named violin modes. This type of noise can cause a residual longitudinal displacement of the test mass at the end of the pendulum chain. The spectral density of violin modes is [28]

$$S(f,T) = \frac{k_B T}{(2\pi)^3} \sum_{n=1}^{\infty} \frac{\psi_n^2 \phi_n(f,T) f_n^2}{f\left[(f_n^2 - f^2)^2 + \phi_n^2(f,T) f_n^4\right]} \ , \tag{2.55}$$

with mode amplitudes

$$\psi_n^2 = \frac{2\rho L}{\pi^2 m^2}\frac{1}{n^2} \tag{2.56}$$

and resonant frequencies

$$f_n^2 = \frac{mg}{4\rho L^2}n^2 \ , \tag{2.57}$$

where ρ is the linear mass density of the suspensions.

For an interferometer with mirrors of ~ 20 kg each, suspended to 0.7-m long steel wires [31, 32] (which is the typical configuration of present detectors), the pendulum mode is the dominant contribution of suspension thermal noise from few Hz up to 50 Hz, where it is equal to $\sim 5 \cdot 10^{-23}$ Hz$^{-1/2}$. The thermal noise of violin modes is larger for frequencies higher than 300 Hz, which is the frequency of the lowest violin mode. However, beyond 500 Hz, thermal noise of violin modes is below 10^{-24} Hz$^{-1/2}$ (except for the narrow peak of resonances), so that other noise sources like shot noise are much larger in this band. In summary, compared to all the other noise sources, suspension thermal noise is typically the dominating source of noise around $10 - 20$ Hz.

Mirror thermal noise

The fluctuation-dissipation theorem provides a general approach for the computation of the amplitude spectral density of mirror thermal noise, in the case of a generic read-out beam transverse intensity distribution $I(x, y)$ [33, 34]. Let $u_z(t, x, y)$ be the time-dependent displacement of the mirror surface along the optical axis of the beam. The equivalent displacement of the mirror is

$$x(t) = \iint u_z(t, x, y)I(x, y)\ dxdy \ , \tag{2.58}$$

so the measurement of the mirror position is the average of the displacement field of the surface, weighted by the intensity distribution of the read-out beam. If $F(t) = F_0 e^{i2\pi ft}$ is a generalized oscillating force applied to the mirror, the response formula of the system is

$$Y(f) = i2\pi f\frac{x(f)}{F(f)} \ , \tag{2.59}$$

where $x(f)$ and $F(f)$ are the displacement and the force in the Fourier domain. The oscillating displacement caused by the generalized force is

$$u_z(f, x, y) = (1 - i\phi(f))u_z(x, y) \ , \tag{2.60}$$

where $\phi(f)$ is the dissipation in the system, so that the admittance $Y(f)$ is

$$Y(f) = i2\pi f\frac{(1 - i\phi(f))\iint u_z(x, y)I(x, y)\ dxdy}{F} \ . \tag{2.61}$$

The spectral density of mirror thermal noise is then

$$S_{TN}(f, T) = \frac{4k_B T}{\pi f}\frac{W}{F^2}\phi(f) \ , \tag{2.62}$$

where

$$W = \frac{1}{2}\iint u_z(x, y)P(x, y)dxdy \tag{2.63}$$

is the elastic energy stored in the mirror, which is stressed by a generalized pressure distribution $P(x,y) = |F|I(x,y)$ that has the same profile of the read-out beam. By defining the strain energy $U \equiv W/F^2$, the spectral density of eq.(2.62) writes

$$S_{TN}(f,T) = \frac{4k_BT}{\pi f} U\phi(f) \ . \tag{2.64}$$

Thus the mirror thermal noise can finally be estimated by computing the mirror strain energy U for the desired read-out beam profile. Hereafter we will deal the case of Gaussian beams, whereas in chapter 7 we will see what is the mirror thermal noise due to some particular non-Gaussian beam profiles, focusing our attention especially on Laguerre-Gauss modes.

Mirror thermal noise is the result of various contributions, due to different physical mechanisms that drive the dissipation processes in the optics. The dissipations are in general located in the coated surface as well as in the mirror substrate. When the dissipation is due to the internal damping of spatially distributed sources of mechanical friction, thermal fluctuations can be classified as Brownian thermal noise. According to the fluctuation-dissipation theorem, the frequency-dependent spectral density of substrate and coating brownian noise is [35]

$$S(f,T) = \frac{2k_BT(1-\sigma^2)}{\pi^{3/2}\, Yw} \frac{\Phi}{f} \ , \tag{2.65}$$

where w is the beam size on the mirror, σ and Y are the Poisson's ratio and the Young modulus of the substrate, and Φ is the loss term, assuming different values in the substrate ($\Phi \equiv \phi_s$) and in the coating ($\Phi \equiv \phi_c$).

As for the suspensions, thermo-elastic noise affects also the mirrors. Elastic deformations in a solid body lead to inhomogeneous distribution of temperature through the thermal expansion coefficient $\alpha(T)$, hence inducing dissipative fluxes of heat and losses of energy. For the mirror substrate, the spectral density of thermo-elastic noise is [36]

$$S(f,T) = \frac{8}{\sqrt{2\pi}} \alpha^2 (1+\sigma)^2 \frac{k_BT^2 w}{\kappa} J[\Omega] \ , \tag{2.66}$$

where κ is the thermal conductivity of the substrate material and $\Omega = f/f_c$ is a dimensionless parameter depending on the thermal properties of the sample, with

$$J[\Omega] = \sqrt{\frac{2}{\pi}} \int_0^\infty du \int_{-\infty}^{+\infty} dv \frac{u^3 e^{-u^2/2}}{(u^2+v^2)\left[(u^2+v^2)^2+\Omega^2\right]} \ . \tag{2.67}$$

The spectral density of thermo-elastic noise for a multilayer-coating of thickness l is [37]

$$S(f,T) = \frac{8k_BT^2}{\pi^2 f} \frac{l}{w^2} \frac{\alpha_s^2 C_c}{C_s^2} (1+\sigma_s)^2 \Delta^2 g(f) \ , \tag{2.68}$$

C_c and C_s being the heat capacity per unit volume of coating and substrate, respectively, and α_s is the thermal expansion coefficient for the substrate material. The explicit expressions of Δ and $g(f)$, omitted for concision, can be found in [37]. It is worth noting here that both the Brownian and thermo-elastic coating thermal noises also depend on the properties of the substrate material, as well as both are inversely proportional to some power of the beam radius w.

In transmissive optics, the rise of a temperature gradient additionally cause local random changes in the refractive index by means of its temperature dependence. This noise contribution is called thermo-refractive noise, and $\beta(T) = dn(T)/dT$ is the associated thermo-refractive coefficient. For a coating of multiple alternate layers of two different materials, with $\beta_1(T) = dn_1(T)/dT$ and $\beta_2(T) = dn_2(T)/dT$, illuminated by a laser of wavelength λ, the thermo-refractive noise spectrum is [38]

$$S(f,T) = \frac{k_B T^2 \beta_{eff}^2 \lambda^2}{\pi^{3/2} w^2 \sqrt{\rho \kappa C f}} \ , \tag{2.69}$$

where

$$\beta eff = \frac{\beta_1 n_2^2 + \beta_2 n_1^2}{4(n_1^2 - n_2^2)} \ , \tag{2.70}$$

ρ is the mass density of the substrate. The validity of eq.(2.69) is limited to the case when, for every layer of material, $\beta(T) >> \alpha(T)$. When this condition is not fulfilled, coating thermo-elastic and thermo-refractive noises are correlated, giving rise to a global thermo-optic noise. The spectral density of thermo-optic noise, not reported here for brevity, can be found in [39].

For an interferometer with mirrors of fused silica (SiO_2, currently used in present detectors) with multiple-layer coatings of Ti-doped Ta_2O_5/SiO_2 stacks (the best solution for low-loss coating up to date), and with a beam size of 6 cm on the mirror surfaces, the dominant contribution to mirror thermal noise is coating brownian noise for all frequencies within the $1 - 10^4$ Hz band [40]. We will see in chapter 7 that coating brownian noise is expected to limit the sensitivity of future gravitational-wave interferometers in the most sensitive region of their detection band, around 100 Hz, at about $3.5 \cdot 10^{-24}$ $\mathrm{Hz}^{-1/2}$.

2.4.6 Other Sources of Noise

In order to isolate the mirrors of the interferometer from acoustic vibrations, and to avoid phase noise due to fluctuations of the refractive index along the laser beam path, the whole detector has to be placed into a ultra high vacuum system of pipes and tanks. The residual gas pressure in this system is usually of the order of $10^{-7} - 10^{-8}$ mbar, which yields a negligible phase noise due to refractive index fluctuations.

Another important source of noise is diffused light, caused by photons of the laser beam that are scattered around by mirror imperfections and are reflected back by the vacuum pipes. The phase of scattered photons is modulated by the pipe vibrations, and when these photons recombine with the main laser beam a phase noise arises. To get rid of this problem a set of mechanical light absorbers can be placed along the vacuum pipe, avoiding the recombination of the spurious photons with the main laser beam.

An additional noise source is the electronic noise in the main interferometer read-out system and in the control system used to keep the interferometer in its working point. The electronic noise can be introduced by both the sensors and the actuators of the feedbacks. The other noises mentioned above (diffused light, etc.) can also pollute the auxiliary signals used in the control systems and then degrade the interferometer sensitivity.

Also the laser source contributes to the total noise of the detector. Fluctuations of laser amplitude and frequency generate additional noise at the detector output, as well as the fluctuations of the laser beam position (*beam jitter*) couple to mirror misalignments and induce phase noise.

2.5 Thermal Effects

Interferometric detectors of gravitational waves are also affected by thermal effects, which arise when a fraction of the circulating power is absorbed by the optics. Absorption may take place at the dielectric coatings and also inside the substrate of transmissive optics, like the beamsplitter or, as we will see in the following, the coupling input mirror of Fabry-Perot cavites. The optics are locally heated and consequently deformed, causing wavefront deformations of the reflected or transmitted beam known as *thermo-elastic effects*.

In addition to the geometric deformation by local heating, a temperature gradient inside the substrate will introduce also a gradient of the index of refraction. Thus, if the laser beam is transmitted through a material with a temperature gradient, the heated region of the substrate will act as a *thermal lens*, deforming the wavefront. The change in the refractive index induced by the temperature gradient $T(r, z)$ is

$$\delta n(r, z) = \frac{dn}{dT} T(r, z) \ , \tag{2.71}$$

where $\beta = dn/dT$ is the temperature index coefficient. The thermal lens is equal to the integrated excess optical path of the beam transmitted through the substrate, given by

$$Z(r) = \frac{dn}{dT} \int_{h/2}^{-h/2} T(r, z) \ dz \ , \tag{2.72}$$

for a mirror of thickness h. The presence of the thermal lens causes a mismatching of the beam which goes through it, resulting in coupling losses of the transmitted beam.

We will see in chapter 4 that, in order to mitigate the impact of thermal effects on the beam wavefront, a thermal compensation system is necessary.

2.6 Sensitivity Improvements with Optical Resonators

We know from eqs.(2.16) and (2.36) that the sensitivity of the interferometer is limited by the length of its arms and by the laser power. A ground-based detector cannot have arms longer than few kilometers. The present laser sources with the required specifications for gravitational wave detection can generate laser beams of the order of ~ 100 W.

The laser power and the optical path traveled by the beam can be increased by using optical resonators. The optical path can be increased by replacing the end mirrors of the interferometer with Fabry-Perot cavities, as shown on fig.2.6. The light inside the arm cavities is reflected back and forth by the input and the end mirrors, so that the optical path is folded in the cavity and is equal to the arm length times the number of the round trips made by the beam.

The laser power can be increased by coupling an additional mirror, also shown on fig.2.6, between the laser and the beamsplitter to form an optical resonator for *power recycling*. Furthermore, the amplitude and frequency noise of the laser, as well as the beam jitter, can be filtered with an input mode-cleaner, which is a particular Fabry-Perot resonator. At the output of the detector, an output mode-cleaner might be used to filter the signal in order to increase the signal-to-noise ratio.

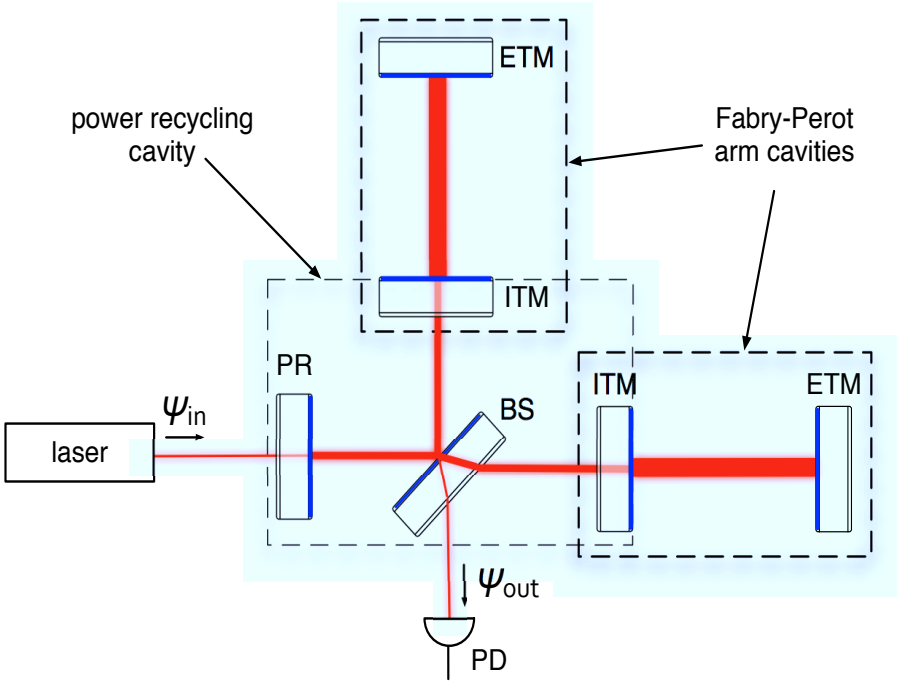

Figure 2.6: Optical scheme of a power-recycled Michelson interferometer with Fabry-Perot arm cavities.

In the following we will describe the working principle and the main properties of the optical resonators of the detector.

2.6.1 Fabry-Perot Arm Cavities

A Fabry-Perot cavity is a standing-wave resonator for the laser beam. In its simplest configuration, the cavity is formed by two semi-reflecting mirrors, M_1 and M_2, separated by a distance L. The arrangement is schematically shown on fig.2.7, and the convention for propagated, transmitted and reflected fields is the same used in section 2.2. If ψ_{in} is a laser beam of wavelength λ, the equations for the fields inside and outside the cavity are

$$\begin{aligned}
\psi_{res} &= t_1\psi_{in} - r_1\psi_b \\
\psi_b &= -r_2\psi_{res}\, e^{2i\phi} \\
\psi_t &= t_2\psi_{res}\, e^{i\phi} \\
\psi_r &= r_1\psi_{in} + t_1\psi_b \ ,
\end{aligned}$$

where $\phi = kL = 2\pi L/\lambda$ is the phase shift cumulated by the beam in a single trip from M_1 to M_2. The light that enters the cavity is reflected back and forth between the two mirrors, and is stored in the cavity for a finite time equal to

$$\tau_s = \frac{2L}{c}\frac{\sqrt{r_1 r_2}}{1 - r_1 r_2} \ . \tag{2.73}$$

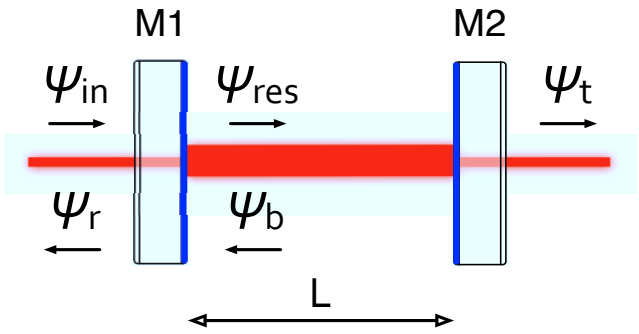

Figure 2.7: Optical scheme and field notation of a Fabry-Perot cavity.

Thus the explicit equations of the resonant, transmitted and reflected fields are, respectively,

$$\begin{aligned}
\psi_{res} &= \psi_{in}\frac{t_1}{1-r_1 r_2\exp(2i\phi)} \\
\psi_t &= \psi_{in}\frac{t_1 t_2\exp(i\phi)}{1-r_1 r_2\exp(2i\phi)} \\
\psi_r &= \psi_{in}\frac{r_1-r_2(t_1^2+r_1^2)\exp(2i\phi)}{1-r_1 r_2\exp(2i\phi)} = \psi_{in}\frac{r_1-r_2(1-L_1)\exp(2i\phi)}{1-r_1 r_2\exp(2i\phi)} \ .
\end{aligned} \tag{2.74}$$

The cavity is resonant when $\phi = k\pi$, so that the incident light ψ_{in} can interfere constructively with the light stored inside the cavity. The normalized power and the phase of the transmitted, resonant and reflected fields are shown in figs.2.8, 2.9 and 2.10.

Transmitted power

The power transmitted by the cavity is

$$P_t(\phi) = |\psi_t(\phi)|^2 = P_{in}\Big(\frac{t_1 t_2}{1-r_1 r_2}\Big)^2 \ \frac{1}{1+\frac{4r_1 r_2}{1-r_1 r_2}\sin^2\phi} \ , \tag{2.75}$$

where

$$A(\phi) = \frac{1}{1+\frac{4r_1 r_2}{1-r_1 r_2}\sin^2\phi} \tag{2.76}$$

is the Airy function. The separation between two consecutive resonances is the *free spectral range* (FSR), equal to

$$\begin{aligned}
\Delta f &= \tfrac{c}{2L} \quad \text{in terms of frequency} \\
\Delta L &= \tfrac{\lambda}{2} \quad \text{in terms of length} \ .
\end{aligned} \tag{2.77}$$

The ratio of the free spectral range to the full width at half maximum (FWHM) of the resonance peak is the cavity *finesse*,

$$\mathcal{F} = \frac{\text{FSR}}{\text{FWHM}} = \frac{\pi\sqrt{r_1 r_2}}{1-r_1 r_2} \ . \tag{2.78}$$

Resonant power

The power stored in the cavity at the resonance is

$$P_{res} = |\psi_{res}(\phi = \pi)|^2 = P_{in} \frac{T_1}{(1 - r_1 r_2)^2} \ , \tag{2.79}$$

where

$$G_{opt} = \frac{T_1}{(1 - r_1 r_2)^2} \tag{2.80}$$

is the optical gain of the cavity. When $r_1 \simeq r_2 \simeq 1$, the optical gain can be approximated as $G_{opt} \approx \mathcal{F}/\pi$.

Reflected field

The ratio between the reflected field and the input field defines the complex reflectivity of the Fabry-Perot cavity:

$$\frac{\psi_r}{\psi_{in}} = \frac{r_1 - r_2(1 - L_1)\exp(2i\phi)}{1 - r_1 r_2 \exp(2i\phi)} \ . \tag{2.81}$$

Three possibilities are given:

- *optimal coupling*: $r_1 - r_2(1 - L_1) = 0$
  The reflected field at resonance is null. In this case the light that is promptly reflected by the input mirror interferes destructively with the stored light leaking outside the cavity, through M_1. If the optical loss of M_1 is null ($L_1 = 0$), this condition is verified when $r_1 = r_2$.

- *low coupling*: $r_1 - r_2(1 - L_1) < 0$
  The amplitude of the reflected field at resonance is negative, thus there is a phase shift of π between the input field and the reflected field. This is verified when $r_1 < r_2$, for $L_1 = 0$.

- *over coupling*: $r_1 - r_2(1 - L_1) > 0$
  The amplitude of the reflected field at resonance is positive, thus the input field and the reflected field are in phase. This condition is verified when $r_1 > r_2$, for $L_1 = 0$.

For small phase shifts $\delta\phi$ around the resonance, the phase of the reflected field varies according to

$$\frac{d\phi_r}{d\phi} = \frac{d}{d\phi} \arg\left(\frac{\psi_r}{\psi_{in}}\right) = r_2 \frac{(1 - L_1) - r_1^2}{(1 - r_1 r_2)(r_1 + r_2(1 - L_1)} \ . \tag{2.82}$$

In the particular case when $r_1 \simeq r_2 \simeq 1$ and $L_1 = 0$, eq.(2.82) simplifies to

$$\frac{d\phi_r}{d\phi} \simeq \frac{2\mathcal{F}}{\pi} \ . \tag{2.83}$$

Thus eq.(2.83) shows that for a small detuning in the proximity of the resonance (like the strain induced by an impinging gravitational wave), the phase shift of the reflected field is amplified by a factor proportional to the cavity finesse. This is the reason why Fabry-Perot cavities are used in the arms of the interferometer to increase the optical path length of the laser beam.

Transfer function

In the low frequency condition $\Omega_{\rm GW} << c/2L$, that is when the frequency of the impinging gravitational wave is much smaller than the typical frequency of a round trip cycle of the laser in the arms, it can be shown that the frequency response of the interferometer with Fabry-Perot cavites is [2]

$$\Delta\phi = h\tau_s \frac{8\pi c}{\lambda} \frac{1}{\sqrt{1+(2\Omega_{\rm GW}\tau_s)^2}} \ , \tag{2.84}$$

with a pole at angular frequency $f_{FP} = 1/4\pi\tau_s$. Thus for frequencies $\Omega_{\rm GW}/2\pi >> f_{FP}$ the phase sensitivity of the detector decreases, as shown on fig.2.14. Below the cavity pole ($\Omega_{\rm GW}/2\pi << f_{FP}$), the ratio between the phase response of the Fabry-Perot detector of eq.(2.84) and the response of the Michelson detector of eq.(2.16) is

$$\frac{\Delta\phi_{\rm FP}}{\Delta\phi_{\rm Mich}} = h\frac{2L}{c}\frac{\mathcal{F}}{2\pi}\frac{8\pi c}{\lambda}\Big(hL\frac{4\pi}{\lambda}\Big)^{-1} = \frac{2\mathcal{F}}{\pi} \ . \tag{2.85}$$

This is another way to describe the improvement in sensitivity due to Fabry-Perot arm cavities, alternative to that of eq.(2.83). The enhancement is once again evident: when Fabry-Perot cavities of finesse $\mathcal{F}$ are inserted in the arms, the effective length of the interferometer arms is equal to

$$L_{\rm eff} = L\ \frac{2\mathcal{F}}{\pi} \ . \tag{2.86}$$

For example, if $L = 1$ km and $\mathcal{F} = 100$, the effective optical path length is $L_{\rm eff} \simeq 64$ km.

2.6.2 Power Recycling

If the interferometer is close to the dark fringe condition and the reflectivity of the arm end mirrors is high, almost all of the fringe power is reflected back to the laser. This power can be stored in the detector by adding a semi-reflective mirror between the laser and the beamsplitter, in order to form an optical resonator for the power reflected towards the laser. The resonator will be composed by the mirror itself and by the rest of the interferometer, considered as a composite mirror of equivalent reflectivity r_{ITF}. This particular resonator is a *power recycling* cavity, with optical gain G_{PR}.

The recycling gain can be computed in the simple case where the power recycling cavity is coupled to a single Fabry-Perot arm cavity of the interferometer. The equation of the resonant field for the coupled cavities is then

$$\psi_{res} = \psi_{in}\frac{t_{PR}}{1-r_{PR}r_{FP}\exp(2i\phi_{PR})} = \psi_{in}\frac{t_{PR}}{1-r_{PR}\Big(\frac{r_1-r_2(R_1+T_1)}{1-r_1r_2}\exp(2i\phi_{FP})\Big)\exp(2i\phi_{PR})} \ , \tag{2.87}$$

where r_{PR} is the reflectivity of the power recycling mirror, r_{FP} is the equivalent reflectivity of the Fabry-Perot cavity from the last of eqs.(2.74), ϕ_{PR} and ϕ_{FP} are the phase shifts acquired by the beam in the power recycling cavity and in the arm cavity, respectively. The double resonance of the coupled cavities happens when $\phi_{PR} = m\pi$ and $\phi_{FP} = n\pi$. The optical gain of the system can be computed by taking the square modulus of eq.(2.87), and is equal to that of the power recycled interferometer with both Fabry-Perot arm cavities.

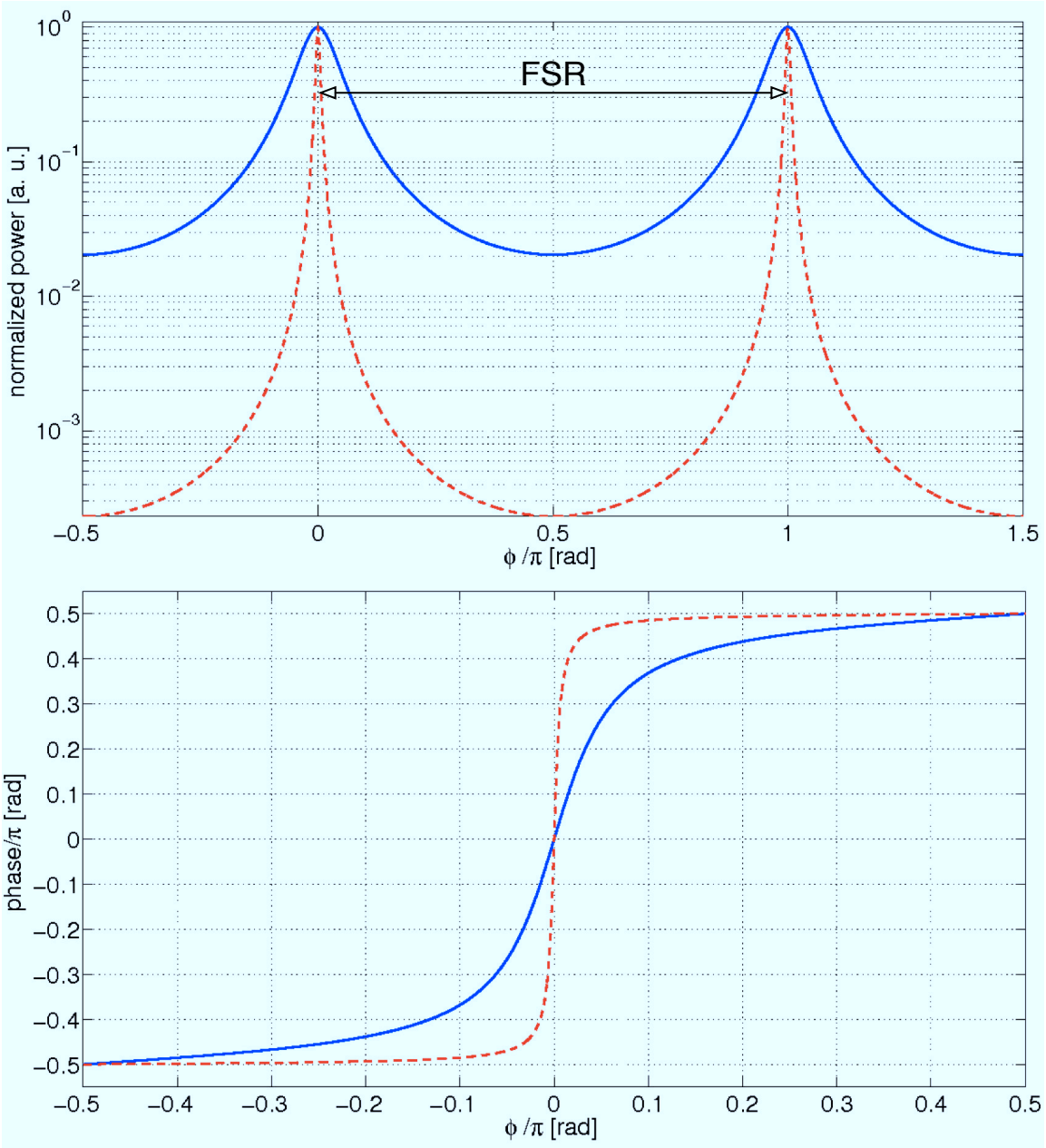

Figure 2.8: Normalized transmitted power (top) and phase of the transmitted field (bottom) of a Fabry-Perot cavity with $L = 1$ km, no loss, $r_1 = r_2$, for $\mathcal{F} = 10$ (blue solid curve) and $\mathcal{F} = 100$ (red dashed curve).

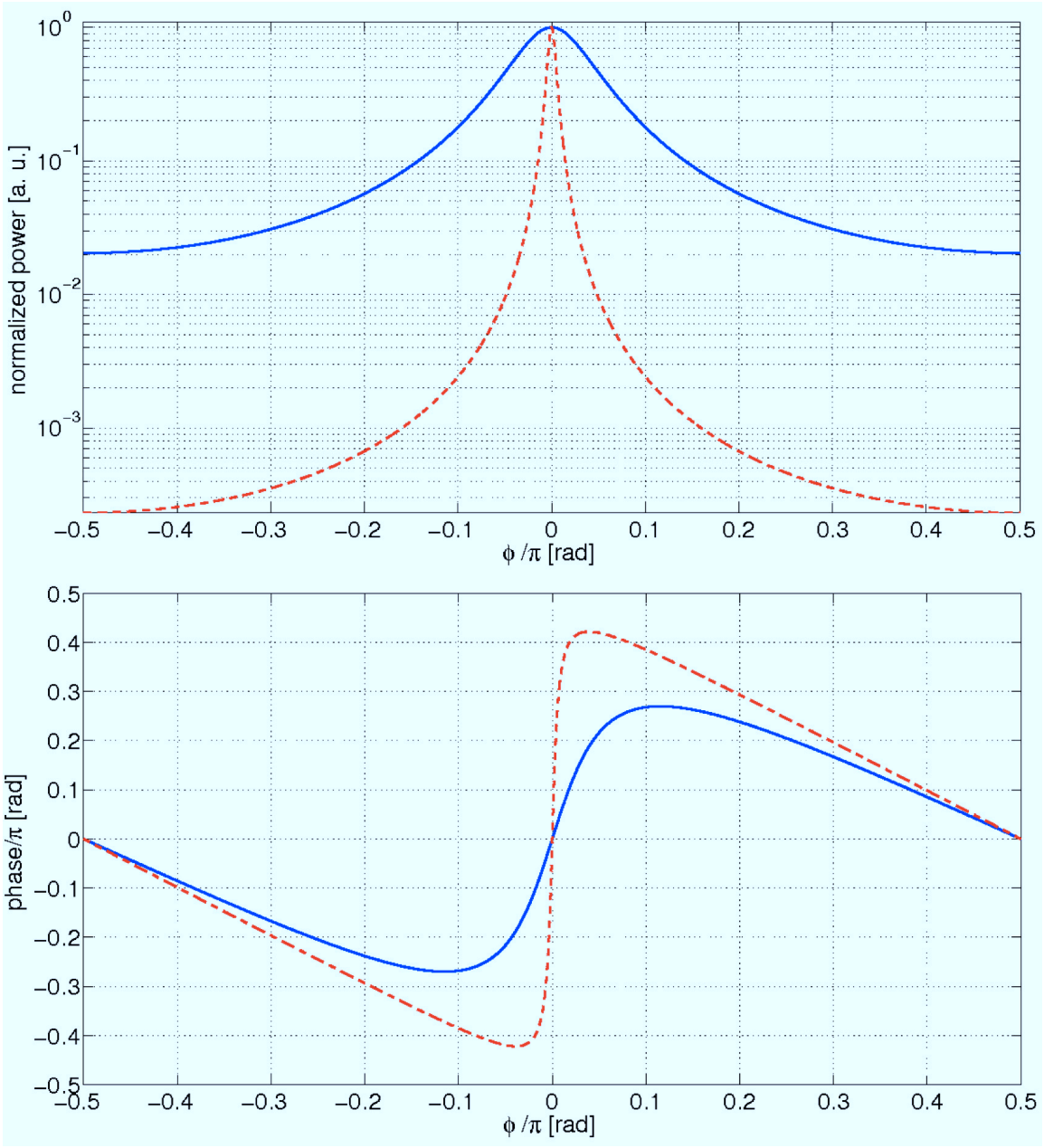

Figure 2.9: Normalized resonant power (top) and phase of the resonant field (bottom) of a Fabry-Perot cavity with $L = 1$ km, no loss, $r_1 = r_2$, for $\mathcal{F} = 10$ (blue solid curve) and $\mathcal{F} = 100$ (red dashed curve).

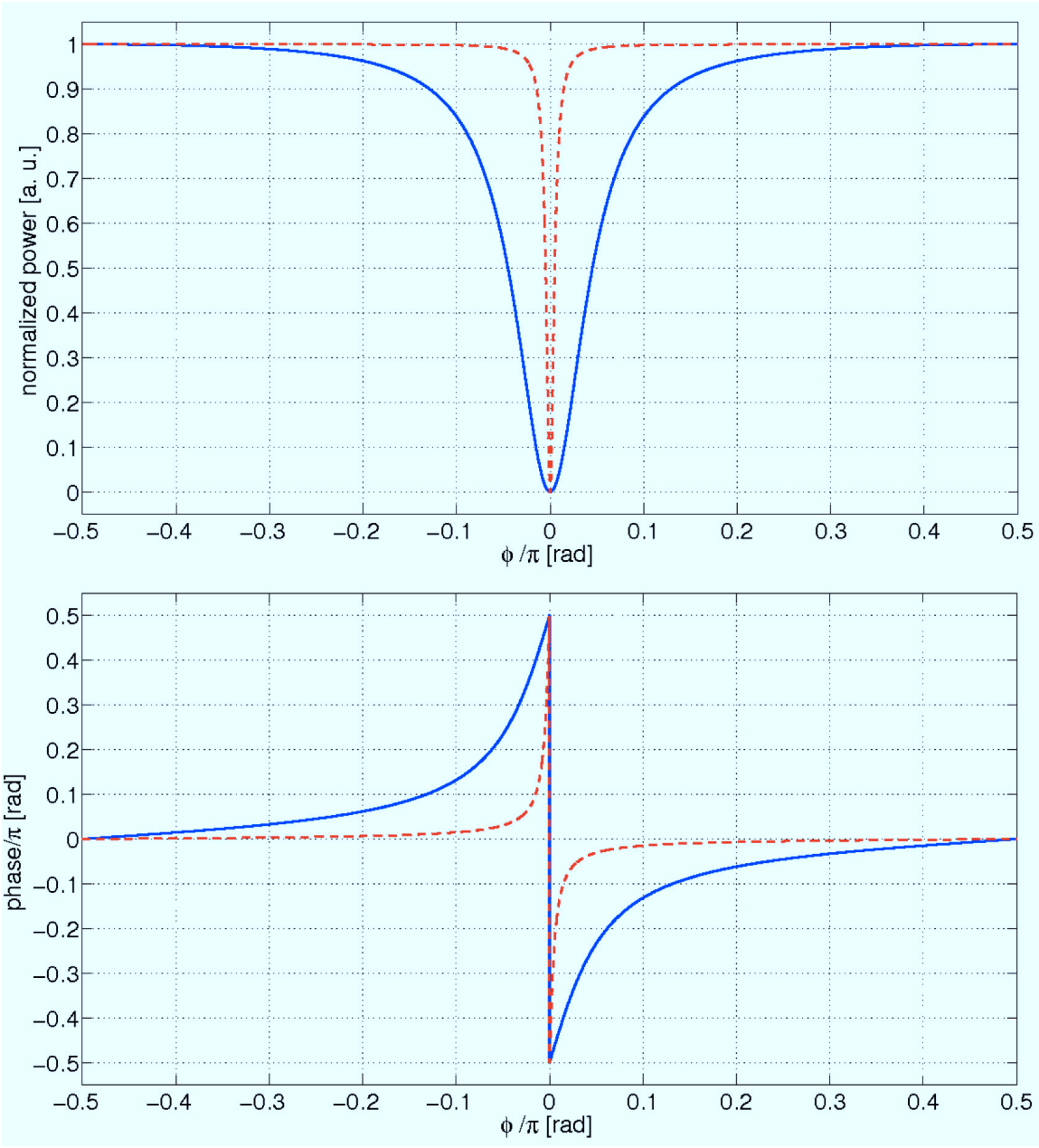

Figure 2.10: Normalized reflected power (top) and phase of the reflected field (bottom) of a Fabry-Perot cavity with $L = 1$ km, no loss, $r_1 = r_2$, for $\mathcal{F} = 10$ (blue solid curve) and $\mathcal{F} = 100$ (red dashed curve).

2.6.3 Mode-Cleaner Cavities

The noise due to the laser source might be filtered out by an input mode-cleaner cavity, placed between the laser and the power recycling mirror. A mode-cleaner is a Fabry-perot cavity with optimal coupling, for the total transmission of the incoming beam. The mode-cleaner filters the amplitude and frequency noise of the laser like a low pass filter with cut-off frequency $f_{FP} = 1/4\pi\tau_s$, where τ_s is the storage time defined in eq.(2.73). Moreover, the cavity filters the beam jitter and the spatial defects of the beam [41], so that the Gaussian beam that enters the interferometer can have an optimal coupling to the arm cavities of the detector. The spatial defects and the beam jitter are reflected by the mode cleaner as higher-order laser modes, which are described in detail in section 5.1.

Some spatial defects of the beam might also be present at the output of the detector, on the photodiode, whereas the gravitational wave signal is only due to the phase modulation of the Gaussian beam that resonates in the arm cavities. Thus an output mode-cleaner could be also used to filter the spatial defects of the output beam, in order to increase the signal-to-noise ratio of a potential detection.

Chapter 3

Present and Future Ground-Based Gravitational-Wave Detectors

Nowadays four gravitational-wave interferometers have been built and are operating worldwide: TAMA300, GEO600, Virgo and LIGO. These instruments approximately reached their design sensitivities, demonstrating the technical feasibility of the detection principle. LIGO, Virgo and GEO600 form a network of detectors which have completed several joint observational runs. No detection of gravitational waves has been reported so far. The observational results of the searches are upper limits, either for the rate of binary coalescence or for the intensity of the gravitational radiation emitted by other sources, like for example pulsars.

If we refer only to the coalescence of binaries (since the associated gravitational-wave signal is the best known among those of expected sources), the predicted rate of detection for present interferometers is of the order of 10^{-3}/yr. Given this rate, the detection of a signal still remains plausible, but is very unlikely. A tenfold improvement of the sensitivity (in the whole detection band) of present interferometers might provide the needed increase of detection rate. Improving the sensitivity of an order of magnitude would increase the detection horizon by approximately the same factor and hence the accessible volume of the Universe by its cube. Assuming that astrophysical sources of gravitational waves are isotropically distributed in space, this sensitivity improvement would increase the present expected detection rate by a factor $\sim 10^3$, allowing the first direct detection of gravitational waves and leading to the detection of several events per year. This is the motivation of the proposal of a second generation of interferometers, like Advanced LIGO, Advanced Virgo and the Large-scale Cryogenic Gravitational-wave Telescope (LCGT). All these projects have been presently funded and advanced LIGO and Advanced Virgo are currently under construction.

In any case, the expected rate and signal-to-noise ratio of second generation instruments are expected to be too low for precise astronomical studies of gravitational-wave sources. For this reason, the project of a third-generation detector named Einstein Telescope has been proposed, which should provide an increase of sensitivity of about one hundred times that of present detectors (corresponding to an increase of 10^6 times the present expected detection rates). The aim of this project, which is currently at phase of design study, is to initiate the era of *precision* gravitational-wave astronomy.

This chapter is intended to give a picture of the state of the art of present and future gravitational-wave interferometers, whose sensitivity evolution is significantly resumed by fig.3.1. To describe

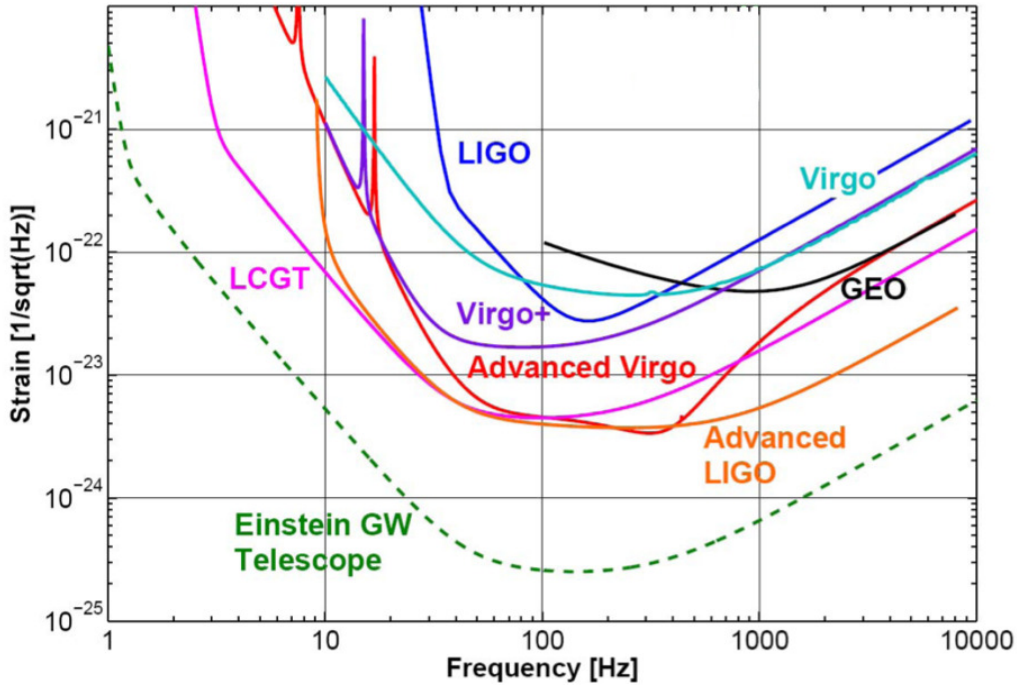

Figure 3.1: Sensitivity target (green dashed curve) of the Einstein Telescope interferometer, compared to the sensitivity curves of first (LIGO, Virgo/Virgo+, GEO600) and second generation (advanced LIGO, Advanced Virgo, LCGT) gravitational-wave interferometers, from [75].

this first generation of detectors in section 3.1, we will take Virgo as example. This choice is motivated by the fact that part of this thesis work is dedicated to the optical design of Advanced Virgo. The description of the present Virgo interferometer will be useful to put the emphasis on its future upgrade, thus we will present its optical layout and its sensitivity curve. In the subsequent section 3.2, we will briefly summarize some of the most important observational results achieved by the LIGO-Virgo-GEO600 network so far: we will present the results of the search for signals emitted by coalescing binaries, burst sources, known pulsars (with electromagnetic counterpart observations) and coming from the stochastic background of cosmological origin. Section 3.3 will present a short global overview of the projects of future detectors of second generation, and we will briefly discuss there their science case. Again, we will assume Advanced Virgo as reference. At the end of the chapter, in section 3.4, we will describe the project of the Einstein Telescope, since the second part of this thesis work (about Laguerre-Gauss beams) is intended to be a contribution to the optical design of this third-generation detector (besides the fact of possibly being part of an upgrade of second-generation detectors).

3.1 The Network of First Generation Detectors

Four large ground-based interferometers are currently operating around the globe. The Virgo interferometer [42, 43] is a detector located in the plain of Cascina, near Pisa in Italy. It has been built by the *Virgo Collaboration*, a scientific collaboration between the laboratories of the Centre National de la Recherche Scientifique (CNRS) of France and the Istituto Nazionale di Fisica Nucleare

Figure 3.2: Aerial view of the Virgo interferometer in Cascina, Pisa (Italy).

(INFN) of Italy. Recently also groups from Holland, Poland and Hungary joined the Collaboration. The first proposal of Virgo was made in 1989, and the project has been inaugurated in 2003. The experimental site is managed by a CNRS-INFN consortium, the European Gravitational Wave Observatory (EGO) [44]. On fig.3.2 an aerial view of the detector is shown.

LIGO [45, 46] is a project of three kilometer-scale detectors, built at two sites in the United States. At Hanford, Washington, there are two power-recycled Fabry-Perot interferometers with arm cavities of 2 and 4 km, in the same vacuum tube. At Livingston, Louisiana, there is a single detector with 4-km long arm cavities. LIGO reached its design sensitivity in 2005, with an equivalent-strain noise of $\sim 3 \cdot 10^{-23}$ Hz$^{-1/2}$ in the most sensitive frequency band, around 100 Hz.

A detector with 600-m long arms, GEO600 [47, 48], has been operational near Hannover, in Germany, since 2001, gathering research groups principally in Germany and Britain. Its maximum sensitivity is $\sim 10^{-21}$ Hz$^{-1/2}$ at 100 Hz. A Japanese detector with 300-m long arms, TAMA300 [49, 50], is operating near Tokyo with a maximum sensitivity of $\sim 10^{-21}$ Hz$^{-1/2}$ at 1 kHz. TAMA300 was the first large-scale interferometer to achieve a continuous operation, and is now used as a development prototype. The detectors of LIGO, GEO600 and TAMA300 are shown on fig.3.3.

LIGO and GEO600 have worked together within the frame of the LIGO Scientific Collaboration (LSC) since the beginning of observational runs. The collaboration comprises research groups from universities around the world, contributing to data analysis and technology developments. Virgo has signed an agreement with the LIGO collaboration in order to pool the data in a joint analysis, thereby creating a single worldwide network of long-baseline gravitational wave interferometers.

The simultaneous data taking among detectors located at separated sites is of fundamental importance, for several reasons. The coincident measurement of a gravitational wave signal in different detectors would strongly improve the confidence of the detection. Since noise-induced random triggers from a network of detectors are less likely to be consistent with each other, coinci-

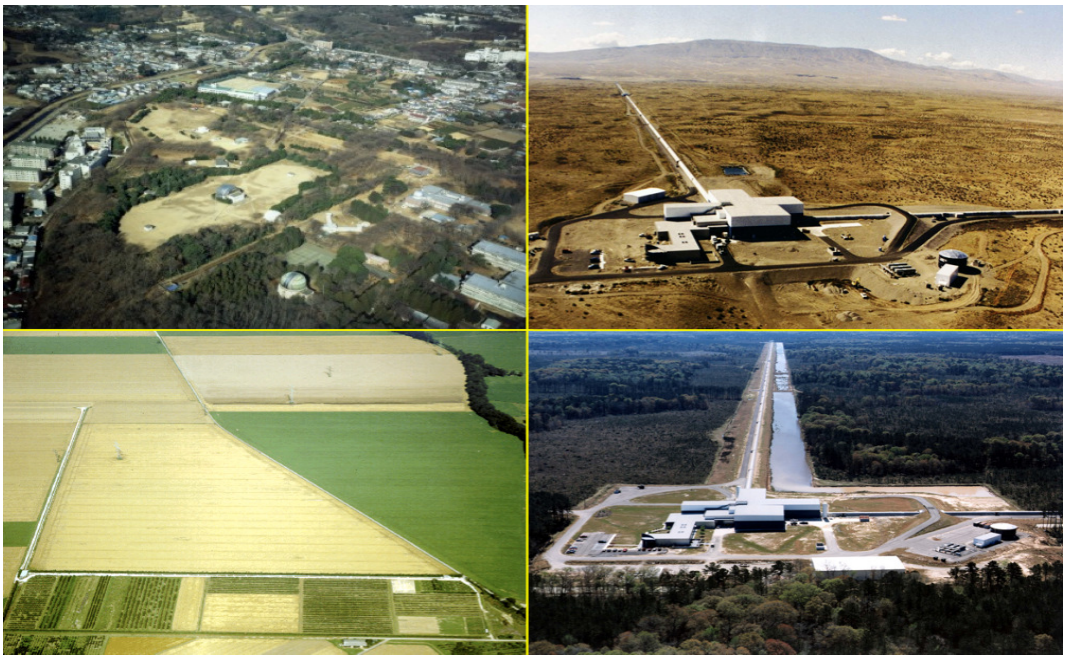

Figure 3.3: Worldwide network of detectors. From top right, clockwise: aerial views of LIGO Hanford, LIGO Livingston, GEO600, TAMA300.

dence analysis is a very powerful tool to veto out spurious events. Furthermore, the position of the emitting source in the sky might be reconstructed through triangulation, by looking at the delay in the arrival times of the signals recorded by several detectors [51]. The reconstruction of the source position could allow for potential follow-ups of electromagnetic counterparts. The observation of an electromagnetic signal would improve the robustness of the gravitational wave detection and would yield complementary informations about its source. All the observing instruments are expected to receive the same gravitational wave polarizations, but the gravitational wave should couple differently to each detector, according to the single antenna patterns. The result of this coupling might be modeled through a phase shift and a scale factor in the reconstruction of the observed wave signal in each detector, from which it could be possible to infer the polarization of the incoming wave [52].

To describe the technical features of present gravitational-wave interferometers we will use Virgo as example, its sensitivity curve is similar to those of the other detectors of the network. This will be useful for the following: the first part of this thesis work concerns the optical design of Advanced Virgo, which is the project (illustrated in chapter 4) of upgrading Virgo to a more sensitive second-generation detector. Thus we will describe here especially the present optical layout of Virgo, to allow for the comparison with the changes discussed later on in this thesis.

Optical layout of Virgo

Virgo is a power-recycled Michelson interferometer with 3-km long Fabry-Perot cavities in the arms, its schematic optical layout is shown in fig.3.4. The two arm cavities (conventionally called North and West), are composed of (North or West) input and end mirrors, and the first mirror

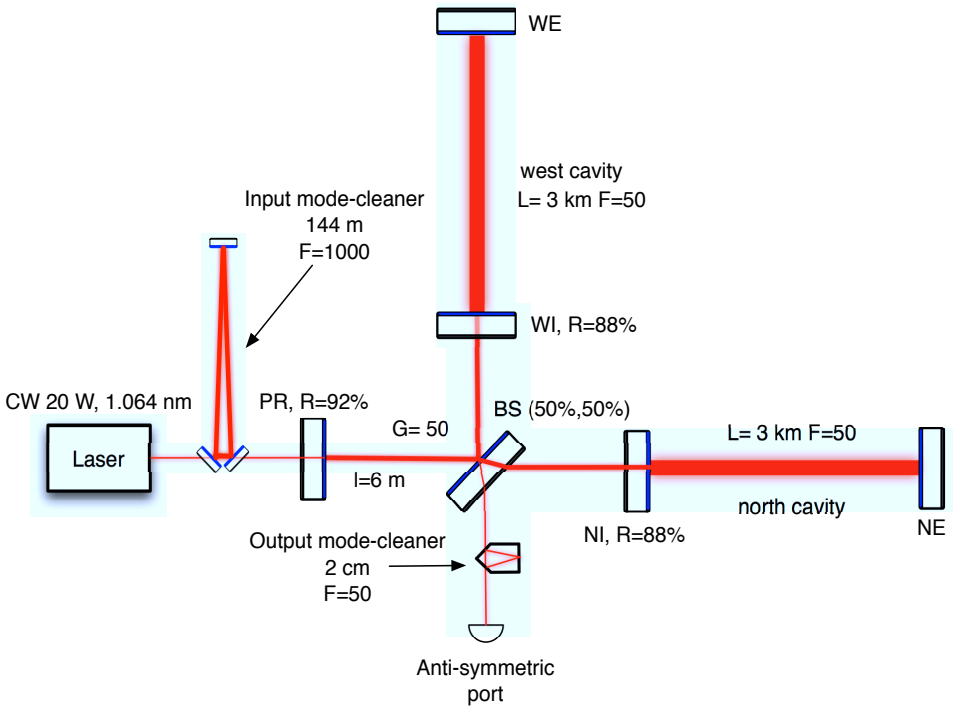

Figure 3.4: Optical layout of the Virgo interferometer.

encountered by the input laser beam is the power recycling mirror. The distance between the beam splitter and the power recycling mirror is approximately 6 m, equal to the distance between the beam splitter and the two input mirrors. Many upgrades have been made from the first installation of Virgo on 2003, here we report the original configuration of the detector.

The input beam ($\lambda = 1.064\ \mu$m) is generated by a system composed of a high-stability solid-state Nd:YAG master laser and a Nd:YVO_4 high-power slave laser, with a continuous power of about 20 W. Before entering the interferometer, the beam passes through the *input mode-cleaner* (IMC), a triangular Fabry-Perot cavity 144-m long with a finesse of about 1000 and suspended mirrors. The main motivation for the input mode-cleaner is the filtering of the position noise of the beam, but the cavity is also used for laser frequency stabilization. The beam then goes through the power recycling mirror (PR), which has a reflectivity $R = 92\%$.

The laser light is split by the beamsplitter mirror (BS) in two beams, which enter the two long Fabry-Perot arm cavities with a finesse of 50 (corresponding to an optical gain of about 31). This finesse is obtained with a reflectivity $R = 88\%$ of the input mirrors and a reflectivity for the end mirrors almost equal to 1. The optical gain of the power recycling cavity is about 50, the power impinging on the beamsplitter is 500 W and the power stored in the arm cavities is about 7 kW. In order to propagate along kilometer-scale distances with small divergence, the beam entering the arm cavities is large: the radius w is 2 cm on the input mirrors and 5 cm at the end mirrors.

The mirrors used in Virgo are made of high quality fused silica, with a diameter of 35 cm and a mass of about 21 kg for power recycling and cavity mirrors. The beam splitter is slightly smaller, with a diameter of 23 cm and a mass of 5 kg. All mirrors are flat, except the two end arm mirrors which are concave with a radius of curvature of about 3.6 km. To increase the contrast of

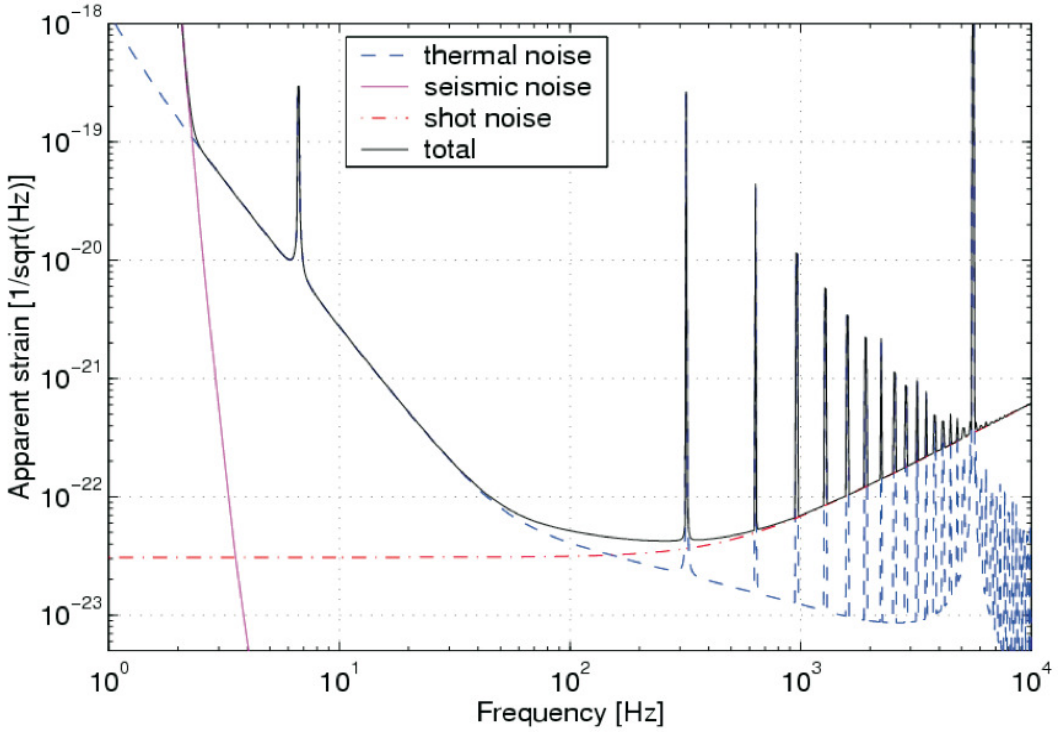

Figure 3.5: Virgo design sensitivity curve. The spectra of fundamental limiting noises are shown.

the interferometer, the output beam is filtered by an output mode-cleaner (OMC), a monolithic Fabry-Perot cavity 2-cm long made of fused silica.

Each mirror of the layout is suspended from a chain of seismic filters, the *Superattenuator* [53], which provides the attenuation of ground vibrations. This is to date the most efficient seismic isolation system of ground-based detectors, allowing the extension of Virgo detection band down to ~ 3 Hz. The Superattenuator is even compliant with the low-frequency sensitivity requirement of Advanced Virgo and will be part of this project, thus it will be described in detail in chapter 4.

Sensitivity curve of Virgo

From 2003 to 2007 the Virgo interferometer underwent a commissioning period, which is the phase of the project between the end of the detector construction and the beginning of data taking. This phase involves mainly the development and the tuning of the control system of the detector, which allows to keep the interferometer at its working point. The objective of the commissioning phase is twofold: to reach the design sensitivity and to have sufficiently high duty cycle over long periods of time, of the order of several months. The duty cycle of the detector depends mainly on the robustness of the control system.

Before reaching the sensitivity limit caused by *fundamental* noise sources (seismic noise, thermal noise and shot noise), several technical noises (like laser noises and control noises) have to be reduced. The progress marked by the commissioning (continued also beyond 2007) allowed to decrease the measured noise approximately to the design level, shown on fig.3.5, which is equal to $\sim 3 \cdot 10^{-21}$ Hz$^{-1/2}$ at 10 Hz and $\sim 7 \cdot 10^{-23}$ Hz$^{-1/2}$ at 100 Hz.

joint data taking runs [LSC: Si − Virgo: VSRi]	results to date [upper limits/triggers]
S5 (Nov. 05 - Sept. 07) & VSR1 (May 07 - Oct. 07)	binary coalescence rates [55, 56] burst event rates [57] burst emission from magnetars [8] emission of known pulsars [58] energy density of stoch. background [10] multimessenger events [59, 60, 61]
S6 (July 09 - Oct. 10) & VSR2 (July 09 - Jan. 10)/VSR3 (July 10 - Oct. 10)	Vela pulsar emission [62]

Table 3.1: Main observational results of the joint data taking runs of the LSC-Virgo network so far.

Since 2007, Virgo went through several technical upgrades with the aim of improving the sensitivity. The latest one, occurred on 2010, concerned the replacement of the steel wires of the mirror suspension system with monolithic fibers of silica with low mechanical loss, in order to decrease the suspension thermal noise [31, 54]. This upgrade led to an enhanced configuration of the detector, called Virgo+, whose design sensitivity is shown on fig.3.1.

3.2 Observational Results of the LSC-Virgo Network

In 2005 LIGO began a two-year data taking run, S5, which ended on 2007. From 2009 to 2010 LIGO collected data during the S6 run. Since 2007, Virgo has accomplished three scientific data taking runs: VSR1, VSR2 and VSR3. VSR1 overlapped with the last months of S5, and VSR2 and VSR3 have been coordinated to be in coincidence with S6.

The analysis of the data acquired during the first S5-VSR1 joint run is now complete, and no detection of gravitational waves has been reported. Data collected so far have been used to put upper limits on the expected rates of coalescence of binary systems [55, 56] and on burst sources rates and emission [57, 8], to constrain the amount of gravitational radiation emitted by known pulsars [58], to constrain the spectrum of a stochastic background of gravitational waves [10] and to search for multimessenger events [59, 60, 61].

The analysis of the data of the joint run S6-VSR2/VSR3 is ongoing, but a first important result, constraining the gravitational-wave emission of the Vela pulsar, is already available [62]. Hereafter we review the main experimental results achieved by the LSC-Virgo network so far, also summarized in table 3.1.

Search of signals from coalescing binaries

The method used for the search of signals from coalescing binary systems is coincidence analysis, were data from each detector are analyzed separately by applying relevant filters and search algorithms. Then coincidences are searched in the multi-dimensional space of intrinsic (masses of the component stars, their spins, etc.) and extrinsic (arrival times, reconstructed source location, etc.) parameters. Therefore data are analyzed only for times when at least two detectors of the LSC-Virgo network are operating.

source	rate $\mathcal{R}$ [$\mathrm{yr}^{-1}L_{10}^{-1}$]	rate $\mathcal{R}$ [$\mathrm{Myr}^{-1}\mathrm{MWEG}^{-1}$]
NS-NS	$8.7 \cdot 10^{-3}$	$14.8 \cdot 10^{3}$
NS-BH	$2.2 \cdot 10^{-3}$	$3.7 \cdot 10^{3}$
BH-BH	$4.4 \cdot 10^{-4}$	$7.5 \cdot 10^{2}$

Table 3.2: Measured upper limits of coalescence rates for binary systems with total mass from 2 $M_{\odot}$ to 35 $M_{\odot}$, from [55].

The analysis is made on data that have passed a series of *veto categories*, based on data quality criteria. Environmental and instrumental monitoring channels of the detectors report about identified noise transients, so that vetoes remove a limited time series of data in an interval centered around the transients. The list of gravitational wave detection candidates is made from the remaining volume of data.

Detection candidates are selected through search algorithms which are adapted to the expected signal waveforms, the *templates*. These latter are predicted by Post-Newtonian theory and numerical simulations. It is then possible to apply a matched-filtering technique for efficient search, where templates are correlated to the data [55].

To estimate the significance of candidate events, the distribution of events due to background noise is measured. A sample of background noise events is created, by time-shifting data of one or more detectors with respect to the others by time delays of no physical meaning (i.e. much larger than the maximum time-of- flight of a gravitational wave between the detectors). Shifts typically range from 1 s to a few minutes. Any triggers that are coincident in the time-shifted data cannot be due to a true gravitational-wave signal. These coincidences therefore sample the noise background.

For all the searches, search algorithms are tested with hardware and software *injections* [55, 57]. At random times during the run, simulated waveforms are added to the detector output data, via software, or are sent to the mirror position control system. Search algorithms work correctly if they detect the injected signal and reconstruct the parameters of the simulated source. These injections provide an end-to-end verification of the detector instrumentation, the data acquisition system and the data analysis software.

The general search for signals from coalescing binaries in S5-VSR1 data has been conducted for systems of total mass from 2 $M_{\odot}$ to 35 $M_{\odot}$, for the following astrophysical objects: binary neutron stars (BNS), binary black holes (BBH), and black hole-neutron star binaries (BHNS). These objects are expected to emit gravitational waves in the frequency band where LIGO and Virgo detectors are most sensitive ($40 - 1000$ Hz). Since no detection candidate passed the severe criteria of data analysis, upper limits on rates of binary coalescence have been established [55].

At present, there are significant uncertainties in the astrophysical rate predictions for compact binary coalescences, which can vary over two orders of magnitude. Uncertainties arise from the small sample size of observed galactic binary pulsars, from poor constraints for predictions based on population-synthesis models, and from the lack of confidence in a number of astrophysical parameters such as the pulsar luminosity distribution. Thus the direct measurement of coalescence rates are important, since they might impose constraints on the theoretical models of stellar evolution and compact binary formation.

The measured upper limits are reported in table 3.2. Rates are reported in units of number

per L_{10} per yr, where L_{10} is 10^{10} times the blue solar luminosity $L_{B\odot} = 2.16 \cdot 10^{26}$ J s^{-1}, derived from the blue solar magnitude. Binary compact objects are usually produced via the evolution of massive stellar binaries, whose birthrate and evolution can be traced in a galaxy by measuring the amount of emitted blue light. Thus the blue luminosity of a galaxy should linearly scale with its compact binary coalescence rate [63]. By using the conversion factor 1.7 L_{10}/MWEG [5], rates can be converted in units of number per Myr per MWEG, also reported in table 3.2. Unfortunately, these upper limits are still 2 to 3 orders of magnitude larger than astrophysical expectations [5], reported in table 1.1. These limits cannot yet provide any significant constraint to stellar evolution models.

A separate search for signals from binary black-hole coalescences with total mass $25M_\odot \leq M \leq 100M_\odot$, component masses $1M_\odot \leq m_1$ and $m_2 \leq 99M_\odot$ and negligible spin has also been performed [56]. No plausible gravitational-wave candidate event has been detected, and the coalescence rate of nonspinning black holes with component masses $m_1 \leq 19M_\odot$ and $m_2 \leq 28M_\odot$ has been constrained to be less than 2.0 Mpc^{-3}Myr^{-1}. This limit is still about one order of magnitude higher than astrophysical estimates for such systems.

Search of signals from burst sources

The analysis performed for burst sources is similar to that of coalescing binary systems. The method used is coincidence analysis, with the same class of veto categories for data quality selection. However, since burst sources are currently not understood well enough to generate accurate waveforms, *excess-power* algorithms are employed instead of matched-filter searches with templates. By measuring power in the data as a function of time and frequency, one may identify regions where the output power is not consistent with the anticipated fluctuations of detector noise [57]. The estimation of background noise in the detectors is performed by time-shifting of the data, like in the case of search for binary coalescence signals. Also software and hardware injections are used to test the efficiency of the search algorithms, though only by using approximated waveforms of the expected signal.

No gravitational-wave event has been detected by the general search for burst source emissions. The main result [57] is a rate limit $\mathcal{R}$ for strong gravitational wave signals, equal to 2.0 yr^{-1} in the frequency band below 2 kHz and equal to 2.2 yr^{-1} for frequencies above 2 kHz. This rate is larger than astrophysical estimations, which quote 0.5 yr^{-1} within ~ 5 Mpc from Earth [6].

No evidence of a gravitational wave signal came also from a separated search for burst signals from 6 known magnetars [8]. The search put upper limits on the gravitational wave energy emitted for the lowest-order pulsational mode (the *f-mode* at 1090 Hz) and the *white noise* burst at $100-200$ Hz. The two lowest limits of the search are estimated for the source SGR 0501+4516: these are $1.4 \cdot 10^{47}$ erg (at a nominal distance of 1 kpc) for the f-mode and $3.5 \cdot 10^{44}$ erg for the white noise burst. This latter is, for the first time, comparable to the electromagnetic emission observed in magnetar flares.

Search of signals from known pulsars

Within our Galaxy there are currently over 200 known pulsars with spin frequencies greater than 20 Hz, which therefore fall into the detection band of gravitational wave interferometers. Thus the search looks for signals from pulsars of known position and spin frequency in the S5-VSR1 data, assuming that: (i) pulsars are triaxial stars emitting gravitational waves at precisely twice their

observed spin frequencies, and (ii) that gravitational waves are phase-locked with the electromagnetic signal. The observed pulsar phase evolution is modeled using a Taylor expansion about a fixed epoch time t_0,

$$\phi(T) = \phi_0 + 2\pi[\nu_0(T - t_0) + \dot{\nu}_0(T - t_0)^2/2 + ...] \tag{3.1}$$

where ϕ_0 is the initial spin phase, ν_0 and its time derivatives are the pulsar spin frequency and spin-down coefficients at t_0, and T is the proper time of the pulsar. The expected signal in an interferometer from a triaxial pulsar is then [64]

$$h(t) = \frac{h_0}{2}(1 + \cos^2 \iota)F_+(t, \psi)\cos 2\phi(t) + F_\times(t, \psi)h_0 \cos\iota \sin 2\phi(t) \ , \tag{3.2}$$

where $\phi(t)$ is the phase evolution in the detector time t, F_+ and $F_\times$ are the detector antenna patterns for the $+$ and $\times$ wave polarizations, ψ is the wave polarization angle, and ι is the angle between the rotation axis of the pulsar and the line of sight. The detector time differs from the pulsar proper time by a relativistic Doppler effect, which is estimated and corrected before performing the data analysis [64].

Data from gravitational wave detectors are heterodyned using twice the known electromagnetic phase evolution of each pulsar. The heterodyne removes the rapidly varying component of the signal and leaves only the daily varying amplitude modulation, due to the motion of the source through the antenna pattern of the interferometer [65]. Heterodyned (complex) data are low-pass filtered and fed to the search algorithm, which estimates the Bayesian *posterior* probability of the unknown parameters $(h_0, \phi_0, \cos\iota, \psi)$ over the signal model of eq.(3.2). By using the posterior probability on h_0, the search sets an upper limit on the gravitational wave amplitude emitted by known galactic pulsars [58], with 95% degree of belief.

Amplitude upper limits can be used to constrain the *spin-down limit* amplitude h_{sd} of each pulsar, which can be calculated by assuming that the observed spin-down rate of the object is entirely due to energy loss through emission of gravitational radiation. For the sample of pulsars considered in the S5 data search, the resulting median upper limit of the search on h_0 is $7.2 \cdot 10^{-26}$. For the Crab pulsar (PSRB0531+21, PSRJ0534+2200), the measured limit $h_0 \simeq 2 \cdot 10^{-25}$ is a factor of 7 below the spin-down limit. This limits the power radiated via gravitational waves to be less than $\sim 2\%$ of the available spin-down power. For all of the other pulsars, the median ratio to the spin-down limit is $h_0/h_{sd} = 108$. For the millisecond pulsars of the sample, several of the measured upper limits are only about an order of magnitude above their spin-down limits. Through eq.(1.25), these results can be interpreted as limits on the pulsar ellipticity, yielding a median value of $\epsilon = 1.1 \cdot 10^{-6}$.

One of the first results of the analysis of data from the S6-VSR2/VSR3 joint run is an upper limit on the gravitational wave emission from the Vela pulsar (PSR B0833-45, PSR J0835-4510) [62], which is one of the nearest known pulsar at ~ 290 pc from Earth. Vela is observed to pulsate at $\nu_0 = 11.19$ Hz in radio, optical, X-ray and γ-ray radiation and is associated with the Vela Supernova remnant. The frequency of the expected gravitational waves emitted by the Vela pulsar ($\Omega_{\rm GW}/2\pi = 2\nu_0 = 22.38$ Hz) is within the detection band of Virgo, because of the very effective seismic isolation provided by the Superattenuator. This frequency range is inaccessible to all other gravitational wave detectors to date, thus only Virgo data have been used in the search of signals from the Vela pulsar.

Three independent methods of data analysis have been used in the search (all assuming that gravitational wave emission follows the radio timing), the first being the Bayesian approach de-

scribed above, the others being two different frequentist approaches based on Monte Carlo simulations. The first method yielded an upper limit $h_0 = 2.1 \cdot 10^{-24}$, with 95% confidence. The other two produced the upper limits $h_0 = 1.9 \cdot 10^{-24}$ and $h_0 = 2.2 \cdot 10^{-24}$, with 95% confidence. All these limits are below the Vela spin-down limit of $3.3 \cdot 10^{-24}$, and correspond to a limit on the star ellipticity of $\sim 10^{-3}$. This is above the maximum ellipticity sustainable by a neutron star with a standard equation of state, but still comparable with the value allowed by some exotic equations of state [66]. These results have also constrained the internal toroidal magnetic field of the Vela to be less than 10^{16} G.

Search of signals from the stochastic background

The search for the stochastic gravitational wave background is performed by cross-correlating data from pairs of interferometers of the network, in order to extract the background signal (supposed to be the superposition of the astrophysical and the cosmological backgrounds) from the instrumental noise of the detectors, which are supposed to be uncorrelated. In the frequency domain, the cross-correlation between two interferometers is multiplied by a filter function [10]

$$\tilde{Q}(f) = N \frac{\gamma(f)\Omega_{\rm GW}(f)H_0^2}{f^3 P_1(f) P_2(f)} \ , \tag{3.3}$$

in order to optimize the signal-to-noise ratio. In eq.(3.3), $\Omega_{\rm GW}(f)$ is the energy density spectrum of gravitational waves defined in eq.(1.27), $P_i(f)$ is the noise of the $i-$th detector, $\gamma(f)$ is the overlap reduction function, arising from the overlap of antenna patterns of interferometers at different locations and with different orientations. This filter enhances the frequencies at which the signal of the template gravitational-wave spectrum is strong, while suppresses the frequencies at which the detector noise is large.

As in the network detection band most theoretical models are characterized by a power-law spectrum, the search assumes a power-law template gravitational-wave spectrum with index α, $\Omega_{\rm GW}(f) = \Omega_\alpha (f/100 \text{ Hz})^\alpha$. The normalization constant N in eq.(3.3) is chosen such that the expected value of the optimally filtered cross-correlation is Ω_α. The cross-correlation between the data of the two most sensitive detectors of the network, the 4-km LIGO interferometers at Hanford and Livingston, in the frequency band $41 - 169$ Hz (which contains 99% of the sensitivity) leads to the estimate for the frequency independent ($\alpha = 0$) gravitational-wave spectrum $\Omega_{\alpha=0} = (2.1 \pm 2.7) \cdot 10^{-6}$. This corresponds to a 95% confidence upper limit $\Omega_0 < 6.9 \cdot 10^{-6}$, and for other values of the power index α in the range $(-3, 3)$, the 95% confidence upper limit varies between $1.9 \cdot 10^{-6}$ and $7.1 \cdot 10^{-6}$ [10].

Before these results, the most constraining bounds on the stochastic gravitational wave background around 100 Hz came from observations of Big Bang nucleosynthesis (BBN) and cosmic microwave background (CMB) anisotropies, as reported in eqs.(1.29) and (1.30) [10, 9]. In the LIGO frequency band and for $\alpha = 0$, these bounds are $\Omega_0^{BBN} < 1.1 \cdot 10^{-5}$ and $\Omega_0^{CMB} < 9.5 \cdot 10^{-6}$, which are about 5.2 and 4.5 times larger than the bound measured by the interferometer network, respectively. This new limit is anyway many order of magnitude larger than the expected energy density due to the standard inflationary cosmological model, which is $\Omega_0^{\rm inflation} \sim 10^{-14}$.

Multimessenger astrophysics

A first multimessenger cooperation has been established between present interferometric detectors and γ-ray satellites, for externally-triggered searches of gravitational wave bursts in coincidence with γ-ray bursts [59, 60], though it yielded no detection. Multimessenger searches have been also conducted the other way, by triggering the electromagnetic follow-up of sky regions identified by the network of detectors [61], but so far no trigger has been confirmed by the observation of an electromagnetic counterpart.

3.3 Advanced Detectors

In this section we introduce the projects of a second generation of instruments, which aim to achieve a tenfold sensitivity improvement with respect to the reference sensitivity of present km-scale interferometers. These projects are Advanced LIGO [67, 68] (hereafter aLIGO), Advanced Virgo [69] (AdV) and – though with some difference with respect to the previous two – the Large-scale Cryogenic Gravitational-wave Telescope [70] (LCGT). Thanks to the sensitivity improvement of one order of magnitude in all the detection band, each of these detectors will be able to scan a 10^3 times larger volume of the Universe than initial instruments. Expected detection rates (assuming that sources are isotropically distributed in space) will increase correspondingly, leading to several detections of gravitational-wave signals per year.

aLIGO, AdV and LCGT will be power-recycled Michelson interferometers with FabryPerot arm cavities, with an additional mirror at the interferometer output. This *signal-recycling* mirror will form an optical cavity with the interferometer, allowing the gravitational-wave signal sidebands either to be re-injected and stored in the interferometer or extracted, depending on the cavity resonance condition [71]. aLIGO and AdV will use their initial buildings and vacuum systems but will otherwise consist of new instruments. The present three LIGO interferometers will be upgraded and the arms of the shorter interferometer at Hanford will be extended to 4 km. According to the present planning of the two projects, the installation of the hardware at the sites will start at the end of 2011. Both aLIGO and AdV are expected to finish their commissioning phase in order to be operative at design sensitivity for 2014.

LCGT will have 3-km long arm cavities, and will be the first km-scale interferometer to be built underground and with a cryogenic system for the cooling of the arm cavity mirrors. Ground motion of underground sites is expected to be sensibly smaller than that of surface facilities [72]. On the other hand, as it will be discussed in chapter 7, the cooling of the mirrors will reduce the thermal noise of the optics. The construction of LCGT is planned to end on 2015, and the data taking will start at the beginning of 2018, after a phase of commissioning.

We will describe in the following the science case of second generation instruments. Given that advanced detectors will have comparable sensitivities in the same detection band, we will assume AdV as a reference example, since the first part of this thesis work concerns its optical design.

3.3.1 Sensitivity and Science Case

The reference sensitivity curve of AdV with the main noise contributions is shown in fig.3.6. The presence of the signal recycling cavity allows for tuning of the shape of the shot-noise-limited sensitivity curve of the interferometer, a technique that can be used to optimize the detector sensitivity for detecting expected astrophysical sources.

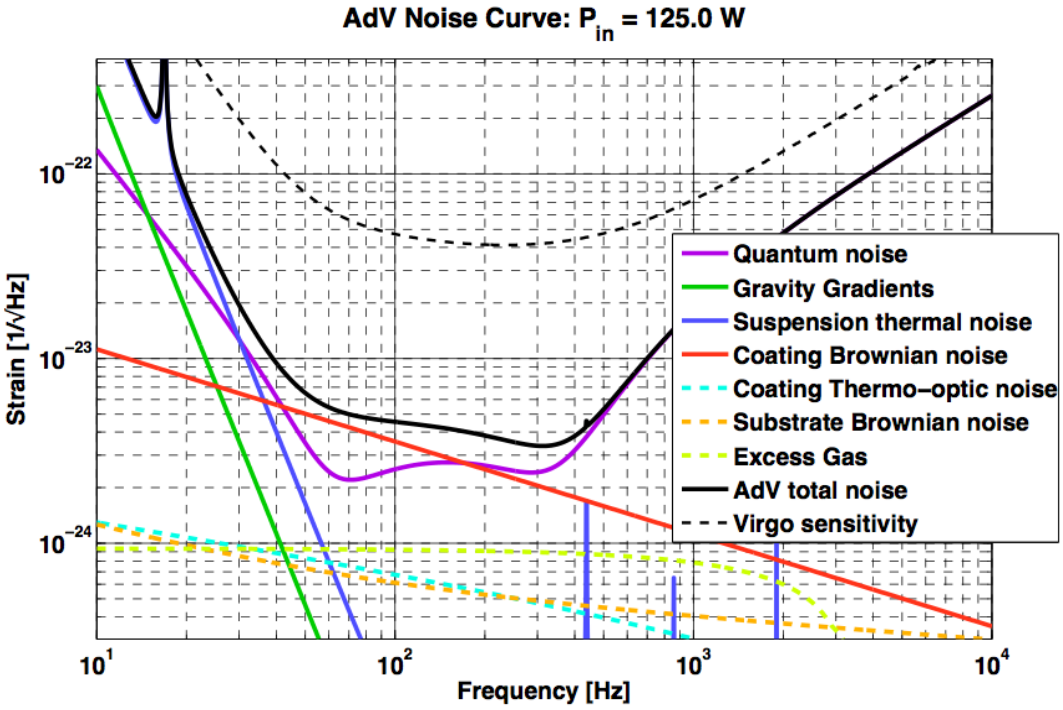

Figure 3.6: Advanced Virgo design sensitivity (black solid curve) compared to the Virgo design sensitivity (black dashed curve), from [69]. The spectra of fundamental limiting noises are also shown.

For fig.3.6, the sensitivity has been tuned in order to maximize the sight distance for binary neutron stars (NS-NS). The figure of merit that is used to evaluate the sensitivity of the detector for coalescing binaries is the *event horizon*, which is the maximal distance for an optimally-oriented observable source in the sky, in order to be detected with signal-to-noise ratio equal to 8. For frequencies below ~ 30 Hz, the sensitivity of AdV is limited by suspension thermal noise. Within $30 - 200$ Hz, the dominating source of noise is the thermal noise of mirrors, due to brownian noise of coatings. Between 200 Hz and 400 Hz, coating thermal noise is comparable to shot noise, though this latter is expected to be larger. For $f > 400$ Hz, the noise curve is completely determined by the shot noise of the laser.

The sensitivity curve might be tuned as well to [69]:

- enhance the low-frequency response in order to increase the detectability of large mass black-hole binary systems (BH-BH)
- enhance the sensitivity in a narrow frequency range, to target young pulsars
- widen the detector response and increase the high-frequency sensitivity for burst search.

The sensitivity curves corresponding to different tunings are shown on fig.3.7 and summarized in table 3.3. Hereafter, for the sake of simplicity, we will only consider a sensitivity curve optimized for a maximum binary-neutron-star detection horizon, as the basis for quantitative considerations.

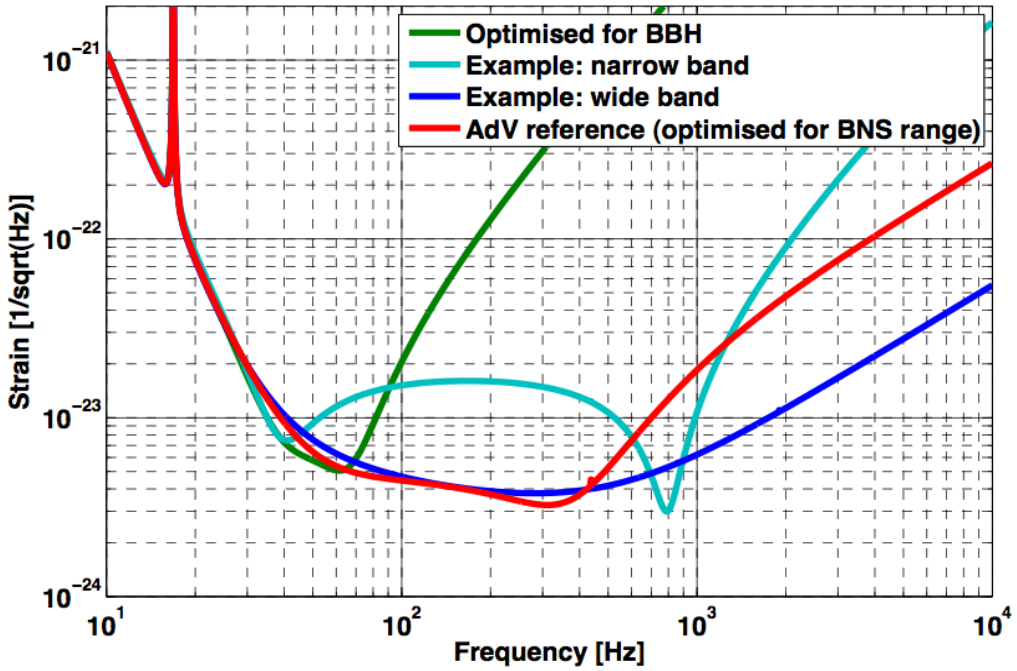

Figure 3.7: Tuning of the sensitivity curve of Advanced Virgo (red curve), from [69]. Maximum detection horizon for black hole-black hole binary systems (green curve), narrow-band tuning for pulsar search (cyan curve), wide-band tuning for burst search (blue curve).

sensitivity curve tuning	NS-NS range [Mpc]	BH-BH range [Mpc]	h at 1 kHz $[1/\sqrt{Hz}]$
Virgo (design)	11	58	$7.2 \cdot 10^{-23}$
AdV NS-NS (design)	150	1112	$1.8 \cdot 10^{-23}$
AdV BH-BH optimized	108	1276	$3.2 \cdot 10^{-21}$
AdV broadband	134	987	$6.2 \cdot 10^{-24}$

Table 3.3: Detection horizon and strain sensitivity for different tunings of the Advanced Virgo sensitivity curve, from [69]. The design sensitivity of Virgo is reported for comparison.

source	AdV det. rate [yr^{-1}]	Virgo det. rate [yr^{-1}]
NS-NS	17	$4.5 \cdot 10^{-3}$
NS-BH	4.7	$1.2 \cdot 10^{-3}$
BH-BH	7.6	$1.9 \cdot 10^{-3}$

Table 3.4: Expected detection rates of compact binary coalescences for Advanced Virgo, from [42]. Expected detection rates for Virgo are reported for comparison.

The scientific motivations and the chances of detecting gravitational waves for different types of sources of AdV (and more in general for advanced detectors) can be synthetically resumed as follows:

- **coalescing binary systems**: as the detection horizon increases accordingly with the increase of sensitivity, by assuming the coalescence rates reported in table 1.1 the expected rate of detection is of the order of tens of events every year. Detection rates are reported in table 3.4, where also the estimated values for Virgo are reported for comparison. The improvement with respect to the first generation of detectors is evident
- **pulsars**: assuming 1 year of integrated observation, AdV is expected to beat by orders of magnitude the spin-down limit for about 40 of the pulsars presently known, mostly at low frequencies [69]
- **core collapse Supernovae**: as already mentioned in chapter 1, the gravitational wave energy emitted by Supernova events might be lower than as previously expected, i. e. as low as $\leq 10^{-8} M_{\odot}$ [6]. This fact strongly reduces the prospects of detection with second-generation instruments. Advanced detectors could however put some constraints on the strength of the gravitational radiation emitted by this kind of events
- **multimessenger astrophysics**: advanced interferometers will play a crucial role in the development of multimessenger astrophysics, since they will potentially observe the gravitational signal related to high-energy neutrinos from extragalactic sources, neutrinos from Supernovae, optical (γ-ray bursts and nearby Supernovae), radio (bursts, afterglows) and X-ray transients [69].

However, apart from extremely rare events, the expected rate and signal-to-noise ratio of second-generation instruments are expected to be too low for precise astronomical studies of gravitational-wave sources, and to yield complementary informations to electromagnetic observations in the study of fundamental systems and processes in the Universe. This is why a third-generation detector with increased sensitivity is presently under study.

3.4 Third-Generation Detectors

Einstein Telescope [73, 74] is a project of a third-generation detector, about one hundred times more sensitive than present ones. This considerably large sensitivity improvement is motivated by the aim of performing *precision* gravitational-wave astronomy. The project is presently at the

phase of design study [75], supported by the European Commission through the 7th Framework Programme of the AStroParticle ERAnet (ASPERA) network [76]. The science case of the Einstein Telescope (hereafter, ET) project is vast and comprehensive:

- to measure in great detail the physical parameters of compact objects in binary systems, constrain the equation of state of neutron stars and solve the enigma of γ-ray bursts. Binary systems of total mass $M = 10 - 100$ $M_\odot$ are expected to be detectable with a signal-to-noise ratio equal to 8 up to a luminosity distance $D_L \sim 200$ Gpc, corresponding to a cosmological redshift $z \sim 17$. Depending on their spinning frequency and ellipticity ϵ, pulsars might be detectedable up to several hundreds of kpc. For millisecond pulsars, the detection horizon is expected to vary between 5 pc ($\epsilon = 10^{-9}$) and 500 kpc ($\epsilon = 10^{-5}$).

- to test General Relativity by comparing observations of massive binary systems with numerical relativity predictions, and to constrain alternative theories of gravity

- to measure cosmological parameters (the matter content of the Universe Ω_m, the energy density Ω_Λ and the equation of state w of the dark energy) from standard sirens, and probe the primordial universe through the measurement of the gravitational-wave stochastic background

- to probe the physics of core-collapse Supernovae, to which ET might be sensitive within few Mpc with an expected event rate of ~ 0.5 yr^{-1}.

The target sensitivity of ET is shown on fig.3.1, compared to the typical sensitivity of an advanced detector. ET is planned to be a interferometer with 10-km long arms. The detector will be dual-recycled, with power and signal recycling cavities, and will have a large detection band, spanning over four orders of magnitude in frequency, starting from 1 Hz. To achieve this target, several limitations of the technologies adopted in the advanced interferometers must be overcome, and new solutions must be developed to reduce the fundamental and technical noises that will limit the next-generation instruments.

From the technical point of view, the favorite arrangement for a detector with the target sensitivity of ET is a 2-band *xylophone* configuration, composed of two distinct interferometers with maximum sensitivity at different frequencies, at an underground site. The low-frequency detector (ET-LF) could be a cryogenic interferometer with moderate optical power, whereas the high frequency detector (ET-HF) could use a high power laser [77]. The basic concept behind this design is the decoupling of conflicting technical solutions, like in the case of cryogenic test masses with high thermal load. The xylophone configuration, combining two detectors specialized on different frequency bands, would allow to optimize the shot noise and the radiation pressure noise separately. A possible realization of such a xylophone strategy is shown on fig. 3.8, while the main parameters of the xylophone detector are summarized in table 3.5.

The sensitivity requirement for the low-frequency part of the detection band is very challenging. The region between 1 and 10 Hz is limited by seismic and gravity gradient noise [78], and will not be accessible by second generation interferometers. This frequency band might become exploitable by realizing an underground observatory. Furthermore, with a subterranean installation, other noises induced by external disturbances like wind, scattered light or temperature fluctuations will be suppressed by the quietness of the site.

The shot noise at high frequency would be lowered by storing high laser power in detector. The design study of ET plans to use an input power of 1 kW, which would be amplified by the power

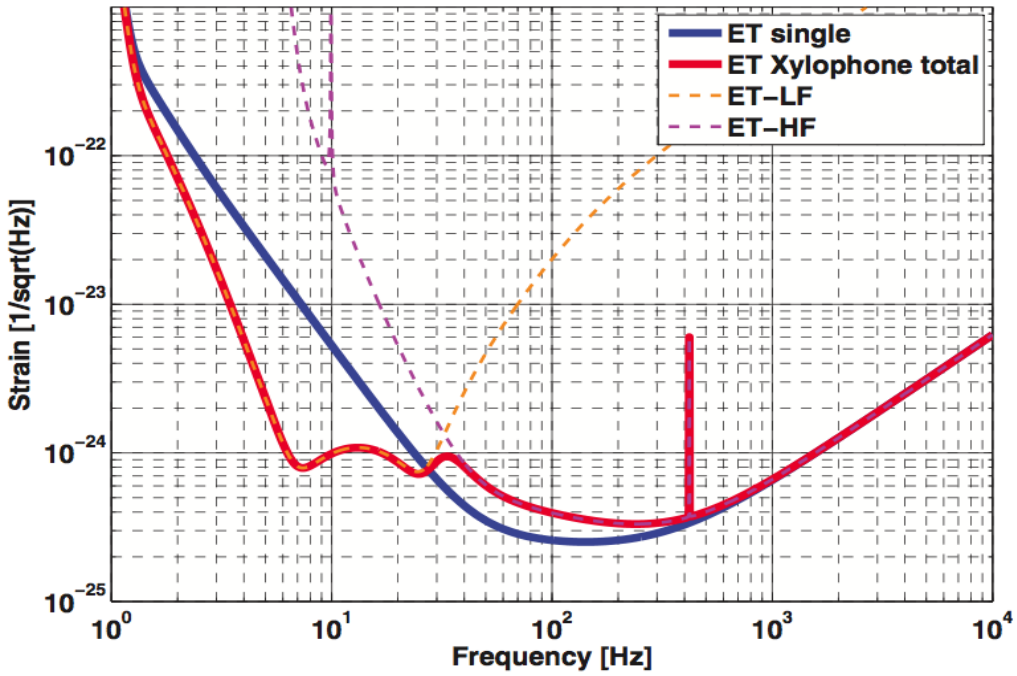

Figure 3.8: Sensitivity of the Einstein Telescope, implemented by two frequency-specialized (low-frequency, ET-LF, and high-frequency, ET-HF) detectors, with respect to a single wide-frequency range interferometer implementation, from [77].

recycling cavity to 20 kW. Because of the high finesse cavities planned for ET, the power stored in the arms of the detector will be about 3 MW. The increase of the laser power will cause the radiation pressure noise to increase below 20 Hz, therefore to lower this noise heavier mirrors of $M \sim 200$ kg could be used. Increasing the mirror mass will decrease the mechanical susceptibility and hence cut down the effect of radiation pressure on the displacement of optics. To decrease further shot and radiation pressure noise, squeezed light will be injected in the interferometer [78].

parameter	ET-HF	ET-LF
arm length	10 km	10 km
arm power	3 MW	18 kW
temperature	290 K	10 K
quantum noise suppression	squeezing	squeezing
beam shape	Laguerre-Gauss	Gaussian

Table 3.5: Summary of the main parameters of the 2-band xylophone detector. ET-HF is the high frequency interferometer, ET-LF is the low-frequency one.

In the most sensitive region of the detection band, the central region around 100 Hz, the high-frequency detector will be limited by mirror thermal noise. This limitation will be discussed in chapter 7, together with a list of possible solutions to decrease this noise. Among those, the use of cryogenics to cool down the optics of the detector is a suitable option. Another solution might be the use of beams with a wide radial distribution of the light intensity, Laguerre-Gauss beams.

In the second part of this thesis work we will present the expected benefits (expected decrease of thermal noise and also of thermal effects) due to the use of higher-order Laguerre-Gauss beams in future detectors, and we will propose a technique for the efficient generation of high purity beams for future generations of gravitational-wave interferometers. We will present in chapter 8 the results of an experimental tabel-top setup which demonstrate the feasibility of this technique, which might be in principle suitable even for the implementation in a later phase of advanced detectors.

PART II

Optical Design of the Non-Degenerate Recycling Cavities of Advanced Virgo

Chapter 4

The Project of Advanced Virgo

This chapter is intended to give a technical overview of the AdV project, and we will focus our description especially on those elements which will be relevant for the following of this thesis work. We will present the optical layout of the detector, which features four major upgrades with respect to Virgo: (i) the change of the arm cavity configuration, from plano/concave to bi-concave mirrors, (ii) the change of arm cavity finesse to 450, (iii) the implementation of signal recycling and (iv) the introduction of compensation plates.

The arm cavity configuration is changed to increase the beam radius on the cavity mirrors, to decrease the mirror thermal noise which will limit the sensitivity of the detector in the central part of the spectrum. The bi-concave configuration is used to avoid the effect of tilt instability due to the torque of radiation pressure [79], which is enhanced in a configuration with nearly flat mirrors. We will see in the following chapters that the change of the arm cavity configuration has important consequences for the optical design of the recycling cavities.

Then we will describe the thermal compensation system, which will be used to compensate for effects of wavefront distortion caused by thermal effects in the optics. The mitigation of thermal effects is necessary because the aberrations in the beam wavefront can cause a loss of detector sensitivity, and also severely disturb the detector control. The compensation system will be composed of a series of sensors for the reconstruction of the phase front of the aberrated beam, which will be used as error signal, and by two different types of actuators: ring heaters and CO_2 lasers. The ring heaters will act directly on arm cavity mirrors. The lasers will illuminate a transmissive optic, the compensation plate, positioned between the arm input mirror and the beamsplitter, in order to generate a phase pattern in the plane transverse to the beam. The pattern will be used to cancel or attenuate the phase distortion caused by thermal effects.

Finally we will describe the mechanical suspension system, the *Superattenuator*, which is already used in Virgo: it is composed of a chain of oscillators and of a last pendular suspension stage, the *payload*. Its description will be useful for the understanding of some crucial topics presented in the next two chapters.

4.1 Laser and Injection System

The laser of AdV will provide a power of 200 W, in order to have at least 125 W at the input of the interferometer. The increase of input power (about 6 times larger than in Virgo) will lower the shot noise, improving the detector sensitivity at high frequency. The design of the laser will be

based on a completely new technology with respect to the present laser system of Virgo, a Nd:YAG master oscillator with one- or two-stage fiber amplifier.

The optics between the laser and the power recycling mirror are called *injection system*. It will include a Faraday isolator specific for the high-power laser beam, an electro-optical modulator, the input mode-cleaner and a *mode-matching* telescope. The Faraday isolator will be used to protect the laser system from backwards reflection, and the electro-optical modulator will provide the phase modulation of the laser beam at radio-frequency, for the generation of *radio-frequency* sidebands for sensing and control purposes. The input mode-cleaner will have the same 144-m long triangular configuration of the present one of Virgo and a slightly larger finesse, $\mathcal{F} \sim 1200$.

4.2 Optical Layout

The optical layout[1] of the interferometer is shown in fig.4.1: the core of the interferometer will have the same configuration of Virgo, with the short-baseline *central Michelson interferometer* formed by the beam splitter and the input arm cavity mirrors (ITM), and the 3-km arm cavities.

The major upgrades in the optical layout of AdV are the following:

- the change in the arm cavity geometry, from a flat-concave to a concave-concave configuration. The input and the end arm cavity mirror will have radii of curvature of 1420 m and 1683 m, respectively. With this new configuration, the beam focus will have a radius $w_0 = 9.7$ mm and will be close to the center of the cavity. The beam will have a large radius on the cavity mirrors: $w = 4.9$ cm on the input mirror, and $w = 5.8$ cm on the end mirror. The beam size on the optics of the arm cavity is maximized in order to reduce mirror thermal noise. The larger size of the beam spot allows to average more effectively the surface fluctuations due to noise, as discussed in chapter 7

- the increase of the arm cavity finesse to $\simeq 450$ (yielding to an optical gain of about 286) [80], with a transmission $T = 1.4\%$ of input mirrors. This represents an increase of a factor ~ 10 with respect to Virgo, and ~ 3 with respect to Virgo+

- two transmissive optics, the *compensation plates* (CP), will be suspended facing the input arm cavity mirrors, to be used in the thermal compensation system described in section 4.4

- the implementation of signal recycling. A gravitational wave of frequency $\Omega_{\rm GW}/2\pi$ incident on the interferometer generates two signal sidebands of frequencies $(\omega_0 \pm \Omega_{\rm GW})/2\pi$. Since the detection band of ground-based interferometers coincides roughly with the frequencies of audible acoustic waves, these sideband fields are called *audio-frequency* sidebands.

  In a perfect interferometer operated on the dark fringe, the carrier and the signal audio-frequency sidebands come out of the arm cavities and are separated at the beamsplitter. The carrier light is directed towards the power recycling mirror, whereas the sideband fields induced by gravitational waves propagate towards the signal recycling mirror. This mirror

[1] We will refer here to the optical layout as it is described in the baseline design document of AdV [69], with non-degenerate recycling cavities. Recently marginally-stable cavities have been reconsidered, thus this design has partially changed. The difference between these two configurations will be explained and discussed in the next two chapters.

forms a coupled cavity with the arm cavities of the interferometer, for the recycling of the audio-frequency sidebands [71].

The signal recycling cavity allows the signal sidebands either to be stored in the arm cavities or to be extracted, depending upon the cavity resonance condition. The reflectivity of the signal recycling mirror determines the finesse of the recycling cavity, and thus the storage time of the signal. This latter sets the detection band of the interferometer, while the microscopic tuning of the recycling cavity length changes the frequency of maximal sensitivity [81].

The baseline configuration for the signal recycling cavity of AdV is the resonant sideband extraction, where the signal recycling cavity is used to widen the detection band of the detector.

The semi-transparent power-recycling mirror (PRM1) will have a transmission $T = 3.5\%$[2], yielding a finesse $\mathcal{F} = 105$ and a recycling gain of 40. The power stored in the arm cavities will be of the order of 700 kW, while about 5 kW will be stored in the power recycling cavity. The signal recycling cavity will have a finesse of $\mathcal{F} = 26$, given by a transmission $T = 20\%$ of the signal recycling mirror (SRM1). At the output of the detector there will be a short rigid mode-cleaner cavity before the photodiode, to filter out the spatial defects of the beam. The parameters of the layout are summarized in table 4.1.

The arm cavity mirrors will have a thickness of 20 cm and a weight of 40 kg, to decrease the radiation pressure noise. The quality of their reflective surfaces will be very high, with *flatness* < 5 nm (which is the rms of the difference between the perfect spherical surface and the actual surface for low spatial frequencies, < 1 mm^{-1}) and *roughness* < 0.1 nm (which is the rms of the difference for higher spatial frequencies). We will see in chapter 6 that the quality of the mirror surface is very important for having a high recycling gain of the sideband fields in the recycling cavities.

4.3 Fields Inside the Interferometer

For a clear understanding of the next two chapters it is important to distinguish all the fields that will resonate in the detector, thus we present here the following synopsis.

The beam entering the interferometer will be the sum of a carrier and radio-frequency sidebands, which will be used to acquire and maintain the resonant condition of all the optical cavities [82]. Two modulation frequencies will be used. At each frequency a pair of sidebands will be generated, satisfying different resonance conditions: (i) the first pair will be resonant in the power recycling cavity and almost anti-resonant (at half of the free spectral range) in the arm cavities and in the signal recycling cavity, (ii) the second pair will be simultaneously resonant in both the recycling cavities. These sidebands will be used in a standard Pound-Drever-Hall technique [83, 84] to extract the longitudinal error signal for mirror positions. In summary:

- the carrier field will resonate in the power recycling cavity and in the arm cavities, then it will *see* the whole interferometer
- one pair of radio-frequency sidebands, used for the control of the interferometer, will resonate in both recycling cavities (but not in the arm cavities)

[2] 5% for the marginally-stable cavities, see the previous note.

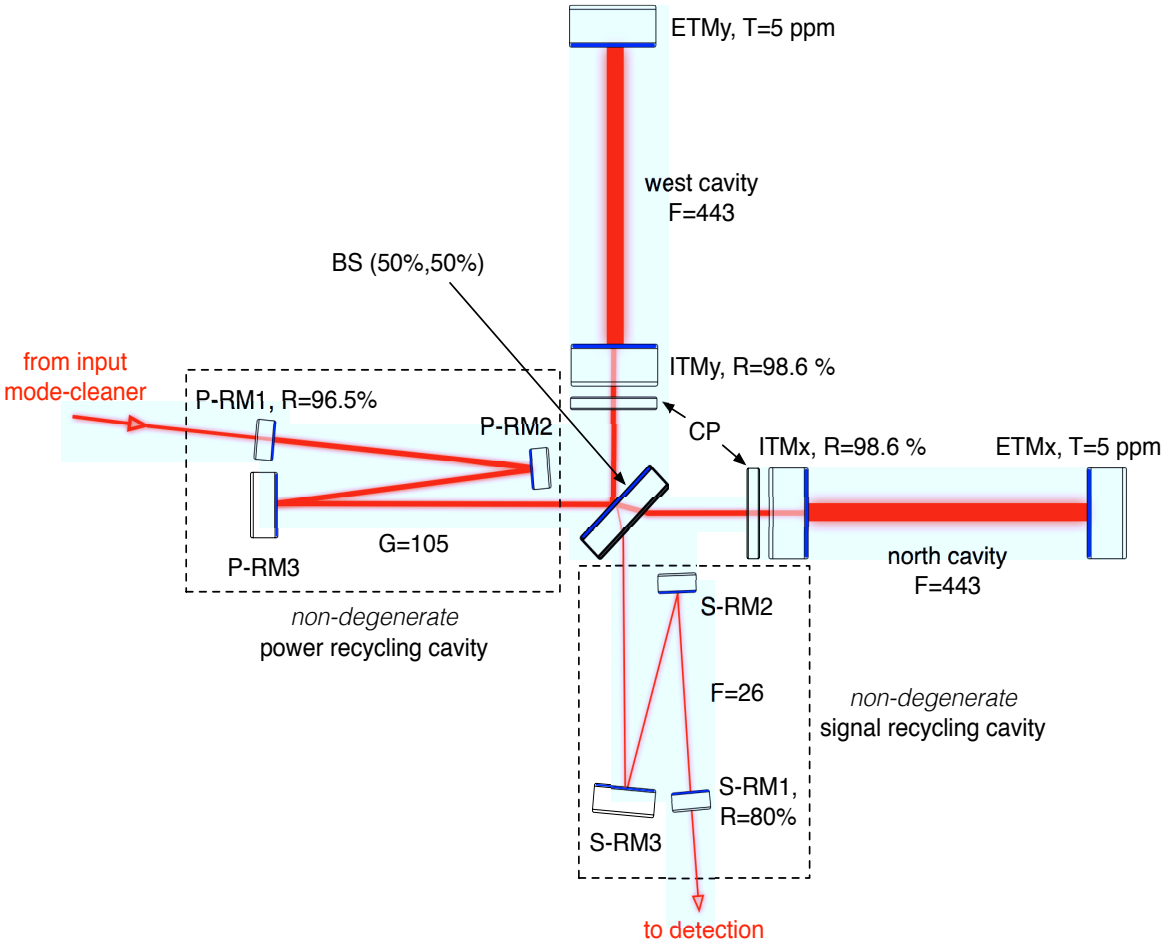

Figure 4.1: Optical layout of the Avanced Virgo interferometer.

Advanced Virgo Optical Parameters			
Light Power			
arm cavity power	704 kW	power on BS	5 kW
Arm Cavity Geometry			
cavity length	2999.8 m		
input mirror RoC	1420 m	end mirror RoC	1683 m
beam size on input mirror	48.7 mm	beam size on end mirror	58.0 mm
waist size	9.69 mm	waist position	1363 m
Arm Cavity Finesse			
finesse	450	round trip losses	75 ppm
input mirror transmission	1.4%	end mirror transmission	5 ppm
Power Recycling Cavity			
recycling mirror transmission	3.5 %	recycling gain	40
Signal Recycling Cavity			
recycling mirror transmission	20 %	finesse	26
Mirrors			
input mirror diameter	35 cm	end mirror diameter	35 cm
input mirror thickness	20 cm	end mirror thickness	20 cm

Table 4.1: Parameters of the Advanced Virgo interferometer.

- a second pair of radio-frequency sidebands, also used for control purposes, will resonate only in the power recycling cavity
- the audio-frequency signal sidebands will resonate in the signal recycling cavities and partially in the arms.

The resonance conditions of carrier and radio-frequency sidebands in the detector are illustrated on fig.4.2, where for the sake of simplicity recycling cavities are depicted with one recycling mirror.

4.4 Thermal Compensation System

The thermal compensation system will mitigate the thermal effects due to the absorption of laser power in the optics[3]. In Virgo this system [85] is composed of a *phase camera* [86] and a CO_2 laser that shines a heating pattern onto the reflective surface of both the arm cavity input mirrors. In AdV, the compensating system will be upgraded to a blend of different sensors for the measurement and reconstruction of the aberrated beam wavefront, and a series of actuators to actively compensate the wavefront distortions: the system is shown on fig.4.3.

Sensing

To lowest order, the degree of thermal aberration will be manifest in the main beam of the interferometer, which will be sampled at the output of the detector and through the extraction of

[3]As we will see in chapter 6, in marginally-stable cavities it will be necessary to use the thermal compensation system to compensate also for mirror figure errors.

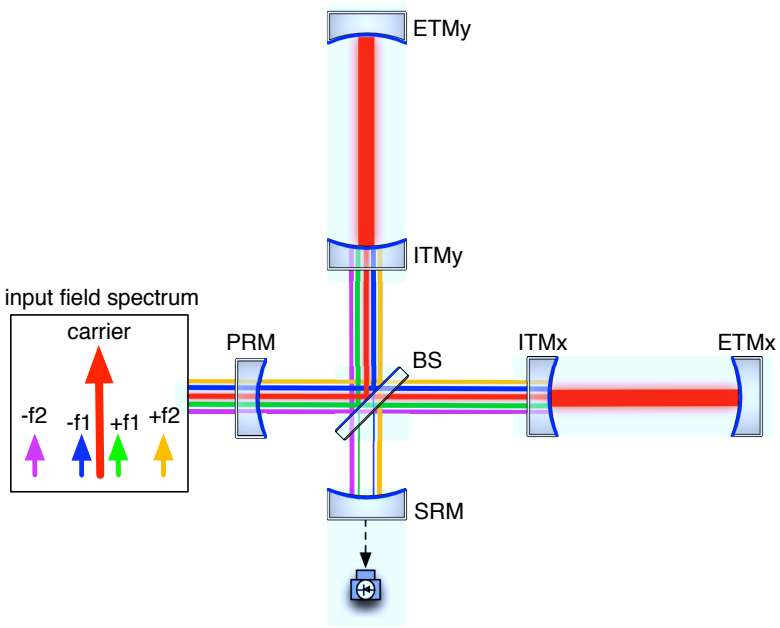

Figure 4.2: Resonance condition of carrier and audio-frequency sideband fields in Avanced Virgo.

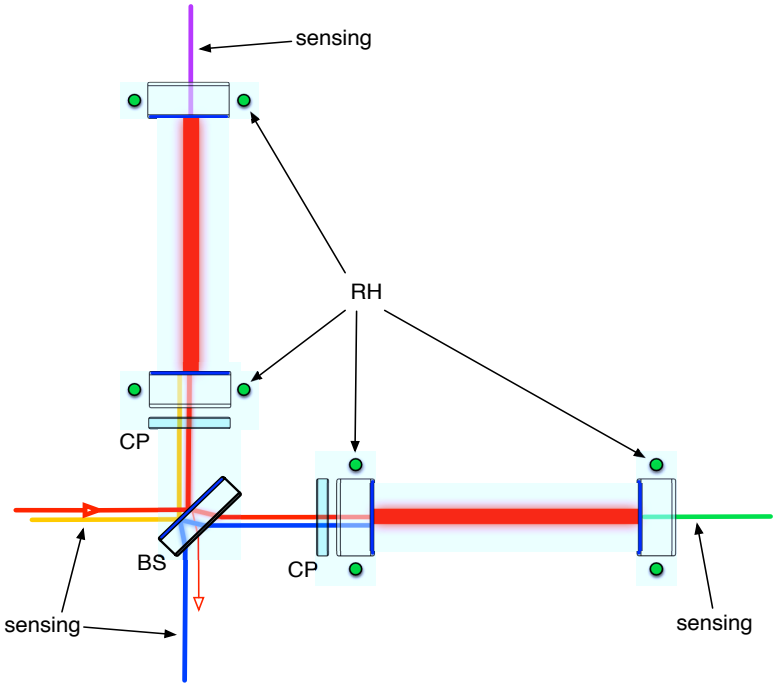

Figure 4.3: Scheme for sensing and actuation of the thermal compensation system: the sensing beams (in different colors), the compensation plates (CP) and the ring heaters (RH) are shown.

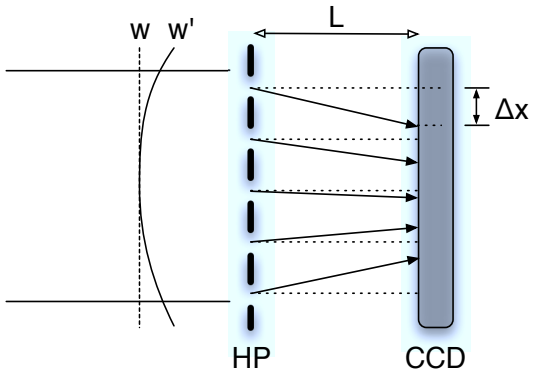

Figure 4.4: Scheme of the Hartmann wavefront sensor: W is the reference wavefront, W' the aberrated wavefront, HP is the Hartmann plate and $\Delta x/L$ is the wavefront gradient.

secondary *pick-off* beams. These beams will be sensed by phase cameras, which can measure the spatial distribution of amplitude and phase for carrier and sidebands at the same time [86].

In addition, each optic with a significant thermal load will be independently monitored. Knowledge of the phase profile of optics is valuable, completing the information from the mode profile of the interferometer beam. The reflective surface of each arm cavity mirror (input and end) will be monitored in reflection for deformation. The phase profile of input mirror and compensation plates (described here below in the actuation system) will be monitored in reflection from the recycling cavity side. To date, the sensing of the beamsplitter is under investigation. Optics will be monitored with beams of wavelength yet to be determined.

The sensitivity required for the wavefront sensor is at the level of 1.35 nm, corresponding to a maximum acceptable phase error of $\lambda/593$ at $\lambda = 800$ nm. A sensor that might achieve this sensitivity is the Hartmann sensor, shown on fig.4.4, composed of an opaque plate (the *Hartmann plate*) with an array of apertures, and of a CCD detector. The Hartmann sensor measures the change in the gradient of a wavefront, with respect to a reference wavefront. The gradient change is then numerically integrated to give the wavefront change due to aberrations.

The basic operation of a Hartmann sensor is the following: the wavefront to be measured is incident on the Hartmann plate and divided into a set of rays, known as *Hartmann rays*, which diffract from the holes of the plate. The rays propagate over a known distance L, where the pattern of spots on the CCD is recorded as a digital image. The displacement of each spot from a previously measured reference position is calculated, and used in the reconstruction of the wavefront. For AdV, a differential Hartmann sensor [87] with two CCD detectors at different positions has been proposed [69]. A prototype of this sensor has been already tested, and will be developed to be integrated in the thermal compensation system.

Actuation

The system of actuators will compensate for thermal lensing and thermo-elastic deformation: the former is expected to affect the recycling cavities, the latter will affect the recycling and the arm cavities. Thereby the system will act on both input and end arm mirrors, as depicted in the actuation scheme shown in fig.4.3.

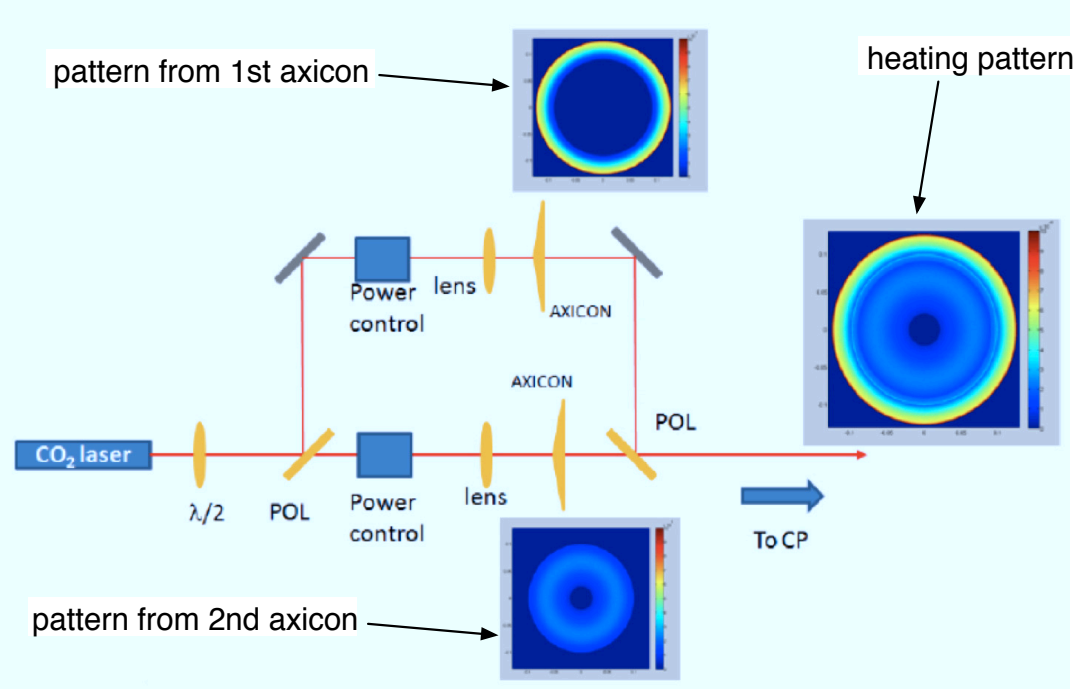

Figure 4.5: Scheme of the double-axicon telescope for generating an annular heating pattern, from [88].

The wavefront distortions in the recycling cavities will be corrected by shining an annular heating pattern on a transmissive optic positioned between the beamsplitter and each arm cavity input mirror, the *compensation plate*. Shining the pattern on the plates instead that directly on the mirrors will avoid that power fluctuations of the CO_2 laser induce a residual mirror displacement. The pattern will be generated by sending the Gaussian beam of a CO_2 laser through a telescope based on a double-*axicon* system (an axicon is a special lens with one conical surface), whose optical scheme is shown on fig.4.5.

The annular pattern is suitable to heat the edge of the mirror reflective surface, in order to compensate for the radially-symmetric power absorption in the central area of mirrors. We will see later in chapter 6 that relevant effects of wavefront distortion will come also from non-axisymmetric effects, like mirror figure errors and absorption inhomogeneities. An additional adaptive system to compensate for non-axisymmetric distortions is presently under study for the implementation in the detector [89].

To compensate the radii of curvature of the test masses, a circular resistor named *ring heater* will be placed around each arm cavity mirror. The ring will radiatively heat the barrel of the optic, so that the additional corrective thermal load will flatten the radial profile of absorption (peaked around the laser beam spot at the center of the mirror). The heater will be embedded in the recoil mass which surrounds the mirror, and will be placed into the focus of a parabolic reflecting shield. The shielding will be used to concentrate the heating radiation only on the edge of the mirror, thus decreasing the total emitted power for equivalent required compensations. Ring heaters will also compensate for aberrations due to mostly-symmetric absorption patterns in the optics.

4.5 Suspensions

AdV will adopt the passive seismic isolation system of Virgo, the *Superattenuator* [53]: this system allows Virgo to be presently the most sensitive gravitational wave interferometer in the low-frequency region, and it will also be compliant with the low-frequency sensitivity requirement of AdV (a residual mirror displacement noise of $6 \cdot 10^{-18}$ m/$\sqrt{\text{Hz}}$ at 10 Hz). We will describe hereafter the design of the Superattenuator, since it will be a relevant constraint for the optical design of the recycling cavity layout (as we will see in chapters 5 and 6).

The suspension system exploits the properties of attenuation of simple oscillators: the mirrors are suspended to a chain of seven pendulums, about 8-m long. Because of the long pendulum chain, all the normal modes of the system are confined below 2.5 Hz, in order to have an attenuation of the seismic noise of the ground by more than 10 orders of magnitude in the horizontal (on axis) direction, starting from a few Hz.

The suspension point of the chain is at the top stage of an *inverted pendulum* with a three-leg elastic structure. The legs of the inverted pendulum are about 7-m long, and seismic noise is filtered above its resonance frequency of about 30 mHz. The inverted pendulum is used as passive pre-isolation stage to reduce the seismic motion of the top suspension point. For the very low frequency motion ($\sim$ DC), the position of the suspension point is actively controlled through a system of position sensors and actuators. The Superattenuator structure is shown on fig.4.6.

The vertical seismic vibrations are not attenuated by the pendulum chain, and are partially transferred to the longitudinal direction of the laser beam, by means of unavoidable mechanical couplings and because of the curvature of the Earth. Vertical attenuation is obtained by replacing the upper five pendulum masses with seismic filters, shown on fig.4.6, each with a set of concentric cantilever blade springs with low stiffness [90]. The blades support the next mechanical filter through a 1 m-long steel wire, forming a chain of low frequency oscillators also in the vertical direction. The blades work in parallel with a *magnetic anti-spring* system [90], assembled on each filter: it acts with two magnets on the steel wire as a spring with negative elastic constant. The anti-spring system decreases the stiffness of the chain, thereby all vertical modes are below 2 Hz.

The two lower stages of the Superattenuator form the *payload*, shown on fig.4.7, composed of the mirror and two other mechanical elements [91]. The role of the payload is to compensate the residual seismic noise and to steer the mirror, maintaining the relative position of the interferometer optics. It is essentially a double-stage branched system with the *marionette* as first pendulum, and a recoil mass and the mirror as branches suspended from the marionette. The marionette is an anvil-shaped mechanical element used to steer the mirror and its recoil mass. This latter is a cylindrical mass of metal that surrounds the mirror. The position of the mirror is controlled by two sets of coil-magnet actuators, placed at the level of the marionette and of the recoil mass.

In initial Virgo the suspension wires of the mirror were made of steel and were wrapped around its body in a cradle configuration. In Virgo+, to decrease suspension thermal noise, the wires have been replaced with fibers of fused silica with low mechanical bulk loss [54]. For steel wires, in fact, the loss $\Phi_{bulk}(f)$ is in the range of 10^{-4}–10^{-3} at 100 Hz, whereas for fused silica fibers the loss is $\Phi_{bulk}(f) \sim 10^{-7}$ at 100 Hz [31]. Fibers have a diameter of ~ 280 μm and are fixed into silica supports, the *ears*, which are chemically bonded to the lateral surface of mirrors to realize a *monolithic* suspension [31]. This technology is now tested in Virgo+, and will be used in AdV [69].

The design of the Superattenuator has a well-defined symmetry around the axis of suspension: the inverted pendulum and the chain of filters are radially symmetric, and the elements of the

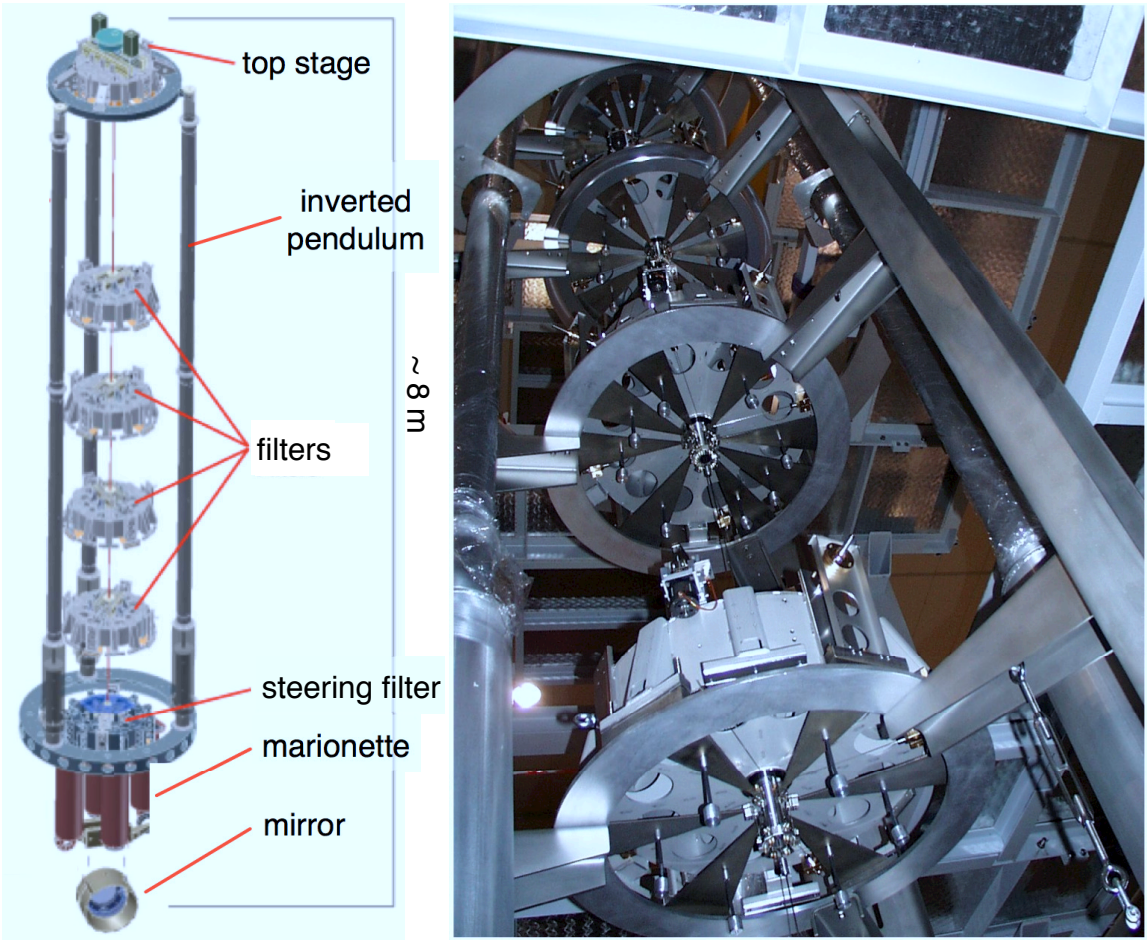

Figure 4.6: Scheme (left) and picture (right) of a Superattenuator of Virgo.

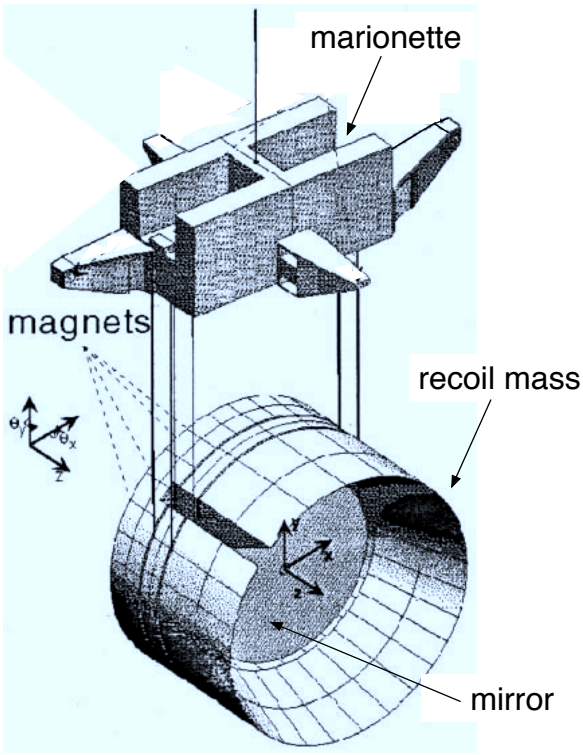

Figure 4.7: Scheme of the last suspension stage for the mirror: the Virgo payload, from [91].

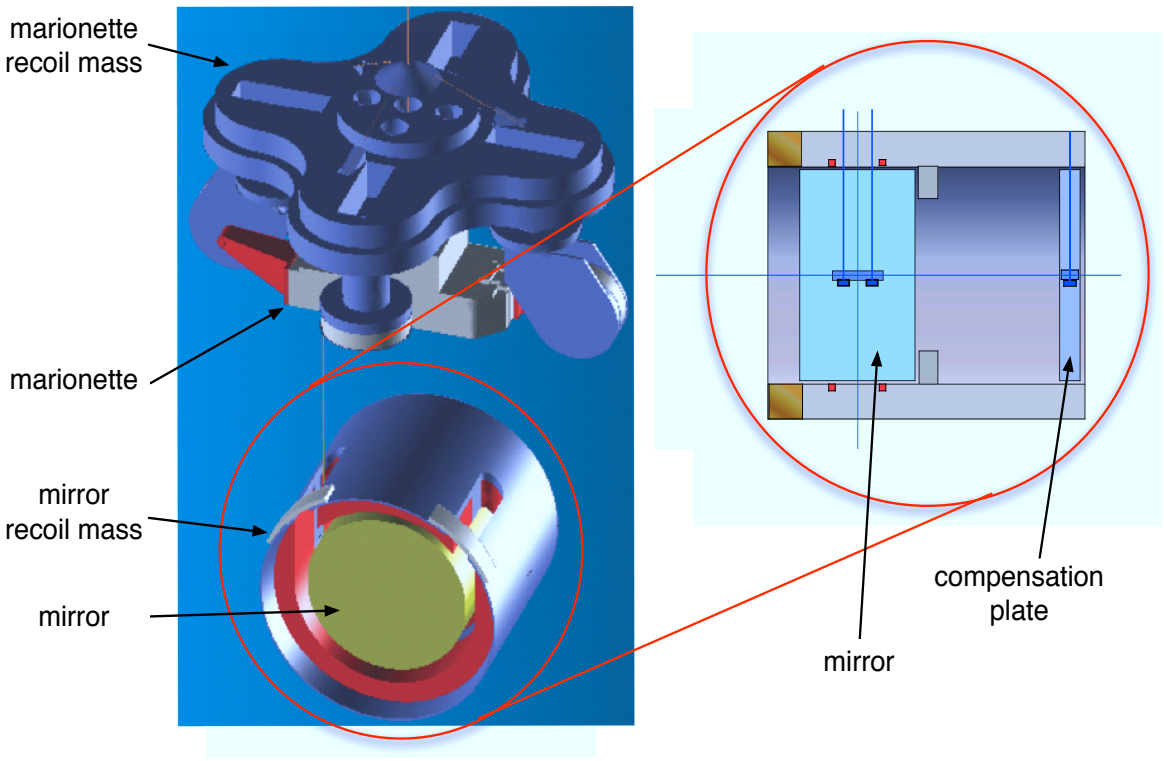

Figure 4.8: Scheme of the last suspension stage for the mirror: the AdV payload (left) from [69], and the design of the mirror recoil mass with the compensation plate (right) from[92].

payload are suspended with the center of mass *on-axis*. This minimizes the coupling between the degrees of freedom of the elements of the payload, and simplifies the control of mirror position. We will see in chapter 6 that the symmetry of the Superattenuator (and in particular the on-axis suspension of the payload) will be a critical element in the choice of the optical layout of the recycling cavities.

The design of the inverted pendulum and of the chain of filters will be substantially unchanged in AdV. The main modification will concern the control of the system of the suspension point at the top stage: presently the inverted pendulum is controlled in four degrees of freedom only (the three translations and the rotation around the vertical axis), whereas in AdV the Superattenuator design will include the control of the tilt around the two horizontal axes [69].

More considerable changes will concern the payload, whose new design is shown on fig.4.8. Possibly a new mechanical element will be added: a recoil mass for the marionetta, which could greatly simplify the installation of the payload in the vacuum tank which host the mirror [69]. The design of the recoil mass of the arm cavity input mirrors will be adapted to accomodate the suspension of the compensation plates [92].

Chapter 5

Stable Recycling Cavities for Advanced Virgo

The experience with initial Virgo and LIGO demonstrated that the control of the detector can be severely affected by higher-order mode contamination in the radio-frequency sidebands, due to thermal effects in the power recycling cavity. This happens because power recycling cavities of initial detectors like Virgo or LIGO are degenerate, i.e. higher-order modes can resonate at the same time with the fundamental mode, degrading the shape of the sideband fields.

This problem will even be enhanced for advanced detectors, where the increase of the beam size in the arm cavities, necessary to decrease mirror thermal noise, will also increase the degeneracy. Furthermore, advanced detectors will use higher input power, with consequent rise of thermal effects. Also the signal audio-frequency sidebands are expected to be concerned by this issue, due to thermal effects and mirror figure errors in the signal recycling cavity.

To solve the problem of mode contamination, aLIGO decided the implementation of *non-degenerate* or *stable* recycling cavities [93, 94]. A cavity is non-degenerate when its resonance linewidth is much smaller than the frequency spacing of higher-order modes, so that when the fundamental mode resonates in the cavity, higher-order modes cannot.

The scope of our work within the Optical Design and Simulation (OSD) group was the study and design of non-degenerate cavities for the requirements and constraints of AdV. We will show that the recycling cavity layout should have a folded optical path with three mirrors, where two of them form a telescope for focusing the beam inside the cavity. Therefore two additional mirrors per recycling cavity must be suspended. This layout must fit the present infrastructure and suspension system of Virgo, which suffer of lack of flexibility: the Superattenuator was designed to suspend a single mirror, in a vacuum chamber of narrow space. This technical constraint limits the choice of suitable layout configurations. Furthermore, the construction budget of the project does not allow for large modifications of the infrastructure.

To design a layout which satisfies these constraints we developed a set of optical simulations. We drew and studied several configurations (including some that had never been considered for aLIGO), and finally we chose the *vertical layout*. In collaboration with the Thermal Compensation System (TCS) group of Virgo, we also simulated the optical performances of this layout with respect to realistic thermal effects and mirror figure errors in the power recycling cavity of AdV. The results showed the expected sideband higher-order mode suppression in the cavity.

Only recently, budget and time-schedule constraints and progress in the development of the

TCS led to reconsider degenerate cavities. Even if finally the non-degenerate layout will not be implemented in AdV, we believe that these studies will be useful for the optical design of third-generation detectors.

In this chapter we will treat the design of the non-degenerate recycling cavities of AdV. Section 5.1 will introduce the properties of laser modes and resonators, with particular attention to the relevance of the Gouy phase in the resonance of higher-order modes. We will describe in section 5.2 the strong motivations towards the implementation of non-degenerate cavities. In section 5.3 we will present the conceptual design of non-degenerate recycling cavities, and we will show in section 5.4 the technical constraints of AdV concerning this layout. The work of optical simulation of recycling cavities will be presented in the next chapter.

5.1 Laser Modes and Resonators

We will introduce in this section the formalism and the fundamental notions used to describe laser beams, optical resonators and their coupling. We will focus our attention especially on higher-order modes, Gouy phase and mode degeneracy inside a cavity.

Let $E(\vec{r},t)$ be a field component, function of space $\vec{r}$ and time t, which satisfies the wave equation

$$\Big(\nabla^2 - \frac{1}{c^2}\frac{\partial}{\partial t^2}\Big)E(\vec{r},t) = 0 \ , \tag{5.1}$$

where c is the speed of light. Since we are interested in the spatial part of the field, we will assume that the component can be factored as $E(\vec{r},t) = u(\vec{r})f(t)$, where the dependence on time and space variables has been separated. Then, the function $u(\vec{r})$ must satisfy the Helmoltz equation

$$\Big(\nabla^2 + k^2\Big)u(\vec{r}) = 0 \ , \tag{5.2}$$

$k = 2\pi/\lambda$ being the propagation constant and λ being the laser wavelength. For the beam traveling in the z direction, we can write

$$u(\vec{r}) = \psi(x,y,z)e^{-ikz} \ , \tag{5.3}$$

where $\psi(x,y,z)$ is a complex function which represents the non-uniform amplitude distribution and the phase front curvature of the beam. We will assume that the paraxial approximation holds:

$$\Big|\frac{\partial^2\psi}{\partial z^2}\Big| << \Big|2ik\frac{\partial\psi}{\partial z}\Big|, \quad \Big|\frac{\partial^2\psi}{\partial x^2}\Big|, \quad \Big|\frac{\partial^2\psi}{\partial y^2}\Big| \ , \tag{5.4}$$

i.e. ψ is assumed to vary slowly across the direction of propagation. Thus the Helmoltz equation can be approximated as

$$\frac{\partial^2\psi}{\partial x^2} + \frac{\partial^2\psi}{\partial y^2} - 2ik\frac{\partial\psi}{\partial z} = 0 \ , \tag{5.5}$$

where

$$\psi = \sqrt{\frac{2P}{\pi}}\frac{1}{w(z)}\exp\Big[\frac{-r^2}{w^2(z)}\Big]\exp\Big[-i\Big(k\Big(z + \frac{r^2}{2R(z)}\Big) - \Phi_G(z)\Big)\Big] \tag{5.6}$$

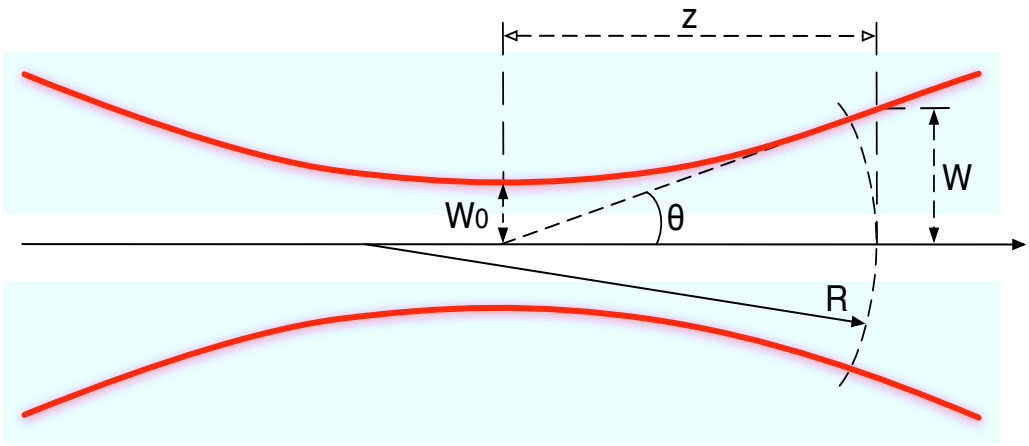

Figure 5.1: Parameters of a Gaussian beam.

is one of the possible solutions [95]. In eq.(5.6), P is the beam power, $w(z)$ is the beam radius, $R(z)$ is the radius of curvature of the phase front and $r^2 = x^2 + y^2$. The radius $w(z)$ is a measure of the decrease of the field amplitude with the distance from the axis, and indicates the distance at which the amplitude is $1/e$ times the maximum. The beam radius and the front curvature have the following dependence on z:

$$w(z) = w_0 \sqrt{1 + \left(\frac{z}{z_R}\right)^2} \ , \tag{5.7}$$

$$R(z) = z\left[1 + \left(\frac{z_R}{z}\right)^2\right] \ . \tag{5.8}$$

$w_0 = w(z = 0)$ is the beam size at its focus, called the *beam waist*, and $z_R = \pi w_0^2/\lambda$ is the *Rayleigh range*, a characteristic length equal to the distance from the beam waist (in the propagation direction) where the beam radius is increased by a factor $\sqrt{2}$. The width of the beam is an increasing function of z, whose evolution is shown on fig.5.1. The beam has a flat wavefront at the waist ($z = 0$, yielding infinite radius of curvature), which becomes more and more spherically curved as long as it propagates.

The Rayleigh range determines the depth of focus, which is the length on the optical axis where the beam is approximately collimated. For $z << z_R$ (in the proximity of the waist), the beam is said to be in *near-field* regime, whereas for $z >> z_R$ the beam is in *far-field* regime and starts to diverge. The beam contour $w(z)$ across z is a hyperbola with asymptotes inclined to the axis at an angle called *beam divergence*,

$$\theta = \frac{\lambda}{\pi w_0} \ . \tag{5.9}$$

The term $\boldsymbol{\Phi_G \equiv \arctan(z/z_R)}$ in eq.(5.6) ***is the Gouy phase***, which represents the phase difference with respect to the spherical wave. As shown on fig.5.2, the phase shift increases very rapidly around the beam waist, in near field, whereas in far field the increment is almost null: we will see in section 5.3 that this property will be crucial for the design of stable recycling cavities.

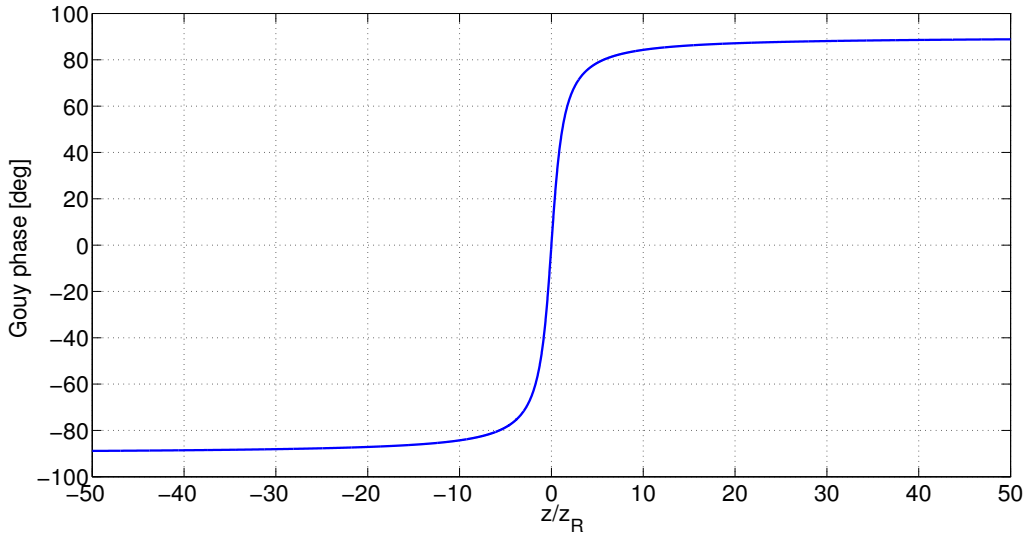

Figure 5.2: Gouy phase shift versus the z/z_R ratio.

Eq.(5.6) describes a beam with a Gaussian intensity profile, called *fundamental mode* or TEM_{00}, presently used in gravitational wave interferometers. It is characterized by the complex parameter q, defined as

$$\frac{1}{q} = \frac{1}{R(z)} - i\frac{\lambda}{\pi w^2(z)} \ , \tag{5.10}$$

or, in terms of distance from waist and Rayleigh range,

$$q = z + iz_R \ . \tag{5.11}$$

In the reference with the origin in the beam waist, z is negative for a beam converging to the waist, and positive for a beam diverging from it. The knowledge of the q parameter allows to compute all the other beam parameters like radius, front curvature and Gouy phase.

Higher-order modes

Eq.(5.5) has also other solutions than eq.(5.6), with similar properties. These form a complete and orthogonal set of functions, called transverse electromagnetic modes of propagation (TEM) or *higher-order modes*. Every arbitrary distribution of monochromatic light can be expanded in terms of these modes. In Cartesian coordinates (x, y, z), higher-order modes write [95, 96]

$$\begin{aligned} u_{mn}(x,y,z) = \ & \sqrt{\frac{P}{\pi m!n!\ 2^{N-1}}}\frac{1}{w(z)} \exp\left[-\frac{x^2+y^2}{w^2(z)}\right] H_m\left(\frac{x\sqrt{2}}{w(z)}\right) H_n\left(\frac{y\sqrt{2}}{w(z)}\right) \\ & \times \exp\left[-i\left(k\left(z+\frac{x^2+y^2}{2R(z)}\right) - (m+n+1)\Phi_G(z)\right)\right] \ , \end{aligned} \tag{5.12}$$

where $H_k(x)$ are the Hermite polynomials, m and n are the transverse mode numbers and $N = m+n$ is the order of the mode. Eq.(5.12) defines the *Hermite-Gauss* modes (HG_{mn}), whose transverse intensity patterns $I_{mn}(x, y) = |u_{mn}(x, y, z)|^2$ are shown on fig.5.3.

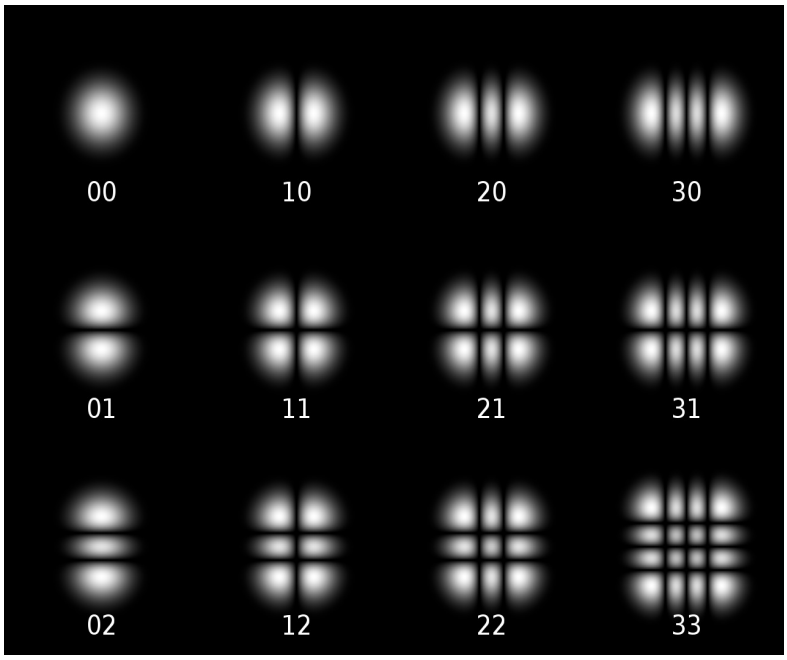

Figure 5.3: Transverse intensity patterns of HG_{mn} modes, from [97].

For a system with cylindrical symmetry and coordinates (r, θ, z), higher-order modes are *Laguerre-Gauss* modes (LG_p^ℓ) with radial and azimuthal indices p and ℓ, respectively, and order $N = 2p + |\ell|$. Their complex amplitude is given by [95, 96]

$$\begin{aligned} u_p^\ell(r,\theta,z) = \; & \sqrt{\tfrac{2P}{\pi}}\tfrac{1}{w(z)}\exp\Big[\tfrac{-r^2}{w^2(z)}\Big] \times \sqrt{\tfrac{p!}{(p+|\ell|)!}}\Big(\tfrac{2r^2}{w^2(z)}\Big)^{|\ell|/2} L_p^{|\ell|}\Big(\tfrac{2r^2}{w^2(z)}\Big) \\ & \times \exp\Big[-i\Big(k\Big(z+\tfrac{r^2}{2R(z)}\Big) - (2p+|\ell|+1)\Phi_G(z)\Big)\Big] \times \exp\Big[-i\ell\theta\Big] \;, \end{aligned} \tag{5.13}$$

where $L_p^\ell(x)$ is the Laguerre generalized polynomial. Fig.5.4 shows the transverse intensity patterns $I_p^\ell(r,\theta) = |u_p^\ell(r,\theta,z)|^2$ of the first LG_p^ℓ modes up to $N = 9$.

LG_p^ℓ beams with $\ell \neq 0$ have $p+1$ radial nodes and spiral phase fronts with spherical curvature, carrying orbital angular momentum of $\ell\hbar$ per photon [98]. These are *helical* LG_p^ℓ modes. The spiralling phase distribution implies the presence of a phase singularity on the optical axis, also called an optical vortex, and is characterized by a locally vanishing intensity. By changing the mode base, the field of LG_p^ℓ modes can also be written as

$$\begin{aligned} (u_p^\ell \pm u_p^{-\ell}) = \; & \sqrt{\tfrac{2P}{\pi}}\tfrac{2}{w(z)}\exp\Big[\tfrac{-r^2}{w^2(z)}\Big] \times \sqrt{\tfrac{p!}{(p+|\ell|)!}}\Big(\tfrac{2r^2}{w^2(z)}\Big)^{|\ell|/2} L_p^{|\ell|}\Big(\tfrac{2r^2}{w^2(z)}\Big) \\ & \times \; \exp\Big[-i\Big(k\Big(z+\tfrac{r^2}{2R(z)}\Big) - (2p+|\ell|+1)\Phi_G(z)\Big)\Big] \times \begin{cases} \cos(l\theta) \\ \sin(l\theta) \end{cases} \;, \end{aligned} \tag{5.14}$$

which are *cosine/sine* LG_p^ℓ modes. Since helical modes are the most studied in literature, we will refer only to this kind of modes throughout the rest of this thesis work.

Figure 5.4: Transverse intensity patterns of LG_p^ℓ modes.

The parameters $w(z)$ and $R(z)$ which appear in eqs.(5.12) and (5.13) are the same for all modes of the same set, implying that beam radius and phase-front curvature are the same and change in the same way for modes of all orders. Then all modes can be characterized through the same complex parameter q, and the fundamental Gaussian mode is a particular HG_{mn} or LG_p^ℓ mode with $m = n = 0$ or $p = \ell = 0$, respectively. It is worth nothing that for higher-order modes, the value of the Gouy phase shift is a function of the mode order N.

Fabry-Perot optical resonators

The beam resonance in a Fabry-Perot cavity is allowed if the cavity is *stable*. For a simple cavity composed of two spherical mirrors M1 and M2 spaced by a distance L, like the one shown on fig.2.7, the stability condition is satisfied if the laser that bounces back and forth between the mirrors of the resonator experiences a periodic focusing action. Only certain ranges of values for the radii of curvature (given L) would determine a stable resonator, in which periodic refocussing of the intra-cavity beam is produced. If R_1 and R_2 are the radii of curvature of the cavity mirrors, the stability condition translates in a geometric condition given by [95]

$$0 < \Big(1 - \frac{L}{R_1}\Big)\Big(1 - \frac{L}{R_2}\Big) < 1 \ . \tag{5.15}$$

On the contrary, if the cavity is unstable, the beam size will grow indefinitely.

If a cavity is a stable resonator, there exist a set of cavity eigenmodes (all with the same parameters) which have a self-consistent field configuration and form the axial standing waves of

the resonator: if an eigenmode can be represented by a beam propagating back and forth between the mirrors, its beam parameters have to be the same after a complete round trip in the cavity.

The cavity eigenmodes are important since they form a complete base, which can be used to perform the expansion of any arbitrary field in terms of the resonating modes. This base is completely determined by the size and position of the cavity waist, which in turn are functions of the cavity geometry through R_1, R_2, L. The cavity waist size is given by [95]

$$w_0^4 = \Big(\frac{\lambda}{\pi}\Big)^2 \frac{L(R_1 - L)(R_2 - L)(R_1 + R_2 - L)}{(R_1 + R_2 - 2L)^2} \ , \tag{5.16}$$

and the waist distance from mirror M1 is

$$d_1 = \frac{L(R_2 - L)}{(R_1 + R_2 - 2L)} \ . \tag{5.17}$$

The waist position with respect to M2 can be computed from eq.(5.17) by replacing $R_2 \to R_1$ and vice-versa (or alternatively by imposing $d_2 = L - d1$).

The formalism developed for spherical resonators (i.e. for resonators with spherical mirrors) can be also extended to the case of astigmatic resonators. This is of crucial importance since, as we will see further in this chapter, the recycling cavities of AdV will be astigmatic. In the astigmatic resonator, the incidence of the beam on the mirror is non-normal and the beam senses two different radii of curvature for the two transverse directions (x, y). If R is the radius of curvature of the mirror and θ is the incidence angle between the beam and the normal direction to the mirror, the beam is focused by a radius $R\cos\theta$ in the *tangential* plane that contains θ, and by a radius $R/\cos\theta$ in the perpendicular *sagittal* plane. Thereby the fundamental mode that resonates in the cavity can be expanded in the transverse (x, y) plane as

$$\psi = \sqrt{\frac{2P}{\pi w_x w_y}} \exp\Big[-x^2\Big(\frac{1}{w_x^2} + i\frac{k}{2R_x}\Big) - y^2\Big(\frac{1}{w_y^2} + i\frac{k}{2R_y}\Big) + i\Big(-kz + \frac{\Phi_{Gx}}{2} + \frac{\Phi_{Gy}}{2}\Big)\Big] \ , \tag{5.18}$$

The two planes have independent sets of parameters: beam radius, Gouy phase, waist size and position, Rayleigh range. Since $w_x \neq w_y$, the beam spot of the astigmatic fundamental mode is elliptical. According to this formalism, the propagation of the astigmatic eigenmode in the resonator can be treated for the two planes independently (as long as both are stable), as it would happen for two distinct beams.

Gouy phase and cavity degeneracy

The laser beam is resonant inside the cavity when the total phase shift experienced by the light in a complete round trip is equal to 2π. For a generic mode of order N, the resonance condition is

$$2kL - 2(N + 1)\Phi_G = 2\pi \ , \tag{5.19}$$

which after some simple algebra becomes

$$\nu_N = \nu_0\Big[1 + \frac{N + 1}{\pi}\Phi_G\Big] \ , \tag{5.20}$$

where ν_0 is the free spectral range defined in eq.(2.77) and ν_N is the resonance frequency of the eigenmode of order N (which is equal to $m + n$ or $2p + |\ell|$ for HG_{mn} or LG_p^ℓ modes, respectively).

Thus the resonance frequency is order dependent, and the frequency spacing between two modes of order N and N' is

$$\Delta\nu = \nu_{N'} - \nu_N = \nu_0 \frac{\Delta N}{\pi} \Phi_G \ , \tag{5.21}$$

with $\Delta N = N' - N$, and (for a given ν_0) it depends on the value of the Gouy phase. If the phase is too small ($\Phi_G \simeq 0$), or too large ($\Phi_G \simeq q2\pi$ with $q \in \mathbb{N}$), the frequency spacing $\Delta\nu$ between the modes is approximately equal to a multiple of the free spectral range and the resonance frequencies of all eigenmodes are very close to that of the fundamental mode. Thus if the cavity linewidth is large, all eigenmodes can potentially resonate at the same time in the cavity, if excited. In this case the cavity is said to be *degenerate* or *marginally stable*, since the Gouy phase shift can also be expressed in terms of the geometrical parameters of the cavity,

$$\Phi_G = \cos^{-1}\Big(\sqrt{(1 - L/R_1)(1 - L/R_2)}\Big) \ , \tag{5.22}$$

and when $\Phi_G \simeq 0$, according to eq.(5.15), the resonator is also close to instability.

The optical gain (or *build-up*) of higher-order modes could be suppressed by increasing the Gouy phase shift in the cavity: according to eq.(2.74) for the resonant field, when the fundamental mode is resonant (N=0), the build-up for a mode of order N' is

$$G_{mn}(\Phi_G) = \Big| \frac{t_{RM}}{1 - r_{RM} r_{FP} \cdot \exp\Big[-i2N'\Phi_G\Big]} \Big|^2 \ , \tag{5.23}$$

which strongly decreases for increasing values of Φ_G.

5.2 Motivations for Stable Cavities

In a degenerate recycling cavity, perturbations of the cavity geometry can transfer power from the fundamental TEM_{00} mode to higher-order modes. In general, to first order, the resonance of higher-order modes has little effect on the carrier field, since it is resonant also inside the arm cavities. Instead, as can be demonstrated [99], higher-order mode contamination degrade the mode-matching of sideband fields to the recycling cavity: their optical gain is reduced, and their spatial distribution is aberrated [100].

The power recycling cavity of Virgo is degenerate, since the beam only gets $\Phi_G = 0.5$ deg[1] inside it. The resonance linewidth of the cavity for sideband fields is 166 kHz, thus according to eq.(5.21) the first higher-order modes with $\Delta N = 5$ can resonate with the fundamental mode. Because of thermal effects, mode contamination perturbed the development of a stable control system and slowed down the commissioning phase of Virgo [82]. During the VSR2 data taking run, the recycling gain of radio-frequency sideband fields was heavily reduced because of thermal effects, and the shape of sidebands was highly aberrated [101], as shown on fig.5.5. A similar problem has been encountered also for the degenerate power recycling cavity of LIGO [94].

[1]The Gaussian eigenmode of the arm cavities of Virgo (plano-concave resonators with $R_1 = \infty$ and $R_2 = 3.6$ km) has $q_{\mathrm{arm}} = i1342$ m and $w_0 = 2.1$ cm on the input mirror, where $(\Phi_G)_{\mathrm{arm}} = 0$. The beam propagates across 12 m in the recycling cavity, so that on the recycling mirror it has $q_{\mathrm{RM}} = (12 + i1342)$ m, with $z/z_R \simeq 9 \cdot 10^{-3}$.

	Φ_G [deg]	ΔN
Virgo	0.5	5
AdV	0.1	17

Table 5.1: Comparison of marginally-stable cavities in Virgo and AdV.

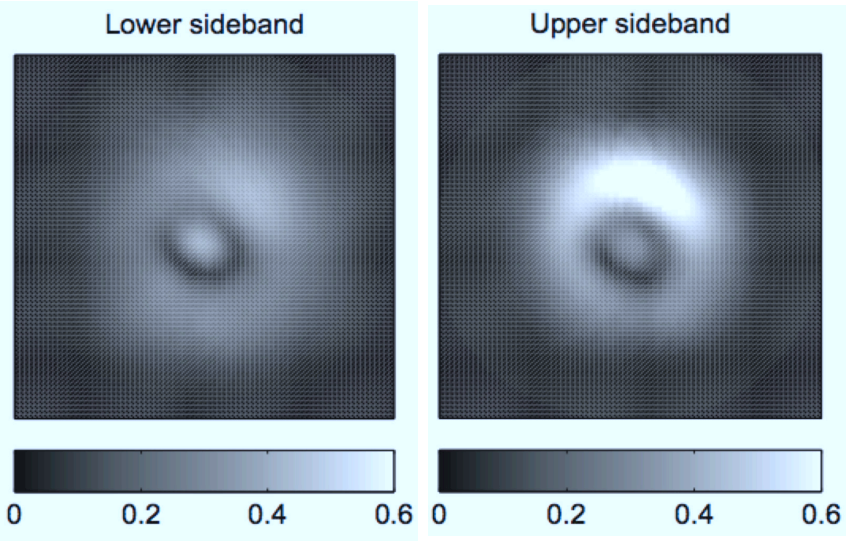

Figure 5.5: Amplitude images of lower (left panel) and upper (right panel) radio-frequency sidebands in the power recycling cavity of Virgo during VSR2, from [101]: because of mode contamination, the aberrated shape is very far from the expected Gaussian amplitude.

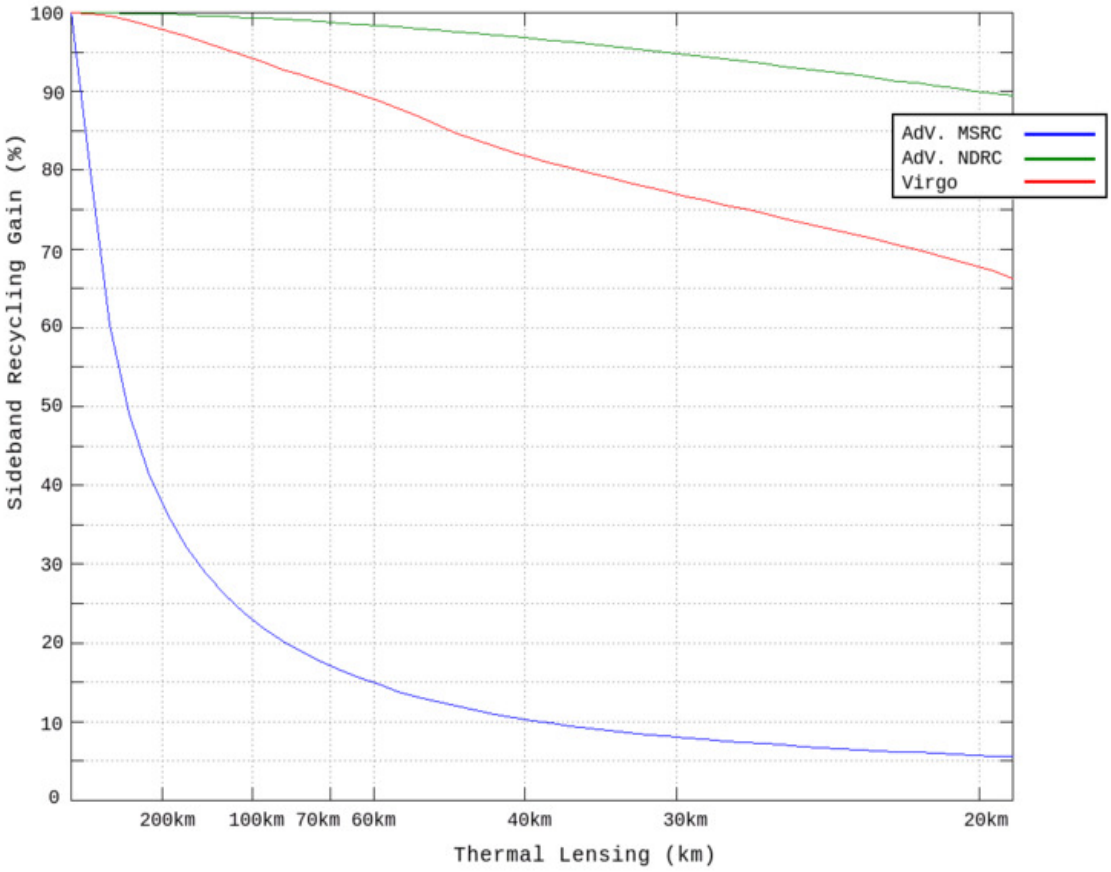

Figure 5.6: Recycling gain of radio-frequency sidebands against the equivalent focal length due to thermal lensing: AdV with marginally-stable power recycling cavity (blue curve), Virgo (red curve), AdV with non-degenerate power recycling cavity (green curve), from [102].

The impact of degeneracy will be even larger in advanced detectors, if marginally stable recycling cavities are used. In a cavity like the power recycling of Virgo, the eigenmode ${q_{\rm arm}}^2$ of the arm cavities of AdV would get $\Phi_G = 0.1$ deg, which is even 5 times lower than the Gouy phase of Virgo. In this case, the first higher-order modes with $\Delta N = 17$ could resonate with the fundamental mode. Table 5.1 summarizes the comparison between Virgo and AdV with marginally-stable cavities.

Therefore if AdV will have degenerate cavities, the relevance of thermal effects will be larger than in Virgo. Fig.5.6 shows the predicted degradation of radio-frequency sidebands with thermal effects in AdV, compared to that of Virgo: here we see a marked difference in the behavior, due to the larger beam size in the arms of AdV. For a thermal lens with equivalent focal length of 200 km, the recycling gain in AdV decreases down to about 35%, whereas for the same thermal lens, the gain in Virgo is above 95%. This is a strong motivating factor in the decision to use non-degenerate cavities.

[2]In the baseline design of AdV, the arm cavity input mirror is a plano/concave thick diverging lens for the arm cavity beam: on its plane surface, the one facing the beamsplitter, the parameter of the beam is $q_{\rm arm} = (960.830 + i134.636)$m, with $z/z_R \simeq 7$.

Mode contamination will be a concern also for signal recycling. If we assume that at the interferometer output the mode-cleaner filters out all higher-order modes in the carrier and signal audio-sidebands fields, the power fluctuation due to shot noise is proportional to the square root of the output carrier power in the fundamental mode:

$$\delta P_{shot} \propto \sqrt{P_{00|carr}} \ . \tag{5.24}$$

The signal power comes from the beating of the signal sideband against the carrier, thus considering only the fundamental mode for both we can write

$$P_S \propto \sqrt{P_{00|carr}}\sqrt{P_{00|sb}} \ . \tag{5.25}$$

By assuming also that shot noise dominates, we have that

$$SNR = \frac{P_S}{\delta P_{shot}} \propto \sqrt{P_{00|sb}} \ , \tag{5.26}$$

i.e. the signal-to-noise ratio is directly proportional to the signal sideband power in the fundamental mode. If the signal recycling cavity is degenerate, thermal effects might reduce the signal-to-noise ratio of potential detections. Moreover, aLIGO showed that also mirror figure errors can induce a signal loss [94].

Non-degenerate recycling cavities show definitely a better behavior with respect to thermal effects and mirror figure errors, since they suppress efficiently the resonance of higher-order modes. Figs.5.7 and 5.8 show the build-up of the first higher-order modes of radio-frequency sidebands in the recycling cavities of AdV, against the Gouy phase: it is possible to tune the value of the phase ($20 \leq \Phi_G \leq 30$ deg, for example) so that higher-order modes are suppressed of several orders of magnitude. This yields a robust optical configuration, as shown on fig.5.6: with non-degenerate cavities, the gain of radio-frequency sideband fields in AdV stays above 90%, up to a thermal lens of 20 km.

The implementation of non-degenerate recycling cavities in AdV could allow to achieve a stable optical configuration and a robust control, and the detector could benefit of a higher signal-to-noise ratio of detected signals. The stable configuration might ease and speed up the commissioning in the early phase of operation, and will be necessary for the full exploitation of the potential of the detector. We will see later in this chapter and in the following one that non-degenerate cavities have also other important advantages:

- they allow the simple extraction of secondary pick-off beams for the sensing and control system of the detector. The beam size attains few mm inside the non-degenerate cavities and about 1 mm on the recycling mirror. Thus secondary beams are small, and can be easily separated from the main beam through the insertion of microscopic wedges (for example in the beamsplitter) or from the reflection on tilted surfaces (for example by tilting the compensation plates). This is not possible with marginally-stable cavities, where the beam always has a radius of ~ 5 cm: thus large wedges (degrees) are needed to isolate secondary beams, which can induce aberrations in the main beam

- they simplify the design of mode-matching telescope of the injection system: with non-degenerate cavities the telescope should match a beam of about 1 mm to the 2-mm beam

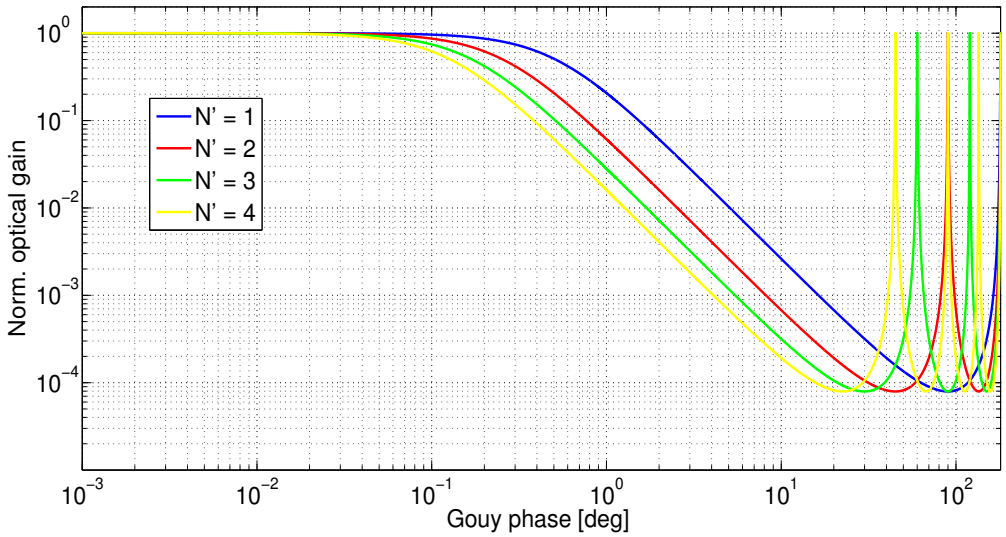

Figure 5.7: Normalized build-up of sideband higher-order modes against the Gouy phase shift of the beam, in the power recycling cavity of AdV.

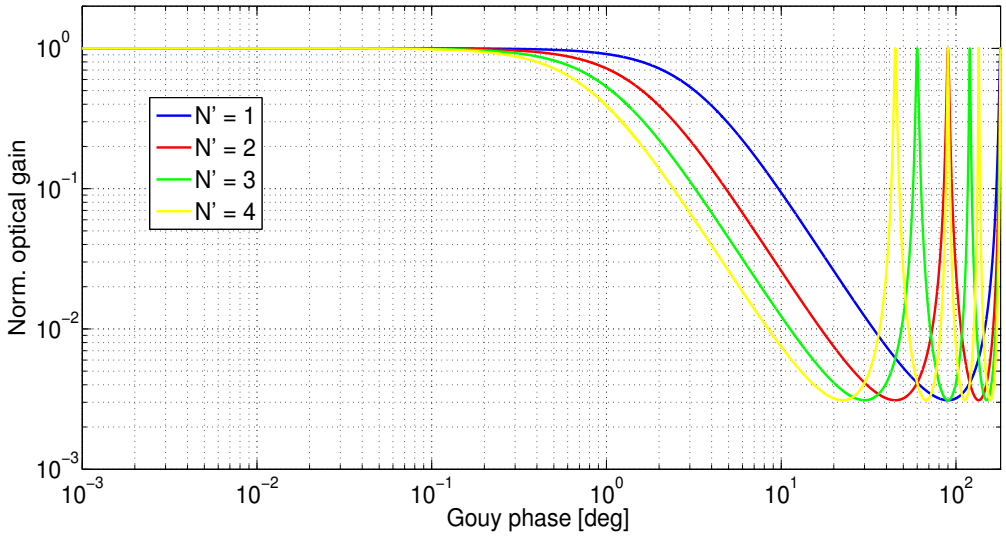

Figure 5.8: Normalized build-up of sideband higher-order modes against the Gouy phase shift of the beam, in the signal recycling cavity of AdV.

inside the Faraday isolator, so a magnifying factor of 2 must be achieved. With marginally-stable cavities, the telescope should match a beam of 5 cm and thus achieve a magnifying factor of 25: this requires long telescopes and large mirrors to be placed on benches of limited size. The use of a lens behind the power recycling mirror might be possibly necessary with marginally-stable cavities, like it is presently in Virgo, with the risk of having problems of spurious reflections on the bench. The same considerations hold also for the output telescope that matches the beam to the detection photodiode

- we can use small recycling mirrors of 10-cm diameter, which can be easily installed and possibly replaced (to change the finesse of the signal recycling cavity, for example)

- they allow to adjust the distances between the recycling cavity mirrors if errors in their radii of curvature are present, to optimize the matching of the beam to the cavities. This is not possible with marginally stable cavities.

5.3 How to build a Stable Cavity

In order to have non-degenerate recycling cavities in AdV, the resonant beam must undergo a sufficiently large Gouy phase shift. We can estimate the minimum Gouy phase needed by making the following assumptions:

- cavities will have a length of the order of 10 m

- the first higher-order mode ($\Delta N = 1$) should be sufficiently spaced from the fundamental mode. Three times the cavity linewidth, for instance, is a reasonably (arbitrary) safe spacing.

Let us consider the signal recycling cavity, which has a larger linewidth (FWHM = 536 kHz): then, by means of eq.(5.21), we can compute the minimum phase

$$\Phi_G \geq 3\frac{\pi}{\nu_0}\frac{\mathrm{FWHM}}{\Delta N} \simeq 19 \text{ deg.} \tag{5.27}$$

We also know from figs.5.7 and 5.8 that $20 \leq \Phi_G \leq 30$ is a suitable choice, since it would allow to suppress the first higher-order mode of several orders of magnitude. The phase should not be larger, in order to not excite accidentally the resonance of higher-order modes. In AdV, the reference value of the Gouy phase is $\Phi_G = 20$ deg.

To cumulate such a large phase shift, we need a new design of the recycling cavities:

a) we can discard immediately the option of a layout with a single recycling mirror, shown on fig.5.9a. In this case, in fact, km-scale recycling cavities would be needed: the arm cavity eigenmode only gets $\Phi_G = 3$ deg over 500-m propagation. This is not feasible for AdV.

b) To achieve the needed phase shift we have to modify the parameter of the arm cavity eigenmode, by introducing one or more focusing elements in the layout of the recycling cavities, like it is shown on fig.5.9b. We can use a lens (which might be also incorporated in the arm cavity mirror) to increase the divergence of the beam and shorten its Rayleigh range, thus the

accumulation of Gouy phase shift can occur on much shorter distances. The $q_{\rm arm}$ parameter of the beam passing through a generic lens of focal length f changes according to [95]

$$\frac{1}{q'} = \frac{1}{q_{\rm arm}} - \frac{1}{f} \ , \tag{5.28}$$

having defined the complex parameters $q_{\rm arm} = z + iz_R$ and $q' = z' + iz'_R$ for the beam before and after the lens, respectively. Eq.(5.28) implies that for the converging lens of fig.5.9b, the following equations hold:

$$\begin{aligned} z' &= \tfrac{f(zf-z^2-z_R^2)}{(f-z)^2+z_R^2} \\ z'_R &= \tfrac{f^2 z_R}{(f-z)^2+z_R^2} \ . \end{aligned} \tag{5.29}$$

Since the eigenmode of the arm cavity is in far field, eq.(5.29) further simplifies to

$$\begin{aligned} z' &\simeq \tfrac{fz}{f-z} \\ z'_R &\simeq \tfrac{f^2 z_R}{f-z} \ . \end{aligned} \tag{5.30}$$

If in addition $z >> f$, then $z' \simeq -f$ and $z'_R \simeq z_R(f/z)^2$. This is a reasonable approximation since we need to focus the beam over a distance of the order of $f \sim 10$ m in the recycling cavities, while z is of the order of 10^3 m. In synthesis, by inserting a lens we focus the beam over a distance approximately equal to f, and the Rayleigh range of the beam is shortened by a factor $(f/z)^2$. By assuming $f = 10$ m, it becomes $z'_R \simeq 1.5$ cm and the Gouy phase can be accumulated over a distance of the same order.

This layout has an inconvenient: it focuses the beam spot on a very small radius. If $f \sim 10$, then the beam radius inside the Rayleigh range is $w \sim 10^2$ μm. In the baseline design of AdV, the power stored in the power recycling cavity will be 5 kW, so that the power density on the recycling mirror will be about 16 MW/cm^2, higher than the usual damage threshold of fused silica mirrors that will be used in advanced detectors (10 MW/cm^2). Furthermore, this power concentrated on a small area can also cause strong thermal effects in the power recycling mirror.

c) So we should introduce a second diverging lens in the layout, as shown on fig.5.9c, to enlarge the beam size on the power recycling mirror by slightly defocusing the beam. With this setup mm-size beam radius can be achieved, with still a reasonably Rayleigh range for the beam, of the order of 1 m. It is then only necessary to tune the position of the recycling mirror within the Rayleigh range of the beam, so to have $\Phi_G = 20$.

d) Finally, it is preferable to replace the lenses of the layout with mirrors of equivalent focal lengths, in order to avoid spurious reflections of the beam from the anti-reflective coated surfaces of refractive components. Spurious reflections might recombine with the main laser and become a source of noise, so whenever possible it is better to remove their potential sources rather than blocking them after. Moreover, the use of mirrors also allows the extraction of secondary pick-off beams from the rear surface of the optics. By introducing the mirrors in the place of the lenses, the optical path inside the cavity becomes folded, completing the conceptual design of non-degenerate recycling cavities shown on fig.5.9d.

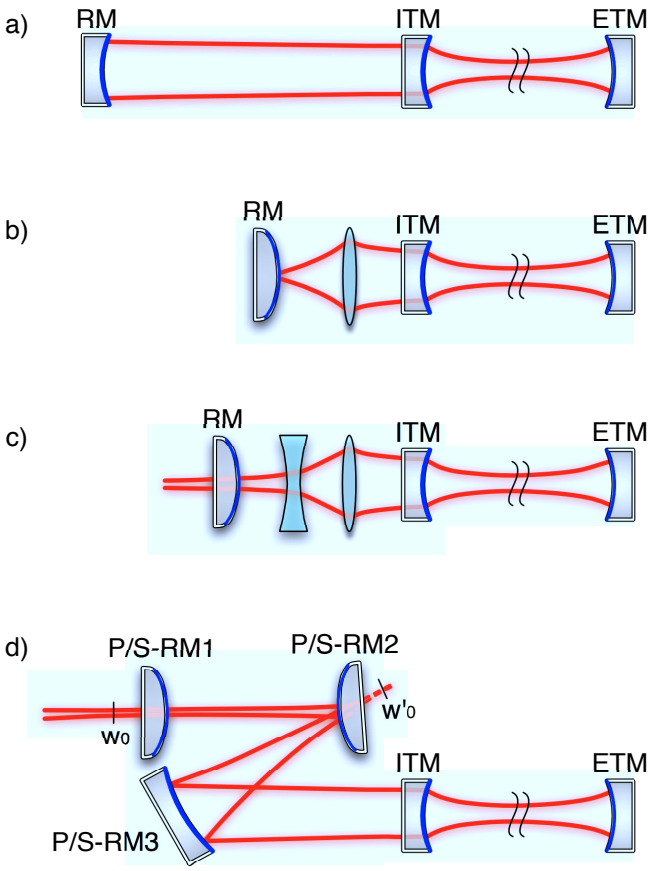

Figure 5.9: Evolution of the design concept of non-degenerate recycling cavities for AdV.

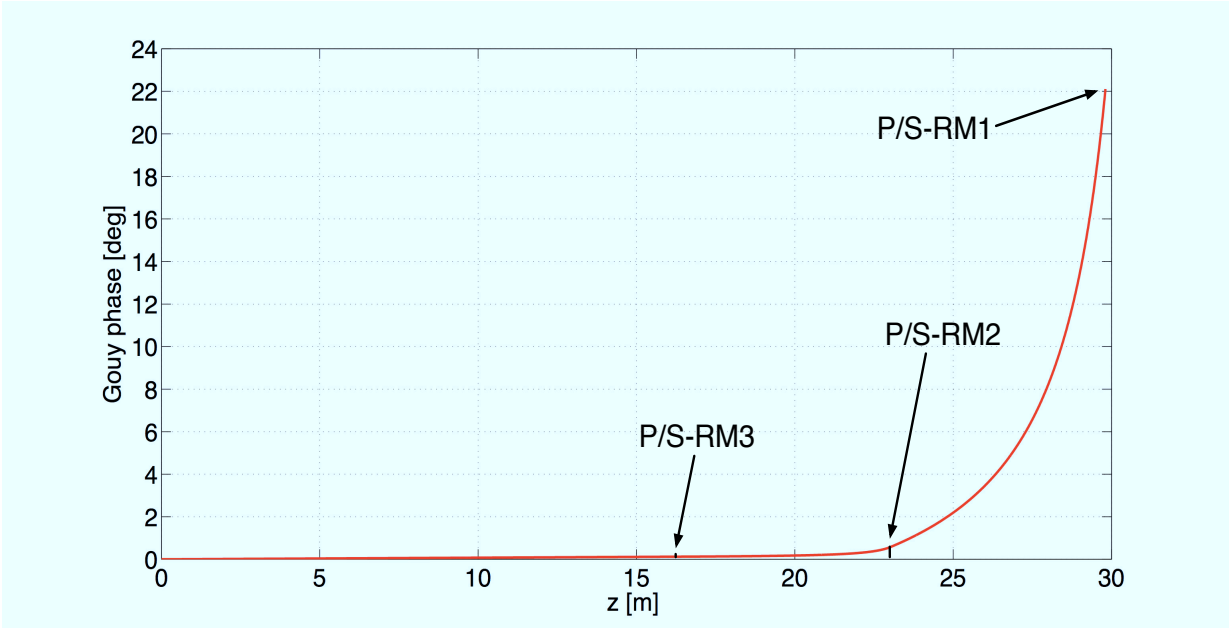

Figure 5.10: Evolution of the Gouy phase inside the non-degenerate layout.

In both cavities, P/S-RM3 (power/signal recycling mirror 3) is the focusing element of the layout, so it is concave, and makes the beam converge. P/S-RM2 is used to reduce the divergence angle of the beam, in order to collimate it over a longer distance into the cavity. It is a diverging mirror, thus it is convex. Mirrors 2 and 3 form a ***telescope*** that changes the beam divergence. The cavity coupler is P/S-RM1, which is also convex since it matches a converging beam.

The beam waist w_0 is behind P/S-RM1, but there is also a smaller virtual waist w_0' behind P/S-RM2, with a very short Rayleigh range. Figs.5.10 and 5.11 show the evolution of the Gouy phase and of the beam radius inside the non-degenerate layout[3], respectively. Between the arm cavity input mirror, P/S-RM3 and P/S-RM2 the beam is in far field and does not get sufficiently close to its waist, so that its Gouy phase shift is negligible. In this layout, the phase shift is cumulated mostly between P/S-RM2 and P/S-RM1. The beam size is effectively reduced to few mm inside the cavity.

Because of the folded optical path, the incidence angle on mirrors 2 and 3 is not normal, so the eigenmode of the recycling cavities is astigmatic. We will see in the next chapter that this aberration may yield non-negligible coupling loss for the input beam to the recycling cavities.

5.4 Design Constraints

The non-degenerate layout of fig.5.9d has a crucial feature: two extra-mirrors per recycling cavity have to be suspended. Since AdV will use the present vacuum infrastructure of Virgo, this poses a stringent constraint to the choice of the parameters of the layout: mirrors must be placed in the vacuum tanks, shown on fig.5.12, which have been realized to host a single Superattenuator for the

[3]We show here the parameters of the beam inside the *vertical* layout, which will be presented in chapter 6.

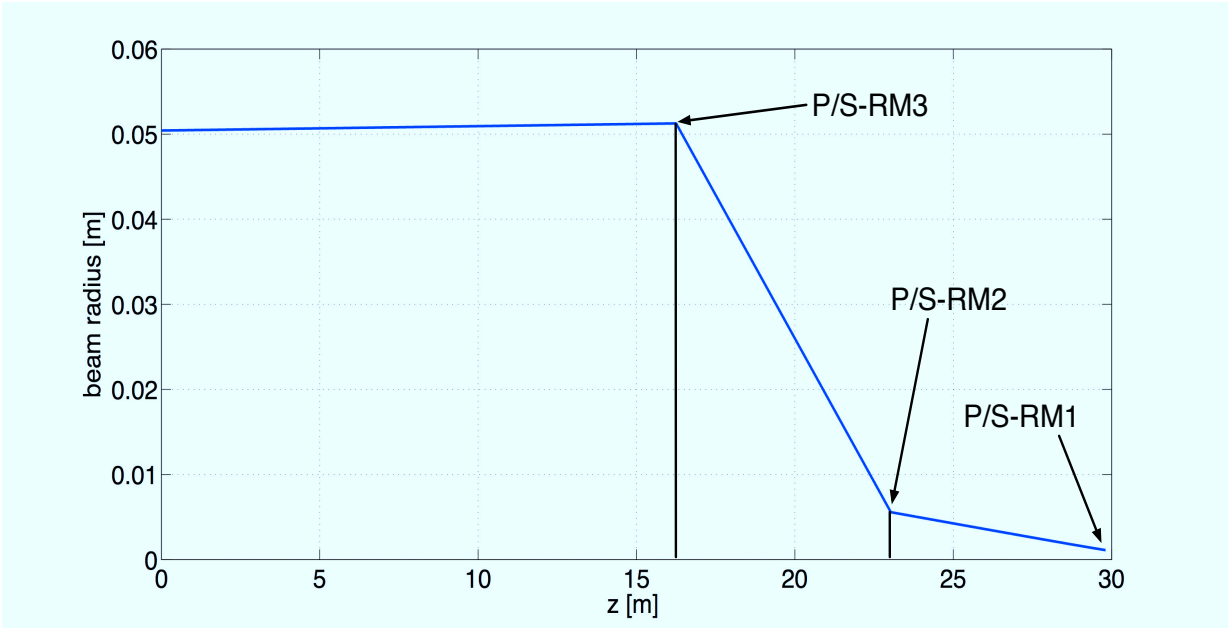

Figure 5.11: Evolution of the beam radius inside the non-degenerate layout.

suspension of only one mirror.

The vacuum system of Virgo lacks of flexibility, since it was not conceived to allow for further modifications after its construction: each vacuum tank can be displaced by few tens of cm, otherwise heavy building works are required. Furthermore, the infrastructure budget of the project is limited, so little modifications can be done to the system.

There are also optical constraints to the choice of parameters, which concern

- coupling: a set of radii of curvature and incidence angles should be found to make astigmatism negligible, so to have the maximum beam coupling to the cavity
- beam size on power recycling mirrors: since a few kW will circulate in the power recycling cavity, we aim to have a beam radius on P/S-RM1 as large as possible
- modulation frequencies: the radio-frequency sidebands of the control system have to be transmitted through the input mode-cleaner and must resonate in the recycling cavities. If f_{mod} is the modulation frequency used for the generation of sidebands, and ν_0^{IMC}, ν_0^{RC} are the free spectral ranges of the input mode-cleaner and of the recycling cavities, respectively, then

$$\begin{aligned} f_{mod} &= N_{IMC}\ \nu_0^{\mathrm{IMC}}, \quad & N_{IMC} &= 2k,\ \forall k \in \mathbb{N} \\ f_{mod} &= N_{RC}\ \nu_0^{\mathrm{RC}}, & N_{RC} &= 2k,\ \forall k \in \mathbb{N}. \end{aligned} \tag{5.31}$$

  This implies that $N_{RC} = N_{IMC} L_{RC}/L_{IMC}$, i.e. the recycling cavity length L_{RC} must be an even sub-multiple of the input mode-cleaner lenght $L_{IMC} = 144$ m

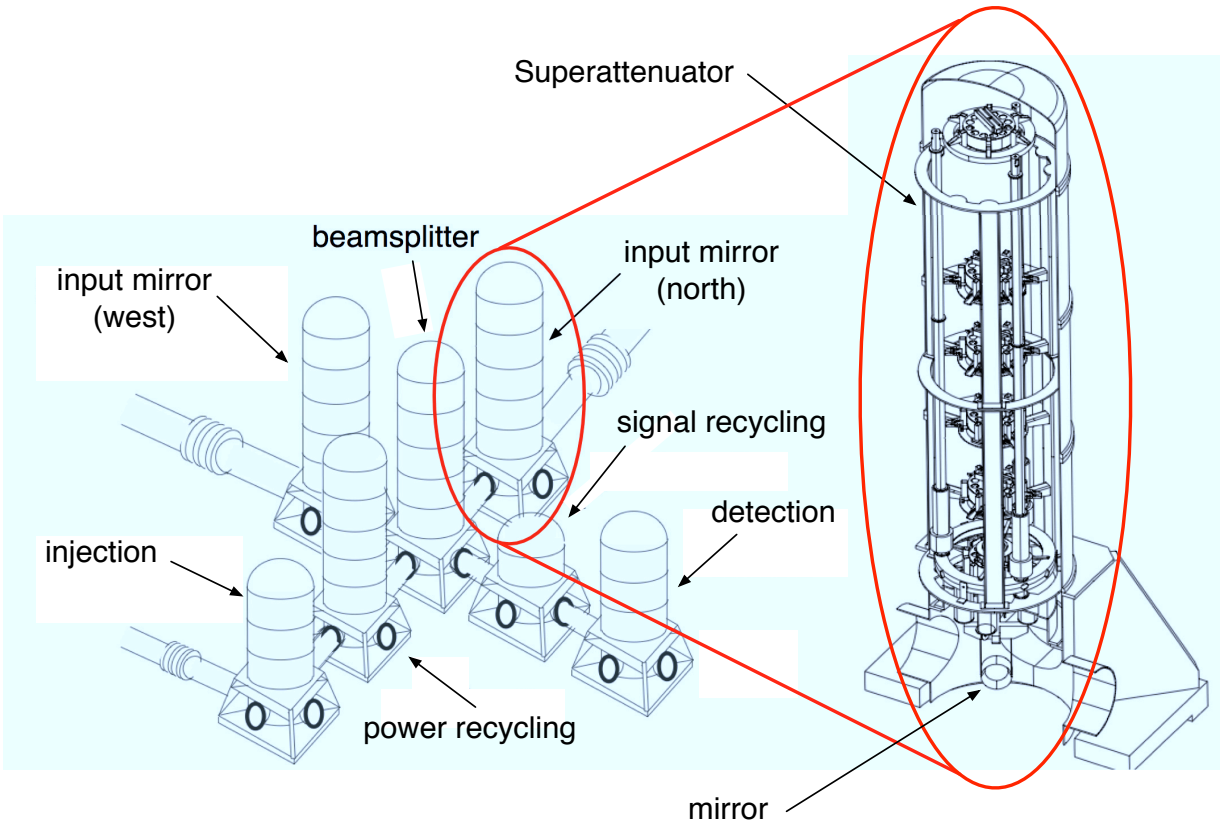

Figure 5.12: Vacuum system of the central part of the Virgo interferometer (left) and tower vacuum enclosure to host a Superattenuator and a mirror (right).

- angular-to-longitudinal couplings: the curved mirrors of the recycling cavities can couple transversal translation to displacement noise on the optical axis. To minimize this effect the RoCs of mirrors should be as large as possible.

Because of all these constraints, the choice of the layout parameters is a complex issue. To solve this problem we defined a general design procedure, based mainly on a set of optical simulation tools that we developed. We could use this procedure to design several alternative layouts, which will be presented in the next chapter.

Chapter 6

Simulation of the Non-Degenerate Recycling Cavities of Advanced Virgo

We have seen in the previous chapter that the layout of the non-degenerate recycling cavities of AdV should have a folded optical path with three mirrors, whereof two should form a telescope for the focusing of the beam. We will present in this chapter the simulation work we carried out to determine the design of the the non-degenerate recycling cavities.

During our work we have drawn and characterized many configurations, here we will present the most important four, following an historical perspective. We will see that the design process has been heavily conditioned not only by the optics requirements, but also by the need of integrating the optical layout with other subsystems like vacuum and suspensions. Finally, the configuration called *vertical layout* has been retained.

The design and the study of the non-degenerate cavities has been achieved using two simulation tools. First, a ray-matrix simulation has been developed to determine the set of parameters (radii of curvature, incidence angles) of the cavity design, and to characterize its optical performances (astigmatism and coupling of the beam to the cavity) and tolerances. Then a Fast Fourier Transform (FFT) simulation has been used to study the astigmatism of the cavity design and its response to thermal effects and mirror figure errors.

In the ray-matrix simulation, the propagation of the beam inside the cavity is described by a product of 2×2 matrices which represent the optical elements of the system. This formalism allows to compute simply and rapidly the behavior of the non-degenerate cavity as a function of the layout parameters, especially when the number of parameters to be scanned is large.

In the FFT simulation the cavity field is expanded in the Fourier space of spatial frequencies, where the propagation is equal to the product of the input field times a propagator of simple mathematical form. The FFT code allows the simulation of the coupled system of the arm and power (signal) recycling cavities with carrier and sideband fields, and the inclusion of phase maps to simulate the defects of optics. It is thus suitable for the simulation of complex physical effects. The FFT code we used has been developed inside the LSC collaboration by H. Yamamoto [103].

We will begin the presentation of our work by illustrating the general design procedure that we used, then we will describe the basic formalism and the steps of the simulations. The optical configurations that we studied will be presented subsequently.

6.1 Design Procedure and Simulation Tools

The design procedure to choose the parameters of the recycling cavity layout can be summarized as follows:

1. choice of lengths, Gouy phase and of beam size on the recycling mirror
2. computation of the radii of curvature (RoCs) through an approximated analytical formula
3. computation of the exact RoCs through a loop which explores the space of parameters
4. computation and (possibly) optimization of the incidence angles
5. characterization of the layout: this step includes the computation of recycling cavity eigenmode astigmatism, beam coupling to the recycling cavity, parameter tolerances for cavity stability
6. simulation of the response of the layout to mirror figure errors and thermal effects.

To perform steps 1 to 5 we developed a Matlab-based ray-matrix code. We chose to implement the ray-matrix formalism because it allows the simple and fast computation of the stability condition and of the eigenmode of the cavity, as a function of the parameters of the layout.

The computation of astigmatism and beam coupling of the eigenmode in step 5 is also performed in parallel with the FFT code SIS (Stationary Interferometer Simulation) [103], developed by H. Yamamoto for the LSC Collaboration. We decided to use SIS in step 5 in order to study the optical performances of the layout with an independent simulation, based on a completely different formalism. We will see later in this chapter that the ray matrix code and SIS can give different results if carrier or sideband fields are considered. This occurs because SIS can simulate the resonance of the carrier field in the coupled cavities of arm and recycling, whereas the ray-matrix code assumes that the two cavities are independent.

As a consequence, SIS is used to compute the astigmatism and the recycling gain of the carrier in the coupled cavities. For the radio-frequency sidebands, which resonate only in the power recycling cavity, SIS and the ray-matrix code agree (in the limit of small astigmatism). Thus we compute the coupling of radio-frequency sidebands with the ray matrix code. We use SIS also to perform step 6, since we want simulate physical effects in the mirrors that cannot be implemented into the ray-matrix code.

In the following we will introduce the ray matrix formalism, and we will detail steps 1 to 5 of the design procedure through the description of the steps of the ray-matrix code. Then we will introduce the basic working principles of FFT codes and some important functions of SIS that we used. We will present the results of step 5 in the next section, where we will cover the design history of non-degenerate cavity, through the discussion of several cavity layouts. In the last part of this chapter we will describe step 6 for the configuration that has been retained, the *vertical layout*.

We will refer to fig.6.1 for the notation of the cavity parameters. Since the optical layout is the same for both recycling cavities, for the sake of simplicity we will refer hereafter only to the power recycling cavity.

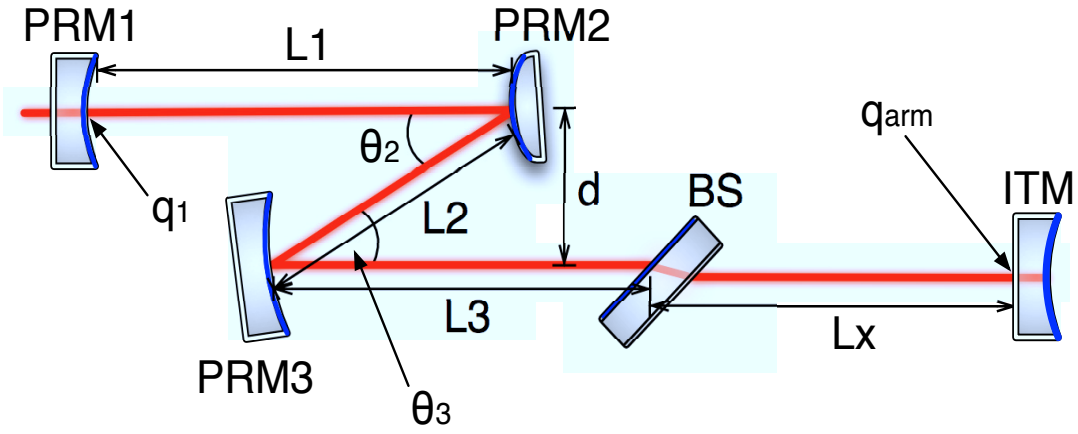

Figure 6.1: Notation for the parameters of the non-degenerate power recycling cavity layout.

6.1.1 Ray-Matrix Formalism

For a light beam in the paraxial approximation, the path through a given optical system can be described by a product of matrices with 2×2 elements [95], where each matrix represents an element of the system: for example, the matrices

$$D = \begin{pmatrix} 1 & d \\ 0 & 1 \end{pmatrix}, \; L = \begin{pmatrix} 1 & 0 \\ \mp 1/f & 1 \end{pmatrix} \tag{6.1}$$

represent the propagation in vacuum along the distance d and through the lens with focal length f (the $\mp$ sign changes for a converging or a diverging lens, respectively). Also mirrors can be represented by a matrix, by simply replacing $f = R/2$, with R being the mirror RoC. If

$$M = M_1 M_2 ... M_n = \begin{pmatrix} A & B \\ C & D \end{pmatrix} \tag{6.2}$$

is the matrix of a system with n elements, the parameter of a Gaussian beam passing through the system changes according to the formula (sometimes called the *ABCD law*)

$$q' = \frac{Aq + B}{Cq + D} \; , \tag{6.3}$$

where q and q' are the parameter of the input and output beam of the system, respectively. Thereby, the propagation back and forth of a laser beam within a resonator can be described by a periodic sequence of identical systems. For example, the round-trip matrix product for the simple resonator of two mirrors shown on fig.2.7 is (starting arbitrarily from the reflectivity surface of M1)

$$M = L_1 D \; L_2 D = \begin{pmatrix} 1 & 0 \\ -2/R_1 & 1 \end{pmatrix} \begin{pmatrix} 1 & L \\ 0 & 1 \end{pmatrix} \begin{pmatrix} 1 & 0 \\ -2/R_2 & 1 \end{pmatrix} \begin{pmatrix} 1 & L \\ 0 & 1 \end{pmatrix} \; , \tag{6.4}$$

where R_1 and R_1 are the RoCs of the mirrors, and where we unfolded the path in the resonator through an equivalent sequence of lenses and propagations in space. The stability condition of the

resonator is expressed through the elements of the matrix product by

$$-1 < \frac{(A+D)}{2} < 1 \ , \tag{6.5}$$

and the parameter of the resonant beam can be computed by postulating self-consistency and imposing $q' = q$ after a round trip in the cavity. The eigenmode of the resonator is then

$$\frac{1}{q} = \frac{D - A \mp i\sqrt{4-(A+D)^2}}{2B} \ . \tag{6.6}$$

For the ray-matrix representation of the non-degenerate layout, we have to deal with the reflection of beams on tilted surfaces: the reflection of a Gaussian beam on a surface with incidence angle θ is represented by

$$M_t = \begin{pmatrix} 1 & 0 \\ \frac{2}{R\cos\theta} & 1 \end{pmatrix}, \ M_s = \begin{pmatrix} 1 & 0 \\ \frac{2\cos\theta}{R} & 1 \end{pmatrix}, \tag{6.7}$$

where t stands for tangential the and s for sagittal. We used the following convention: if the recycling cavity layout lies in the same plane (x, z) of the interferometer, then the tilt axis of mirrors is oriented along the y direction and (x, z) is the tangential plane, whereas (y, z) is the sagittal plane.

6.1.2 Ray-Matrix Code

We simulate the recycling cavity coupled to a single arm of the interferometer, which might be either the x arm (with the transmission through the beamsplitter) or the y arm. Therefore we do not simulate the differential effects of the layout.

In the first part of the code we compute the lengths of the layout, and we set the values of Gouy phase Φ_G and minimum beam radius w on PRM1 that we want to obtain for the eigenmode of the recycling cavity. Then we determine the RoCs of mirrors, $\{R_2, R_3\}$. In this phase we make the assumption of null astigmatism, so we do not consider the incidence angles.

We first compute the RoCs $\{R_2, R_3\}$ with an approximated formula of the telescope, then we change $\{R_2, R_3\}$ in a loop around these values to scan the parameters $\{\Phi_G, w\}$ of the recycling cavity eigenmode. At the end of the loop the code gives as output a list of exact RoCs $\{R_2, R_3\}$ and corresponding beam parameters $\{\Phi_G, w\}$, and we select the RoCs that satisfy the initial choice of phase and radius.

In the second part of the code we compute the incidence angles $\{\theta_2, \theta_3\}$ on the mirrors of the telescope. If the geometry of infrastructures allows it, we also compensate (even only partially) for the astigmatism of the recycling cavity layout by optimizing the angle ratio θ_2/θ_3. At this step all the parameters of the layout have been determined.

Finally we compute the tolerances of the layout: we change the parameters in a loop, in pairs, in an arbitrary range, to compute the stability condition of the recycling cavity versus the percentage variation of parameters. At the same time we compute the parameters of the recycling cavity eigenmode and the coupling with the input beam and the arm cavity eigenmode.

In the following we will give a detailed description of the steps of the code, following the same sequence of the design procedure described previously.

1 - Lengths, Gouy phase and beam size

We first compute the total length of the recycling cavity through eq.(5.31) in order to satisfy the resonance condition of the radio-frequency sideband fields. Then we decide the position of the optics in the vacuum tanks, so we determine the set of lengths $\{L_x, L_1, L_2, L_3\}$. We try to minimize the potential astigmatism of the layout by maximizing the distance L_2, that is the *lever arm* of the telescope: we will see in the following that for a given beam spacing d (determined by size of the beam and the mechanical elements of suspensions), the larger is the lever arm, the smaller are the incidence angles on the telescope mirrors.

Then we set Φ_G and w on PRM1: for the following we will assume the value of phase indicated in the baseline design of AdV, $\Phi_G = 20$ deg, and we will consider $w = 1$ mm, which is a reasonable beam size. Together with the arm cavity eigenmode

$$q_{\rm arm} = z_{\rm arm} + z_R^{\rm arm} = (960.830 + i134.636) \text{ m},$$

$\{\Phi_G, w\}$ represent the initial conditions of the computation that will follow: we need to determine the RoCs of the non-degenerate layout, $\{R_2, R_3\}$. R_1 is already bound, because it has to be equal to the curvature of the beam wavefront on PRM1. We compute it, together with the other beam parameters on PRM1, through the following equations:

$$\begin{aligned}
&z/z_R \simeq \tan(\Phi_G) \\
&w_0 = w/\sqrt{1 + (z/z_R)^2} \\
&z_R = \pi w_0^2/\lambda \rightarrow z = z_R \ \tan(\Phi_G) \\
&R_1 = z\left[1 + \left(\tfrac{z_R}{z}\right)^2\right] .
\end{aligned}$$

where we approximated the total Gouy phase shift in the cavity as the phase on PRM1. This is a reasonable approximation, since as we have seen in chapter 5 most of the phase is cumulated along L_1.

At this stage, step 1 of the design procedure is complete. We now have to determine $\{R_2, R_3\}$.

2 - Approximated computation of RoCs

We compute an initial pair of values $\{R_2, R_3\}$, through an approximated formula for the telescope of the layout, which can be seen as a unique lens with equivalent focal length

$$f_{eq} = \sqrt{\frac{z_R(z_{\rm arm} + L_3)^2}{z_R^{\rm arm}}} . \tag{6.8}$$

Eq.(6.8) is obtained by applying repeatedly eq.(5.28) for PRM3 and PRM2, then imposing $z_{\rm arm} >> R_3, R_2$. This is a reasonable approximation, since $z_{\rm arm}$ is of the order of 10^3 m whereas R_3 and R_2 are of the order of 10 m. The equivalent focal length is known, since it is function of known

parameters, so we can use it to compute the approximated values

$$\begin{aligned} R_3 &= \tfrac{2L_2}{z+L_1-f_{eq}}\ f_{eq} \\ R_2 &= -\tfrac{2(R_3/2+L_2)}{f_{eq}-R_3/2}\ f_{eq}\ , \end{aligned} \tag{6.9}$$

which will be used in the next computation of the code.

3 - Fine tuning

At this stage $\{R_2, R_3\}$ must be fine-tuned to have $\Phi_G = 20$. The code then executes the following instructions:

- the RoCs of PRM3 and PRM2 are scanned in a loop around the initial values R_3 and R_2
- at every step of the loop, for every pair $\{R_2, R_3\}$, the code computes the eigenmode of the recycling cavity and its parameters $\{w,\ R,\ z,\ z_R$ and $\Phi_G\}$ on every mirror of the layout. The computation is carried out through the round-trip matrix product associated to the layout of the recycling cavity,

  $$M_{RC} = \begin{pmatrix} A(L_i, R_j) & B(L_i, R_j) \\ C(L_i, R_j) & D(L_i, R_j) \end{pmatrix}, \tag{6.10}$$

  whose elements depend on the layout parameters. We replace these matrix elements in eq.(6.6) to compute the cavity eigenmode, then we use eq.(6.3) to compute the propagation of the mode inside the cavity. In the same iteration we compute the stability condition of eq.(6.5), and we discard the pairs $\{R_2, R_3\}$ which make the resonator unstable
- the code selects the pairs $\{R_2, R_3\}$ which yield a phase in the range $15 < \Phi_G < 25$ and $w \geq 1$ mm on PRM1. We are interested in this range of values since we might want to tune the phase to avoid accidental resonances of modes of large order, and we would like to have the largest beam radius possible. Then the code sorts a list of these parameters in an output file and plots the results.

Finally we select the best set of RoCs through the output plot shown on fig.6.2, where we arbitrarily chose R_3 as independent variable to project the space of layout and beam parameters on the axes[1].

We always choose the values of the RoCs to be at least larger than 1 m, to minimize the risk that low curvature induce spherical aberration of the beam. This may conflict with the requirement of having $w \geq 1$ mm (R_2 decreases where the beam radius w increases), and in this case, a trade-off between these two requirements should possibly be made.

The choice of the RoCs marks the accomplishment of step 3 of the design procedure.

[1]The plot shows an example of selection of parameters for the *vertical* layout that will be presented later in this chapter.

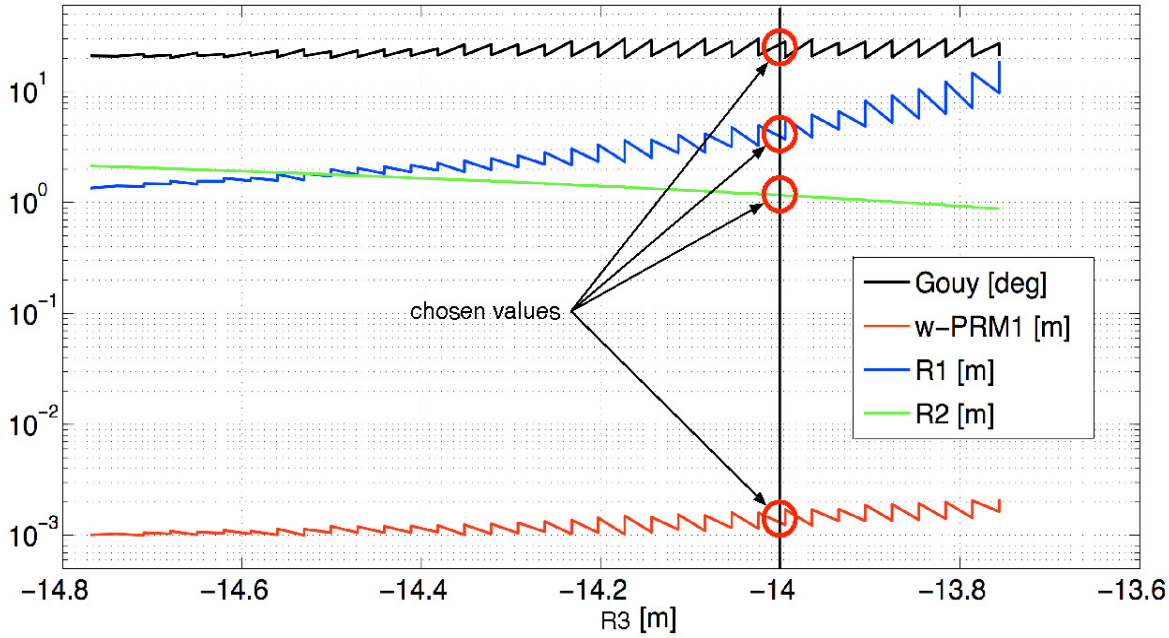

Figure 6.2: Output plot of the space of beam and layout parameters: beam radius w on PRM1 [m] (red curve), RoC of PRM2 [m](green curve), RoC of PRM1 [m] (blue curve) and cumulated Gouy phase shift in the cavity [deg] (black curve) versus the RoC of PRM3.

4 - Incidence angles

In this step we include the incidence angles in the layout. Of course the astigmatism increases with the incidence angles, so we would like to choose the smallest angles possible. However there is a lower limit for the choice of the angles, determined by the spacing d between the beams.

This limit changes according to the set of lengths and RoCs of the layout, but we can give a general estimate to show its order of magnitude. The beam is about $\sim$ 5-cm large between the arm cavity input mirror and PRM3, whereas on PRM2 the beam radius is of the order of 5 mm. The spacing is

$$d = 2.63(5 + 0.5) \simeq 15 \text{ cm},$$

where 2.63 is the ratio of the Gaussian beam radius to the mirror radius to have 1 ppm clipping losses. For small θ_3 we can approximate $\sin(2\theta_3) \simeq 2\theta_3$, thus the smallest incidence angle of the layout is $\theta_3 \simeq d/2L_2 \sim 0.4$ deg for $L_2 = 10$ m, and $\theta_3 \sim 0.9$ deg for $L_2 = 5$ m.

The minimum θ_3 could actually be larger if we consider also the mechanical elements (marionettas and recoil masses) of the mirror suspensions in the computation of the the beam spacing.

In the case the allowable space in the vacuum pipelines and tanks was sufficiently large, instead of choosing $\theta_2 = \theta_3$ we might optimize the incidence angles to compensate exactly for the astigmatism of the layout. This can be done by compensating the astigmatism of the concave mirror PRM3 through the convex mirror PRM2, according to [104]

$$\theta_2 = \sqrt{\frac{R_2}{R_3}} \left| \frac{z_{\text{arm}}}{z_{\text{arm}}(1 - 2L_2/R_3) + L_2} \right| \theta_3 \ . \tag{6.11}$$

Usually the optimal θ_2 is larger than θ_3 by a factor 2 or more, then to fit the layout in the vacuum pipeline (which has a limited diameter) we would like to choose θ_3 as small as possible.

It could possible, in any case, to achieve just a partial compensation. For example, we will see later in this chapter that for the *vertical* cavity layout we could choose $\theta_3 = 1.06$ deg. The optimal θ_2 for a prefect compensation of astigmatism would be 3.2 deg, but the geometry of the infrastructure does not allow to choose such a big angle. Nevertheless we imposed $\theta_2 = 2.53$ and still could achieve a good level of compensation.

When the incidence angles are computed, step 4 of the design procedure is accomplished.

5 - Characterization

In this step we compute the tolerances of the recycling cavity layout, the parameters of the cavity eigenmode, the *overlap integrals* of the recycling cavity eigenmode with the input beam and with the arm cavity eigenmode. The code executes the following instructions:

- the parameters of the layout, $\{L_x, L_1, L_2, L_3, R_1, R_2, R_3, \theta_3, \theta_2\}$, are set as initial condition of the computation

- a pair of parameters (usually we start from $\{R_2, R_3\}$) is changed in a loop within an arbitrary range. For every pair of values the code computes through eq.(6.6) the eigenmode of the recycling cavity on the transverse directions, using two distinct matrix products:

$$M^t_{RC} = \begin{pmatrix} A(L_i, R_j, \theta_k) & B(L_i, R_j, \theta_k) \\ C(L_i, R_j, \theta_k) & D(L_i, R_j, \theta_k) \end{pmatrix}, \; M^s_{RC} = \begin{pmatrix} A(L_i, R_j, \theta_k) & B(L_i, R_j, \theta_k) \\ C(L_i, R_j, \theta_k) & D(L_i, R_j, \theta_k) \end{pmatrix}, \quad (6.12)$$

  where t stands for *tangential* and s stands for *sagittal*. Then the eigenmode parameters $\{w_{RC|t}, R_{RC|t}, \Phi_{G|t}\}$ and $\{w_{RC|s}, R_{RC|s}, \Phi_{G|s}\}$ are computed on every recycling mirror, to study the propagation of the beam in the cavity. Because of the astigmatism, we have that

$$w_{RC|t} \neq w_{RC|s} \; , \; R_{RC|t} \neq R_{RC|s} \; , \Phi_{G|t} \neq \Phi_{G|s} \; .$$

  In the same iteration, the code computes the following *overlap integral*

$$\begin{aligned} \gamma_{\text{input}} \; &\equiv \left\langle TEM_{00}^{\text{input}} \middle| TEM_{00}^{\text{RC}} \right\rangle = \\ &= \frac{2}{\sqrt{w_{input|t} w_{RC|t} w_{input|s} w_{RC|s}}} \quad \sqrt{\frac{1}{\frac{1}{w^2_{input|t}} + \frac{1}{w^2_{RC|t}} - \frac{i\pi}{\lambda}\left(\frac{1}{R_{input|t}} + \frac{1}{R_{RC|t}}\right)}} \\ &\qquad \times \sqrt{\frac{1}{\frac{1}{w^2_{input|s}} + \frac{1}{w^2_{RC|s}} - \frac{i\pi}{\lambda}\left(\frac{1}{R_{input|s}} + \frac{1}{R_{RC|s}}\right)}} \end{aligned} \quad (6.13)$$

  between the input beam (coming from the injection system) TEM_{00}^{input} and the eigenmode of the recycling cavity TEM_{00}^{RC}, taken on PRM1. Its square value $\gamma^2_{\text{input}} \in [0, 1]$ yields the

coupling of the input beam to the recycling cavity. We define the parameters of the input beam as

$$w_{input|t} = w_{input|s} \equiv (w_{RC|t} + w_{RC|s})/2$$

$$R_{input|t} = R_{input|s} \equiv (R_{RC|t} + R_{RC|s})/2 \ ,$$

i.e. the input beam has the average parameters of the tangential and sagittal planes of the recycling cavity eigenmode. This is the input beam that best matches the recycling cavity eigenmode.

Always in the same iteration, the code computes the analogous overlap integral

$$\gamma_{\rm arm} = \left\langle TEM_{00}^{\rm arm} | TEM_{00}^{\rm RC} \right\rangle \tag{6.14}$$

between the arm cavity eigenmode $TEM_{00}^{\rm input}$ and the eigenmode of the recycling cavity $TEM_{00}^{\rm RC}$, taken on the arm cavity input mirror.

As for step 3 of the design procedure, all the quantities computed in this step are discarded if the stability condition of eq.(6.5) is not respected. We require this condition to be fulfilled by both transverse directions at the same time

- the code gives as output a *stability plot*, showing the cavity stability and the beam coupling $\gamma^2_{\rm input}$ versus the percentage variation of the layout parameters. This plot is used to asses the tolerances of the parameters, so we repeat its computation for every parameter of the layout.

The stability plot is the main result of the code and closes the ray-matrix code: we will show this plot in the next section for each layout that will be presented.

6.1.3 Fast Fourier Transform Codes

FFT codes are based on the expansion of the complex amplitude of a coherent electric field $E(x, y, z)$, like a laser beam, in the Fourier space of spatial frequencies. This expansion is equivalent to a decomposition of the field in a sum of elementary plane waves of the form

$$u(x, y, z) = u_0 e^{-i\vec{k}\cdot\vec{r}} = u_0 \exp[-i(k_x x + k_y y + k_z z)], \tag{6.15}$$

where $k = \sqrt{k_x^2 + k_y^2 + k_z^2} = 2\pi/\lambda$ is the wave vector. If we assume the paraxial approximation along z as usual, $k_z >> k_x, k_y$, then we can write

$$k_z = \sqrt{k^2 - k_x^2 - k_y^2} \simeq k - \frac{k_x^2 + k_y^2}{k} \simeq k - \lambda\pi(\nu_x^2 + \nu_y^2) \tag{6.16}$$

with $\nu_x = k_x/2\pi, \nu_y = k_y/2\pi$ being the characteristic spatial frequencies (number of wavelengths per unit of length) of the wave in the transverse plane. If we propagate the wave over a distance d, we can write

$$u(x, y, d) = u_0 \exp[-i(k_x x + k_y y + k_z d)] \simeq u(x, y, 0) \exp[-i(k - \lambda\pi(\nu_x^2 + \nu_y^2))d], \tag{6.17}$$

where $u(x, y, 0)$ is the wave at $z = 0$. Eq.(6.17) is the fundamental equation of FFT codes: it indicates that the propagation of the plane wave along a distance d is simply equal to the product

of the wave at the initial position times a harmonic *propagator*, which is a simple function of the distance. In other words, the propagation is equivalent to a phase shift of the plane wave.

Eq.(6.17) allows to compute the propagation of *any* field $E(x, y, z)$ through the following operations:

- the field is expanded in the Fourier space as a sum of plane waves, through a 2-dimensional Fourier transform:

$$\tilde{E}(\nu_x, \nu_y, 0) = \int_{-\infty}^{\infty} E(x, y, 0) \exp[-i2\pi(\nu_x x + \nu_y y)] \; dxdy \tag{6.18}$$

- each plane wave is propagated in the frequency domain through a phase shift term:

$$\tilde{E}(\nu_x, \nu_y, d) = \tilde{E}(\nu_x, \nu_y, 0) \exp[-i(k - \lambda\pi(\nu_x^2 + \nu_y^2))d] \tag{6.19}$$

- the field is recomposed from the propagated plane waves through an inverse Fourier transform:

$$E(x, y, d) = \int_{-\infty}^{\infty} \tilde{E}(\nu_x, \nu_y, d) \exp[-i2\pi(\nu_x x + \nu_y y)] \; d\nu_x d\nu_y \; . \tag{6.20}$$

These operations are executed through the Fast Fourier Transform, which is an efficient algorithm for the computation of the Fourier transform and its inverse.

The propagation of the field through optical elements is computed as a phase shift in the physical space of distances, according to

$$E_{out}(x, y, z) = E(x, y, z) \exp[-ik\Delta L_{opt}(x, y)], \tag{6.21}$$

where $L_{opt}(x, y)$ is the optical path difference introduced by the optical element. For example, referring to fig.6.3, the optical path difference introduced by the reflection of the field on the surface of a mirror is

$$L_{opt}^{mirr}(x, y) = 2\Delta s = 2(R - \sqrt{R^2 - \Delta r^2}) \; , \tag{6.22}$$

Δs being the change in sagitta, R the RoC of the mirror, $\Delta r^2 = x^2 + y^2$ and the factor 2 indicates the forward and backward propagation of the beam. The reflection on a mirror with non-normal incidence angles can be approximated by replacing $R \to R\cos\theta$ and $R \to R/\cos\theta$ in eq.(6.22) for the tangential and the sagittal directions, respectively.

Stationary Interferometer Simulation (SIS)

In SIS it is possible to simulate a single arm cavity coupled to a recycling cavity. Among the various options of the code, it is possible to simulate:

- either a non-degenerate layout or a marginally stable layout
- the power recycling cavity or the signal recycling cavity
- the resonance of different fields in the cavities: the carrier, the radio- or the audio-frequency sidebands

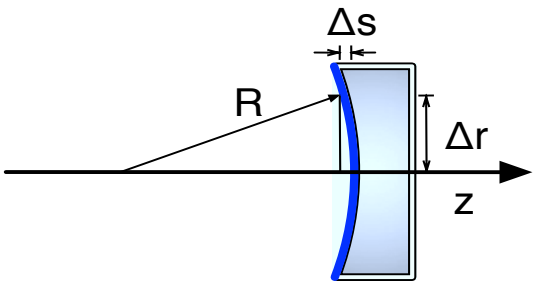

Figure 6.3: Computation of the optical path length difference introduced by a mirror.

- either perfect or realistic optics, by including measured or simulated phase maps of mirrors.

We use SIS in step 5 of the design procedure, to simulate the impact of astigmatism on carrier and radio-frequency sidebands in the non-degenerate power recycling cavity. In step 6 we use SIS to simulate the shape and the recycling gain of carrier and radio-frequency sidebands in presence of realistic mirror defects and thermal effects, by using phase maps for the mirrors.

6.2 Design History: from the Baseline to the Vertical Layout

We applied the design procedure described in the previous section to explore several possible layouts of the non-degenerate recycling cavities. We will present in the following the four most significant configurations that we studied: they illustrate at best the concepts behind the different designs. We will introduce the layouts following the chronological sequence of their conception, to illustrate the evolution of the non-degenerate cavity design. Each of these layouts has been characterized in terms of cavity stability, parameters of the resonant beam, astigmatism, coupling loss and parameter tolerances.

The last configuration we analyzed, the *vertical* layout, is the one that was retained: it features very low astigmatism, and tolerances comparable to those of other designs. Most important, we will see that this layout does not require the off-axis suspension of multiple mirrors from a Superattenuator, which instead is an important issue of the first two designs.

6.2.1 *Baseline* Design

The *baseline* design, shown on fig.6.4, is the first layout we studied [105]. PRM3 is placed in the power recycling tank, PRM2 is in the same vacuum tank of the beamsplitter, PRM1 is suspended in the injection vacuum tank, from the same Superattenuator which carries the bench of the injection system. The beamsplitter tank also hosts SRM2 of the signal recycling cavity, thus three optics have to be suspended from the same Superattenuator. The total length of the cavity is about 27.5 m, the other parameters of the layout are reported in table 6.1.

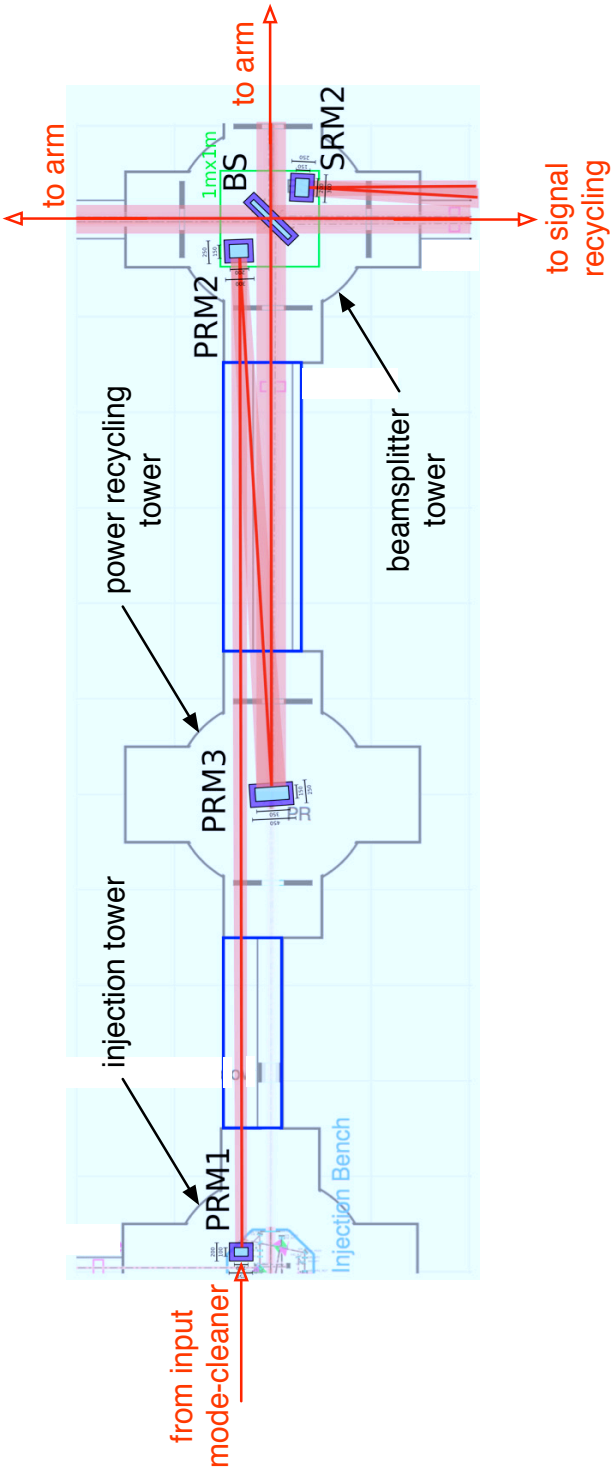

Figure 6.4: *Baseline* layout of the non-degenerate power recycling cavity, from [105].

length [m]	RoC [m]	angle of incidence [deg]
$L_x = 5.5$		
$L_3 = 6$	$R_3 = 12.795$	$\theta_3 = 1.7$
$L_2 = 5.5$	$R_2 = -2.042$	$\theta_2 = 1.7$
$L_1 = 10.5$	$R_1 = -2.033$	

Table 6.1: Parameters of the *baseline* layout.

beam parameter	x (tangential)	y (sagittal)
$q_{\rm arm}$	$(951.632 + i155.174)$m	$(961.782 + i120.728)$m
q_1	$(-0.768 + i0.986)$m	$(-1.561 + i0.858)$m
Φ_G	47.5 deg	25.1 deg
w on PRM1	0.7 mm	1.1 mm

Table 6.2: Eigenmode parameters in the *baseline* layout.

Astigmatism and stability

Since the lever arm of the telescope is short and the spacing between the beams is large to accommodate the mirrors and their recoil masses, the angle of incidence on PRM3 should be large, $\theta_3 = 1.7$ deg. In this configuration it is not possible to increase θ_2 to reduce the astigmatism, since the beam is already close to the edge of the vacuum pipe, so we take $\theta_2 = \theta_3$. Thereby the astigmatism of the layout is considerable: the parameters of the beam are largely different on the transverse directions, including the Guoy phase shift, as shown by table 6.2.

Fig.6.5 shows the *stability plot*, which depicts the stability of the cavity with respect to the percentage variation of the parameters on the axes[2]. The white regions of the plot represent the subsets of values which yield instability of the tangential *or* of the sagittal plane. Colored regions are stable for both the transverse directions. The color scale represents the coupling $\gamma^2_{\rm input}$, computed with the ray-matrix code through eq.(6.13). A similar plot can be obtained for the coupling $\gamma^2_{\rm arm}$, computed through eq.(6.14). The point of coordinates $(0\%, 0\%)$ represents the optimal values listed in table 6.1. In this point, the couplings are $\gamma^2_{\rm input} = 95.6\%$ and $\gamma^2_{\rm arm} = 97.5\%$.

Initially, by assuming that the arm cavity and the recycling cavity are completely independent, we used to compute the total coupling loss for the carrier field as

$$L_{\rm carrier} = 1 - \gamma^2_{\rm input}\gamma^2_{\rm arm} = 6.8\% \ . \tag{6.23}$$

We used to consider eq.(6.23) as an upper limit, since actually the cavities are not decoupled and the light which is not coupled into the arm cavity might still be recycled by the recycling cavity, then not being lost. We also expected $\gamma^2_{\rm input}$ to be the actual estimation of the coupling of the radio-frequency sidebands with the recycling cavity.

Then we studied the astigmatism of the *baseline* layout with SIS, which yielded unexpected results for the carrier field. Results are shown on fig.6.6, where the loss of carrier recycling gain (computed as the ratio of the power resonant in the astigmatic cavity to the power resonant with $\theta_2 = \theta_3 = 0$) is plotted versus the incidence angles $\theta_2 = \theta_3$. For small angles, below 1 deg, the loss is negligible (of the order of percent), and $L_{\rm carrier}$ is overestimated. For larger values of the

[2]Here we show only the analysis of stability versus $\{R_2, R_3\}$, but we repeat the computation for all the parameters.

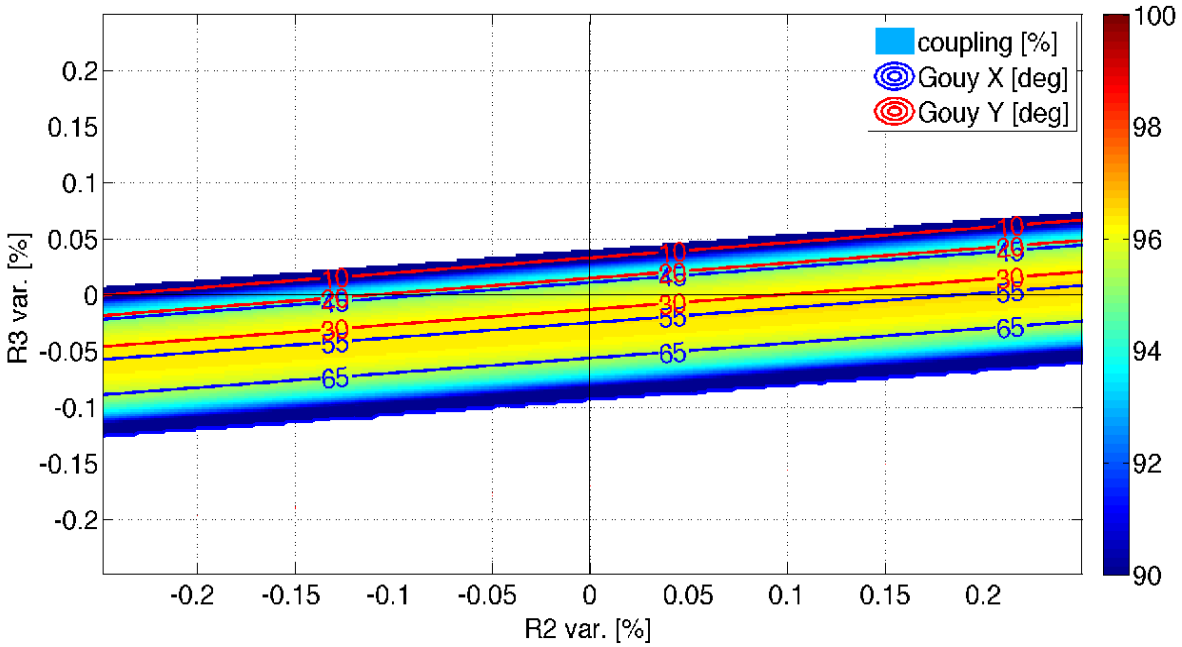

Figure 6.5: Stability plot of the *baseline* layout, γ^2_{input} versus $\{R_2, R_3\}$.

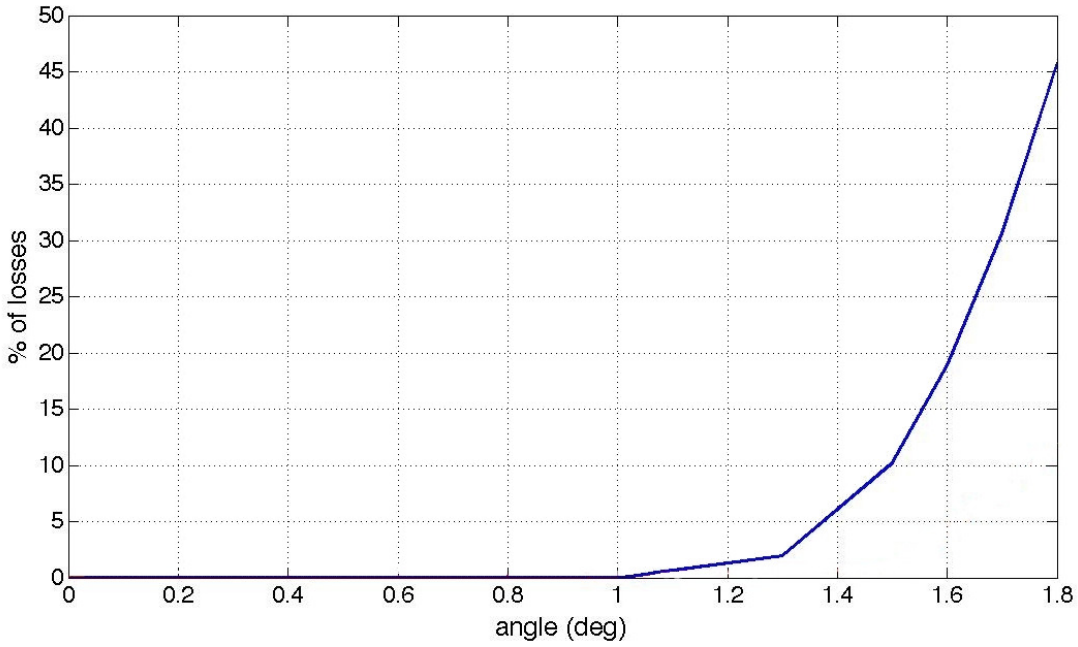

Figure 6.6: Loss of the carrier versus the incidence angles ($\theta_3 = \theta_2$).

parameter	tolerance [%]
L_3/L_x	$\pm$ 100
L_2	$\pm$ 0.04
L_1	$\pm$ 4.0
R_3	$\pm$ 0.03
R_2	$\pm$ 0.3
$R1$	$\pm$ 20

Table 6.3: Tolerance of parameters for a stable *baseline* design.

incidence angles the loss increase rapidly, attaining $\sim 30\%$ for $\theta_2 = \theta_3 = 1.7$ deg. In this case L_{carrier} is largely underestimated.

The discrepancy can be explained by the fact that the coupling between the arm and the power recycling cavity cannot be neglected for the carrier field. For low astigmatism the coupling reduces the loss to a negligible level, for high astigmatism the coupling is affected and the loss is high. SIS allows to simulate the coupling between the recycling cavity and the arm cavity for the carrier field, while the ray-matrix do not. Thereby we realized that the upper limit L_{carrier} was not a reliable estimator for the loss of the carrier.

For the radio-frequency sidebands, instead, the results of SIS confirmed the coupling γ^2_{input} computed with the ray-matrix code. Thus we continued to characterize the astigmatism loss for the radio-frequency sidebands through the computation of γ^2_{input} and of the stability plot, which will be presented hereafter for the other layouts that we studied.

Tolerances

The tolerances for cavity stability are derived from the stability plot: we measure the tolerance on the plot axes as the minimum variation which makes the recycling cavity unstable, starting from the working point $(0\%, 0\%)$. They are summarized in table 6.3.

The critical parameters of the layout are $\{L_2, R_2, R_3\}$. By analyzing other configurations, later on in this chapter, we will see that this is a constant feature of the non-degenerate layout. This happens because the Gouy phase in the cavity is determined essentially by the RoC of PRM2. If this RoC is larger than the phase front curvature of the beam focused by PRM3, the field will diverge and the cavity will be unstable: the Gouy phase in the cavity would be close to 0. Thus the cavity can become unstable for very small detuning of the telescope, either because of RoC errors or because of errors of the distance L_2.

The most critical parameter is R_3, since its tolerance is more severe than the possible achievable manufacturing error: with present technology, mirrors of $\sim$ 10-m RoC like PRM3 can be realized with an accuracy of $\pm 0.1\%$, while in this case an accuracy of $\pm 0.03\%$ is needed.

Tuning

The instability of the cavity as well as manufacturer RoC errors could be compensated by tuning the lever arm of the telescope. One of the interest of the folded design, in fact, is the possibility to adjust the distance between the telescope mirrors in order to tune the focusing of the telescope to recover the mode-matching [93]. Fig.6.7 shows that a percentage variation of L_2 of the same order of the RoC error is needed to recover stability. This implies that in presence of an error of

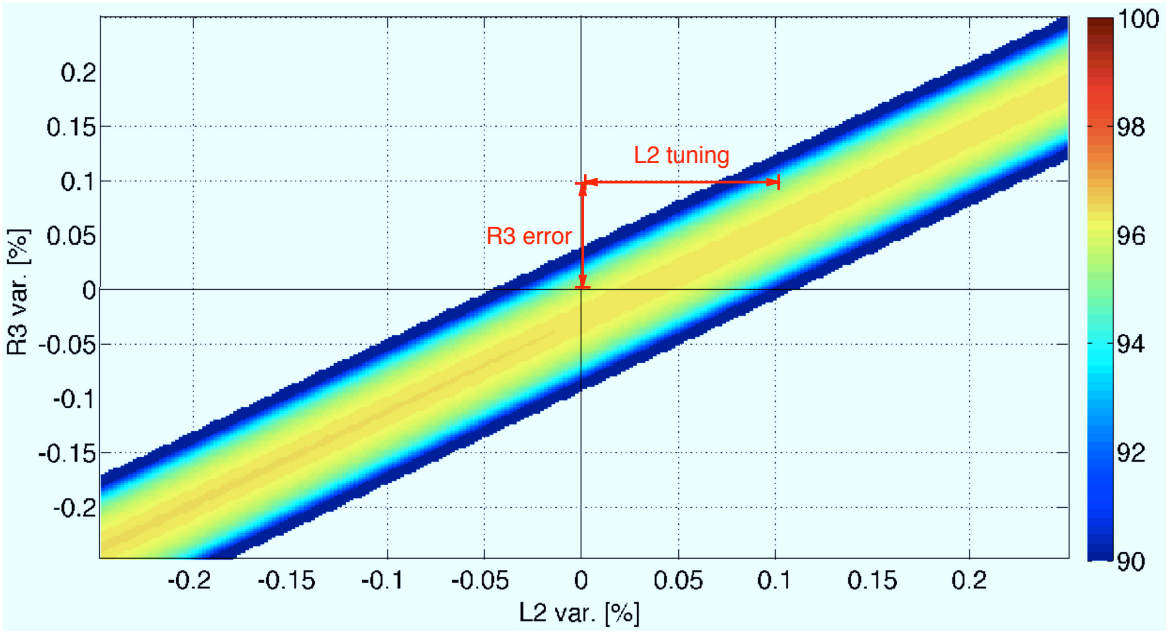

Figure 6.7: Tuning of the lever arm L_2 in the *baseline* design.

+1 cm on R_3 (corresponding to an error of about +0.1 %, making the cavity unstable), L_2 should be elongated of about 5.5 mm (corresponding to a variation of about +0.1 %).

The tuning of the telescope must be achieved by respecting the resonance condition of sidebands, thus the total recycling cavity length has to be left unchanged. As a consequence, the tuning of the lever arm L_2 must be compensated by changing the distance L_1.

With the ray-matrix code we simulated an error of 0.1% on the RoC of PRM3, then we adjusted the length of the telescope and the distance L_1: we could verify that after the adjustments we recovered the same parameters of the recycling cavity eigenmode listed in table 6.2. This confirmed that the working point of the detector can be fully recovered after tuning the cavity matching.

Issues of the *baseline* design

The *baseline* design fits the infrastructure of Virgo, but features two important issues. The first is the high astigmatism, which induces relevant losses for the carrier field, and makes the transverse planes of the recycling cavity eigenmode very different for the sidebands. This could be in principle solved by using parabolic mirrors, even though it is not obvious to obtain such mirrors with a good surface quality.

The second and most important issue concerns the suspension of three optics in the same vacuum tank of the beamsplitter. This requires a modification of the suspension system: several optics might be suspended from the same Superattenuator by implementing a new design of the last suspension stage, a *multi-payload* for off-axis suspension [106], shown on fig.6.8.

The mechanical behavior of the multi-payload was studied by means of simulations. The results showed that the off-axis suspension enhances spurious couplings between degrees of freedom of suspended elements, which instead are negligible in the original design of the payload [106]. The

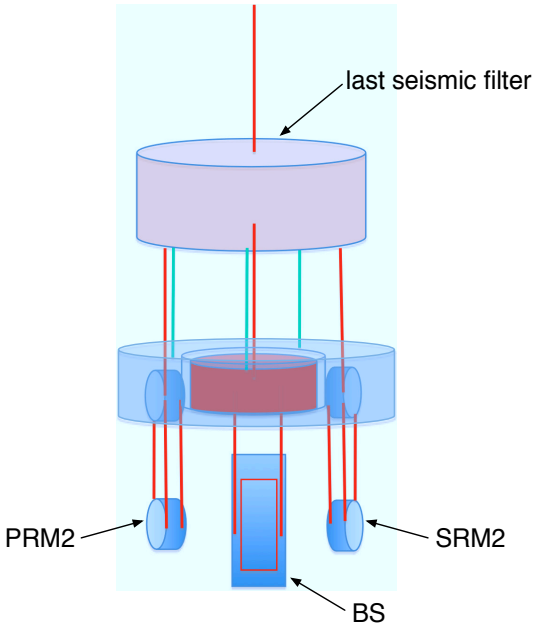

Figure 6.8: Scheme of the beamsplitter multi-payload, from [106].

couplings highly increase the complexity of the control system of the multi-payload, which would need the implementation of a large number of sensors and actuators and the development of a new control strategy. The conclusion of these studies pointed out that the multi-payload design presents a high technical risk and should be discarded [106].

Therefore the issue of the multiple off-axis suspension of mirrors triggered the design of a new optical configuration.

Modification of the *baseline* design

We proposed a new layout to remove the off-axis multi-payload from the beamsplitter tank and to suspend each element on axis with the Superattenuator [107]. This configuration lies in the vertical plane, as shown on fig.6.9. PRM2 is moved to the power recycling tank and PRM3 is moved in the injection tank. PRM1, PRM3 and the optical bench of the injection system are suspended vertically from the same Superattenuator, as shown on fig.6.10. The parameters of this new configuration are listed in table 6.4.

In order to reduce the astigmatism, we moved the power recycling tank towards the beamsplitter to increase the arm lever L_2 as much as possible, from 5.5 m to 6.5 m. At the same time we also optimized the encumbrance of the mechanical elements of the mirror suspensions, to decrease the spacing of the beams. Therefore θ_3 is decreased to 1 deg, so that the astigmatism is partially optimized. The loss of the carrier, computed through a simulation with SIS, is reduced to 0.3%. The coupling of radio-frequency sidebands, computed with the ray-matrix code and confirmed by the simulation with SIS, is $\gamma^2_{\text{input}} = 98.9\%$. Because of the lower astigmatism, the parameters of the recycling cavity eigenmode on the transverse directions have closer values, as shown in table 6.5.

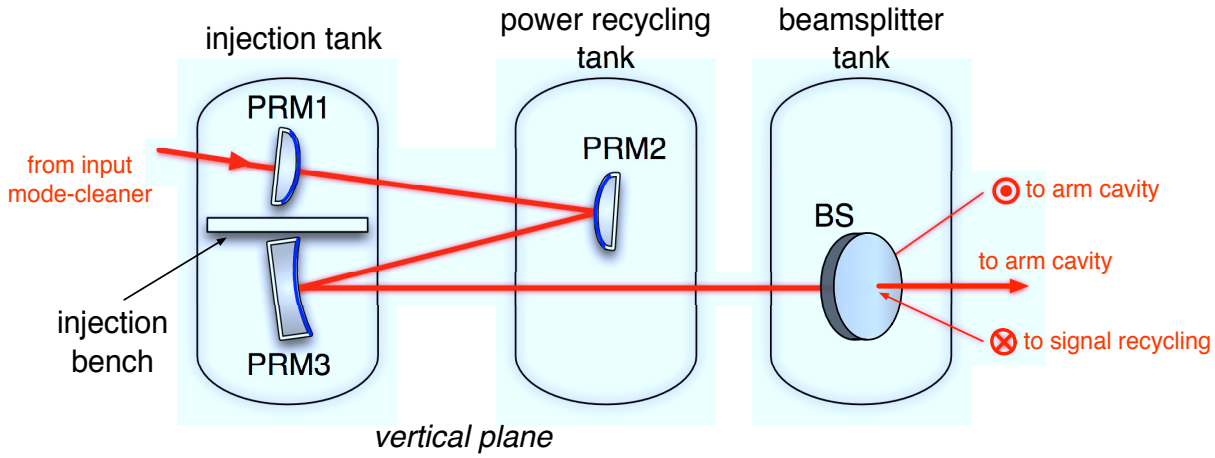

Figure 6.9: Modification of the *baseline* layout in the vertical plane.

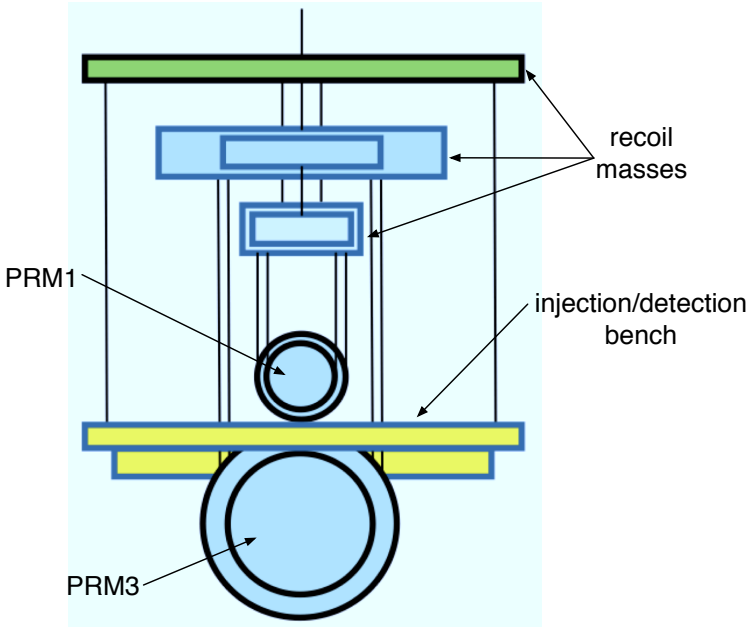

Figure 6.10: Scheme of the payload for the vertical suspension of the elements in the injection vacuum tank, for the *modified baseline* layout. From [107].

length [m]	RoC [m]	angle of incidence [deg]
$L_x = 5.6$		
$L_3 = 11$	$R_3 = 13.868$	$\theta_3 = 1$
$L_2 = 6.5$	$R_2 = -1.009$	$\theta_2 = 1.7$
$L_1 = 6.5$	$R_1 = -6.567$	

Table 6.4: Parameters of the *modified baseline* layout.

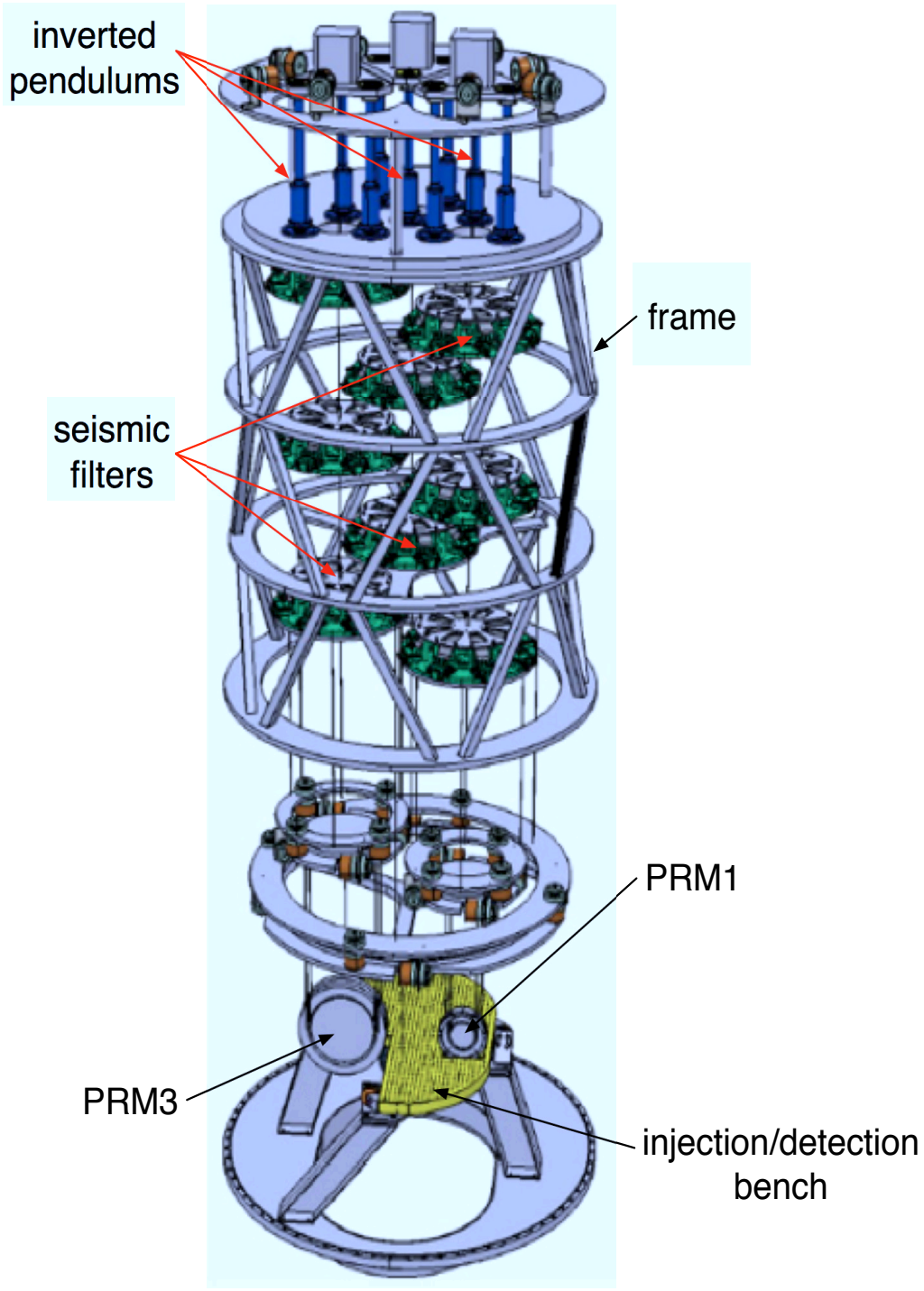

Figure 6.11: Design of the multi-Superattenuator for the injection/detection vacuum tank, from [108].

beam parameter	x (tangential)	y (sagittal)
$q_{\rm arm}$	$(957.224 + i146.661)$m	$(965.154 + i118.470)$m
q_1	$(-3.115 + i3.279)$m	$(-4.214 + i3.149)$m
Φ_G	28.6 deg	21.2 deg
w on PRM1	1.5 mm	1.7 mm

Table 6.5: Eigenmode parameters for the *modified baseline* layout.

However, the suspension of three elements from the same Superattenuator was considered technically challenging and was discarded. Thus we proposed to move the vertical configuration in the horizontal plane, and to suspend each element in the injection tank from its own single Superattenuator [107]. The development of a multi-Superattenuator was proposed [108], where each element is suspended from a single chain of filters by squeezing three standard Superattenuators into the injection tank. The system is shown on fig.6.11: the three chains are suspended from the top stages of three short inverted pendulums.

The multi-Superattenuator configuration represents the best solution to suspend multiple mirrors, since it follows the design concept of the original Superattenuator: each element is suspended on axis, from a single chain of filters. Nevertheless, it requires the re-design of several parts of the Superattenuator: seismic filters, for instance, have to be re-designed with a smaller volume to fit into the tank. The development and construction process of this system was considered too long to meet the schedule AdV, and it was also discarded.

As we will see later on, in order to simplify the suspensions we proposed to move the injection bench out of the injection tank (moving it in a small vacuum tank to be built beside), and we reconsidered the suspension of PRM3 and PRM1 in the vertical plane. This configuration, called *vertical* layout, finally allowed to solve the issue of multiple mirror suspension. It will be presented at the end of this section.

6.2.2 Telescopes in the Differential Part of the Michelson Interferometer

The second layout we present is based on a completely different concept from that of the *baseline*. It has been conceived almost at the same time, and has been analyzed in parallel as an alternative configuration [105]. In this layout, shown in fig.6.12, the telescope is placed in the differential part of the Michelson interferometer (formed by the beamsplitter and the arm cavity input mirrors): PRM3 is suspended in the power recycling tank, PRM2 is suspended together with the arm cavity input mirror (ITM) in the arm input tank, PRM1 is on the injection (detection) bench. The total length of the recycling cavity is 41 m, and its parameters are listed in table 6.6.

This configuration has the advantage of allowing the compensation of thermal effects by acting directly on PRM3 and/or PRM2, with CO_2 lasers and ring heaters. Thus the compensation plates could in principle be removed, with two important consequences: the first is the simplification of the thermal compensation system, the second is the simplification of the design of the payload of arm cavity mirrors. In the current design of the payload, compensation plates are suspended off-axis with respect to the vertical of the Superattenuator, from the recoil mass of the mirror. The removal of compensation plates could allow to avoid the off-axis suspension of optics in the payload of arm cavity mirrors.

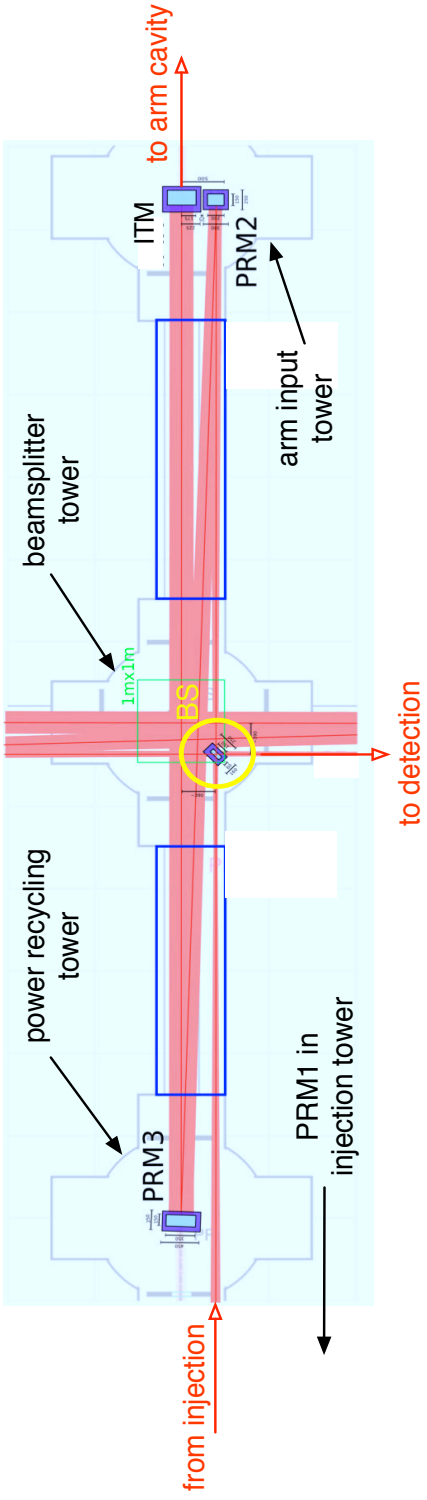

Figure 6.12: Layout of non-degenerate recycling cavities with telescopes in the differential part of the Michelson, adapted from [105].

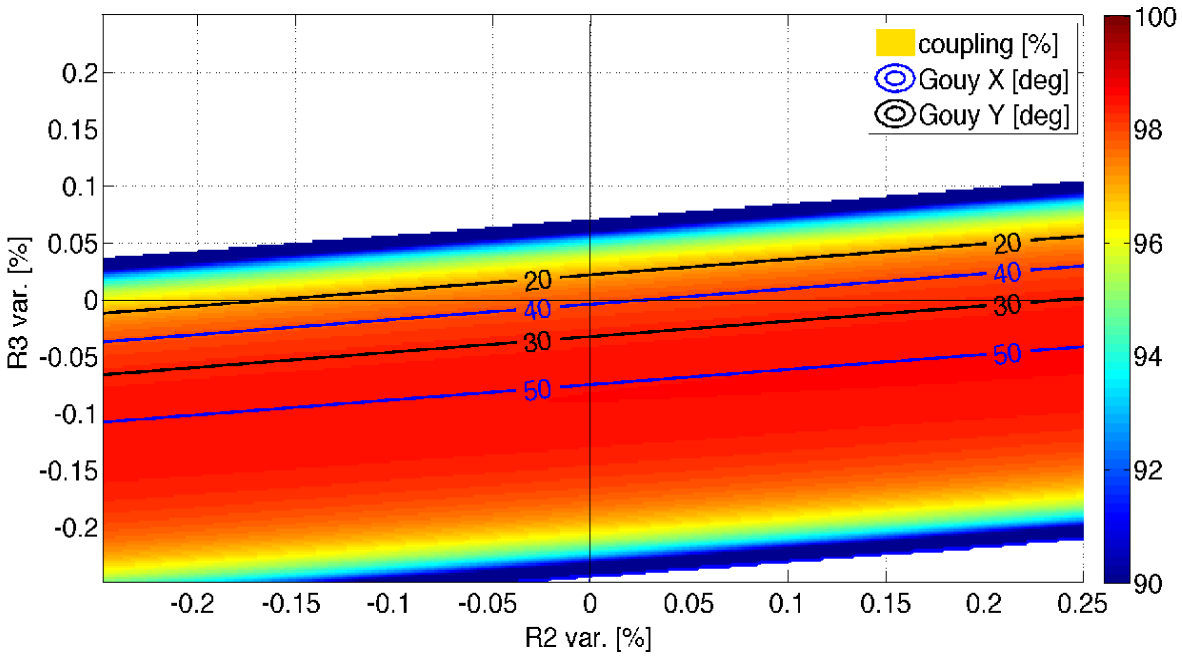

Figure 6.13: Stability plot of the layout with telescopes in the differential part of the Michelson, γ^2_{input} versus $\{R_2, R_3\}$.

length [m]	RoC [m]	angle of incidence [deg]
$L_x = 6.6$		
$L_3 = 12$	$R_3 = 27.960$	$\theta_3 = 1.9$
$L_2 = 12$	$R_2 = -4.890$	$\theta_2 = 1.9$
$L_1 = 10.5$	$R_1 = -4.616$	

Table 6.6: Parameters of the layout with telescopes in the differential part of the Michelson.

Astigmatism and stability

This design has also a lower astigmatism, since it has a much longer arm lever and larger RoCs. The stability plot of the layout is shown on fig.6.13: because of the lower astigmatism, the size of the stable region is increased. Also the parameters of the beam, listed in table 6.7, indicate that the astigmatism of the layout is reduced. The coupling coefficient for radio-frequency sidebands in this layout is $\gamma^2_{\text{input}} = 97.7\%$. It is not possible to simulate this particular configuration with SIS, so we could not study the recycling gain of the carrier field.

Tolerances and tuning

The tolerances for this layout are reported in table 6.8, and are similar to those of the *baseline* design. Manufacturer errors on R_3 may be recovered by tuning the lever arm of the telescopes, as shown by fig.6.14: to recover a RoC error of +3 cm (corresponding to an error of about +0.1 %, yielding an unstable recycling cavity), L_2 should be elongated of about 1 cm (corresponding to a variation of about +0.1 %).

beam parameter	x (tangential)	y (sagittal)
q_{arm}	$(957.435 + i136.642)$m	$(965.829 + i103.582)$m
q_1	$(-2.314 + i2.308)$m	$(-3.570 + i1.932)$m
Φ_G	38.9 deg	23.6 deg
w on PRM1	1.3 mm	1.7 mm

Table 6.7: Eigenmode parameters in the layout with telescopes in the differential part of the Michelson.

parameter	tolerance [%]
L_3/L_x	$\pm$ 100
L_2	$\pm$ 0.04
L_1	$\pm$ 4.0
R_3	$\pm$ 0.03
R_2	$\pm$ 0.3
$R1$	$\pm$ 20

Table 6.8: Tolerance of parameters for a stable layout with telescopes in the differential part of the Michelson.

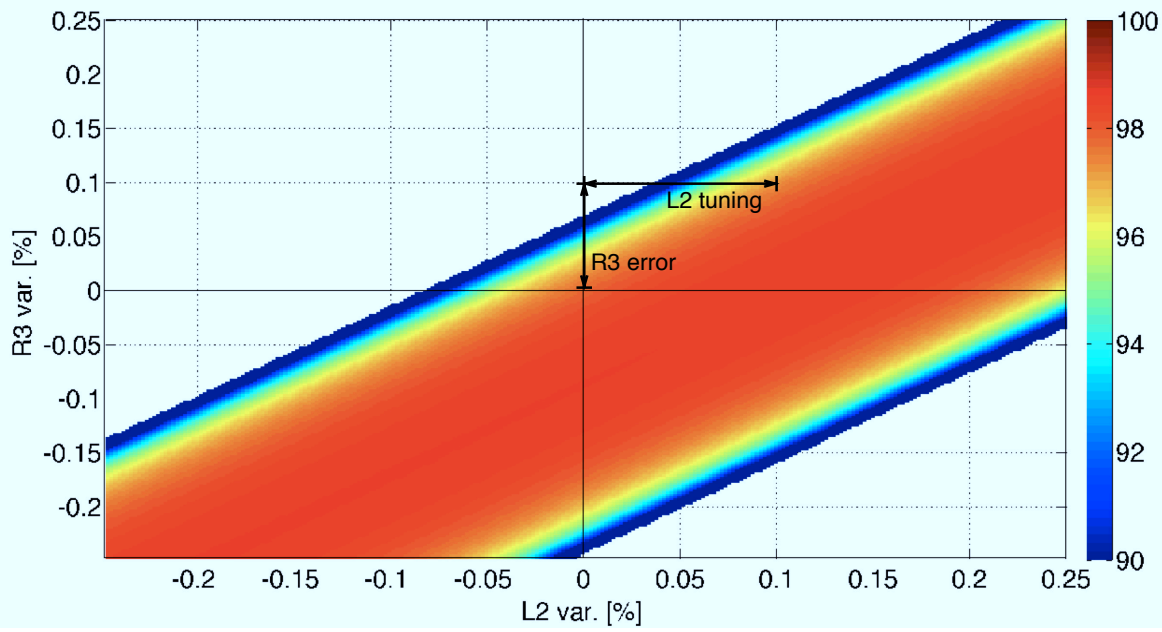

Figure 6.14: Tuning of the lever arm L_2 in the layout with telescopes in the differential part of the Michelson.

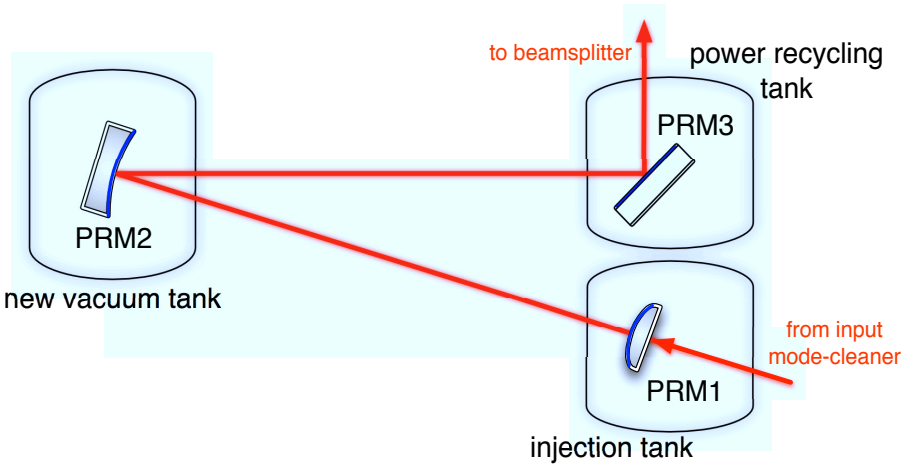

Figure 6.15: Layout of *long* non-degenerate recycling cavities.

length [m]	RoC [m]	angle of incidence [deg]
$L_x = 5.6$		
$L_3 = 6$	R_3 = Inf (plane)	$\theta_3 = 45$
$L_2 = 80$	$R_2 = 153$	$\theta_2 = 1.8$
$L_1 = 80.5$	R_1 = -2.250	

Table 6.9: Parameters of the *long* layout.

Issues of the layout with telescopes in the differential part of the Michelson

This configuration has two main drawbacks: first, the potential impact of differential noises introduced by the suspension of two additional mirrors per arm. More important, the P/S-RM2 suspension are close to the monolithic fibers of arm cavity input mirrors. Fibers are fragile and can be destroyed by accidental contact with any other object. This issue was considered too risky, and this configuration of the recycling cavity has been discarded.

6.2.3 *Long* Cavities

We studied a third configuration, shown on fig.6.15, in order to solve the issue of mirror suspensions. PRM3 is placed in the power recycling tank, PRM2 is placed in a new building to be constructed (a new building must be constructed also for SRM2), PRM1 is suspended in the injection tank. Therefore in this configuration each mirror of the layout is suspended on axis from a single Superattenuator.

The new building is positioned 80 m far from PRM3, so that the arm lever of this layout is very large and the astigmatism is reduced. Because of the much larger cavity length (172 m), we use only a single converging mirror, whose RoC must be as large as $\sim$ 150 m, to focus the beam inside the cavity: PRM3 becomes a flat steering mirror and PRM2 becomes the focusing mirror of the layout. The parameters of this configuration are listed in table 6.9.

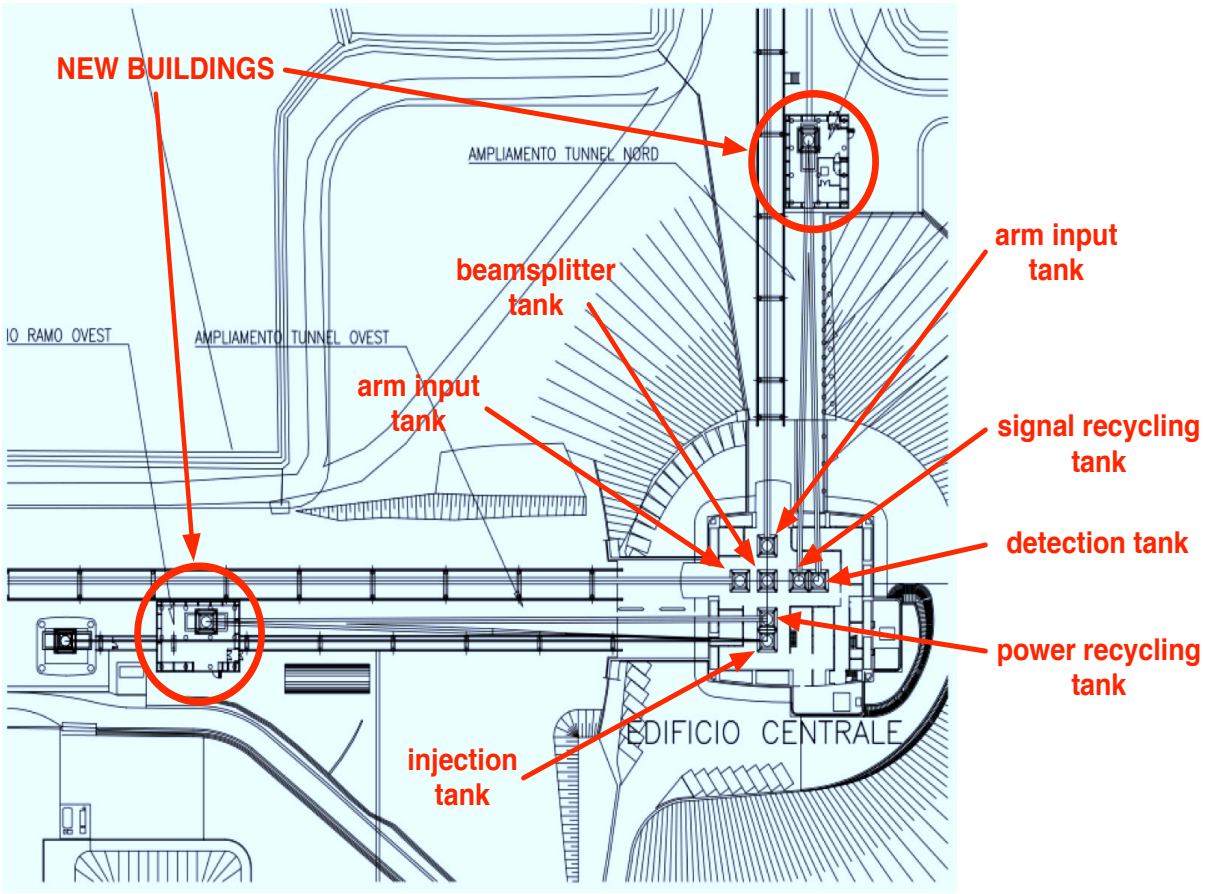

Figure 6.16: Construction of two new buildings for the *long* layout.

beam parameter	x (tangential)	y (sagittal)
$q_{\rm arm}$	$(957.077 + i137.866)$m	$(960.982 + i123.823)$m
q_1	$(-1.878 + i0.836)$m	$(-1.964 + i0.749)$m
Φ_G	24.1 deg	21.0 deg
w on PRM1	1.3 mm	1.4 mm

Table 6.10: Eigenmode parameters of the *long* recycling cavity.

parameter	tolerance [%]
L_3/L_x	$\pm$ 100
L_2	$\pm$ 56
L_1	$\pm$ 0.3
R_3	$-$
R_2	$\pm$ 0.3
$R1$	$\pm$ 12

Table 6.11: Tolerance of parameters for a stable *long* layout.

Astigmatism

Since PRM3 is a flat mirror, the astigmatism of the layout is entirely due to the incidence angle on PRM2. Though $\theta_2 = 1.79$ deg is similar to the angles of previous layouts, astigmatism is very low since R_2 (determined by the arm lever) is very large. The beam parameters have closer values on the transverse directions (see table 6.10), and coupling coefficient for the radio-frequency sidebands is larger: $\gamma^2_{\rm input} = 99.9\%$ with the input beam.

Tolerances and tuning

The values reported in table 6.11 and the stability plot of fig.6.17 indicate that RoC tolerances are more relaxed in this configuration, of about an order of magnitude. For comparison, the central area in the rectangle on fig.6.17 indicates the stability range for the *baseline* design (fig.6.5) and the layout with telescopes in the differential part of the Michelson (fig.6.13).

R_2 is a critical parameter: its tolerance, $\pm 0.3\%$, is smaller than the achievable manufacturing accuracy for a RoC of ~ 150 m, which is $\pm 1\%$. The plot of fig.6.18 indicates that to compensate for a RoC error of +1.5 m (corresponding to an error of +1 %, yielding an unstable recycling cavity) L_1 should be elongated of 0.8 cm (corresponding to a variation of about +0.1 %). The tuning of L_1 should be made by moving the suspension point at the top stage of the inverted pendulum of the Superattenuator, either of PRM1 or PRM2.

However the inverted pendulum only allows displacements of of ± 4 mm, thus the dynamics needed to tune the matching of the cavity is larger by orders of magnitude than the achievable adjustment of the length. In order to tune the matching of this layout it would be necessary to correct the RoC of PRM2 by acting on PRM2 (SRM2) with ring heaters of the thermal compensation system [109].

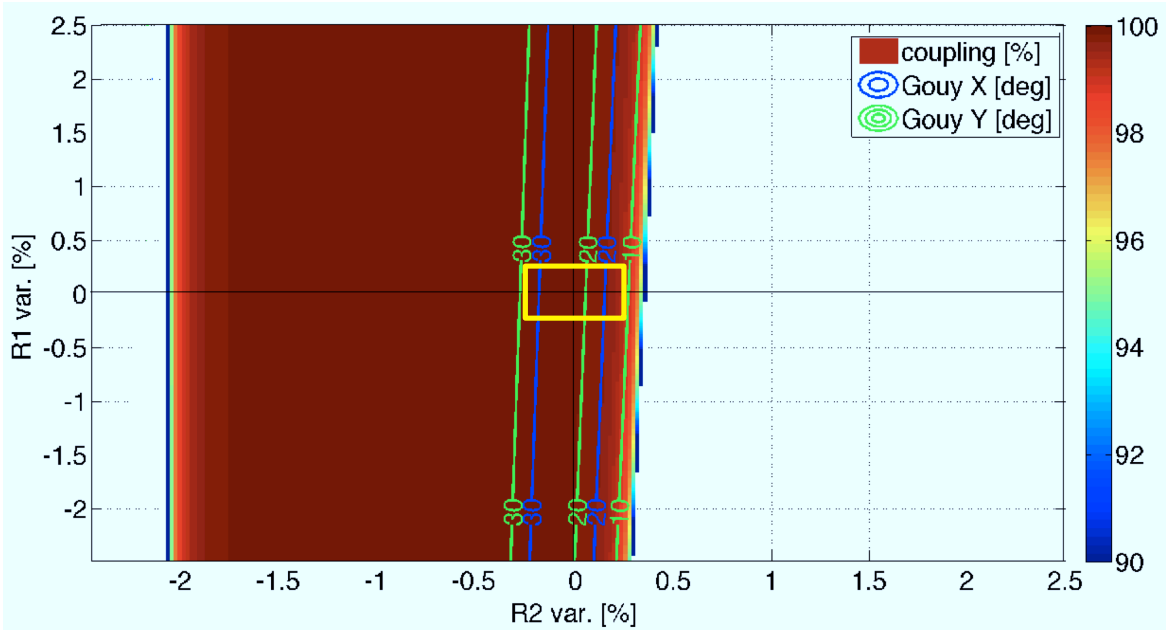

Figure 6.17: Stability plot of the *long* layout, γ^2_{input} versus $\{R_1, R_2\}$.

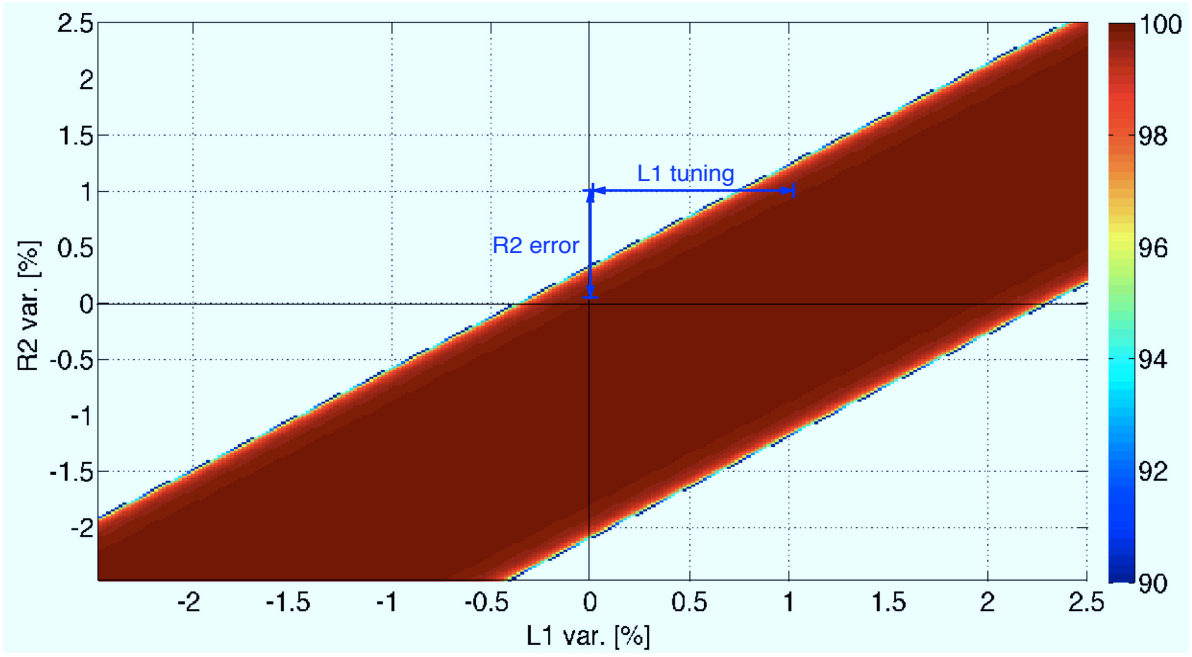

Figure 6.18: Tuning of the lever arm L_1 in the *long* layout.

length [m]	RoC [m]	angle of incidence [deg]
$L_x = 5.6$		
$L_3 = 10.7$	$R_3 = 15.098$	$\theta_3 = 1.1$
$L_2 = 6.8$	$R_2 = -1.837$	$\theta_2 = 2.5$
$L_1 = 6.8$	$R_1 = -1.870$	

Table 6.12: Parameters of the *vertical* layout.

Issues of the *long* cavities

This layout solves most of the issues of previous designs: it does not require off-axis suspension of multiple mirrors, has negligible astigmatism and larger tolerances. Its main technical drawback is the need of ring heaters to tune the mode-matching of the cavity. However, there are two crucial concerns with this layout:

- the additional cost for the construction of the new buildings for P/S-RM2 and of the vacuum tube and pumping system
- the risk of delays due to the construction works of the new buildings

These reasons pushed us to explore other configurations.

6.2.4 *Vertical* Layout

In order to solve the problems related to the suspensions of the *modified baseline* configuration, and in order to limit the construction works necessary for the *long* cavity configuration, a new solution has been proposed. The key elements are the following:

- the recycling cavities lie in the vertical plane
- the injection bench is moved to a smaller vacuum tank, to be built beside the injection tank (a new small vacuum tank has to be built also for the detection bench)
- PRM3 and PRM1 are suspended vertically along the axis of the Superattenuator of the injection tank
- PRM2 is suspended in the power recycling tower.

This configuration is shown on fig.6.19, and the parameters of the layout are listed in table 6.12. The payload for the double vertical suspension of PRM3 and PRM1 is re-designed as on fig.6.20, where mirrors are suspended from a new marionetta.

Astigmatism

To decrease the astigmatism of the layout, the optimization of θ_2 is simulated with SIS and with the ray-matrix code for the radio-frequency sidebands. Results are shown on fig.6.21, where the ellipticity of the beam w_x/w_y is plotted versus the angle θ_2. The astigmatism is completely compensated ($w_x/w_y = 1$) if $\theta_2 = 3.2$ deg. Since the diameter of the vacuum pipe do not allow such beam spacing, we chose $\theta_2 = 2.5$ deg: for this value, $w_x/w_y > 0.9$. The other parameters of the

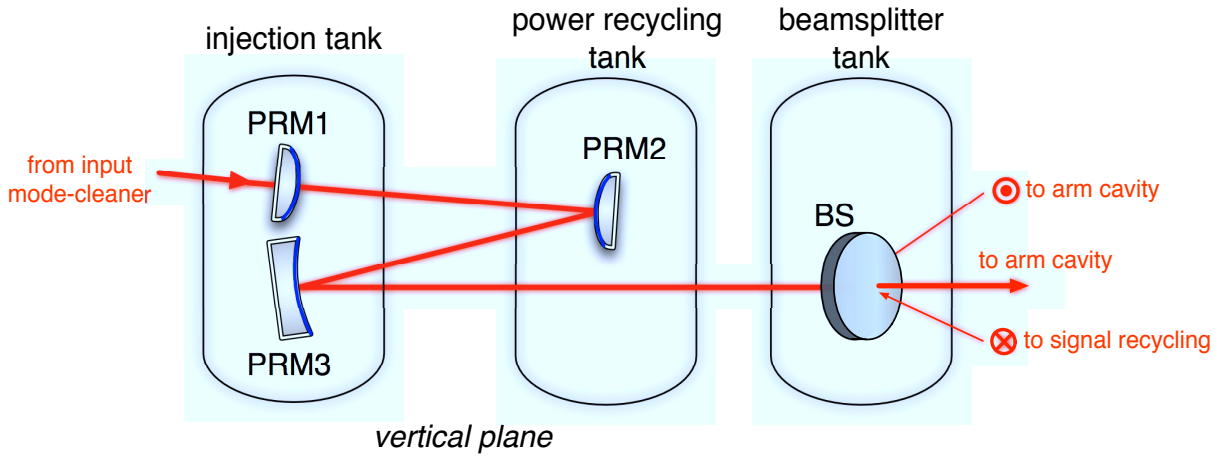

Figure 6.19: Layout of *vertical* non-degenerate recycling cavities.

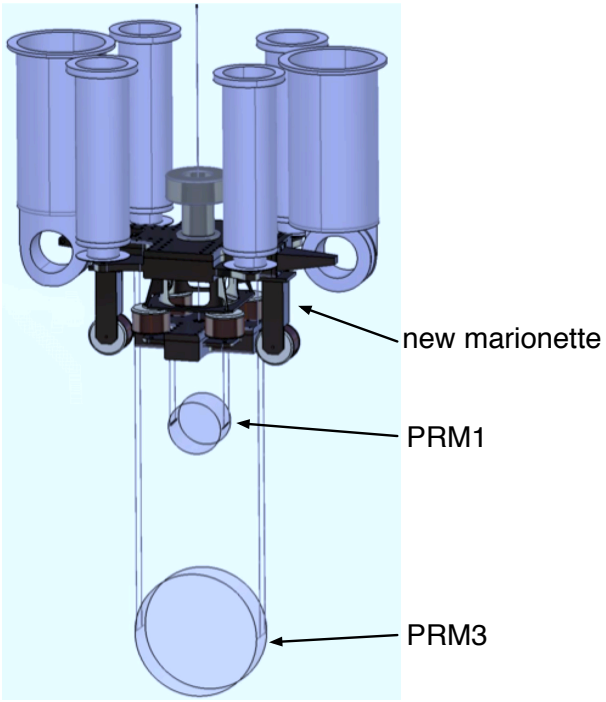

Figure 6.20: Design of the Superattenuator PRM1-PRM3 payload for the *vertical* layout, from [110].

beam parameter	x (tangential)	y (sagittal)
$q_{\rm arm}$	$(958.589 + i142.239)$m	$(963.285 + i125.731)$m
q_1	$(-1.360 + i0.833)$m	$(-1.492 + i0.751)$m
Φ_G	26.3 deg	22.1 deg
w on PRM1	1.0 mm	1.1 mm

Table 6.13: Eigenmode parameters in the *vertical* layout.

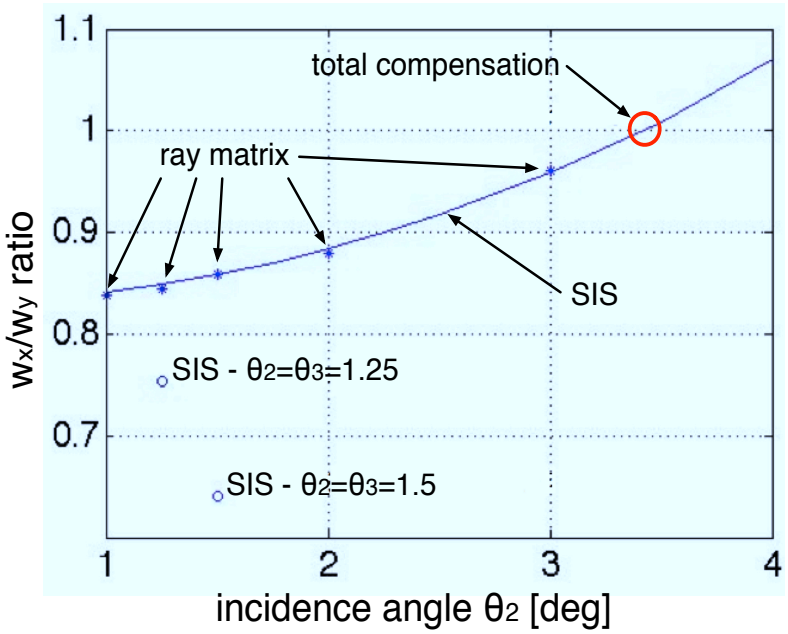

Figure 6.21: Simulation of astigmatism of radio-frequency sidebands in the *vertical* layout: the plot shows the ratio w_x/w_y versus θ_2, computed for $\theta_3 = 1$ deg with the ray-matrix code (stars) and SIS (blue curve), and for $\theta_3 = 1.25$ deg and $\theta_3 = 1.5$ deg with SIS (empty circles), from [107].

layout are summarized in table 6.12, and the parameters of the recycling cavity eigenmode are listed in table 6.13.

The stability plot of this configuration is shown on fig.6.22, the coupling coefficient for the sideband is $\gamma^2_{\text{input}} = 99.8\%$, also confirmed by SIS. The loss of the carrier, computed with SIS, are 0.1%. These results confirm that the impact of the astigmatism is negligible in this layout.

Tolerances and tuning

Tolerances are of the same order of magnitude of those of the *baseline* layout, as shown by table 6.14: R_3 is the most critical parameter, and its tolerance is smaller than the achievable manufacturing accuracy (0.1%). In presence of RoC errors for R_3, the matching of the cavity could be recovered by adjusting the lever arm of the telescope, as indicated by the plot of fig.6.23: an error of +1.5 cm (corresponding to an error of about +0.1 %, yielding an unstable recycling cavity) could be compensated by adjusting L_2 about +7 mm (corresponding to a variation of about +0.1 %). This tuning should be achieved by moving the top stage of the inverted pendulum of the Superattenuator of PRM2, which has a dynamics of only ±4 mm.

Moreover, the need of keeping the recycling cavity length constant after the tuning of the telescope requires a larger dynamics. Since PRM3 and PRM1 are suspended from the same Superattenuator, in fact, the mode-matching of the cavity requires two steps [111]:

- PRM2 is moved of ΔL to tune the arm lever L_2
- all the recycling mirrors (PRM1, PRM2, PRM3) are moved together by a length $2\Delta L$ in the same direction than in the previous step.

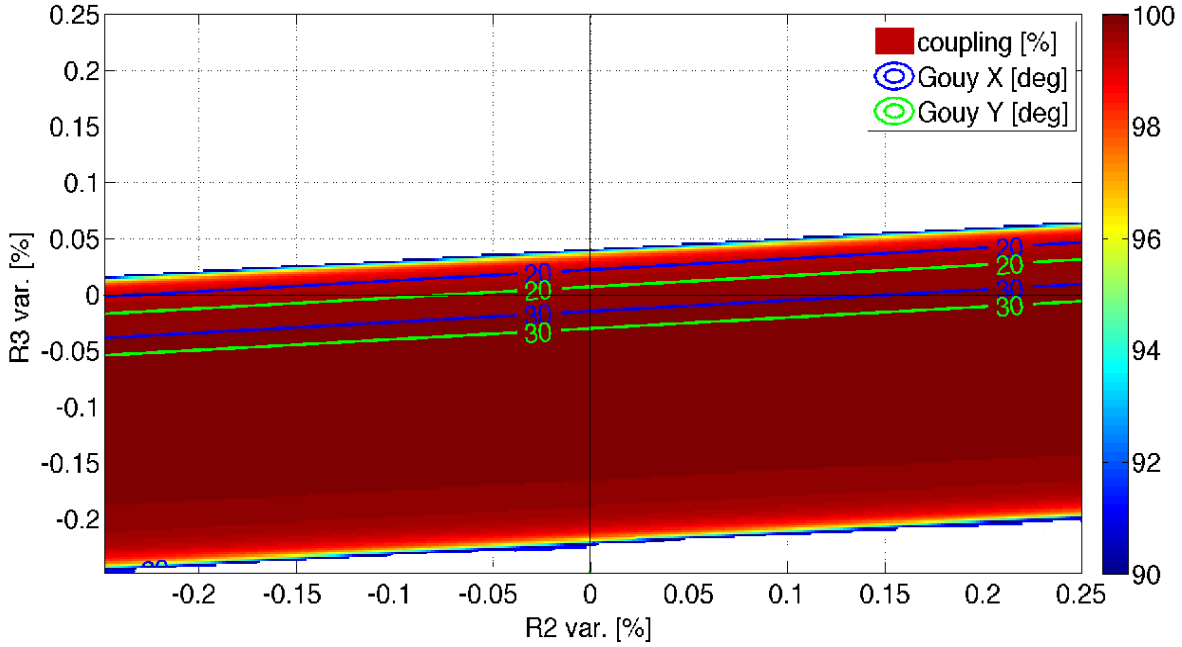

Figure 6.22: Stability plot of the *vertical* layout, γ^2_{input} versus $\{R_3, R_2\}$.

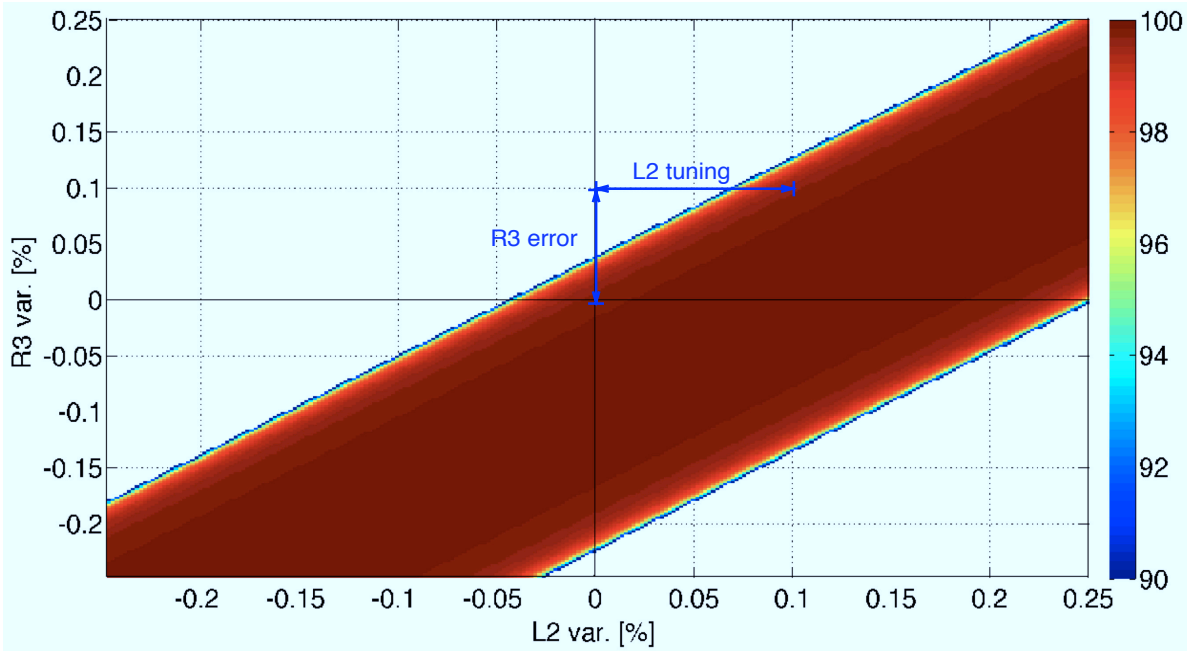

Figure 6.23: Tuning of the lever arm L_2 in the *vertical* layout.

parameter	tolerance [%]
L_3/L_x	$\pm$ 100
L_2	$\pm$ 0.04
L_1	$\pm$ 4.6
R_3	$\pm$ 0.04
R_2	$\pm$ 0.4
$R1$	$\pm$ 17

Table 6.14: Tolerance of parameters for a stable *vertical* layout.

Thus finally PRM2 has to be moved of $3\Delta L$, and PRM1 and PRM3 have to be moved of $2\Delta L$ each. If $\Delta L = 7$ mm, the displacements required for the suspension of each recycling mirror becomes larger than 1 cm. To solve this issue we can measure the RoC of PRM3 with great accuracy, in order to realize the pre-positioning of the suspension system before the installation of the mirror.

The RoC of PRM3 can be measured with 0.01% precision [112], corresponding to a tuning of the telescope length of ~ 1 mm. Nevertheless, the pre-positioning of the vacuum tanks is precise to 1mm, and the pre-positioning of the Superattenuator inside the tank (measured at the top stage of the inverted pendulum) can be achieved within 2 mm accuracy [112]. Therefore the pre-positioning could not be achieved with an accuracy smaller than $\Delta L \sim 3$ mm. Knowing that PRM2 has to be displaced of $3\Delta L$, we can see that the needed adjustment is once again beyond the inverted pendulum dynamics.

The tuning of the cavity mode-matching should be achieved with another actuator than the inverted pendulum. Two solutions have been studied in parallel: we might either use mechanical actuators, or act with the thermal compensation system to change the RoC of PRM3.

Tuning - mechanical actuation

The mechanical actuators could be hydraulic jacks placed below the vacuum tanks. Their dynamics is of the order of ~ 4 cm [112] with an accuracy of the order of ~ 0.5 mm [113], with mirrors and suspensions mounted in the vacuum tanks. However, it is not clear whether with this kind of actuators the vacuum tanks should be vented for safety reasons before moving.

Tuning - thermal actuation

The control of the RoC of PRM3 with the thermal compensation system could be realized with several different actuators [114]. In order to increase the RoC, a central heating pattern could be shined on the high-reflectivity surface, either with a CO_2 laser or with an infrared source. For the CO_2 laser, for instance, reasonable dynamics would be needed: a beam with 2 cm radius could increase the RoC of PRM3 of 0.5% (5 times the achievable RoC manufacturing error for this mirror) by shining 5 W on the mirror, 14 W would be needed to increase the RoC of the same amount with a beam of 6-cm radius [114]. The RoC could be increased also by shining an annular heating pattern (achievable either with a ring heater, a CO_2 laser or an infrared source) on the high-reflectivity surface of the mirror, but in this case the dynamics of the actuation would be too low, requiring too much power [114].

In order to decrease the RoC, an annular heating pattern could be shined on the back of the mirror (provided by a ring heater, or a CO_2 laser or an infrared source), or a ring heater could heat the lateral surface of the mirror. Both options could decrease the RoC of PRM3 of 0.5% requiring ~ 5 W [114], which is a reasonable amount of power.

The use of thermal actuators will induce residual mirror figure errors, whose impact on the matching of the cavity should be studied with SIS. Also the allowed level of astigmatism induced by the thermal actuators should be studied. This will be the subject of future study.

Pick-off extraction

The *vertical* layout allows the simple extraction of four pick-off beams[3]: two beams can be extracted in transmission through P/S-RM2, where the beam has a radius $w = 5.5$ mm. The hardware for the detection of pick-offs will be installed in vacuum, and will require the construction of two small vacuum enclosures beside the tank of power (signal) recycling.

Issues of the *vertical* layout

The *vertical* layout has several advantages, which led us to retain this configuration. It solves the problem of multiple mirrors suspension, limiting the infrastructure works to the construction of several new vacuum chambers. Because of the astigmatism optimization, the losses for the carrier and the radio-frequency sidebands are negligible.

Nevertheless, this layout also features two critical points. The first is the increase of cost due to the construction of vacuum chambers. The second critical factor is the time required for developing and testing the vertical double-mirror payload, which may delay the schedule of the project.

6.3 Simulation of the *Vertical* Layout

The *vertical* layout was extensively simulated with SIS, in order to study its optical performances with respect to realistic mirror defects in the coupled cavities of arm and power recycling. We simulated the carrier and the radio-frequency sidebands to measure the recycling gain and the higher-order mode content of the resonating fields. We did not include in the simulation also the audio-sideband fields, thus this will be the subject of future study.

However, given the low astigmatism of the *vertical* layout and since the audio-frequency sidebands resonate in the signal recycling cavity and partially in the arm cavity, we reasonably expect the audio-frequency sidebands to show an intermediate loss between the one of the carrier and the one of radio-frequency sidebands.

By applying phase maps of residual optical path on the surface of the arm cavity input mirror, we simulated two different kinds of mirror defects. In one case we simulated the response of the coupled cavities in presence of substrate index inhomogeneities (*cold defects*). In the other case, we simulated the coupled cavities in presence of residual thermal effects after compensation (*hot defects*), due to uniform and non-uniform absorption patterns.

[3]The system for the longitudinal and angular control of mirrors requires the extraction of secondary beams, or *pick-offs*, from the beam of the interferometer.

In both cases we simulated the coupled cavities without the beamsplitter, thus the layout is the one shown on fig.5.9d. The cavity parameters used in the simulation are those listed in tables 4.1 and 6.12. We used 1 W for the input beam, to have a direct measurement of the recycling gain through the power resonant in the cavity. The modulation frequency used for the sidebands is $f = 7.47025$ MHz.

Initially we simulated the coupled cavities with perfect optics and null incidence angles, in order to measure the recycling gain in the case of perfect coupling: it is $G_{CARR} = 40$ for the carrier and $G_{SB} = 112$ for the radio-frequency sidebands. Then we included the incidence angles in the simulation, though we can reasonably consider the effect of astigmatism negligible.

Finally we included the defects of the mirror, and we performed the simulations with the following steps:

1. we put the carrier field in resonance with the coupled cavities: this is done in SIS with the command 'lock'. The lengths of the two cavities refer to the 'lock' point

2. we inject the upper and lower sidebands. Because of the presence of defects, the resonance of the sidebands is shifted with respect to that of the carrier

3. we change the length of the recycling cavity to find the resonance of the sidebands, thus we make a scan of the cavity length. The carrier gets out of resonance, but we can neglect this effect since it is always possible to adjust the length of the arm cavity to put the carrier in resonance again. At each step of the scan we compute the resonant power in the coupled cavities, and we measure the recycling gain of the fields

4. we plot the recycling gain versus the scan length, for carrier and sideband fields, and we compare the results with the case of perfect coupling. We also observe the shape of sideband fields at the resonance peak and we measure the fraction of higher-order mode content.

We will present in the following the features of the phase maps we used and the results of our simulations. In our analysis we will also compare the optical performances of non-degenerate cavities with those of marginally-stable cavities, for cold and hot defects. We will see that non-degenerate cavities are much more robust and yield a much better performance.

6.3.1 Cold Defects

For the simulation of cold defects we used a map of substrate index inhomogeneities of an aLIGO mirror, measured at the Laboratoire des Matériaux Avancés (LMA) in Lyon. In the central area (within a radius of 10 cm), the inhomogeneity is about 0.03 ppm peak-valley for a mirror of 20-cm thickness, yielding about 6 nm. The total area of the map is slightly smaller than the actual mirror size (70 cm of diameter), but this has a negligible effect in the simulation.

The scan of the recycling cavity with cold defects is reported on fig.6.25. We can observe that:

carrier the recycling gain is more than 99% of the maximum and the field has a negligible content of higher-order modes

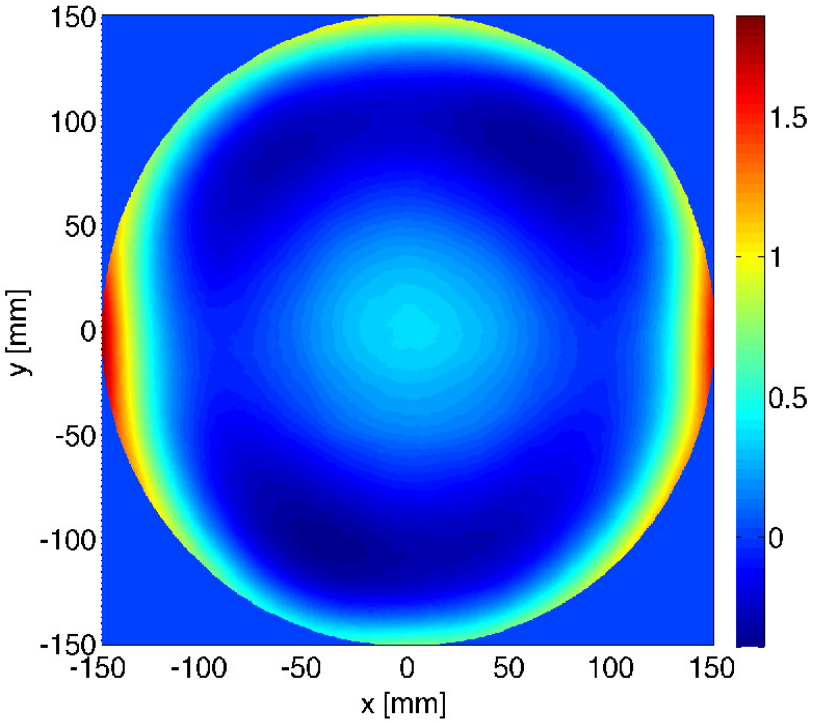

Figure 6.24: Phase map [rad] of substrate inhomogeneities of one arm cavity input mirror of aLIGO.

radio-frequency sidebands the curves of lower and upper sidebands are completely superposed, showing that upper and sideband fields behave exactly the same way (we will see that this is not the case with marginally-stable cavities). The resonance peak indicates a recycling gain of 104, i.e. 93% of the maximum, and is shifted of 1.8 nm with respect to that of the carrier. The normalized intensity pattern at resonance is shown on fig.6.27: it has a Gaussian shape. Its higher-order mode content is $\sim 2.7\%$, whereof 2.5% is due to LG_1^0 mode.

These results indicates that the resonating fields in the non-degenerate recycling cavity are not appreciably affected by the presence of cold defects in the arm cavity input mirror.

Comparison with marginally-stable recycling cavities

We can make a comparison between our results and those of a simulation of the marginally-stable power recycling cavity of AdV, reported in [115]. The comparison can be only qualitative, since the two simulations have some different features: $T = 5\%$ was used for the power recycling mirror of the marginally-stable cavity (yielding a lower finesse), and mirror surface defects were added to the substrate inhomogeneities of fig.6.24. However, the presence of mirror surface defects only had a little influence on the results of the simulation [115].

The simulation of the marginally-stable power recycling cavity and our simulation have been performed with the same steps, therefore we can compare the results of the two cases one by one: the scans of the recycling cavity length, the recycling gain of the resonant fields, the shape of sidebands.

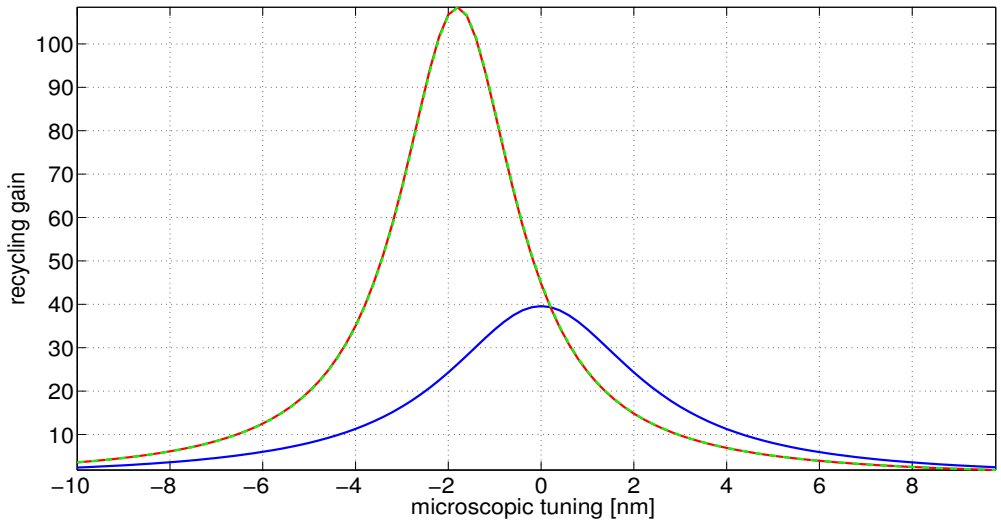

Figure 6.25: Scan of the recycling gain of carrier (blue curve), upper (red curve) and lower sideband field (green dashed curve) in the non-degenerate cavity with cold defects.

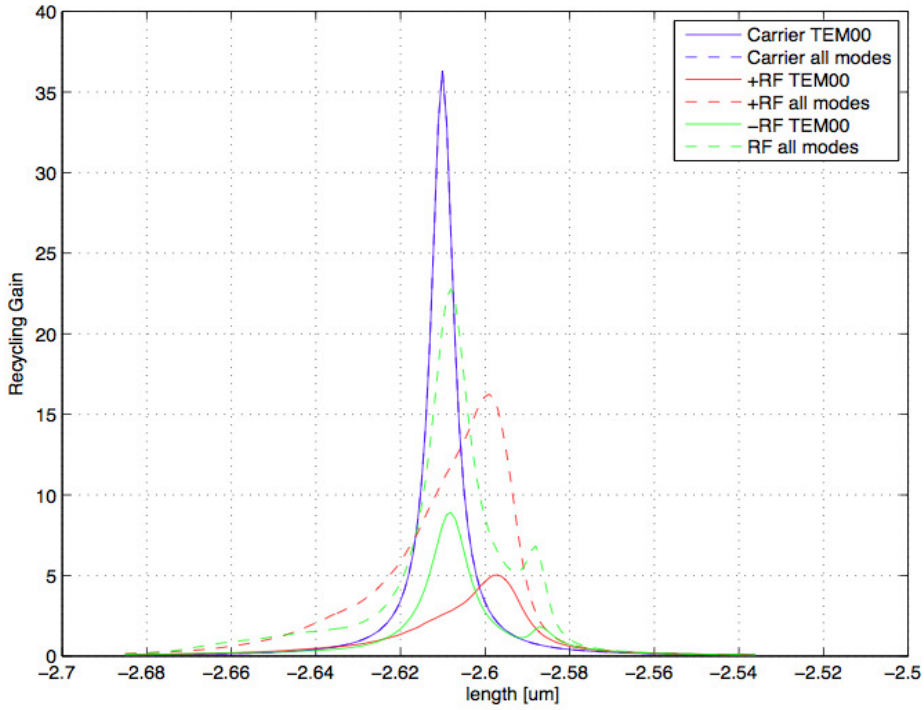

Figure 6.26: Scan of the recycling gain inside the marginally-stable cavity with cold defects, from [115].

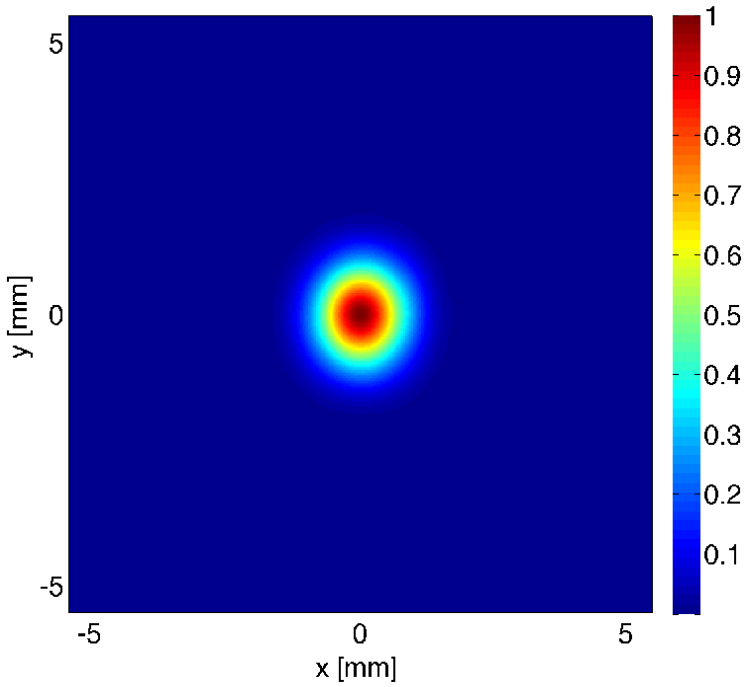

Figure 6.27: Normalized intensity of the upper side-band in the non-degenerate cavity with cold defects.

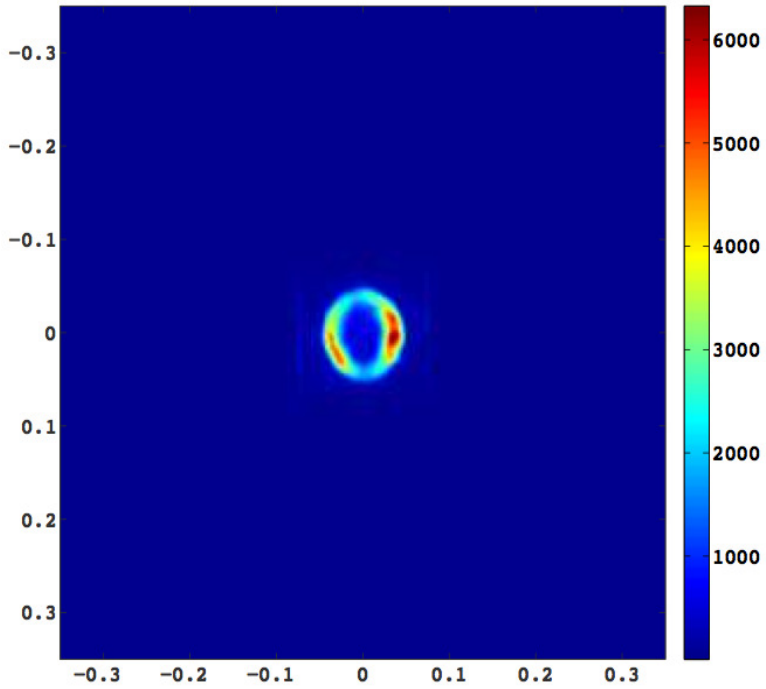

Figure 6.28: Intensity of the upper side-band in the marginally-stable recycling cavity with cold defects, from [115]. Units on the axes are [m].

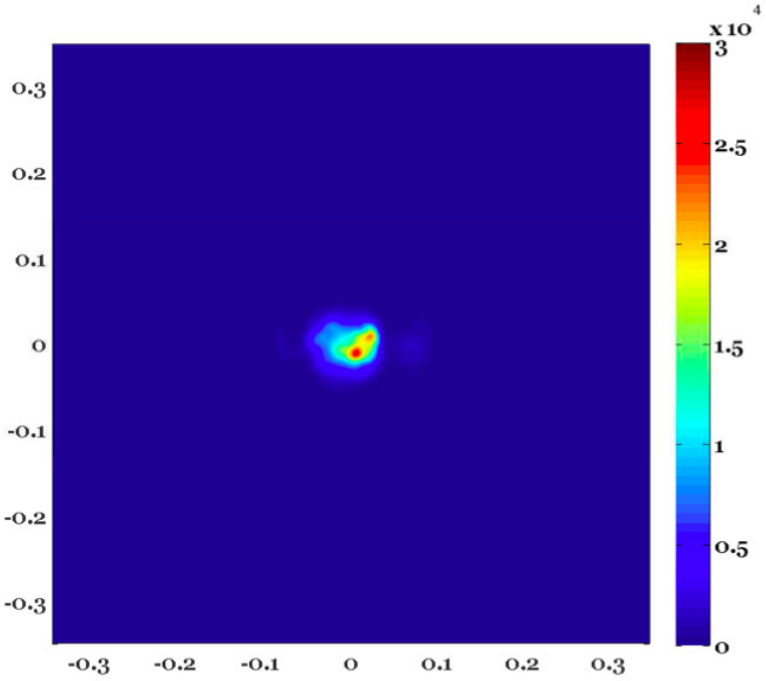

Figure 6.29: Intensity of the lower side-band in the marginally-stable recycling cavity with cold defects, with the annular heating pattern applied. From [116], units on the axes are [m].

Fig.6.26 shows the scan of the marginally-stable cavity (the scale of the axes is different from that of fig.6.25):

carrier the recycling gain is more than the 99% of the maximum, which is $G_{CARR} = 36$, thus losses are negligible

radio-frequency sidebands the degradation is much larger than in the case of non-degenerate cavities. The losses in the TEM_{00} mode are around 90% (the maximum gain being 77), whereof only 15% is due to the presence of surface defects. The two sidebands behave very differently, their resonances show some structures and their TEM_{00} content is reduced to a minor fraction. Fig.6.28 shows the shape of the upper sideband at resonance: the Gaussian pattern is almost totally lost.

The results of the comparison between the non-degenerate and the marginally-stable cavities are summarized in table 6.15.

The impact of substrate inhomogeneities is so relevant that marginally-stable cavities will need the thermal compensation system to compensate also for the cold defects of the interferometer. The use of the annular heating pattern will improve the shape of sidebands, as shown on fig.6.29, and will decrease the loss of their recycling gain to $\sim 45\%$ [116].

In order to achieve a further improvement of the recycling gain and shape of the sidebands, a non-axisymmetric thermal compensation system for the correction of asymmetric defects will be necessary, and is currently under study [117].

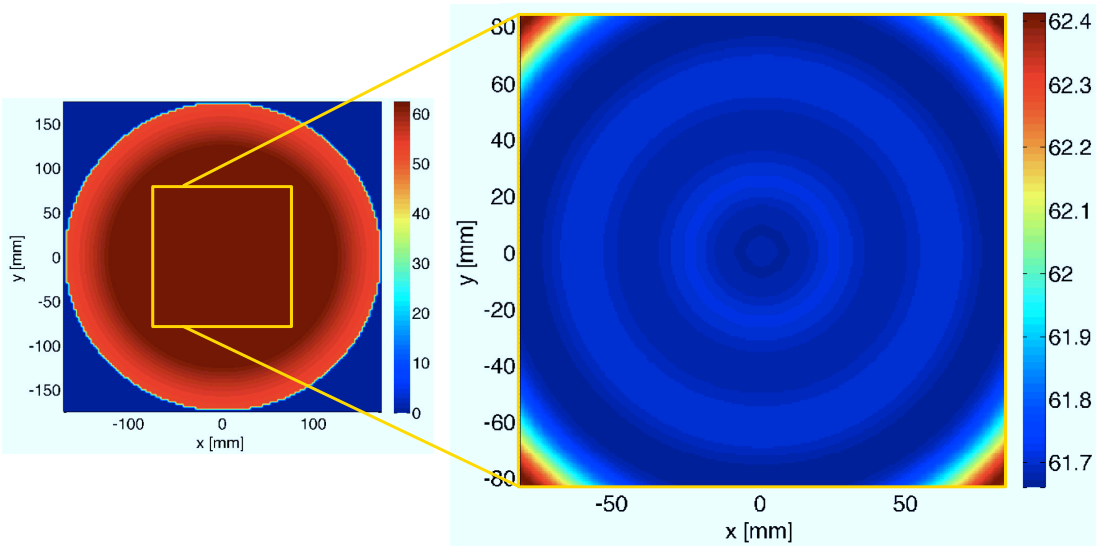

Figure 6.30: Phase map [rad]of residual thermal effects from uniform absorption.

With cold defects it will not be possible to sense the wavefront distortions with a Hartmann sensor, since substrate inhomogeneities cause the aberration of the reference wavefront used for the measure. Thus another wavefront sensor, like the phase camera, will have to be used.

6.3.2 Hot Defects

We used two phase maps provided by the TCS group of Virgo of Università di Roma Tor Vergata, to simulate hot defects. Maps have been computed through simulations of thermal effects performed with ANSYS [118] (a code for finite element analysis), assuming the interferometer running with 125 W of input power.

The group simulated two patterns of absorption: the first is uniform, the second is produced from a real measurement of absorption of an aLIGO mirror (performed at LMA). In both cases the annular heating pattern (generated by the double-axicon system of fig.4.5) has been applied to compensate for thermal effects. Therefore the maps we used in our simulations represent the optical path due to *residual* thermal effects. We will present in the following the results concerning the two cases of hot defects.

We will also compare our results with those reported in [119], where the same hot defects have been simulated in a marginally-stable power recycling cavity with recycling mirror transmission $T = 1\%$. The sensitivity of marginally-stable cavities to hot defects depends on this parameter: the higher is the cavity finesse, the the larger is the impact of the defects[4]. Therefore the comparison will be qualitative. Even though the simulated configurations are different, the conclusions will remain the same: as we will see, the non-degenerate cavities achieve better performances than the marginally-stable cavities.

[4]For this reason, the reference value of the transmission of the power recycling mirror has been presently increased to $T = 5\%$.

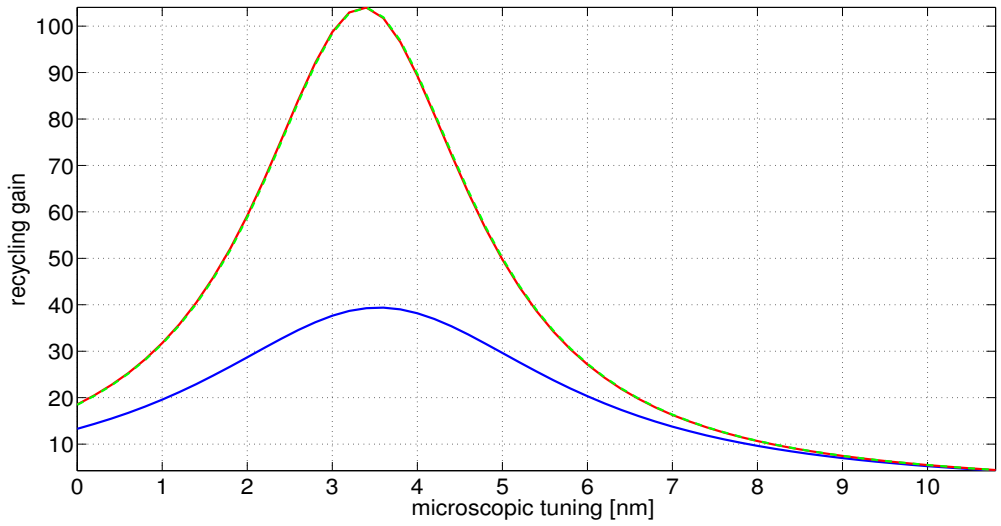

Figure 6.31: Scan of the recycling gain of carrier of carrier (blue curve), upper (red curve) and lower sideband field (green dashed curve) in the non-degenerate cavity with hot defects from uniform absorption.

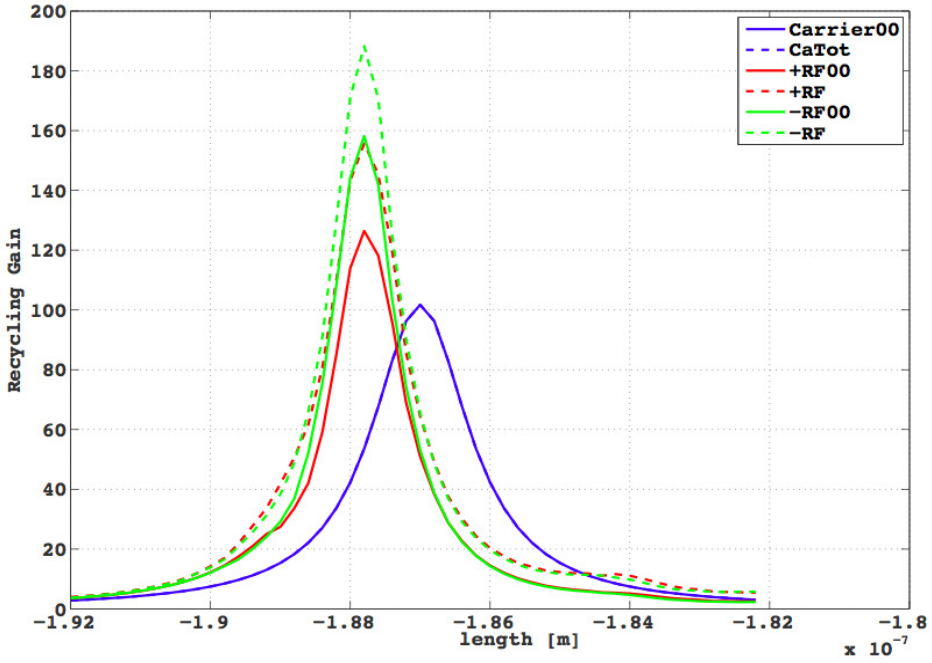

Figure 6.32: Scan of the recycling gain inside the marginally-stable cavity with hot defects from uniform absorption, from [119].

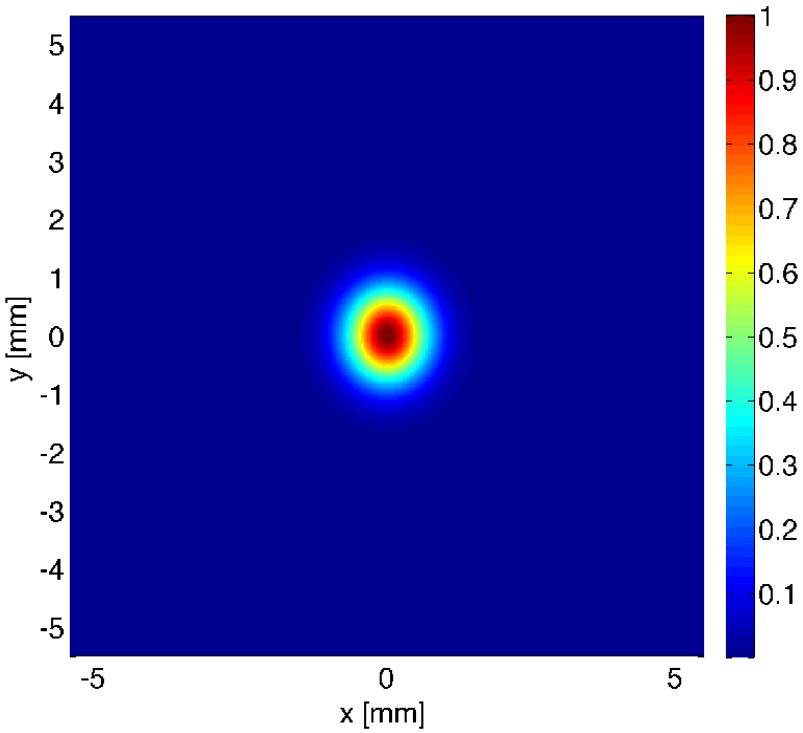

Figure 6.33: Normalized intensity of the upper side-band in the non-degenerate cavity with hot defects from uniform absorption.

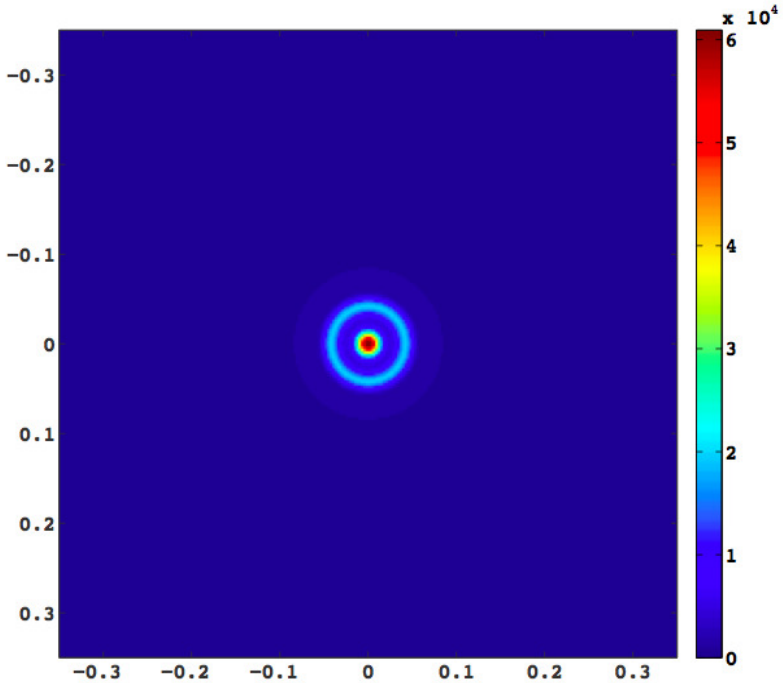

Figure 6.34: Intensity of the upper side-band in the marginally-stable recycling cavity with hot defects from uniform absorption, from [119]. Units on the axes are [m].

Uniform absorption

Fig.6.30 shows the phase map computed in the case of uniform absorption of 0.6 ppm, which then has a radial symmetry.

The scan of the recycling cavity length is shown on fig6.31. We can observe that

carrier the recycling gain is higher than 99%, and the content of higher-order modes is less than 0.5%

radio-frequency sidebands the behavior of the upper and lower sidebands is the same, the recycling gain is 93%. The resonances of sidebands and carrier are spaced of 0.2 nm. The shape of sidebands is illustrated on fig.6.33: they have a Gaussian shape. The higher-order mode content is less than 0.5%.

The results of the simulation indicate that the residual thermal effects due to a uniform absorption pattern do not affect considerably the fields resonating in the non-degenerate cavity.

Uniform absorption - comparison with marginally-stable recycling cavities

Fig.6.32 shows the results of the simulation of the same hot defects due to uniform thermal absorption in the marginally-stable power recycling cavity [119]:

carrier the recycling gain is higher than 99% of the maximum, which is $G_{CARR} = 100$

radio-frequency sidebands the recycling gain is 58% of the maximum, which is $G_{SB} = 380$. The 19% and 16% of the resonant power is transferred to higher-order modes for upper and lower sideband, respectively. The shape of sidebands is degraded, as shown by fig.6.34.

As expected, the behavior of non-degenerate cavities is better than that of marginally stable cavities, which show a degradation of sidebands in presence of axisymmetric hot defects. The results of the comparison are summarized in table 6.15.

Non-uniform absorption

The map used in the simulation of non-uniform hot defects is shown on fig.6.35. It has been obtained from a measured absorption map of 0.57 ppm average level, with two point absorbers of 1.4 ppm and 1.9 ppm [120].

The scan of the recycling cavity length is reported in fig.6.36:

carrier the recycling gain larger than 99% of the maximum, the higher-order mode content is negligible

radio-frequency sidebands upper and lower sideband behave equally, and their resonance is spaced of 0.4 nm from that of the carrier. The recycling gain is 103, equal to the 92% of the maximum, and their higher-order mode content is less than 0.8%. The shape at resonance is that of a pure Gaussian mode.

Therefore we can conclude that the carrier and the sideband fields resonating in the non-degenerate cavity are not appreciably affected by the presence of non-uniform residual thermal effects.

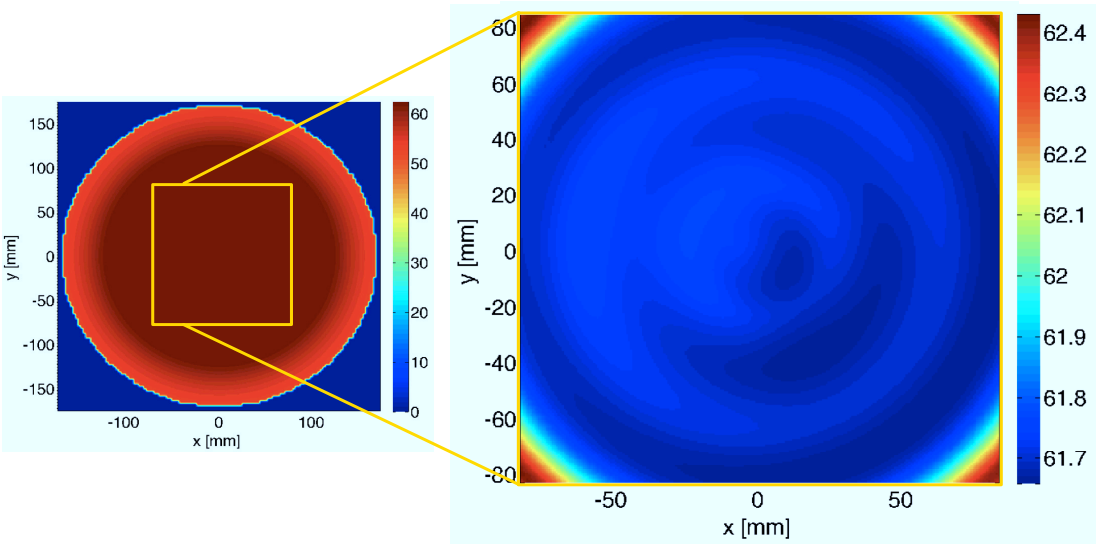

Figure 6.35: Phase map [rad] of residual thermal effects from non-uniform absorption.

Non-uniform absorption - comparison with marginally-stable recycling cavities

The same non-uniform hot defects have been simulated in the marginally-stable power recycling cavity [119]. The scan of the cavity length is reported in fig.6.36, where we can see that

carrier the recycling gain larger than 99% of the maximum, which is $G_{CARR} = 100$

radio-frequency sidebands the Gaussian mode of upper and lower sideband is almost disappeared due to the 96% of loss of recycling gain (the maximum being $G_{SB} = 380$).

Thus also in the case of hot defects due to non-uniform absorption, we can conclude that the optical performances of non-degenerate cavities are much better than those of marginally-stable cavities. The results are summarized in table 6.15.

The results of the simulations with hot defects indicate that non-degenerate cavities will work properly with 125 W of input power and with the axisymmetric heating pattern of the thermal compensation system, for any kind of absorption pattern in the arm cavity input mirror. Marginally-stable cavities instead, will require the implementation of a non-axisymmetric thermal compensation system to work with the same input power, in presence of a non-uniform absorption pattern in the arm cavity input mirrors.

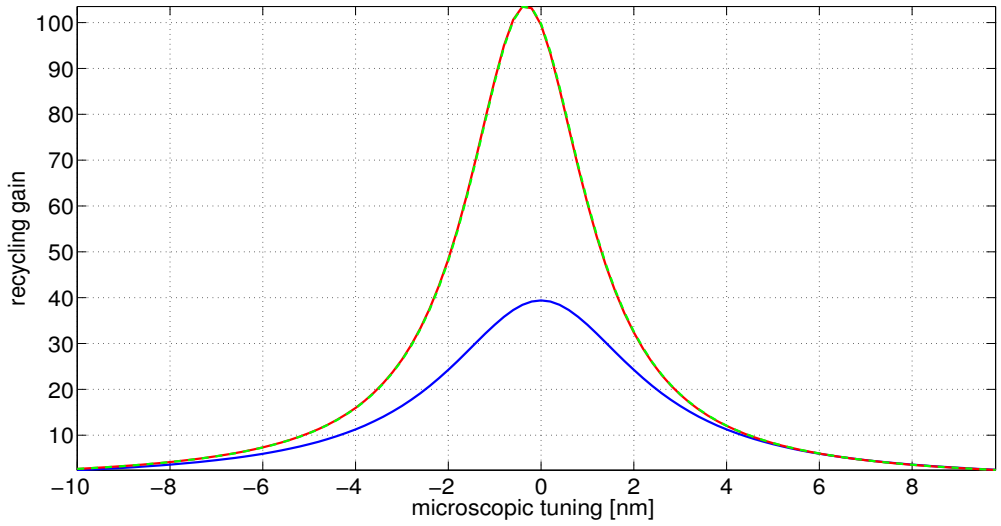

Figure 6.36: Recycling gain of carrier (blue curve), upper (red curve) and lower sideband field (green dashed curve) in the non-degenerate cavity with hot defects from non-uniform absorption.

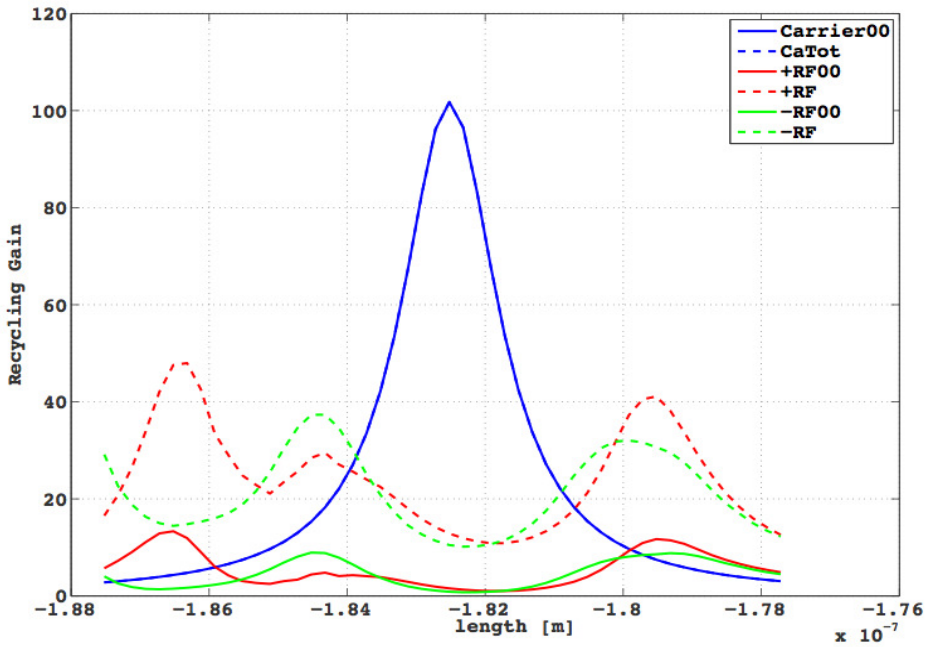

Figure 6.37: Recycling gain inside the marginally-stable cavity with hot defects from non-uniform absorption, from [119].

defect/configuration	recycling gain [%]	higher-order modes [%]
cold defects/NDRC	93%	2.7
cold defects/MSRC	10%	–
uniform hot defects/NDRC	93%	< 0.5
uniform hot defects/MSRC	42%	upper s.b. 19% / lower s.b. 16%
non-unif. hot defects/NDRC	92%	< 0.8
non-unif. hot defects/MSRC	4%	–

Table 6.15: Comparison of simulation results for the radio-frequency sidebands: non-degenerate recycling cavities (NDRC) versus marginally-stable recycling cavities (MSRC, from [115, 119]).

Conclusions and Perspectives - Part I

The experience with initial Virgo and Ligo showed that higher-order mode contamination in marginally-stable cavities can considerably affect the operation of the detector, slowing down the commissioning phase and making the control complex and difficult.

The issue of mode degeneracy will be even more relevant for advanced detectors, where the increase of the beam size on the arm cavity mirrors will be necessary to decrease mirror thermal noise, which will be one of the major noise sources. Moreover, due to the implementation of signal recycling, mode degeneracy will also cause a loss of signal of potential detections.

In order to remove mode degeneracy, the implementation of non-degenerate recycling cavities (proposed by aLIGO as first [93, 94]) was adopted in AdV as reference solution [69].

The achievement of the optical design of the non-degenerate recycling cavities of AdV took about two years and a half, starting in fall 2008, and required several steps:

- initially we studied the general features of non-degenerate cavities (Gouy phase and beam focusing), and we confirmed the design originally proposed by aLIGO, featuring a folded optical path with three mirrors. Two of these mirrors form a telescope for the focusing and the collimation of the beam inside the cavity. This design has several advantages:
  - it allows to adjust the distance between the telescope mirrors, in order to tune the mode-matching of the cavity
  - it allows the simple extraction of secondary pick-off beams, since the beam radius attains few mm inside the cavity
  - it simplifies the design of the telescopes of injection and detection systems, which should match a beam radius of the order of 1 mm on the recycling mirrors
  - it allows to use small recycling mirrors which could be easily installed and replaced, if it is necessary or to change the optical parameters of the cavity
- then we studied the implementation of non-degenerate recycling cavities in AdV: the optical design is limited by infrastructure and budget constraints (which are not present in aLIGO, for instance)
- subsequently we developed the optical simulations that we used to draw the design of the cavities. These simulation tools are flexible, so we used them to follow the design process of various layouts
- then we chose a configuration: the choice was determined not only by the optics requirements, but also by those of the mirror suspension system

- finally we characterized the performances of the chosen design by means of optical simulations.

The *vertical* layout

We retained the so-called *vertical* layout, since it requires small changes to the infrastructures of AdV and necessitate a limited re-design of the payload of one Superattenuator. We simulated this configuration with the ray-matrix code and with the FFT code SIS:

- we optimized the astigmatism, reducing the coupling loss to 0.1% for the carrier field and 0.2% for the radio-frequency sideband fields
- we tested its robustness with respect to different classes of mirrors defects, *cold* (substrate index inhomogeneities) and *hot* (residual thermal effects after axisymmetric compensation):
  - the recycling gain of the carrier is beyond 99% of the maximum ($G_{CARR} = 40$) for all the defects that we simulated: the loss is always negligible, as well as the higher-order mode content
  - the recycling gain of radio-frequency sidebands is larger than 90% of the maximum ($G_{SB} = 112$) for all the defects, and the higher-order mode content is always negligible:
    - with cold defects the gain is 93% and the higher-order mode content is $\sim 2.7\%$
    - with hot defects due to uniform absorption the gain is 93%, and the higher-order mode content is less than 0.5%
    - with hot defects due to non-uniform absorption the gain is 92%, and the higher-order mode content is less than 0.8%.

    we did not simulate the audio-frequency sidebands of the signal, but we reasonably expect them to show an intermediate behavior between those of the carrier and the radio-frequency sidebands.

The results show that our design is robust and achieves good optical performances with respect to cold and hot mirror defects.

However, the *vertical* layout incurs some budget and schedule risks, related to the infrastructure works and to the development of the vertical payload for the double-mirror suspension. Furthermore, the achievement of an optimal axisymmetric compensation pattern (realized with the double-axicon system) for the thermal compensation system led in the spring of 2011 to reconsider the choice of marginally-stable cavities for AdV.

Perspectives

The implementation of marginally-stable cavities will require a solution for two crucial issues. The first is the extraction of pick-off beams for purposes of sensing and control, since the beam has a radius of several cm everywhere in the marginally-stable cavities. The second concerns cold and hot defects in the mirror.

Later analysis [115, 119] demonstrated that marginally-stable cavities will be highly sensitive to substrate index inhomogeneities and non-uniform coating absorption, which will yield significant sideband degradation. For this reason the development and the implementation of a non-axisymmetric thermal compensation system will be necessary for the detector operation [117].

Though non-degenerate cavities will not be implemented in AdV, we believe that they still might be part of a possible upgrade of the project, and that the optical design of third-generation detectors may benefit of the studies developed in this work.

PART III

Use of Higher-Order Laguerre-Gauss Modes in Future Gravitational-Wave Interferometers

Chapter 7

Reduction of Mirror Thermal Noise with Laguerre-Gauss Modes

Mirror thermal noise is expected to dominate the thermal noise spectrum in the mid-frequency range of all currently planned terrestrial detectors. Its reduction is of fundamental importance to improve the sensitivity of the second-generation detectors (and to operate what are sometimes called 2.5-generation detectors), and to build the third-generation detectors as ET.

The spectral density of mirror thermal noise shows a clear dependence on temperature, material properties and read-out beam spot size. Several technical solutions may thus be adopted for its reduction:

- the cooling of mirrors using cryogenics
- the choice of materials with good mechanical properties, for coatings and substrates
- the increase of the beam size on mirrors
- the reduction of the coupling of the laser beam with thermal noise fluctuations, using larger or non-Gaussian beams

These solutions are not mutually exclusive in principle, and might be used jointly to reduce mirror thermal noise. In section 7.1 of this chapter we will describe the solutions to decrease thermal noise with better materials and cryogenics, pointing out the possible difficulties. In the same section we will describe the limitations related to the increase of the beam size.

The option of using flat and wide non-Gaussian readout beams had been initially suggested for so-called *mesa* or *flat-top* beams, and later on *conical* beams had been proposed as the optimal beam shape for maximum coating thermal noise reduction. The main inconvenient of mesa and conical beams is that they resonate in cavities with non-spherical mirrors.

Higher-order LG_p^ℓ modes have been proposed in 2006 in alternative to mesa beams. Being solutions of the paraxial wave equation, the LG_p^ℓ modes are eigenmodes of spherical-mirror resonators. Thus from the technical point of view, LG_p^ℓ beams are more appealing since their implementation in gravitational-wave interferometers is in principle simpler.

Analytical calculations indicate that LG_3^3 modes might decrease mirror thermal noise of a factor 1.76 in AdV and 1.83 in ET-HF, using the same mirrors. The reason of this decrease lies in the wider geometry of these beams, which averages out the fluctuations of the mirror surface, due to

thermal noise, better than Gaussian beams do. LG_p^ℓ beams have also an additional advantage: they are expected to induce smaller thermal effects in mirrors, compared to those induced by the currently used Gaussian intensity pattern.

Some fundamental aspects have to be studied before LG_p^ℓ beams could be used in km-scale interferometers. Topics to be addressed are the generation of LG_p^ℓ beams and their optical performances in power-recycled Fabry-Perot interferometers. We need to analyze the feasibility of higher-order LG_p^ℓ beams interferometry by studying the achievable contrast of an LG_p^ℓ detector, the compatibility of LG_p^ℓ beams with the control scheme of gravitational-wave interferometers (for example with respect to the extraction of longitudinal and angular error signals of mirror position), and the tolerance of LG_p^ℓ beams to mirror misalignments and figure errors.

Studies on these subjects must be carried out by means of an experimental table-top setup and of optical simulations of real detectors (with realistic control schemes, defects of optics, etc.). In the next chapter we will address some of these fundamental questions going through the results of a dedicated experimental setup.

7.1 Techniques to Reduce Mirror Thermal Noise

Cryogenics

The linear spectral density of mirror thermal noise has a twofold dependence on temperature, through the fluctuation-dissipation theorem: its $\sqrt{T}$ dependence is determined by the thermal energy of the system, and it is function of the mechanical properties of materials which can largely vary with the temperature. If mirrors can be made of a material with low mechanical dissipation at low temperature, cryogenics is one of the most appealing technologies to reduce thermal noise.

However, the fundamental technical issue to be solved in a cryogenic gravitational-wave interferometer is how to cool down the mirrors without introducing additional vibrations that would spoil the low-frequency part of the detection band. Mirrors and suspensions are isolated in vacuum enclosures, where the heat of the laser power absorbed by the optics cannot be evacuated neither by convection of air nor by irradiation. Heat can only be extracted through mechanical-thermal links between the mirror last suspension stage and the cold reservoir, which is usually a vibrating pulse-tube cryostat. Therefore cryogenics is technologically challenging.

So far, it has been tested only in a small-scale detector prototype with no power recycling [121], thus with reduced circulating power. Among the second-generation detectors, only LCGT [70] will make use of cryogenics, testing for the first time its application to a kilometer-scale power recycled interferometer. The use of cryogenics seems unlikely for the upgrade of advanced detectors (sometimes called 2.5-generation), due to the heavy infrastructures it requires. It is planned for ET-LF, where low power is circulating, whereas ET-HF will be at room temperature [75].

Choice of materials

Currently, all gravitational wave detectors operating at room temperature use fused silica (SiO_2) as optical substrate material, due to a combination of excellent optical, thermal and mechanical properties. Therefore fused silica will be the substrate material also in advanced detectors [68, 69].

However, fused silica is unsuited for cryogenic use, because of its high mechanical loss at low temperature [40]. This is why sapphire has been selected as mirror substrate materials for LCGT [70],

and silicon and sapphire are under investigation as mirror substrate material for third-generation detectors [75]. Both materials feature a high thermal conductivity $\kappa(T)$ and a low thermal expansion coefficient $\alpha(T)$ at low temperature, where sapphire has also low mechanical loss [40].

For what concerns the coating, the reference solution is the use of Ti-doped Ta_2O_5 layers [69, 68]. The mechanical losses of this material are the lowest possible, so far. Several research projects are under development for third-generation detectors, in order to assess the possibility of decreasing further thermal noise with new coating technologies [78].

Beam size

The power spectral density of the substrate and coating Brownian noise is inversely proportional to the beam radius w on optics. Thereby the detector sensitivity increases using a larger beam size on the mirrors of the Fabry-Perot arm cavities. This is the reason why the beam size on the arm cavity mirrors of AdV has been increased with respect to initial Virgo.

However, the beam size on mirrors is limited by the cavity length L, because of the stability condition of the resonator (see eq.(5.15)). Consider for instance the simple case where the RoCs of the cavity mirrors are equal, $R_1 = R_2 \equiv R$. Then the beam size on the mirror is [95]

$$w^4 = \Big(\frac{\lambda}{\pi}\Big)^2 \frac{LR}{2 - L/R} \ , \tag{7.1}$$

and the cavity is stable as long as $R > L/2$. We might choose $R \to \infty$, but the beam size increases slowly with respect to the RoC, thus it is very difficult to have large beams with very large RoCs. For example, if we take $L = 3$ km like in the case of AdV, we should choose $R = 25$ km only to get $w = 4.6$ cm. Furthermore, for too large RoCs we would start also to have problems of degeneracy: the frequency spacing of higher-order modes (see eq.(5.21)),

$$\Delta\nu = \nu_0 \frac{\Delta N}{\pi} \cos^{-1}(1 - L/R) \ , \tag{7.2}$$

decreases as R increases.

Otherwise the beam size can be increased by taking $R \to L/2$, but then the cavity gets close to instability: we have to choose R with some safety margin, and the beam size is limited. Thereby the reference design of Fabry-Perot arm cavities in advanced and third-generation detectors is a trade-off between the need of increasing the beam size on mirrors and the proximity to cavity instability. Of course, as the mirror size increases, the technical difficulties in their realization (quality of the surface, coating, etc.) increase as well.

Mesa and conical beams

Mirror thermal noise might be reduced by using mesa beams [122] and conical beams [123]. Historically, mesa beams have been the first to be studied for the purpose of decreasing mirror thermal noise. They are large-radius, flat-topped beams with steep edges to constrain diffraction losses. Mesa beams can be generated by overlapping many narrow Gaussian beams at waist over a circular surface D of radius b:

$$\Psi(x, y, 0) = \frac{A}{\pi b^2} \int_D \exp\Big[- \frac{(x - x_0)^2 + (y - y_0)^2}{w_0^2} \Big] dx_0 dy_0 \ , \tag{7.3}$$

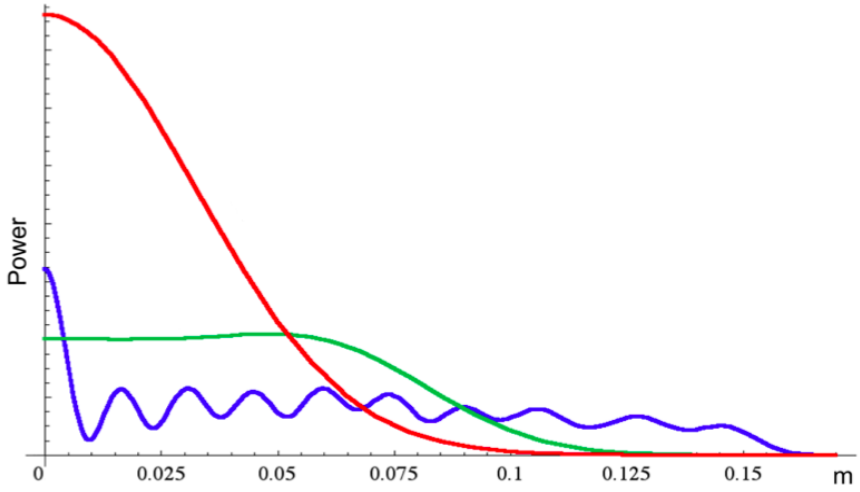

Figure 7.1: Intensity profiles of LG_0^0 (red curve), mesa (green curve) and conical (blue curve) beams versus the radial coordinate r, from [123].

where A is a normalization factor, and $w_0 = \sqrt{L\lambda/2\pi}$ is the optimal waist size for propagation in a cavity of length L [122]. Let $z_R = \pi w_0^2/\lambda$ be the Rayleigh range of the beam, and z be the propagation distance. By defining $Z \equiv 1 - iz/z_R$, $w = w_0\sqrt{Z\overline{Z}}$ and $r = \sqrt{x^2+y^2}$, the normalized amplitude of a mesa mode propagated over the distance z from waist is [34]

$$\Psi(r,z) = \frac{2Z}{b\sqrt{\pi M}} \int_0^{b/w} \exp\Big[-Z(r/w - x)^2\Big] \exp(-2Zrx/w) I_0(2Zrx/w)\, dx\ , \tag{7.4}$$

where

$$M \equiv 1 - \exp(-b^2/w_0^2)\Big[I_0(b^2/w_0^2) + I_1(b^2/w_0^2)\Big]\ , \tag{7.5}$$

$I_n(x)$ being the modified Bessel functions. The intensity profile of a mesa beam is shown on fig.7.1. These beams resonate in Fabry-Perot cavities with non-spherical mirrors, which have a shallow bump in the middle and a steep outer rim to match the mesa beam wavefront [124].

However, even if mesa beams are expected to provide an effective decrease of mirror thermal noise [34], their implementation in gravitational-wave interferometers presents some issues. As demonstrated experimentally, the alignment tolerances for a mesa-beam cavity are expected to be from 3 to 5 times more stringent than those of spherical resonators in advanced detectors [122, 124].

In a spherical resonator, a tilted mirror induces a shift and a tilt of the optical axis, and the cavity resonates the same transverse-mode spectrum centered on the shifted axis. In contrast, any misalignment of the non-spherical mesa-beam mirrors destroys the cylindrical symmetry of the cavity. In this case the resonant beam senses a mismatching mirror profile, and the cavity mode thus have a radically different intensity distribution and phase front [124]. Moreover, mesa beams are particularly sensitive to mirror imperfections, especially in the central part of the mirror that determines the resonant beam shape [122, 124].

Conical beams are another type of non-Gaussian beam, obtained by computing the optimal beam shape which minimizes mirror thermal noise in a cavity with fixed mirror radius and for

fixed beam diffraction losses [123]. In fact, conical beams are even wider than mesa beams, though maintaining the same diffraction losses and total integrated power intensity. Their intensity profile is shown on fig.7.1: it extends more towards the boundaries of the mirror, but cuts off more sharply at the edge, keeping clipping losses low. The phase front of these beams has a conical shape, like the *Gauss-Bessel beams* of the form [34]

$$\Psi(r,z) = A\exp\Big[-\frac{Z(r^2+\theta^2 z^2)}{w^2(z)}\Big]J_0\Big(\frac{kr\theta}{\overline{Z}}\Big)\ . \tag{7.6}$$

Conical beams are expected to decrease mirror thermal noise even more efficiently than mesa beams [123]. Nevertheless, a Fabry-Perot resonator with conical mirrors is expected to be sensitive to mirror translations, misalignments and figure errors even more than a mesa-beam cavity [123].

7.2 Thermal Noise Reduction with Laguerre-Gauss Modes

LG_p^ℓ modes have been proposed in alternative to mesa and conical beams [125]. For the same mirror diameter and for equivalent diffraction losses and beam power, higher-order LG_p^ℓ beams have a multi-ringed power distribution which is wider than the distribution of the fundamental Gaussian LG_0^0 mode. This is shown on figs.7.2 and 7.3: the first plot compares the intensity cross sections of LG_0^0, LG_3^3 and LG_5^5 modes, the second plot shows the integrated power of these modes as function of the radial coordinate r.

Because of their wider intensity distribution, higher-order LG_p^ℓ modes can decrease the impact of mirror thermal noise on the detector sensitivity. The beam size on optics should however be adapted to limit the diffraction losses: for every given LG_p^ℓ mode of radius w and mirror diameter a, there is a ratio a/w yielding 1 ppm of losses [125], as shown on fig.7.4. For example, for the LG_3^3 mode this ratio is 4.31, for the LG_5^5 mode is 5.05.

The reduction of noise can be estimated by means of the mirror strain energy U_p^ℓ associated to the LG_p^ℓ mode through eq.(2.64). Here we will limit our analysis to the case of substrate and coating brownian noise, in the case of infinite mirrors. This approximation is useful to illustrate in a simple way the decrease of thermal noise, when LG_p^ℓ modes are used. This is also a good approximation when the beam size is much smaller than the radius of the mirror, so that the diffraction losses are negligible. The accurate computation of brownian noise and thermoelastic noise with finite mirrors can be found in [34, 126].

We will describe the approach developed in [34]: for infinite mirrors, the strain energy U_p^ℓ for the substrate is

$$U_p^\ell = \frac{1-\sigma^2}{2\sqrt{\pi}Yw}\Gamma_p^\ell\ , \tag{7.7}$$

with σ and Y being the Poisson ratio and the Young modulus of the substrate material, respectively. Γ_p^ℓ is a numerical factor that comes from the integration of eq.(2.63) and decreases for increasing indices p and ℓ. For example:

$$\begin{aligned}\Gamma_0^0 &= 1\\ \Gamma_3^3 &= 0.31\\ \Gamma_5^5 &= 0.25\ .\end{aligned} \tag{7.8}$$

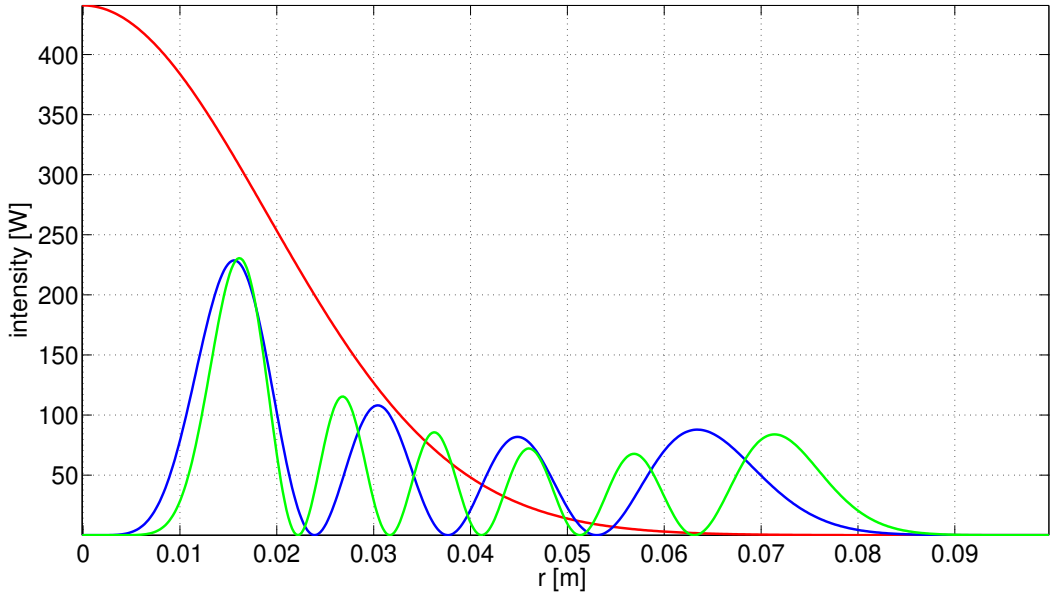

Figure 7.2: Intensity profiles of LG_0^0 (red curve), LG_3^3 (blue curve) and LG_5^5 (green curve) modes versus the radial coordinate r, for a beam power $P = 1$ W and for 1 ppm clipping loss on a mirror with 10-cm radius.

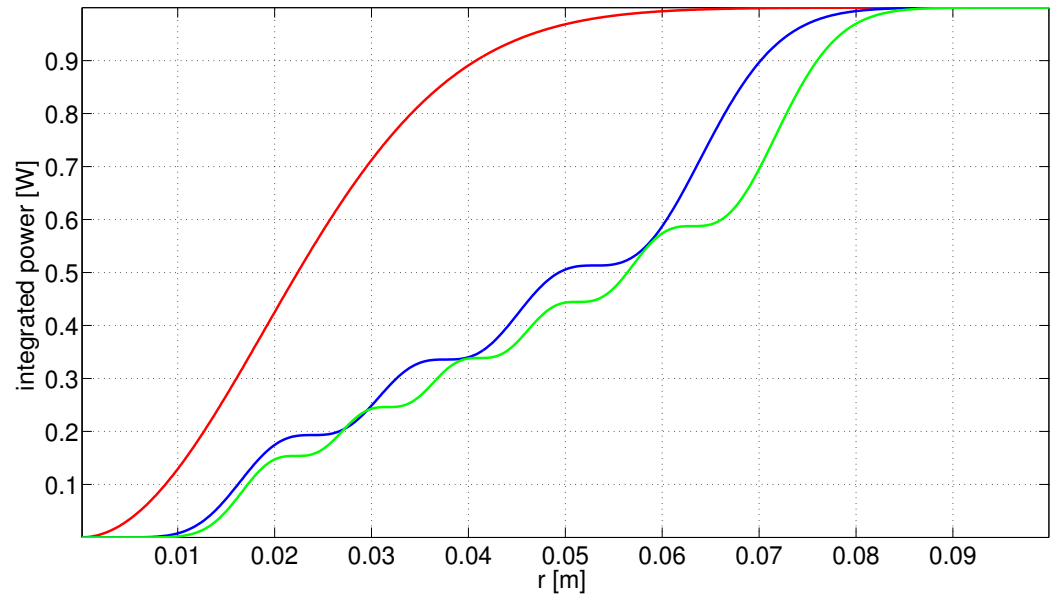

Figure 7.3: Integrated power of the LG_0^0 (red curve), LG_3^3 (blue curve) and LG_5^5 (green curve) modes shown on fig.7.2, versus the radial coordinate r.

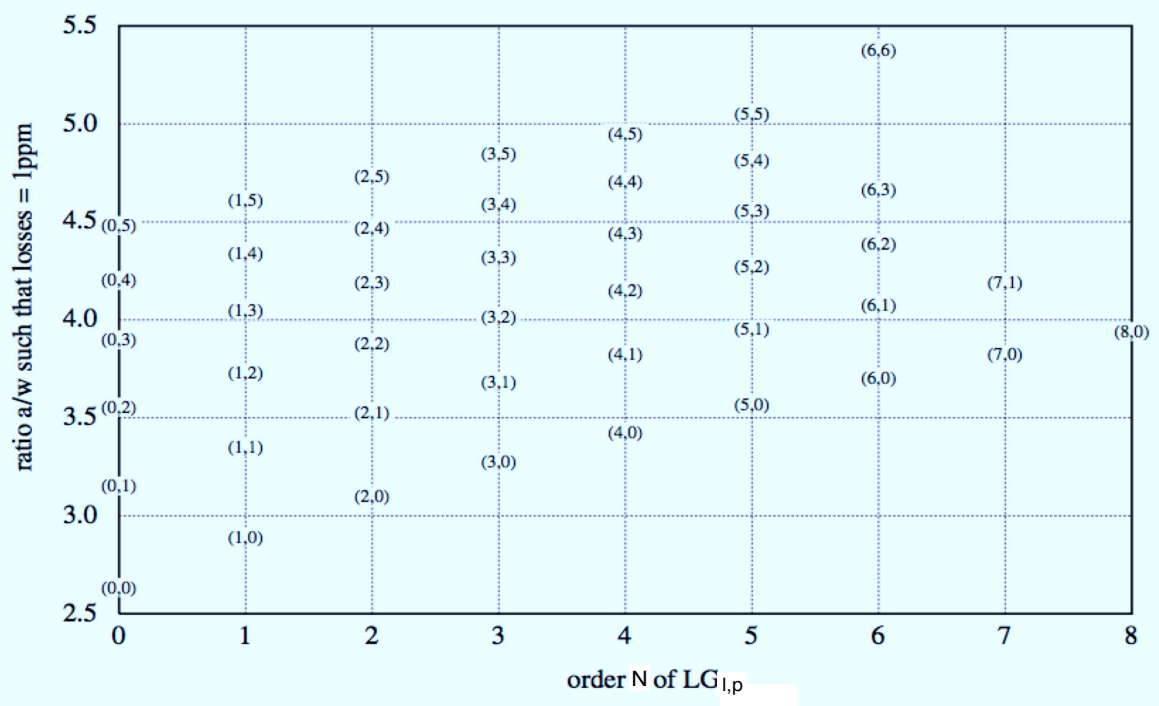

Figure 7.4: Ratio a/w yielding 1 ppm of diffraction losses versus the order of the LG_p^ℓ mode, from [125].

For larger values of p and ℓ, Γ_p^ℓ approaches asymptotically the value $\sqrt{2p+|\ell|+1}$. By replacing eq.(7.7) in eq.(2.64), for the power spectral density of substrate brownian noise we find

$$S_p^\ell(f,T) = \frac{2k_BT(1-\sigma^2)}{\pi^{3/2}Ywf}\phi(f)\ \Gamma_p^\ell\ . \tag{7.9}$$

Thus if we consider an LG_3^3 mode, the linear spectral density of substrate brownian noise is lower by a factor

$$\sqrt{\frac{S_0^0}{S_3^3}} = \sqrt{\frac{\Gamma_0^0}{\Gamma_3^3}} \simeq 1.8\ . \tag{7.10}$$

Similarly, for an infinite mirror, the strain energy U_p^ℓ of a coating layer of thickness l is [34]

$$U_p^\ell = \frac{l(1+\sigma)(1-2\sigma)}{\pi Y w^2}\chi(\sigma,\sigma_c,Y,Y_c)\Lambda_p^\ell\ , \tag{7.11}$$

where

$$\chi \equiv \frac{1-2\sigma_c}{2(1-\sigma_c)}\Big[\frac{Y(1+\sigma_c)}{Y_c(1+\sigma)(1-2\sigma)} + \frac{Y_c(1+\sigma)}{Y(1+\sigma_c)}\Big]\ , \tag{7.12}$$

Y_c, σ_c indicate the material properties of the coating, Λ_p^ℓ is a decreasing numerical factor versus p and ℓ. The first values for Λ_p^ℓ are:

$$\begin{aligned}\Lambda_0^0 &= 1\\ \Lambda_3^3 &= 0.14\\ \Lambda_5^5 &= 0.10\ .\end{aligned} \tag{7.13}$$

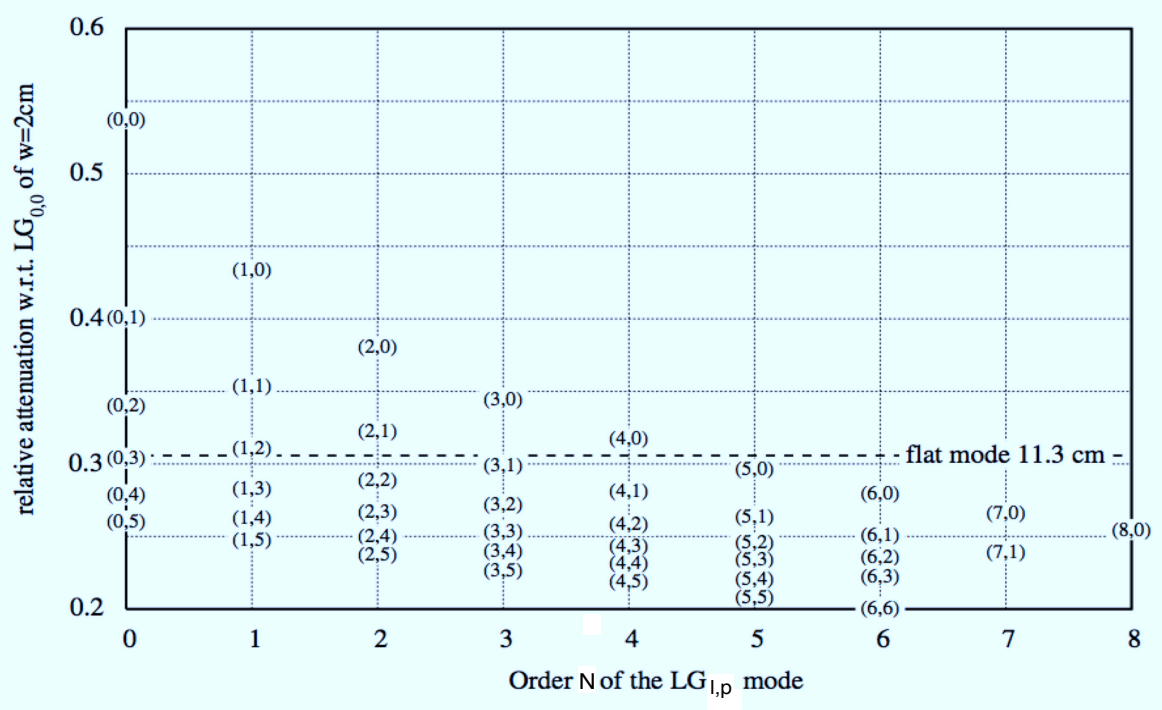

Figure 7.5: Relative reduction of the linear spectral density of mirror thermal noise versus the order of the LG_p^ℓ mode (with w tuned for 1 ppm diffraction losses), with respect to the configuration of the arm cavity input mirror of initial Virgo (LG_0^0 with $w = 2$ cm on a mirror of radius $a = 17.5$ cm and thickness $h = 10$ cm). From [125].

By replacing eq.(7.11) in eq.(2.64), we find

$$S_p^\ell(f,T) = \frac{4k_B T(1+\sigma)(1-2\sigma)l}{\pi^2 Y w^2 f}\chi(\sigma,\sigma_c,Y,Y_c)\phi(f)\ \Lambda_p^\ell\ , \tag{7.14}$$

so that if again we consider an LG_3^3 mode, the coating brownian noise is lowered by a factor

$$\sqrt{\frac{S_0^0}{S_3^3}} = \sqrt{\frac{\Lambda_0^0}{\Lambda_3^3}} \simeq 2.7\ . \tag{7.15}$$

From eqs.(7.7) and (7.11) it is clear that (within the approximation of infinite mirrors) the reduction of mirror brownian noise with LG_p^ℓ modes depends on the order $N = 2p+|\ell|$ of the mode considered. Higher N values lead to larger beams and thus are expected to yield lower thermal noise (fig.7.5).

In case of finite mirrors, the estimation of brownian noise is a complex calculation whose results cannot be expressed with a simple and compact analytical form. We then report here only the results from [126] about the detailed computation of mirror thermal noise decrease with an LG_3^3 beam for finite mirrors, for AdV and ET-HF. We will justify the choice of the LG_3^3 mode in the next chapter. Considering the overall thermal noise contribution (brownian and thermo-elastic noise of coating and substrate) of the four mirrors of the Fabry-Perot arm cavities, mirror thermal noise in AdV is reduced by a factor **1.76** with respect to the case with an LG_0^0 beam. In ET-HF this factor is equal to **1.83** [126].

Chapter 8

A Table-Top Experiment to Test Generation and Interferometry of Higher-Order Laguerre-Gauss Modes

Before the implementation of LG_p^ℓ modes in future gravitational-wave interferometers, mode generation and interferometry must be studied carefully through experiments and optical simulations. We will address in this chapter the topic of generation of LG_3^3 modes, together with some aspects of LG_3^3 mode basic interferometry, from the experimental point of view.

There exist presently many techniques to generate LG_p^ℓ beams, originally developed for applications other than gravitational-wave detection. We need to understand wether one of these techniques could satisfy the requirements of gravitational-wave experiments, in terms of beam quality, efficiency and compatibility with other technical solutions that will be adopted in interferometers of future generations. In section 8.1 of this chapter we will define a series of criteria to evaluate the generation technique to be adopted, and we will go through a review of all the generation methods presently available.

Fused-silica etched diffractive plates are particularly interesting, since they could generate modes of reasonable quality, starting from an input Gaussian beam, and in principle they can handle the high-power necessary in future gravitational-wave interferometers. The quality of the generated modes might be further increased by using a mode-cleaner cavity, to filter the spatial defects of the beam. Thus we propose in this chapter the development of a new generation technique, suitable for future detectors, by using a diffractive plate (a converter) and a mode-cleaner cavity (a filter).

We used our technique on a table-top setup to generate high-purity LG_3^3 modes with good power efficiency. Though initially the scope of the setup was only limited to the development of the generation technique, we could accomplish a first step towards the assembly of a table-top power-recycled Fabry-Perot interferometer with LG_3^3 beams. We illuminated a simple Michelson interferometer with the generated high-purity LG_3^3 mode, and we locked it on the dark fringe.

The chapter is organized as follows: in sections 8.3 and 8.2 we will describe the design of the two main elements of the setup, the mode-cleaner and the LG_3^3 diffractive plate, respectively. The main objectives and the detailed scheme of the experimental setup are presented in section 8.4, and the results will be presented in the next sections. The mode-matching of the input LG_0^0 beam to the diffractive plate is described in section 8.5. The LG_3^3 mode generated through the plate is analyzed in section 8.6. The alignment of the optics of the setup is achieved following a procedure

described in section 8.7. Section 8.8 describes the servo loop for the lock of the laser frequency on the resonance of LG_3^3 mode-cleaner eigenmode, section 8.9 reports about the characterization of the cavity spectrum. The high-purity transmitted LG_3^3 mode is analyzed in section 8.10. The global efficiency of our generation technique is discussed in section 8.11.

8.1 Techniques for Higher-Order Mode Generation

LG_p^ℓ modes should be generated through a technique with the following features:

- acceptable purity
- capability of handling high-power
- reasonably-high power efficiency
- long-term stability.

According to techniques presently available, LG_p^ℓ modes might be generated either inside the optical resonator of a laser system or through the conversion of an input Gaussian beam. These techniques for *intra-* and *extra-cavity* generation have been experimentally demonstrated in the past, for applications of LG_p^ℓ modes in quantum optics experiments about entanglement of orbital momentum of photons [127], or tweezers for optical manipulation of microscopic particles [128].

The intra-cavity generation can be achieved by inserting phase plates [129] or cylindrical lenses [130] in the layout of a laser resonator. So far this technique has been demonstrated exclusively for LG_0^1 modes and only qualitative analysis of the generated modes can be found in literature. Intra-cavity generation seems a complex solution with respect to the implementation in gravitational-wave interferometers, since it would require a new design of laser sources. Thus we rather prefer to choose the extra-cavity option, since it allows to use the well-established laser technology.

Extra-cavity generation is based either on *astigmatic mode converters* or on phase modulation of the input beam, through diffractive optics. Among these latter, we can distinguish *spiral phase plates*, *etched-glass plates*, *spatial light modulators* and *computer-generated holograms*. The working principle of phase modulation is the following: spiral plates or diffractive optics are used as phase retarders, placed at the waist of the input Gaussian beam where the wavefront is plane. Here they imprint a spiralling phase pattern to the input beam, which is converted into an LG_p^ℓ mode by self-diffraction along propagation. Hereafter is a brief description of the mentioned extra-cavity generation techniques:

- **astigmatic mode converters** [131] are systems of two cylindrical lenses which can convert HG_{mn} of arbitrarily high order in LG_p^ℓ modes of the same order, with $p = \min(m, n)$ and $\ell = m - n$, by imposing a controlled Gouy-phase shift to the input beam.
- **spiral phase plates** [132, 133] are optics whose thickness along the optical axis increases proportionally to the transverse azimuthal coordinate θ, as shown on fig.8.1. The induced spiral phase delay is
$$\phi(\theta) = k(n - n_0)\frac{\theta}{2\pi}h_{SPP} = \ell\theta, \tag{8.1}$$
where n is the refractive index of the plate material, n_0 is the refractive index of the surrounding medium, $k = 2\pi/\lambda$ is the wave number, h_{SPP} is the period of the helix on the optical axis and ℓ is the winding number.

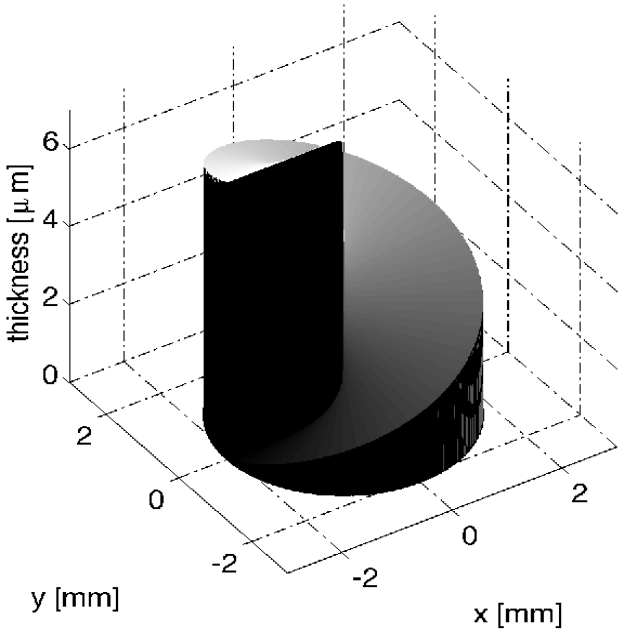

Figure 8.1: Design of a fused silica (n = 1.44963) spiral phase plate for the generation of a LG_0^3 mode.

- **spatial light modulators** [134, 135] are made of translucent or reflective liquid-crystal pixels, supported by a monolithic silicon circuit. An electrical signal flowing through the circuit drives the orientation of the liquid-crystal molecules inside each pixel, and determines the optical properties of the modulator surface. The driving electrical signal is steered through an external digital controller, usually a computer, so that modulators can act as dynamic optical elements.

- **etched-glass diffractive plates** [136, 137] are slabs of glass with patterns etched on the surface, causing the diffraction of the incident wavefront in the plane (x, y) transverse to the beam optical axis. Diffracted wavefronts propagate along a given distance z, and the resulting profile of the propagated beam is the superposition of the diffracted waves. One of the simplest example of etched diffractive plate is a transmissive diffraction grating, but the pattern might also be more complex as well. Etched plates can work in transmission or reflection.

- **computer-generated holograms** [138] are digitally-computed patterns that contain a coded record of an optical wave, including its amplitude and phase properties. The record is defined as the interference in the transverse plane between any desired object wavefront to be reproduced, and a plane (or more rarely a spherical) reference wave. Fig. 8.2 shows an example of computer-generated hologram for the generation of an LG_1^1 mode. These patterns are usually printed on a thin-photographic film support and reduced to transmissive masks. The object wave is then generated by illuminating the hologram with the plane reference wave.

Astigmatic converters, spiral phase plates and etched-glass diffractive plates satisfy the crucial requirement of high-power handling capability, whereas holograms and spatial light modulators

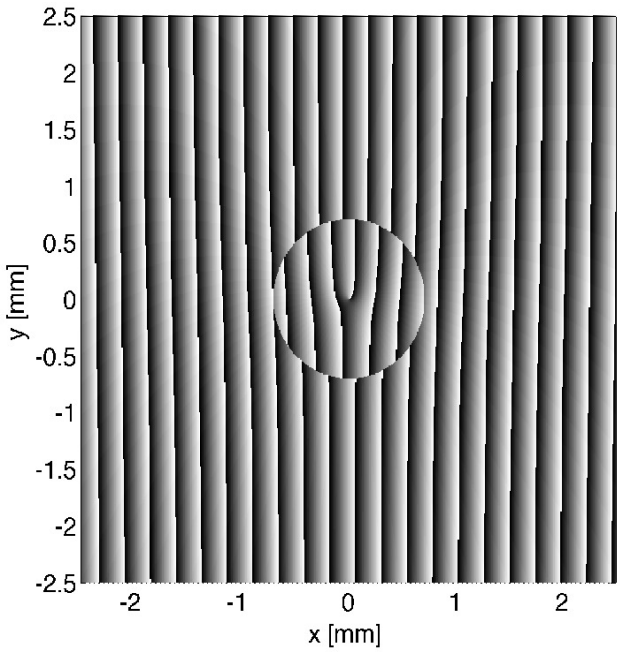

Figure 8.2: Phase pattern of a computer-generated hologram for the generation of an LG_1^1 mode.

(due to the low damage threshold of thin films and liquid crystals) do not.

However, spiral phase plates can only generate LG_0^ℓ modes of lower order N, whose winding number ℓ is also limited by the achievable thickness of the plate and the refractive index of the material. The use of astigmatic converters is limited by the ability to generate higher-order HG_{nm} input beams, requiring the implementation of an input laser system of unfeasible complexity. For example, a mode HG_{63} would be needed to generate an LG_3^3 mode.

Etched-glass diffractive plates are the most suitable technique for LG_p^ℓ mode generation, fulfilling all the fundamental requirements of gravitational-wave experiments. They are stable passive optics which could handle high-power beams, and have been already used to generate LG_p^ℓ modes of relatively high order, with reasonable results of generation efficiency and purity [137].

We propose here the development of the following generation technique, depicted schematically in fig.8.3: an input Gaussian beam is converted through phase modulation in an LG_p^ℓ mode by a fused-silica etched diffractive plate, and the generated mode is spatially filtered by a mode-cleaner Fabry-Perot cavity to increase its purity. To test the performances of this technique we assembled a table-top experimental setup [139], described in detail in section 8.4 of this chapter.

We chose to generate an LG_3^3 mode, to test the extension of the diffractive plate technique to modes of larger order with several radial intensity maxima. This mode can provide en effective reduction of mirror thermal noise in future detectors, and features a moderate shape complexity. Thus it represents a tradeoff between the need of generating modes of higher order, which may provide larger noise reduction, and the increase of the complexity of the beam shape. However, in principle, this generation technique could be pushed further to generate any mode order.

In the next two sections we will describe the design of the two main elements of the experimental setup, the LG_3^3 diffractive plate and the mode-cleaner cavity.

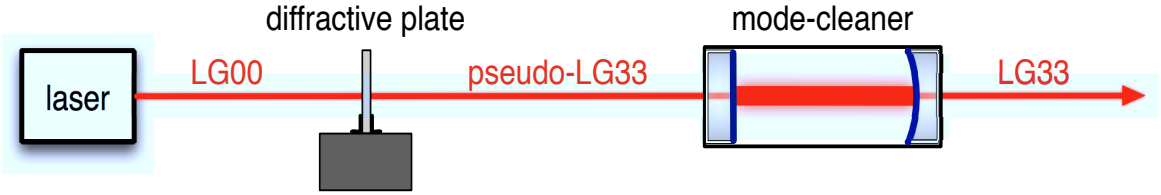

Figure 8.3: Design concept for the generation of a LG_3^3 mode with a diffractive plate (mode converter) and a mode-cleaner Fabry-Perot cavity (spatial filter).

8.2 Design of the LG_3^3 Diffractive Plate

The diffractive plate has been designed and realized by SILIOS Technologies, a company specialized in the design and fabrication of micro-optical components [140]. We characterized the design of the plate by means of FFT optical simulations that we developed starting from the core of the FFT code OSCAR [141, 142].

Simulations indicated that the mode generated by the plate would be reasonably pure. Thus, after approval of the design, SILIOS took care of the fabrication of the plate. In the following we describe the design procedure of the plate and the optical simulations we performed, together with the results about the expected quality and efficiency of mode conversion.

Optical layout

The conversion from the LG_0^0 mode to the LG_3^3 mode might be carried out either with a single phase-modulating plate [136] or with a pair of consecutive plates [137]. SILIOS initially studied this latter option, but finally a single phase-modulating plate for an input LG_0^0 beam with mm-size waist was chosen.

The sole constraint of this layout is the alignment tolerance of the plate to transverse translations, to be controlled within ~ 100 μm on the x and y. This is achievable with optical mounts for precise alignment, available on the commerce.

Design of the phase pattern

The design of the plate pattern has been realized by SILIOS starting from the theoretical phase pattern of an LG_3^3 mode at waist. The concept of the design is to use the phase plate to imprint the phase pattern of an LG_3^3 mode to a large-radius input Gaussian beam at waist, which can be approximated as a uniform plane wave. Thus the input beam is forced by self-diffraction to assume the shape of an LG_3^3 mode along propagation.

The waist size of the LG_3^3 mode pattern on the plate must be $w_0 = 705$ μm, in order to obtain an output LG_3^3 mode waist of $w_0 = 288$ μm at the focal plane of a 600 mm lens, as shown on fig.8.4. The theoretical phase of an LG_3^3 mode is shown in fig.8.6 (in the transverse plane): it features the typical spiral pattern with a phase discontinuity in $r = 0$ (the *optical vortex*), and three radial phase discontinuities at the roots of the Laguerre polynomial

$$L_3^3(2r^2/w_0^2) = -\frac{(2r^2/w_0^2)^3}{6} + 3(2r^2/w_0^2)^2 - 15(2r^2/w_0^2) + 20 \ , \tag{8.2}$$

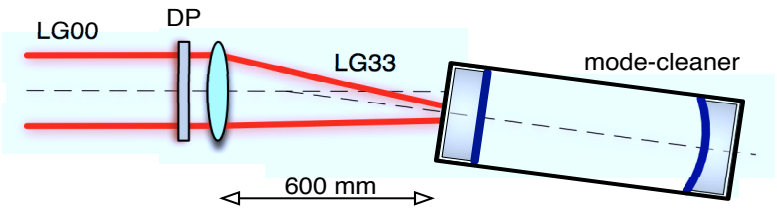

Figure 8.4: Optical layout for the phase-retarding LG_3^3 diffractive plate.

where the polynomial changes sign. The relative positions of the radial discontinuities have an influence on the shape of the resulting mode, then these positions have been slightly adjusted 'by hand' in order to increase the generated mode purity.

Then a blazed grating with period $\Lambda = 235$ μm has been superposed to the adjusted LG_3^3 phase pattern. In the transverse plane (x, y), the grating has a complex spatial harmonic transmittance

$$t_{BG}(x) = \exp(-i2\pi x\nu) \tag{8.3}$$

with characteristic frequency $\nu = 1/\Lambda$. This is a standard technique to reduce the impact of manufacturing defects of the plate on the quality of the phase-modulated mode [134].

According to elementary Fourier optics, in fact, the pattern $t_{BG}(x)$ separates under an angle $\theta = \sin^{-1}\lambda\nu$ the phase-modulated output LG_3^3 beam (sent on the first diffraction order) from the residual unmodulated input LG_0^0 light (the 0th order), which is due to the presence of defects. Thus the modulated beam has larger purity. The grating period chosen by SILIOS yields an angle $\theta = 4.5$ mrad in the (x, z) plane, shown on fig.8.4.

The resulting phase pattern of the plate, shown on fig.8.5, is analogous to that traditionally used for LG_p^ℓ mode generation with computer-generated holograms [138] (see for example fig.8.2), and afterwards used also with spatial light modulators [134]. SILIOS indicated an input LG_0^0 waist of $w_0 = 2.15$ mm, to have a smooth varying intensity profile on the central area of the pattern. As mentioned above, this is usually done to approximate the input Gaussian beam with a uniform plane wave, in order to increase the effect of phase modulation [134].

Simulation of the generated pseudo-LG_3^3 mode

The field generated with the diffractive plate is not a solution of the paraxial wave equation, since it has the amplitude of a Gaussian mode but the phase of an LG_3^3 mode. Such a mode does not feature the structure stability of LG_p^ℓ modes and can change its shape by propagation.

Therefore the phase modulation of the input Gaussian beam is expected to generate a *pseudo*-LG_3^3 mode of limited purity. To estimate this purity, we developed an FFT simulation of the whole layout for mode conversion shown on fig.8.4. We simulated the passage of the input LG_0^0 beam (with waist $w_0 = 2.15$ mm) through the plate, which is assumed without any fabrication error, and the consequent phase modulation of the beam.

Then the beam is sent through the 600 mm lens, and propagates in space (along a direction θ with respect to the input beam axis) to the focal plane of the lens. Here we compute numerically the 2-dimensional overlap integral γ, between the theoretical LG_3^3 field we expect (defined by eq.(5.13) with $w_0 = 288$ μm), indicated as $LG_3^3|_{theory}$, and the complex amplitude of the simulated

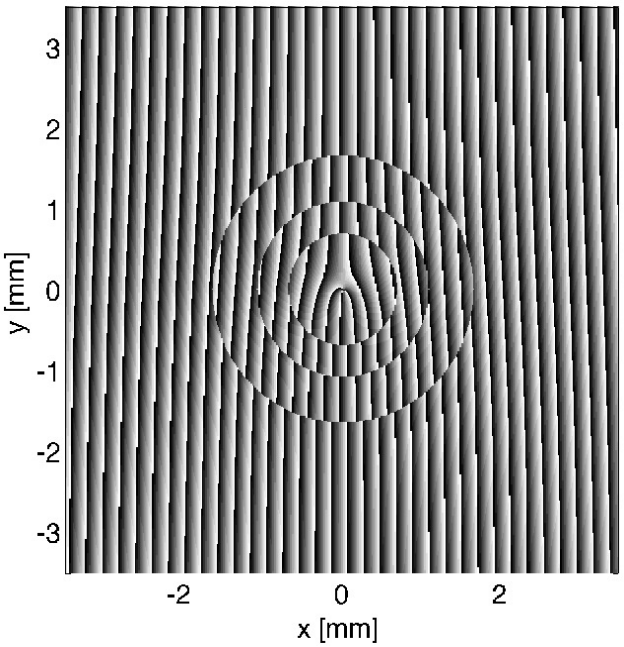

Figure 8.5: Design of the pattern of the phase-retarding LG_3^3 diffractive plate, by SILIOS.

pseudo-LG_3^3 mode, $LG_3^3|_{sim}$, with the following operational definition:

$$\gamma = \left\langle LG_3^3|_{theory} \middle| LG_3^3|_{sim} \right\rangle = \frac{\left| \int (LG_3^3|_{theory})^* \; LG_3^3|_{sim} \; dS \right|}{\sqrt{\int \left| LG_3^3|_{theory} \right|^2 dS \times \int \left| LG_3^3|_{sim} \right|^2 dS}} \; . \tag{8.4}$$

Then γ^2 is the fractional power content of LG_3^3 mode, and the coupling losses are

$$L = 1 - \gamma^2 \; . \tag{8.5}$$

The simulated pseudo-LG_3^3 mode yields $\gamma = 85\%$ and $L = 28\%$.

Optimal input beam size

In order to confirm the choice of $w_0 = 2.15$ mm for the input Gaussian beam, we developed an FFT code to simulate the phase modulation of input beams of different waist sizes.

The scope of the simulation is to investigate what is the optimal size w_0 which yields the best shaping of the pseudo-LG_3^3 mode (and thus the maximum overlap integral), with respect to a phase modulating pattern of a given size. This test has been introduced for computer generated holograms [138], then it has been used also for spatial light modulators [134].

Again, the code simulates the optical layout of fig.8.4. The size of the input LG_0^0 Gaussian beam is changed in a loop, and for each iteration the code computes the overlap integral between the generated pseudo-LG_3^3 mode and the theoretical LG_3^3 mode with $w_0 = 288$ μm, at the mode-cleaner input. The output plot of the code on fig.8.8 shows the overlap integral and the coupling losses of the pseudo-LG_3^3 mode versus the waist w_0 of the input beam. The maximum overlap integral (corresponding to minimal coupling losses) is really achieved for $w_0 = 2.15$ mm.

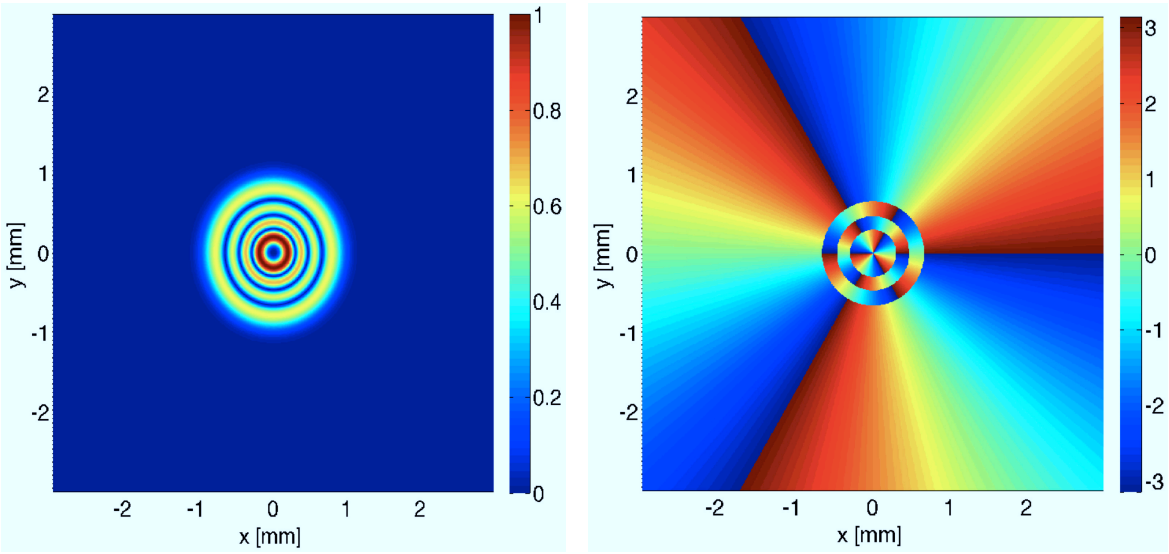

Figure 8.6: Theoretical LG_3^3 mode with $w_0 = 288$ μm: normalized amplitude [a.u.] (left) and phase [rad] (right).

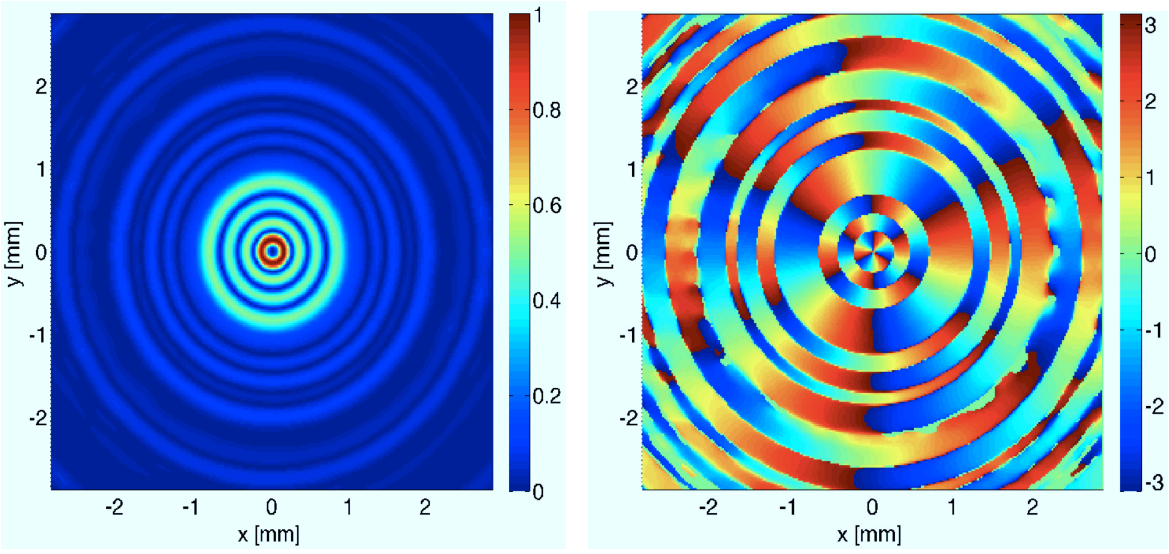

Figure 8.7: Simulated pseudo-LG_3^3 mode generated by the diffractive plate: normalized amplitude [a.u.] (left) and phase [rad] (right).

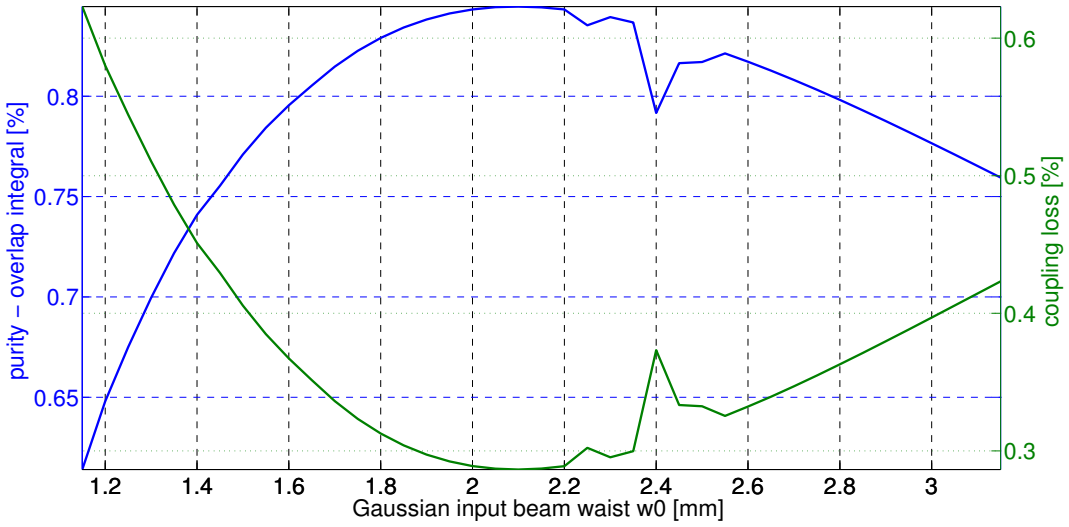

Figure 8.8: Optimization of the Gaussian input beam on the diffractive plate: the overlap integral (blue curve) and the coupling loss (green curve) are shown as functions of the input beam waist w_0.

Fig.8.9 shows the change in shape of the pseudo-LG_3^3 mode profile for an input beam waist varying of ± 0.5 mm with respect to $w_0 = 2.15$ mm, corresponding to a variation of the overlap integral of $\pm 4\%$. This variation sets a reasonable range for the tolerance on the size of the Gaussian input beam.

Estimated power conversion efficiency

The plate is an etched slab of fused silica without anti-reflective coating, and the expected loss due to reflection is 4% of the power on each surface of the plate. Thus the achievable efficiency is limited to $\epsilon_{DP} = (0.96)^2 = 0.92$. Furthermore, the blazing must be considered.

In principle, as long as the blazing angle is small and the depth d of the etched pattern of the plate can be approximated as infinitely thin, the blazing of the grating pattern may send 100% of the transmitted light on the first diffraction order [143]. Actually, when d is comparable with the grating period Λ and/or errors of fabrication are present, the efficiency on the first diffraction order decreases to a lower value and some power is spread on other diffraction orders.

Thereby, the expected power conversion efficiency ϵ_{DP} of the plate is defined as the ratio of the power of the pseudo-LG_3^3 mode on the first diffraction order to the available power of the input Gaussian beam. This efficiency should be equal to 83% [147], which, multiplied by the losses due to reflection on the two uncoated surfaces of the plate, should yield $\epsilon_{DP} = 76\%$.

Production process

The fabrication process used by SILIOS for the manufacturing of the phase-retarding diffractive plate is a recursive etching technique. The phase pattern is etched on the glass substrate through multiple steps of carving, each one removing a thin layer of material whose thickness is a given fraction of the wavelength λ of the incident light. The layers to be removed are located on the

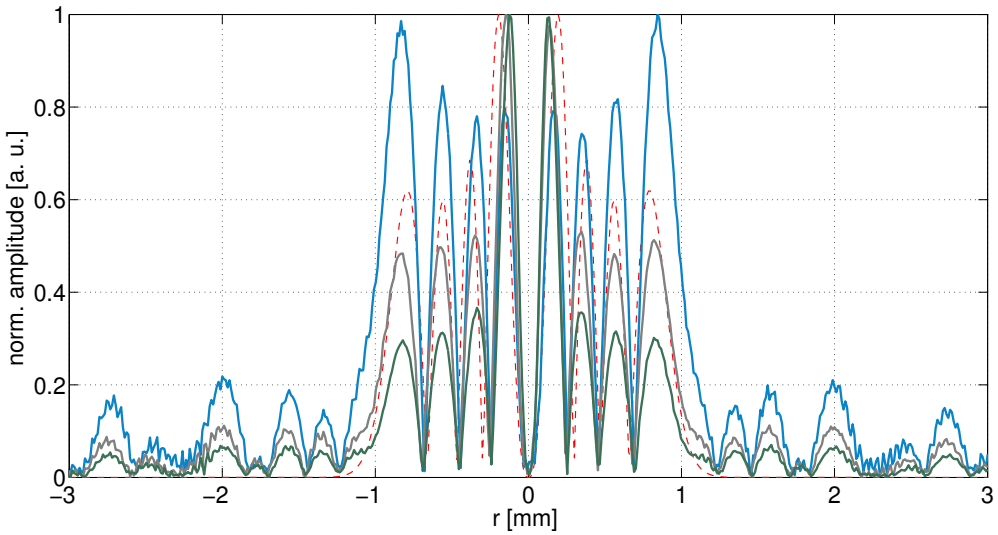

Figure 8.9: Normalized amplitude profile of the simulated pseudo-LG_3^3 mode, as a function of the Gaussian input beam waist: $w_0 = 1.65$ mm (light blue curve), $w_0 = 2.15$ mm (reference value, grey curve), $w_0 = 2.65$ mm (dark green curve). The profile of the theoretical LG_3^3 mode is also shown for comparison (dashed red curve).

surface of the plate by applying a sequence of binary masks of increasing spatial resolution.

The pattern designed by SILIOS has been etched on the surface of a slab of Corning fused silica with 16 levels of phase and 2400×2400 pixels, each one measuring 5.9 μm.

8.3 Design of the Mode-Cleaner

A mode-cleaner is a Fabry-Perot cavity used in transmission, to spatially filter an input laser beam. The injection of the beam into the cavity is equivalent to making the beam decomposition in the base of the mode-cleaner eigenmodes. When the cavity resonates for one of those eigenmodes, it only transmits the fraction of the input beam power with the same spatial distribution. The rest of the power is reflected backward.

The transmitted fraction is the *coupling coefficient* of the beam, whereas the fraction reflected is the *coupling loss*. In the following we will describe the optical design of the cavity, which determines the filtering performance of the mode-cleaner. Then we will describe its mechanical design.

Optical layout

The optical layout of the cavity must have an even number of mirrors, because we want to transmit helical modes with radial symmetry. To demonstrate this assertion, let us expand the field in terms of HG_{mn} modes [144],

$$LG_p^\ell(x,y,z) = \sum_{k=0}^{N} i^k b(m,n,k) HG_{N-k,k}(x,y,z), \tag{8.6}$$

where $p = \min(m, n)$ and $\ell = m - n$, and the real coefficients are

$$b(m,n,k) = \left(\frac{(N-k)!k!}{2^N m!n!}\right)^{1/2} \frac{1}{k!}\frac{d^k}{dt^k}[(1-t)^m(1+t)^n]_{t=0} \ . \tag{8.7}$$

Let us now consider the first two coefficients of the expansion:

$$\begin{aligned} b(m,n,0) = &\ \left(\tfrac{N!}{2^N m!n!}\right)^{1/2} \\ b(m,n,1) = &\ \left(\tfrac{(N-1)!}{2^N m!n!}\right)^{1/2}(n-m) \ . \end{aligned} \tag{8.8}$$

If the azimuthal index ℓ is not null, then $m \neq n$ and at least the amplitudes of the first two HG_{mn} modes of the sum are different from zero. In a cavity with an odd number of mirrors, these modes resonate at different frequencies, and the radial symmetry of the helical LG_p^ℓ modes is broken.

We chose a simple linear layout with two mirrors for the mode-cleaner of the experiment, in order to transmit helical LG_3^3 modes. Furthermore we chose a plano/concave configuration, where the beam can be aligned to the cavity with two external steering mirrors. This configuration allows to recover misalignments without acting on the cavity mirrors, and then simplify the design of the cavity itself, which can have a rigid structure.

Degeneracy

To achieve a good spatial filtering of the input mode, the mode-cleaner must be non-degenerate. This means that the mode frequency spacing

$$\Delta\nu = \nu_0 \frac{\Delta N}{\pi}\Phi_G \ , \tag{8.9}$$

defined in eq.(5.21), must be sufficiently large, and we have to choose the cavity parameters accordingly. Let L be the cavity length, R_1 the radius of curvature of the input mirror and R_2 the radius of curvature of the end mirror. For the plano/concave configuration, $R_1 = \infty$ and the waist of the cavity eigenmodes is on the input mirror.

We chose a cavity length $L = 0.3$ m, yielding a free spectral range of 500 MHz. This length is reasonably small to fit on the optical table, and it is large enough to determine a cavity waist of about 400 μm for a radius of curvature of R_2 of the order of 1 m, which is a reasonable beam size. For such an optical configuration, $R2$ is the only free parameter that sets the base of the eigenmodes and their frequency spacing.

The optimal value of R_2 must minimize the accidental degeneracy of modes of different order with the LG_3^3 mode. If the mode-cleaner is resonant for the LG_3^3 mode, which has $N = 9$, we will have $\Delta N = N' - 9$. As a consequence, the transmission of modes of order N' is attenuated according to

$$T_{\Delta N} = T_{33}\frac{1}{1 + \left(\frac{2}{\pi}\mathcal{F}\sin\left(2\pi\frac{L}{c}\Delta\nu\right)\right)^2} \ , \tag{8.10}$$

where $\mathcal{F}$ is the cavity finesse and T_{33} is the transmission of the LG_3^3 mode. Eq.(8.10) shows that the transmission of modes of different order, due to the expected spatial defects of the input LG_3^3

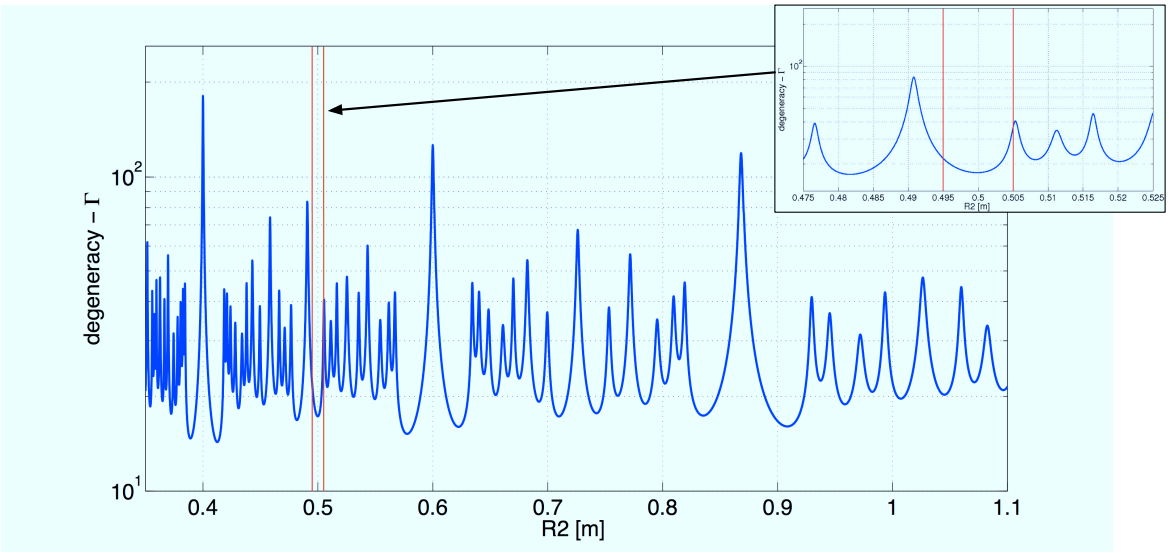

Figure 8.10: Design of the mode-cleaner, choice of the concave mirror radius of curvature: on the y axis the figure of merit for mode degeneracy (blue line) is shown. R = 0.5 m is the optimal choice, vertical red lines indicate ± 1% mirror manufacturing tolerances.

mode, is strongly attenuated for a high cavity finesse and/or a large frequency spacing. The right choice of R_2 can be made using a figure of merit of mode degeneracy, defined through eq.(8.10) as

$$\Gamma(R_2) = \sum_{N'=1}^{\infty} (N'+1)\sqrt{T_{\Delta N}(R_2)} \ . \tag{8.11}$$

A local minimum of this figure of merit corresponds to a value of R_2 that gives an effective separation of modes, minimizing the transmission of modes that are different from the resonant one. It is then sufficient to impose the resonant eigenmode of the mode-cleaner to be an LG_3^3 mode. Fig.8.10 illustrates the behavior of Γ versus R_2 for this set of parameters: $L = 0.3$ m, a reasonable value of finesse, $\mathcal{F} = 100$, and a safely large order difference $\Delta N = 30$.

The plot shows that $R_2 = 0.5$ m corresponds to a local minimum of the figure of merit, and at the same time this is a value that can be easily achieved by manufacturers, according to standard optic catalogues. The vertical red lines show typical ± 1% manufacturing tolerances for R_2, still reasonably close to the minimum degeneracy. Thereby $R_2 = 0.5$ m has been chosen as reference value.

According to this choice, eq.(5.16) yields a beam waist $w_0 = 288$ μm on the input mirror, and consequently the beam size on the end mirror is 455 μm. The ratio between the beam size and the mirror radius for 1 ppm of clipping losses is 4.31 for LG_3^3 modes, thus standard 1-inch mirrors are large enough to ensure negligible loss at input and end cavity mirrors.

Finesse

In order to confirm the choice of the cavity finesse, we run two FFT simulations of the mode-cleaner with OSCAR. According to eq.(8.10) the spatial filtering improves for a larger finesse, thereby we

simulated $\mathcal{F} = 100$ and $\mathcal{F} = 1000$[1]. We injected the pseudo-LG_3^3 mode of fig.8.7 into the cavity, and we computed its spectrum and the purity of the filtered beam in the two cases.

The spectrum has been obtained by simulating a scan of the cavity length L. It is shown on fig.8.11, where we can see the projection of the pseudo-LG_3^3 mode on the mode-cleaner eigenmode base: the modes have been identified through the relation

$$\Delta L = \frac{\lambda}{2}\frac{\Phi_G}{\pi}\Delta N \ , \tag{8.12}$$

which is the homologue of eq.(5.21) for the tuning of the cavity length, and are indicated on the plot. We can see that all the resonances of other modes are well spaced from that of the LG_3^3 mode.

The purity of the filtered mode has been computed by means of the overlap integral of eq.(8.4) with the theoretical LG_3^3 eigenmode transmitted through the cavity. It is $\gamma = 99.8\%$ for $\mathcal{F} = 100$, and $\gamma = 99.9\%$ for $\mathcal{F} = 1000$. Figs.8.13 and 8.12 show the filtered beam and the theoretical transmitted eigenmode, respectively, in the case of $\mathcal{F} = 100$. The purity obtained with the low finesse seems sufficient for our purpose.

In summary, according to simulations, a high finesse of the mode-cleaner cavity is not determinant to achieve a good spatial filtering of the pseudo-LG_3^3 mode. Thus we finally confirmed $\mathcal{F} = 100$, and then the transmission coefficients of the mirrors are $T_1 = T_2 = 0.03$.

Mechanical design

The resonance condition of the beam in the mode-cleaner might be perturbed by fluctuations of the laser frequency or by microscopic fluctuations of mirror positions, changing the cavity length. Mirrors might move because of the vibrations of the ground transmitted through the optical table, or because of acoustic waves in the surrounding environment. Thus the resonance condition has to be stabilized through a control scheme, acting either on the laser frequency or on the cavity length.

The simplest technical solution is to build a cavity of fixed length, where the mirrors have no degree of freedom for displacement (neither translations nor angular tilts), and to control the laser frequency through a feedback loop for stabilization. The alternative would be to control the cavity length by mounting one mirror of the cavity on a piezoelectric stack. This latter solution is more complex: mirror mounts should be adapted to include the actuator, and the piezo should have a large aperture to avoid the clipping of an LG_3^3 beam, which is much larger than a Gaussian beam. Moreover, the mount of the mirror with the actuator should have a negligible coupling between the longitudinal and the angular displacements[2].

We decided to build a cavity of fixed length L with a monolithic design, where the mirror are mounted at the ends of a rigid support, in order to have a stable mechanical separation of the cavity optics. The mechanical design of the cavity has been realized by the mechanical engineers of the AstroParticule and Cosmologie (APC) laboratory, and the model has been manufactured in the laboratory workshop by the mechanical service.

The body of the monolithic mode-cleaner is a cylindrical mirror spacer of $L = 0.3$ m, screwed on a rigid mount with four supports. The whole cavity (spacer plus supports) can be fixed rigidly

[1] To have optimal coupling of the input beam to the cavity, we set equal transmissions for the input and the end mirrors ($T_1 = T_2$), and we simulated perfect optics with no figure errors. No losses have been included as well, except those due to the clipping of the mode on the mirror edge.

[2] The mount with piezoelectric stack has now been realized, for the second phase of the experiment.

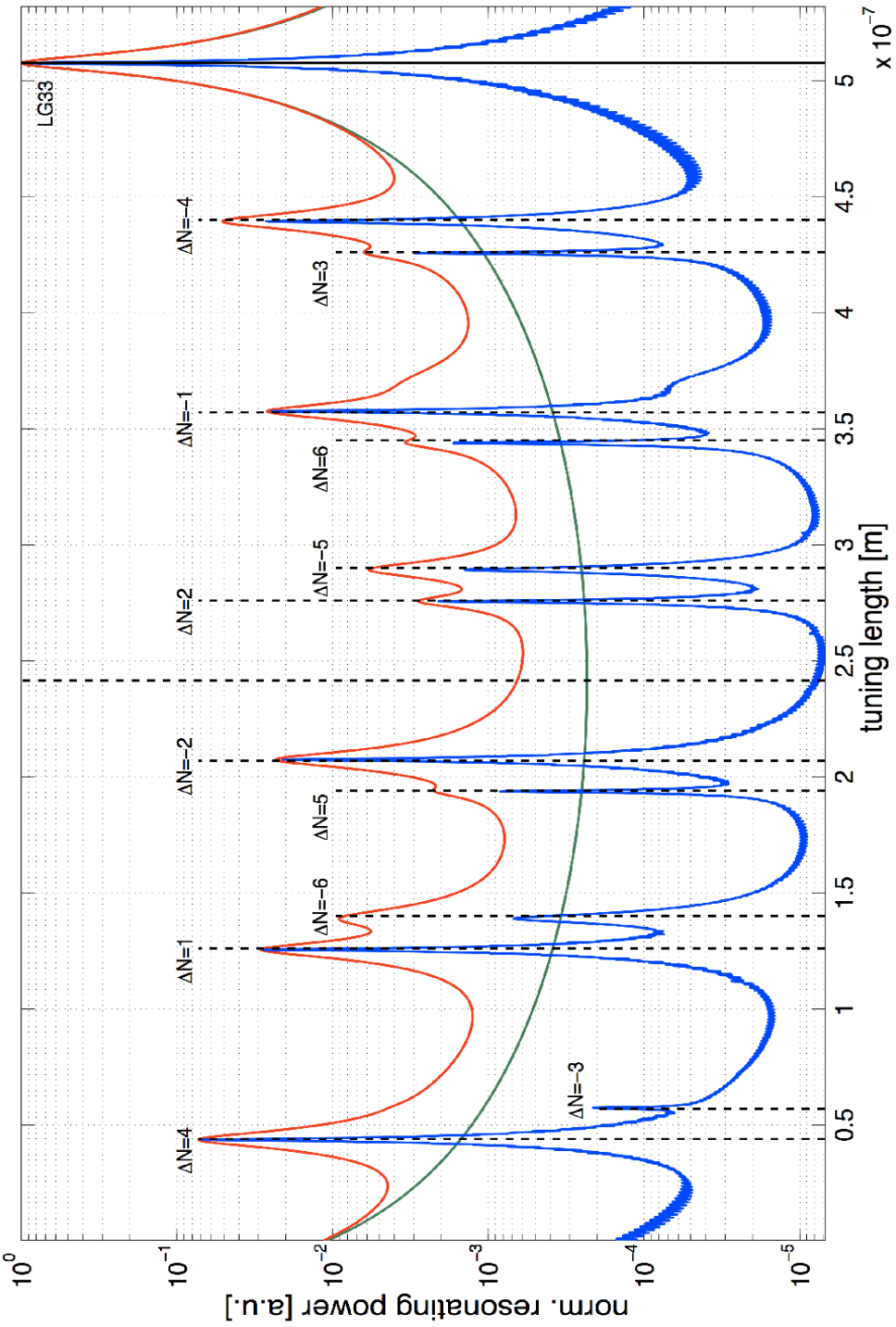

Figure 8.11: Spectrum of the pseudo-LG_3^3 mode versus the tuning of the cavity length, as a function of the mode-cleaner finesse: $\mathcal{F} = 100$ (red curve) and $\mathcal{F} = 1000$ (blue curve). The various components of the input beam in the cavity base (black vertical dashed lines) are identified by the order difference ΔN, the anti-resonance condition (close to $2.5{\cdot}10^{-7}$ m) is also shown. The spectrum of a pure LG_3^3 mode with $\mathcal{F} = 100$ (green curve) is reported for comparison.

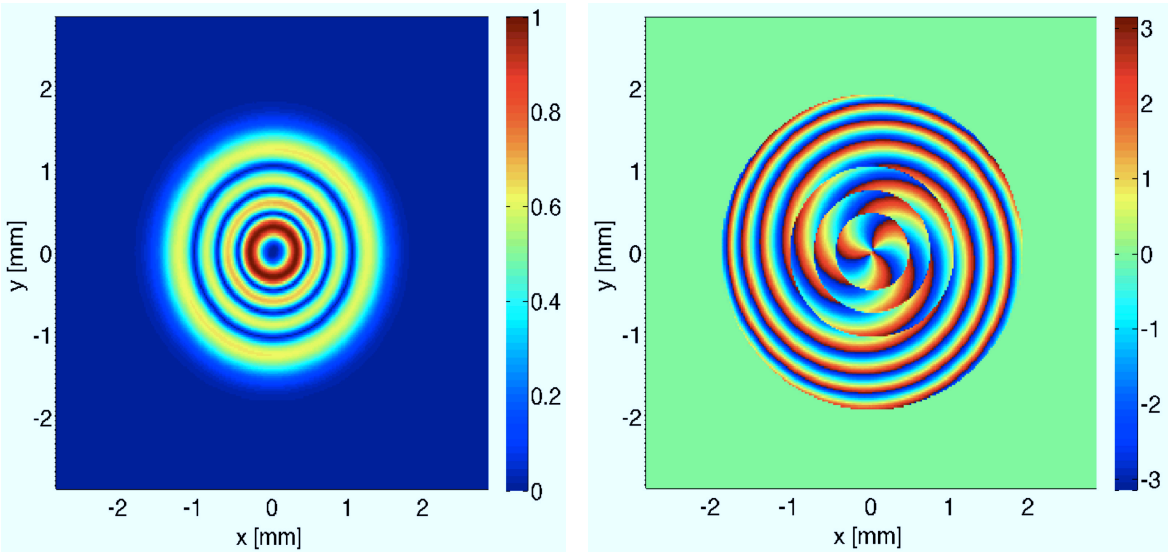

Figure 8.12: Filtered pseudo-LG_3^3 beam transmitted through the mode-cleaner, for $\mathcal{F} = 100$: normalized amplitude [a.u.] (left) and phase [rad] (right).

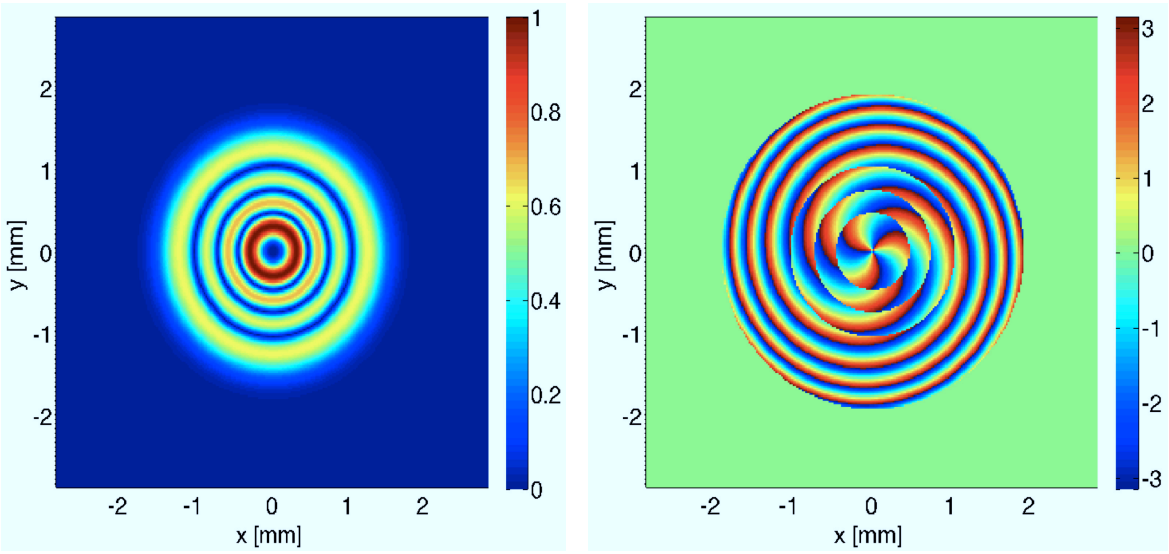

Figure 8.13: Theoretical LG_3^3 eigenmode transmitted through the mode-cleaner, for $\mathcal{F} = 100$: normalized amplitude [a.u.] (left) and phase [rad] (right).

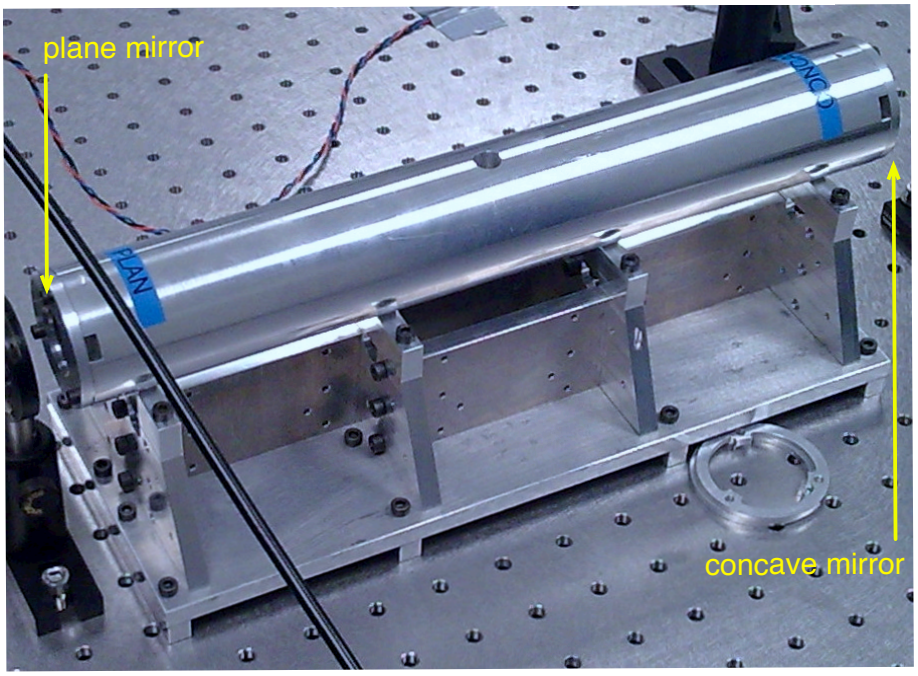

Figure 8.14: Monolithic mode-cleaner cavity.

to the optical table. The mirrors are placed into two inner housings at the extremities of the cavity, fixed by two annular caps of 21-mm aperture, screwed to the cavity body. Rubber joints are placed between the caps and the mirrors, to uniform the pressure of the caps on the mirror surface.

The closed structure of the cavity avoids the effect of acoustic waves on mirrors. The cavity and the mount are designed to be as stiff as possible, in order to move the first vibrational mode of the structure to high frequencies, where the vibrations of the ground are supposed to be negligible.

A prototype of the mode-cleaner has been realized with aluminum (2017A T4), to test the tolerances of fabrication of manufacturing machines. This prototype has been used on the optical table with the Gaussian mode of the laser, to check the global performances of the mechanical design, showing extremely good results of stability. After setting the mode resonance in the cavity, we observed a very slow drift (~ 30 s) of the mode build-up from the resonance condition, indicating that the design satisfies the requirement of protecting the mirrors from external disturbances.

The final model of the cavity, shown on fig.8.14, was realized in Invar, which is a nickel steel alloy with a very low thermal expansion coefficient: $\alpha = 2 \cdot 10^{-6}$ K^{-1}. This material allows to decrease any potential long-term drift of the cavity length, driven by a temperature change of the surrounding environment, to a negligible level.

8.4 The Table-Top Experiment

The aim of the table-top experiment is: (i) to test the conversion of an input LG_0^0 beam into a high-purity LG_3^3 helical beam, using the LG_3^3 plate and the mode-cleaner, (ii) to test the behavior of a Fabry-Perot cavity illuminated by a (pseudo) LG_3^3 mode. We will assess:

- **the purity of the LG_3^3 mode** generated through our conversion-and-filtering technique. We will demonstrate that the phase pattern of the diffractive plate can generate a pseudo helical LG_3^3 beam with the expected initial purity, and we will characterize the purity and the parameters of the filtered LG_3^3 beam transmitted through the mode-cleaner
- **the global conversion efficiency** of the technique, by measuring the power conversion efficiency of the LG_3^3 diffractive plate, and the transmission of the pseudo LG_3^3 beam through our setup and the mode-cleaner
- **the long-term stability of mode generation**
- **the alignment tolerances** of the LG_3^3 beam on the mode-cleaner.

The scheme of the experimental setup is shown in fig.8.15. The Gaussian LG_0^0 beam of the laser is firstly passed through an electro-optic modulator, for the generation of radio-frequency sidebands used for the servo control of the laser frequency. The beam then goes through a magnifying mode-matching telescope, to enlarge the beam radius on the LG_3^3 diffractive plate up to mm size. The generated pseudo-LG_3^3 propagates to the mode-cleaner. At the resonance of the mode-cleaner LG_3^3 eigenmode, the frequency of the laser is locked to the mode-cleaner length using a standard Pound Drever-Hall locking scheme in reflection.

The generated-pseudo LG_3^3 beam is pre-aligned to the mode-cleaner cavity using a Gaussian pick-off, which propagates in the setup without going through the diffractive plate. Either the LG_0^0 or the pseudo-LG_3^3 beam can be blocked independently with a beam dump. The relative alignment of the Gaussian beam and the pseudo-LG_3^3 beam is achieved by using a setup of two CCD cameras, placed in near field and far field on a parallel path with a flip-mount mirror.

We assembled the experimental-setup in a dedicated clean room of the APC laboratory, as shown on fig.8.16, on an optical table of 150×180 cm. The room is a controlled environment, where the circulating air is filtered to limit the number of dust particles, which may deposit on the optics and perturb the measurements. This space is classified class 10^5, meaning that the number of microscopic dust particles between 0.5 μm and 1 μm size is less than $10^5/\text{cm}^3$. The temperature in the room is stabilized within about $\pm$ 1 K.

8.5 LG_0^0 Input Beam

The setup for generating and mode-matching the LG_0^0 input beam to the diffractive plate includes the laser, a Faraday isolator, three polarizers, a converging lens (L0) with focal length $f = 300$ mm, an electro-optical modulator and a mode-matching telescope composed of three lenses: L1, L2 and L3.

Laser

The input LG_0^0 beam is generated with a commercial continuous-wave laser, a model (Mephisto by Innolight) widely used in present gravitational-wave interferometers as master laser. This laser uses a Nd:YAG crystal as a monolithic nonplanar ring oscillator, and emits at $\lambda = 1.064$ μm. The emitted power can be tuned from few mW up to 0.5 W, by changing the current that flows through the diode used as laser pump.

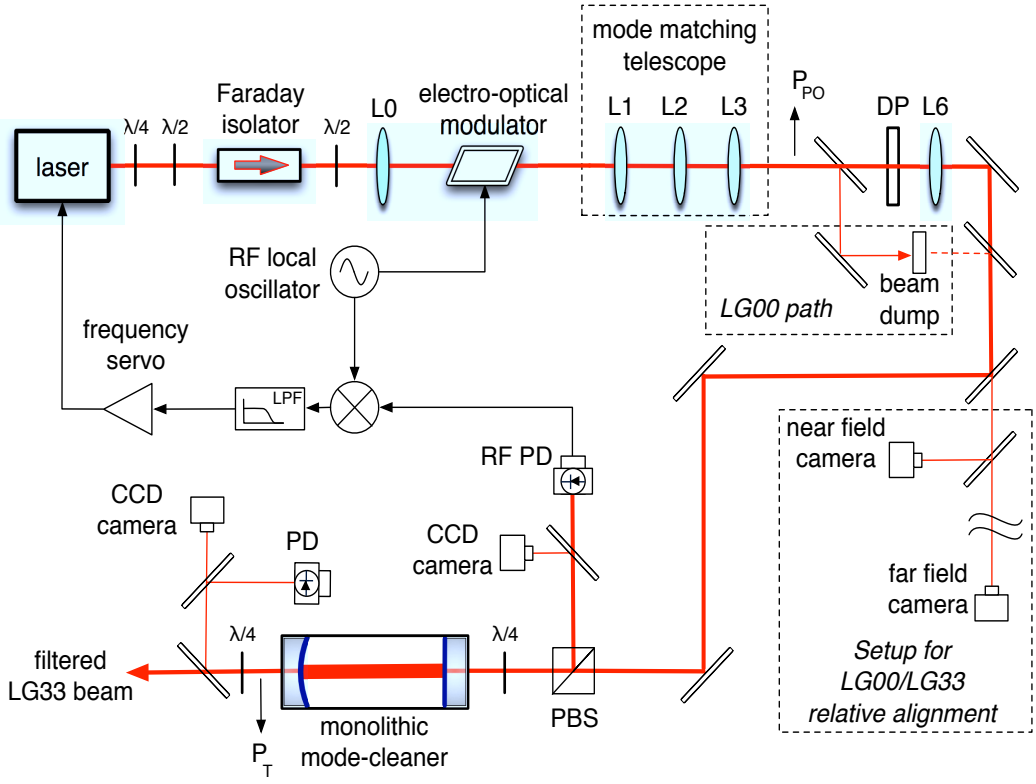

Figure 8.15: Experimental setup for the generating and filtering a pseudo-LG_3^3 mode.

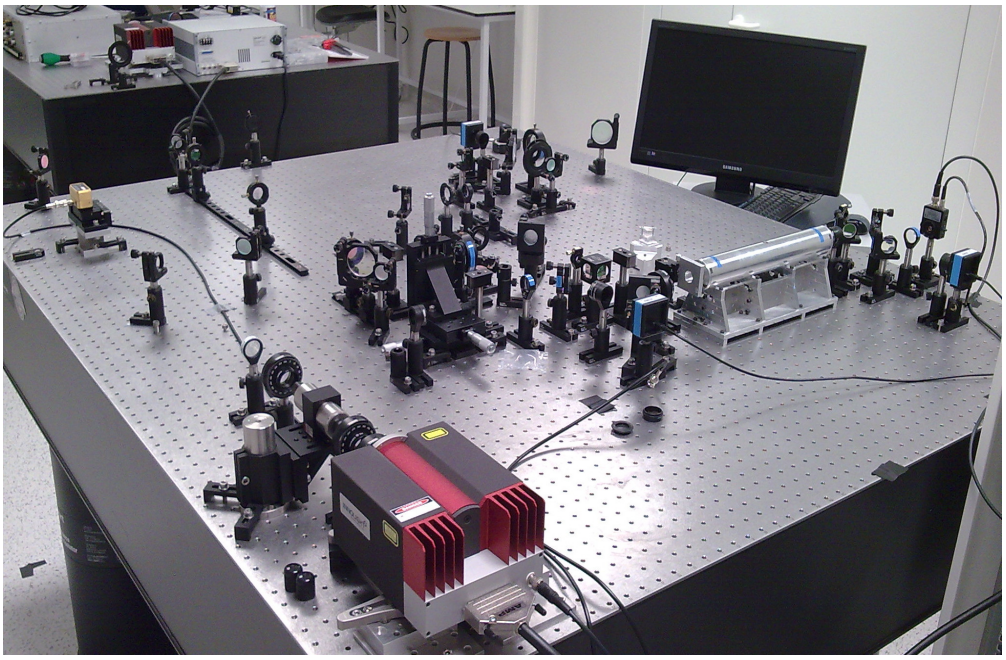

Figure 8.16: Photograph of the experimental setup.

The frequency of the emitted light, $\nu \simeq 2.8 \cdot 10^5$ GHz, can be tuned within a dynamic range of ±150 MHz, with a piezoelectric actuator glued to the crystal (gain of 1.5 MHz/V, maximum voltage ±100 V). For a larger dynamics, a Peltier cell changes the crystal temperature, providing a tuning range of 30 GHz (gain of −3 GHz/K, maximum tuning 10 K). The piezoelectric actuator and the thermal actuator are used in the laser frequency stabilization feedback loop, as described in section 8.8.

Faraday isolator and beam polarization

The laser beam is passed through a Faraday isolator, protecting the laser crystal from backward reflections which could perturb the laser operation. The isolator is made of three parts: an input polarizer (polarized vertically), a Faraday rotator, and an output polarizer (polarized at 45 degrees). Light travelling forward is vertically polarized by the input polarizer, then the Faraday rotator rotates the polarization by 45 degrees. The output polarizer is set to allow the beam transmission.

Light travelling backward becomes polarized at 45 degrees by the output polarizer, and the Faraday rotator again rotates the polarization by 45 degrees and set it horizontal. Thus the light propagating backward is blocked by the input polarizer, which is vertically aligned. The isolator acts as an optical diode, allowing the propagation of light in only one direction. The attenuation of backward reflections is called *extinction factor*.

The isolator used in the setup is an IsoWave I-106T-5, optimized for the highest attenuation at 1.064 μm, with beamsplitter cubes as polarizers. Its extinction factor has been characterized by measuring the ratio P_{out}/P_{in} between the output and the input beam power, with the isolator placed in the reversed position with respect to the laser, as shown on fig.8.17. The beam power is measured with a thermopile Gentec XLP12-3S-H2 powermeter, which measures the integrated power of the beam on a circular surface of 12 mm diameter. The power measurements yield:

$$\text{extinction} = 10\ \text{Log}\left(\frac{P_{out} = 0.190\ \text{mW}}{P_{in} = 500\ \text{mW}}\right) = -34.20\ \text{dB}\ .$$

The measurement of the extinction factor appears to be limited by the sensitivity of the powermeter, which can measure light power down to few hundreds of μW. According to the datasheet, the expected isolation should be equal to -41.5 dB, corresponding to a power of about 35 μW.

The insertion of the Faraday isolator along the optical path of the beam induce a small power absorption, which has been characterized by measuring the output-to-input power ratio in the allowed sense of propagation (see fig.8.17):

$$\text{insertion loss} = 10\ \text{Log}\left(\frac{P_{out} = 448\ \text{mW}}{P_{in} = 500\ \text{mW}}\right) = -0.48\ \text{dB}\ .$$

The measured insertion loss is compatible with the expected value reported on the datasheet, equal to -0.5 dB.

Before the isolator, a $\lambda/4$ wave-plate removes the residual elliptic polarization of the laser beam in order to obtain a pure linear polarization. The whole isolator is rotated such that the backward reflections are deviated by the input polarizer cube to a beam dump, thus a $\lambda/2$ wave-plate before the isolator is used to align the polarization of the beam to the input cube.

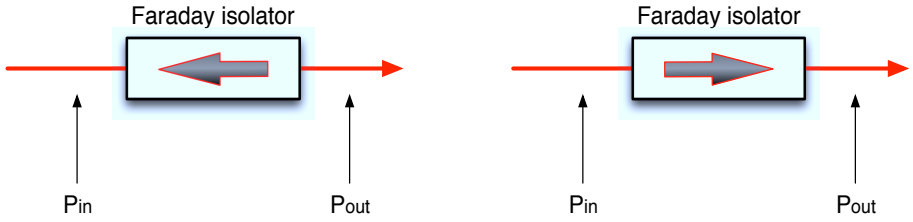

Figure 8.17: Characterization of the Faraday isolator: measurement of the extinction factor (left) and of the insertion loss (right). The allowed direction of propagation in the isolator is shown by the gray arrow.

After the isolator, another $\lambda/2$ retarder rotates the input polarization to make it *s*-oriented, i. e. perpendicular to the plane of the optical table, since several optical components of the setup are optimized for the operation with *s*-polarization. The fraction of light with *s*-polarization at the output of the last $\lambda/2$ wave-plate has been measured with a polarizer cube: the ratio between the total power at the cube input and the *s*-polarized power at the cube output is

$$s\text{-polarized light} = \frac{P_{out} = 349 \text{ mW}}{P_{in} = 350 \text{ mW}} = 99.7\% \ .$$

Electro-optical modulator

The laser beam is focused using the lens L0 into the 2-mm input aperture of an electro-optical modulator, which modulates the phase of the beam to generate the radio-frequency sidebands used in the feedback loop for the laser frequency control. The modulator is a NewFocus 4004 for broadband frequency modulation, formed by a Pockels cell with a birefringent crystal of lithium niobate ($LiNbO_3$) of length l and thickness d. The operation of the modulator is based on the Pockels effect, which is the linear dependence of the crystal refractive index on the applied electric field. By applying a driving sinusoidal voltage, the change in the refractive index causes a periodic phase shift in the input laser beam, which is equivalent to the generation of sidebands.

The effect of the field on the crystal index is described by a three-dimensional electro-optic tensor r_{ij}. If n_e is the unperturbed refractive index and E is the applied field, the induced refractive index change writes

$$\Delta n = \frac{E}{2} n_e^3 \ r_{33} \ . \tag{8.13}$$

The electric field is applied along the crystal axis, transversely to the direction of the laser beam propagation, and is equal to the ratio of the applied voltage V to the crystal thickness: $E \equiv V/d$. The total phase shift corresponding to V is the modulation index m,

$$m = \frac{2\pi}{\lambda} l \Delta n = \beta V \ , \tag{8.14}$$

where

$$\beta = \frac{\pi}{\lambda} \frac{l}{d} n_e^3 \ r_{33} \tag{8.15}$$

in our case is equal to 15 mrad/V. The amplitude of the local oscillator applied to the electro-optic modulator is $V = 14$ V, resulting in a modulation index $m = 0.21$.

Mode-matching telescope

The design of the LG_3^3 diffractive plate requires a collimated LG_0^0 input beam with waist $w_0 = 2.15$ mm, thus we had to realize a mode-matching telescope to magnify the beam coming out of the electro-optical modulator.

The telescope is particularly important, since (as we have seen in section 8.2) the purity of the pseudo-LG_3^3 mode generated by the diffractive plate depends on the parameters of the input LG_0^0 beam. Therefore we need a tunable system, in order to adjust the matching of the input beam to the plate. The limited space available on the optical table puts an additional constraint to the design of the telescope, requiring a design as compact as possible.

We decided to realize a layout composed of three lenses, where the first is used to tune the parameters of the beam and the two others provide its magnification. First we chose the parameters of the telescope (the relative distances of the lenses and the focal lengths) through an approximated analytical computation, then we developed a ray-matrix simulation to optimize this parameters and to study the tolerances of the layout. In the following we will describe the design and the realization of the telescope, and the characterization of its output beam.

Telescope - input beam

As first step of the design process, we characterized the LG_0^0 beam after the modulator[3] through a linear fit of the beam radius w versus the on-axis position z. In the far-field regime, w is expected to follow the relation

$$w = \theta z \ , \tag{8.16}$$

where $\theta = \lambda/\pi w_0^2$ is the beam divergence. The measurements of the beam radius have been acquired with a Beamage Focus II beamscan by Gentec, which is a CCD camera with an active area of 20×15 mm^2 and pixels with 14.5 μm side. The beamscan is equipped with a dedicated software for beam diagnostics, which gives the radius of the detected beam as output.

For each position on the z axis, the beam radius has been measured with five consecutive acquisitions, and the average value and the variance of each sample have been computed. The averages and the square root of the sample variances have been used in the linear fit as data points and measurement errors for w, respectively. The order of magnitude of the error is few μm. The origin of the z axis is set at the position of the first measurement, so the points are fitted with a slope that is

$$w = \theta z \ + \bar{w} \ , \tag{8.17}$$

and the position of the beam waist is computed as $z_0 = -\bar{w}/\theta$, considering that the waist is located behind the z axis origin. The fit, shown in fig.8.18, has been performed for the beam radius on the x and y axis separately, yielding the values reported in table 8.1.

The resulting position of the waist is close to the input aperture of the electro-optic modulator, as expected. The plot of the fit and the large reduced χ^2 values indicate that the fit uncertainties are underestimated. By arbitrarily increasing the error bars to 10^{-5} m, the reduced χ^2 values gets closer to 1. The new fit yields the results reported in table 8.1 for comparison.

[3]The characterization of the beam has been performed after having verified the linear far-field condition with few preliminary measurements of w and z.

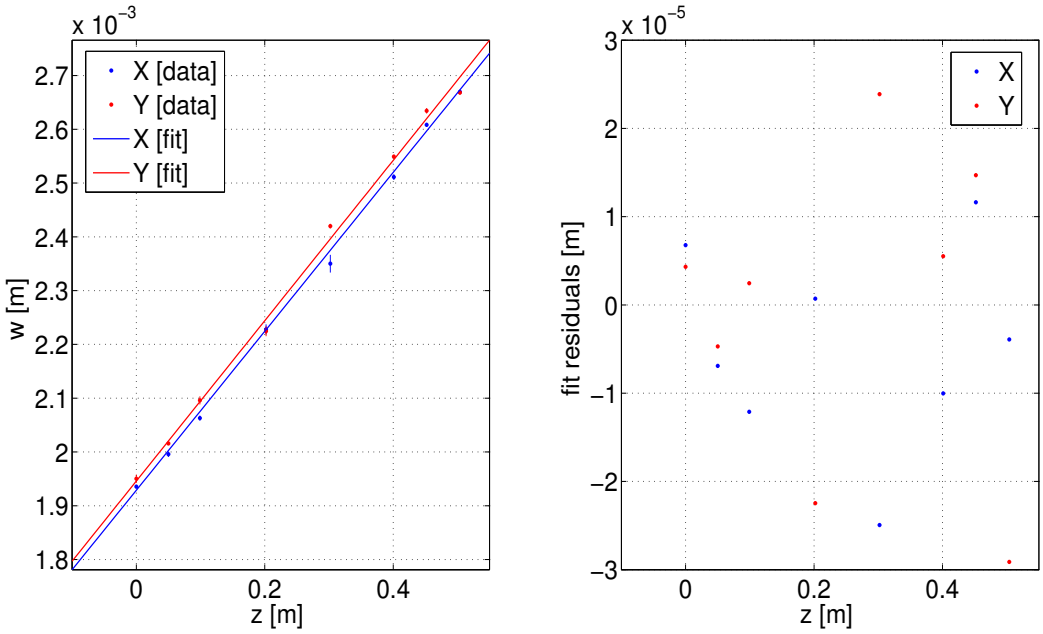

Figure 8.18: Characterization of the LG_0^0 input beam: linear fit of the beam size w versus the position on the optical axis z (left) and dispersion of fit residuals (right).

transverse direction	waist	distance to waist	reduced χ^2
x	$w_0 = 229 \pm 1$ μm	$z_0 = -1.305 \pm 0.005$ m	4.5
y	$w_0 = 227 \pm 1$ μm	$z_0 = -1.306 \pm 0.005$ m	24.1
x	$w_0 = 229 \pm 4$ μm	$z_0 = -1.30 \pm 0.02$ m	0.9
y	$w_0 = 228 \pm 4$ μm	$z_0 = -1.31 \pm 0.02$ m	2.2

Table 8.1: Characterization of the telescope input beam: results of the linear fit of fig.8.18 with statistical uncertainties ($\sim 10^{-6}$ m, top rows), and with arbitrarily increased uncertainties (10^{-5} m, bottom rows).

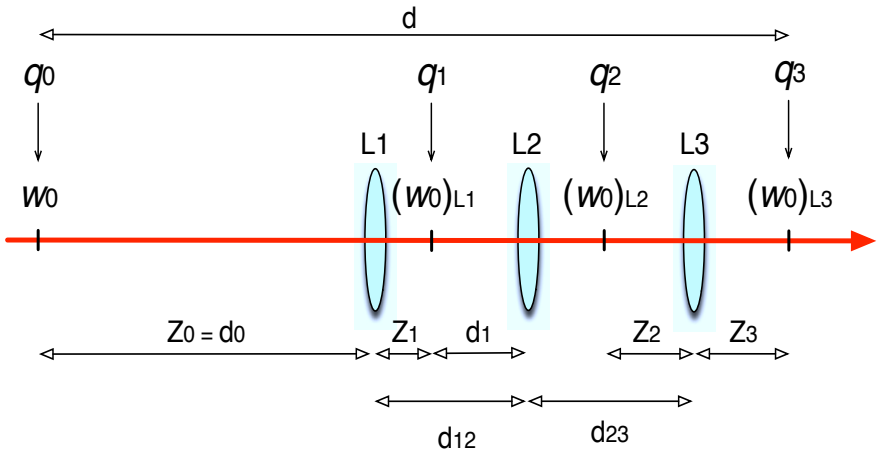

Figure 8.19: Layout of the LG_0^0 beam mode-matching telescope.

Thus the parameters of the telescope input beam are known within $\sim 2\%$ error: the telescope has to magnify the beam size of about one order of magnitude, from $w_0 = 229$ μm to $w_0 = 2.15$ mm.

Telescope - optical layout

The layout of the telescope is shown in fig.8.19: L1, L2 and L3 are three converging lenses, L1 is placed in far field with respect to the input beam waist w_0, L2 and L3 form an afocal system which provides the magnification of w_0. L1 is used for tuning the parameters of the beam that goes through the afocal system.

The working principle of this layout can be understood by computing the complex beam parameter q at different positions inside the telescope. We will refer to fig.8.19 for the notation used hereafter. Let $q_0 = z_0 + iz_{R0}$ be the parameter of the telescope input beam. For L1 we have $z_0 >> z_{R0}$, so we can approximate eqs.(5.29) to compute

$$\begin{aligned} z_1 &\simeq \tfrac{f_1 z_0}{f_1 - z_0} \\ z_{R1} &\simeq \tfrac{f_1^2 z_{R0}}{f_1 - z_1} \ . \end{aligned} \tag{8.18}$$

If moreover $z_0 >> f_1$, then $z_1 \simeq -f_1$ and $z_{R1} \simeq z_{R0}\big(f_1^2/z_0\big)^2$. This means that by tuning the position z_0 of L1 the size of the waist $(w_0)_{L1}$ can be changed, while its position z_1 remains almost constant and equal to $-f_1$ (z_1 is negative because the beam is converging after the lens). In the case of the afocal system formed by L2 and L3, where $z_2 \equiv f_3$, eqs.(5.29) become

$$\begin{aligned} z_3 &= -f_3 \\ z_{R3} &= f_3^2/z_{R2} \ . \end{aligned} \tag{8.19}$$

Thus, by choosing $f_3 = Cz_{R2}$, eq.(8.19) for q_3 yields

$$\begin{aligned} z_3 &= -Cz_{R2} \\ z_{R3}/z_{R2} &= C^2 \ , \end{aligned} \tag{8.20}$$

so the waist $(w_0)_{L3}$ is magnified of a factor C. L2 is used to focus the beam before L3 and shorten its Rayleigh range z_{R2}, in order to keep the distance $z_3 = -Cz_{R2}$ small.

The available space on the optical table allows to choose $z_0 = 75$ cm, which according to the characterization of the telescope input beam (see table 8.1) yields $z_0/z_{R0} \simeq 5$, and is compliant with the beam far-field condition that we imposed initially for L_1. By choosing $f_1 = 10$ cm, also the condition $z_0 >> f_1$ is fulfilled and $(w_0)_{L1}$ is expected to measure about 35 μm.

f_2 is chosen to be as small as f_1 to focus the beam within the afocal telescope, so $f_2 = 10$ cm. The distance d_1 is chosen so that also L2 is placed in the beam far-field range: with this further approximation we can replace $z_{R2} \simeq z_{R1}\left(f_2^2/d_1\right)^2$ in eq.(8.19) to find

$$f_3/f_2 = \sqrt{z_{R3}z_{R1}}/d_1 \ , \tag{8.21}$$

which is the relation used to compute the focal lens of L3. For $d_1 = 150$ mm, $f_3/f_2 \simeq 1.5$ so $f_3 = 150$ mm. The lengths $d_{12} = z_1 + d_1 = 265$ mm and $d_{23} = z_2 + f_3 = 500$ mm were fixed by the layout of the telescope. The total length of this system (computed from w_0 to the expected position of $(w_0)_{L3}$) is $d = z_0 + d_{12} + d_{23} + z_3 = 1715$ mm, and fits well on the optical table.

Telescope - fine tuning and tolerances

The design of the telescope has been finalized by optimizing the layout parameters, calculated so far with approximated equations. The optimization has been performed by computing the beam propagation throughout the telescope, with the ray-matrix formalism [95]. The whole system can be represented by a matrix M_{tel}, whose elements depends on the layout parameters:

$$M_{tel}(f_1, f_2, f_3, d_{12}, d_{23}) = L_3 \ D_2 \ L_2 \ D_1 \ L_1 \ D_0 \ , \tag{8.22}$$

where

$$D_i = \begin{pmatrix} 1 & d_i \\ 0 & 1 \end{pmatrix}, \ L_j = \begin{pmatrix} 1 & 0 \\ -1/f_j & 1 \end{pmatrix} \ . \tag{8.23}$$

Thus the magnified output beam is

$$q_3(f_1, f_2, f_3, d_{12}, d_{23}) = \frac{M_{tel}(1,1)q_0 + M_{tel}(1,2)}{M_{tel}(2,1)q_0 + M_{tel}(2,2)} \ . \tag{8.24}$$

Eq.(8.24) is equivalent to applying sequentially eq.(5.28) for all the lenses of the telescope.

Eq.(8.22) and (8.24) have been implemented in a Matlab script, where:

- q_0 is computed from the fit parameters of eq.(8.17)
- f_2, f_3, d_{12}, d_{23} are automatically changed in a loop, within an arbitrary given interval
- the waist size $(w_0)_{L3}$ is computed at each step of the loop.

telescope design parameters	
f_1	100 mm
f_2	100 mm
f_3	200 mm
z_0	785 mm
z_1	114 mm
z_2	197 mm
z_3	200 mm
d_1	203 mm
d_{12}	317 mm
d_{23}	397 mm
w_0	228 μm
$(w_0)_{L1}$	32.5 μm
$(w_0)_{L2}$	31.5 μm
$(w_0)_{L3}$	2.15 mm

Table 8.2: Parameters of the telescope layout of fig.8.19.

This script has been used first to tune the distances d_{12}, d_{23} in the design, in order to get $(w_0)_{L3} = 2.15$ mm at the telescope output. The parameters that yield this waist size are listed in table 8.2.

Then we used the script to compute the tolerances of the system with respect to manufacturing errors of the focal lengths, and errors in the positioning of the optics. The output tolerances computed through the script are shown in the plots of figs.8.20 and 8.21. In order to have $(w_0)_{L3} = 2.15 \pm 0.05$ mm, the tolerance for the focal length of f_2 is $\pm \simeq 0.3$ %, and ± 1 % for f_3. Concerning the distances, L2 must be positioned with a maximum error of $\pm \simeq 0.5$ mm, and L3 with a maximum error of ± 2 mm.

As declared by the manufacturer, the typical error for the focal lengths is expected to be ± 1 %. Moreover, the lenses have been positioned on the table with an error of ± 3 mm, due to the difficulty of measuring accurately d_{12} and d_{23} with a tape measure. To compensate for manufacturing and positioning errors, the optics have been mounted on optical rails with micrometrical translation stages: the setup used is shown in fig.8.22. It allows to tune the telescope lengths after the optics have been placed on the table, in order to obtain $(w_0)_{L3} = 2.15$ mm at the output of the system, even in presence of errors.

The optical rails provide the possibility to tune the position of the optics with a minimum displacement of few mm, on a large dynamic range of 20 cm. The fine tuning of the position is achieved with the micrometrical translation stages, which provide a longitudinal displacement of few tens of microns over ± 5 mm.

The telescope has been tuned by moving the lenses around their initial positions, while measuring the output beam size with the beamscan. The best tuning has been achieved for $d_{12} = 345$ mm and $d_{23} = 386$ mm, yielding a beam with $(w_0)_{L3} = 2.19$ mm and $(w_0)_{L3} = 2.16$ on the x and y transverse directions, respectively.

An image of the beam is acquired at $z_3 = 200$ mm, where the collimated beam has its waist. It is shown on fig.8.23: the beam features a low astigmatism, which entails an ellipticity of 0.99. To estimate the purity of this beam, the intensity distribution is acquired with the beamscan at

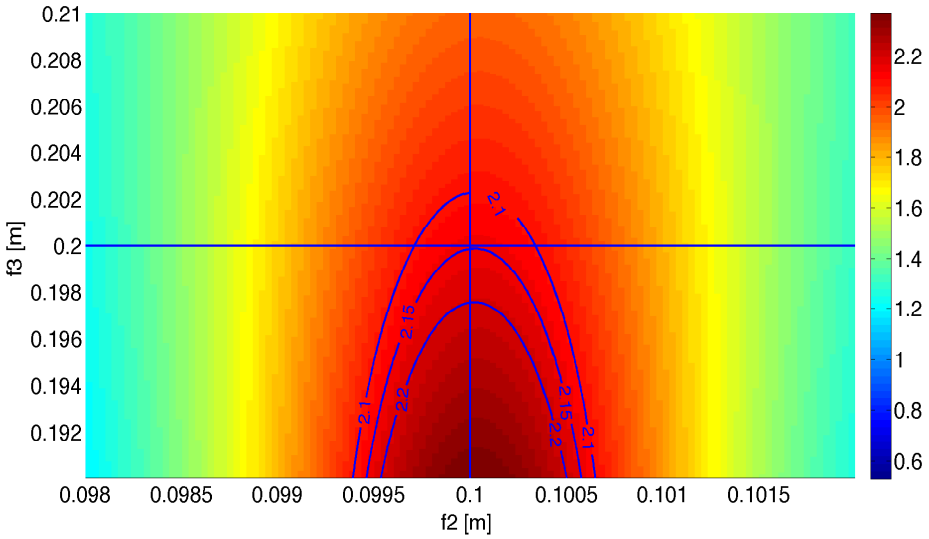

Figure 8.20: Tolerances of the telescope focal lengths: f_2 [m] and f_3 [m] are shown on the x and the y axis, respectively, and the vertical/horizontal lines represent the baseline values. The color scale indicates the size of $(w_0)_{L3}$ [mm], the contours show the region for a change of the waist size of ± 0.05 mm.

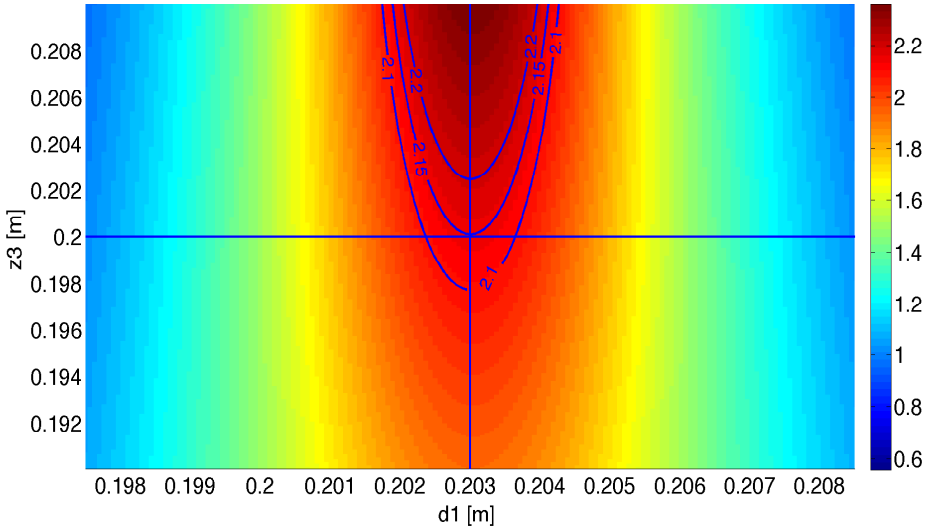

Figure 8.21: Tolerances of the telescope lengths: d_1 [m] and z_3 [m] are shown on the x and the y axis, respectively, and the vertical/horizontal lines represent the baseline values. The color scale indicates the size of $(w_0)_{L3}$ [mm], the contours show the region for a change of the waist size of ± 0.05 mm.

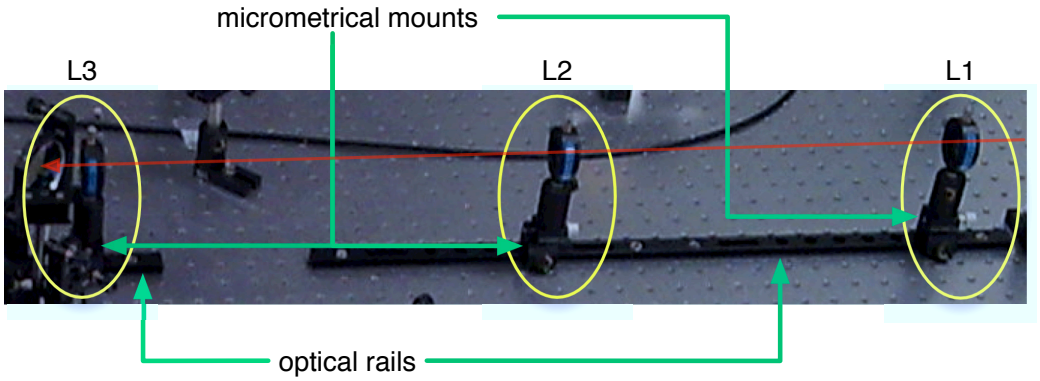

Figure 8.22: Setup for the tuning of the telescope lengths.

the focal plane of L3, and the overlap integral defined in eq.(8.4) is used. The integral is computed between the square roots of the theoretical and the measured intensity distributions, where the theoretical one is given by the square modulus of eq.(5.13) with $w_0 = 2.15$ mm. Since the phase of the modes is neglected, this computation puts an upper limit on the purity of the LG_0^0 mode, measured at the output of the telescope:

$$\gamma = \left\langle LG_0^0|_{theory} \middle| LG_0^0|_{measure} \right\rangle = 99.4\% \ . \tag{8.25}$$

We then decided that the quality of this beam is acceptable for our scope.

8.6 Mode Conversion: LG_0^0 to Pseudo-LG_3^3

The setup for the mode conversion is shown in fig.8.24: the output beam of the mode-matching telescope goes through the LG_3^3 diffractive plate (DP in the figure), mounted on a three-axis translation stage for high-precision alignment. The diffracted beam is focused by a 600 mm lens (L6) on the input mirror of the mode-cleaner cavity. Before the plate, a pick-off (PO1) with reflectivity $R = 9.6\%$ samples a fraction of the LG_0^0 beam, and sends it to the mode-cleaner.

This setup is used to switch between the LG_0^0 and the pseudo-LG_3^3 modes, since each beam can be blocked independently. The swap between the modes is needed for the pre-alignment of the pseudo-LG_3^3 beam to the mode-cleaner, following a procedure explained in section 8.7. The pseudo-LG_3^3 and the LG_0^0 beams recombine at a second pick-off (PO2) which has reflectivity $R = 8.3\%$. The pseudo-LG_3^3 beam reflected by PO2 is sent to a CCD camera.

Alignment of the diffractive plate

According to the study of alignment tolerance performed by SILIOS, in order to generate the optimal pseudo-LG_3^3 mode shape, the diffractive plate has to be centered in the input LG_0^0 beam transverse plane with an accuracy of the order of 100 μm. For this reason the plate is mounted on a three-axis translation stage Thorlabs PT3 which allows a displacement accuracy of 10 μm.

The plate is put in place with the following procedure: first the input LG_0^0 beam is analyzed with the beamscan, in order to fix the position of the beam centroid on the CCD active surface.

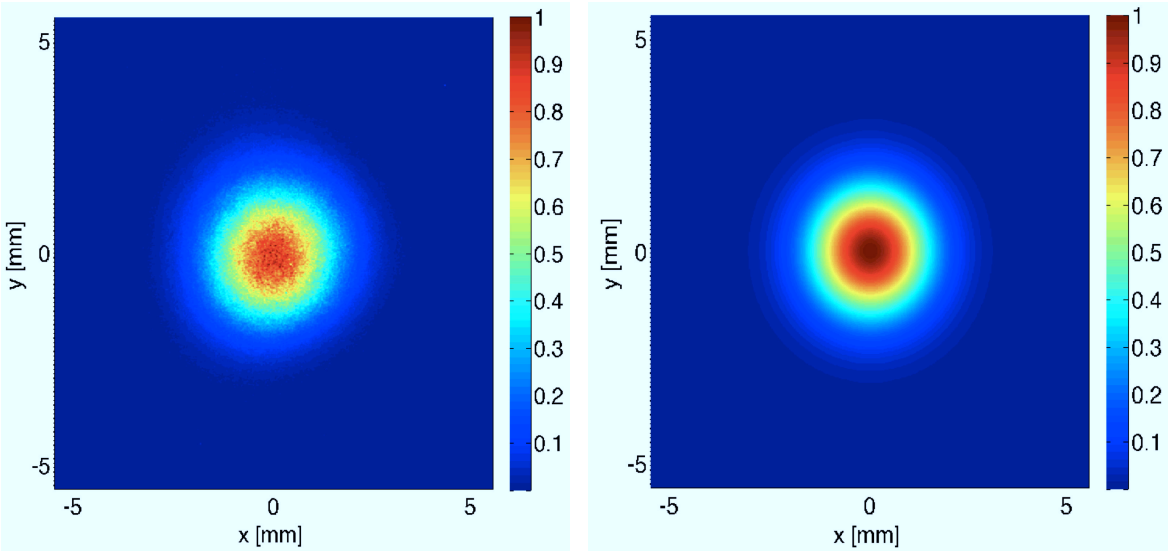

Figure 8.23: Telescope output LG_0^0 mode: normalized measured intensity [a.u.] (left) and normalized theoretical intensity [a.u.] (right).

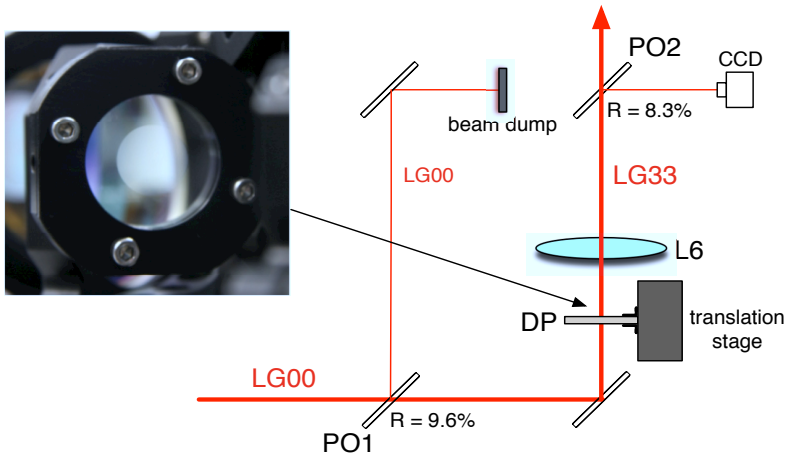

Figure 8.24: Setup for the generation of the LG_3^3 beam.

The centroid is defined as the weighted average of the displacement vector on the transverse plane,

$$\vec{r}_0 = \frac{\int I(r,\theta)\vec{r}\, dS}{\int I(r,\theta)\, dS} \ , \tag{8.26}$$

and in this case it coincides with the geometrical center of the input LG_0^0 beam. The cross hair pointing to $\vec{r}_0$ is recorded on the beamscan, which is kept in the same position during the alignment.

The plate is then roughly positioned on the path of the beam, before the camera, where it is possible to observe the plate pattern covering the cross section of the beam. The alignment is tuned with the translation stage, to superpose the center of the plate (clearly indicated by the diffractive pattern) to the centroid of the beam. This procedure is illustrated on fig.8.25.

Successively the 600 mm lens is installed, and the pseudo-LG_3^3 beam at the focal plane of the lens is monitored with the beamscan: the ultimate tuning of the alignment of the plate is achieved by optimizing the cylindrical symmetry of its power distribution. The residual tilt of the plate with respect to the beam transverse plane is considered negligible.

Characterization of the diffractive plate

In order to characterize the behavior of the plate, we first measured the power conversion efficiency ϵ_{DP}. As expected, when we illuminated the plate with the input LG_0^0 beam, we observed several output diffraction orders, with decreasing intensity with respect to the order m. The intensity distribution of orders up to $m = \pm 2$ can be clearly distinguished by eye with a beam viewer, whereas higher orders are too faint to be seen.

These diffraction orders propagate along different directions, forming an angle θ_m with respect to the optical axis of the input LG_0^0 beam. Supposing that the input beam is perpendicular to the diffractive plate, the angle θ_m is defined through the grating equation,

$$\Lambda \sin\theta_m = m\lambda \ . \tag{8.27}$$

The period of the grating being $\Lambda = 235\ \mu$m, the first order should be spaced from the 0-th order by 2720 μm at the focal plane of the 600 mm lens. For larger distances from the lens, the different orders are more and more spaced, and the power of the first order can be measured with a power-meter placed behind an iris.

Fig.8.26 shows an image of the first diffraction order with the shape of the generated pseudo-LG_3^3 mode, together with a faint spot of the 0-th unmodulated order of Gaussian shape. The distance between the geometric center of the two beams is 2988 μm, compatible with the expected spacing. On the first order, the efficiency of the LG_3^3 diffractive plate is

$$\epsilon_{DP} = \frac{(P_{LG_3^3})_{m=1} = 312 \text{ mW}}{P_{LG_0^0} = 383 \text{ mW}} = 81.5\% \ .$$

This value of efficiency is slightly higher than expected (76%, see section 8.2), possibly due to the presence of some spurious light from other diffraction orders. In any case, the application of an anti-reflective coating on the non-etched surface of the plate is expected to increase this efficiency.

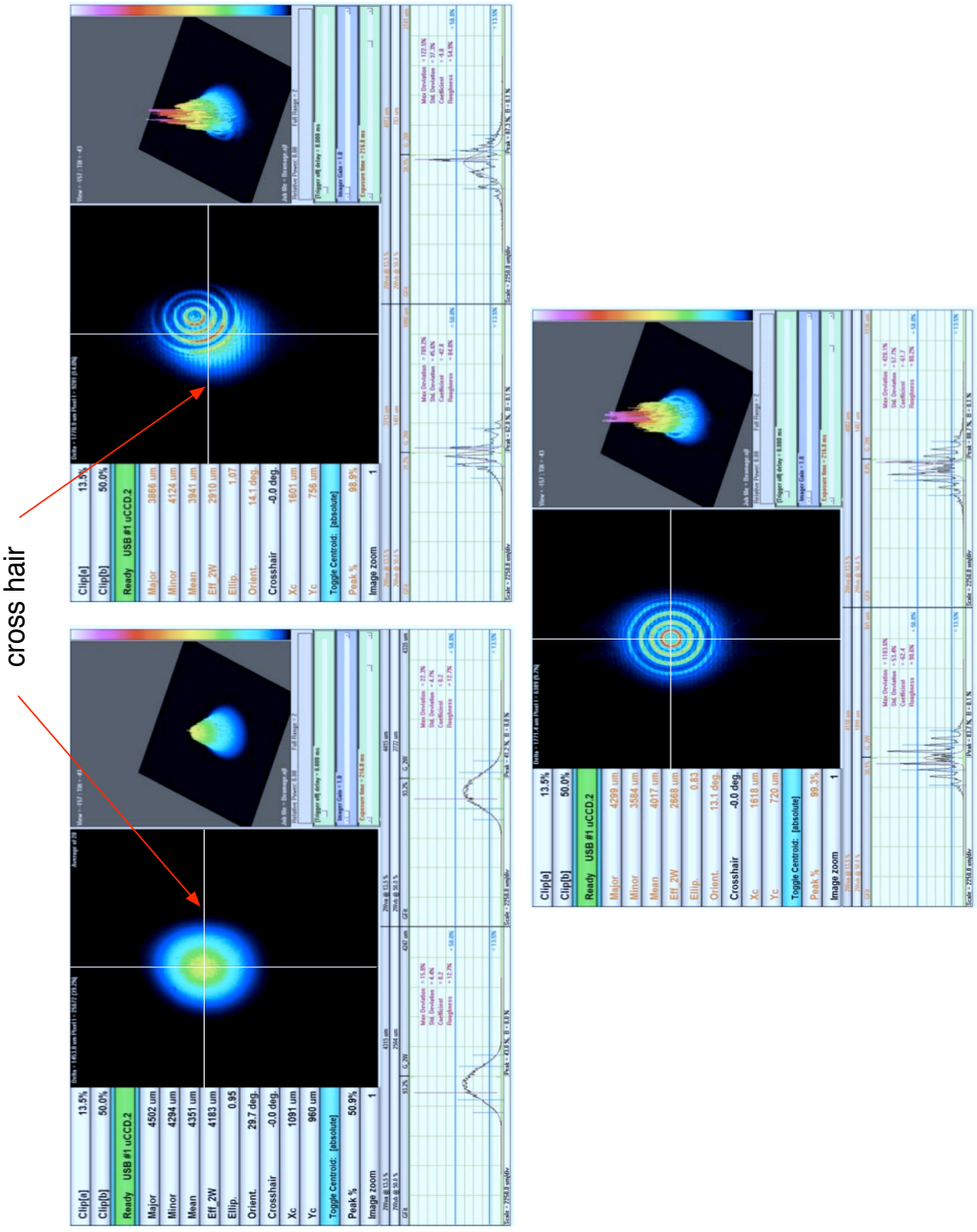

Figure 8.25: Alignment of the LG_3^3 diffractive plate with the beamscan: (i) record of the beam centroid position, indicated by the cross hair on the active area of the detector (top left), (ii) rough positioning of the plate before the beamscan (top right), (iii) superposition of the plate center on the beam centroid (bottom).

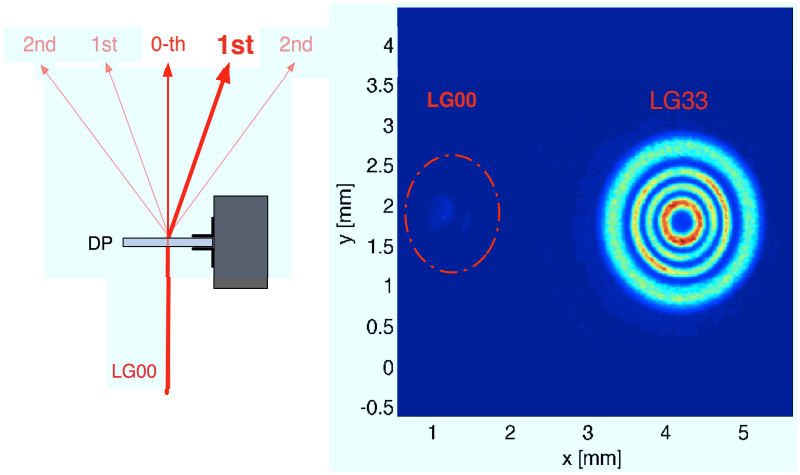

Figure 8.26: Diffraction orders of the LG_3^3 plate: scheme (left) and measured zero-th and first orders (right).

Analysis of the generated pseudo-LG_3^3 mode

The correct evaluation of the generated mode purity would be the computation of the overlap integral γ defined in eq.(8.4), but in our experiment only the information about the intensity distribution of the generated pseudo-LG_3^3 mode is available. The purity can be thus computed using the square root of beam intensities, instead of complex amplitudes, yielding an upper limit estimation.

An image of the pseudo-LG_3^3 mode intensity distribution is acquired with the beamscan in the focal plane of the 600 mm lens, where the mode is expected to have its waist. The position of the waist is found by manually moving the camera along the optical axis, close to the lens focal plane, and looking for the minimum beam size during a continuous run of image acquisition. The waist position is found at 600 ± 50 mm from the lens, where the error is due to the difficulty of appreciating by eye the small variations of the beam size observed with the beamscan. The measured pseudo-LG_3^3 mode yields a purity upper limit $\gamma = 88\%$, compatible with the purity predicted through FFT simulations (85%, see section 8.2). The coupling losses of the generated mode are $L = 1 - \gamma^2 = 23\%$, i. e. 23% of the converted power is not an LG_3^3 mode.

Fig.8.27 shows the measured intensity distribution of the pseudo-LG_3^3 mode, compared to the expected LG_3^3 mode for $w_0 = 288$ μm. Fig.8.28 illustrates the comparison between the cross-sectional profiles of the expected and of the pseudo-LG_3^3 mode intensities. There are several differences between the two. Their overlap is good only for the highest internal peaks, whereas the outer rings of the pseudo mode are shifted outwards, and the mode is globally larger. Some power of the pseudo mode is left at the radial nodes, and the relative amplitude of the peaks of the theoretical mode is not respected.

A least-square fit of the measured intensity profile versus the radial coordinate r is shown in fig.8.29. The radial measured profile $I(r)$ is obtained by carrying out an average over the azimuthal coordinate θ in the transverse plane, as follows:

1. the two-dimensional transverse intensity distribution $I(r, \theta)$ of the mode is discretized with radial bins of the same size of the beamscan pixels, forming concentric annuli

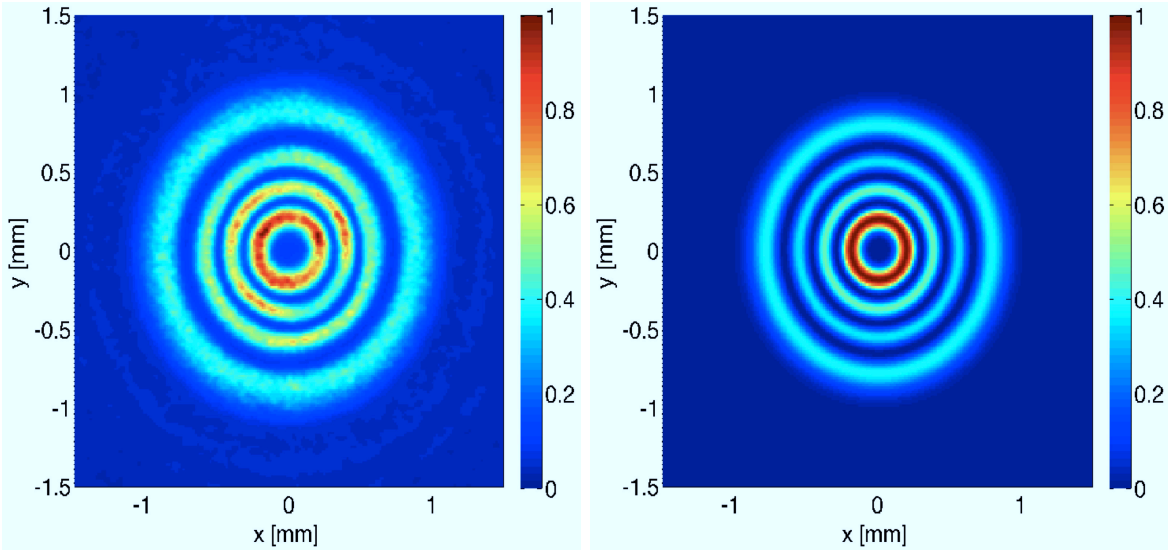

Figure 8.27: Comparison between normalized intensity distributions at waist: measured pseudo-LG_3^3 mode (left) and theoretical LG_3^3 mode for $w_0 = 288$ μm (right).

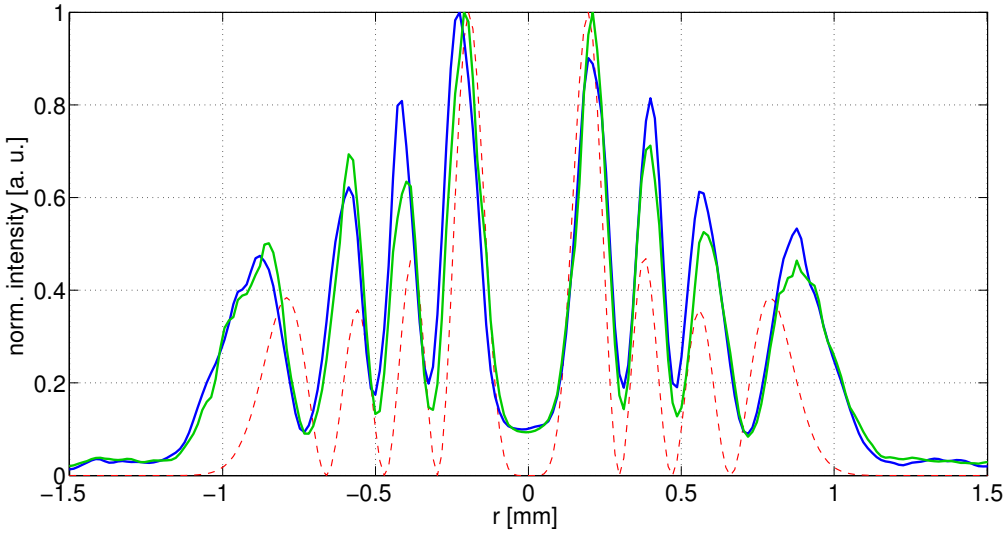

Figure 8.28: Profile comparison: the horizontal (blue solid curve) and the vertical (green solid curve) measured cross sections of the pseudo-LG_3^3 mode are shown, together with the cross section of the theoretical LG_3^3 mode for $w_0 = 288$ μm (red dashed curve).

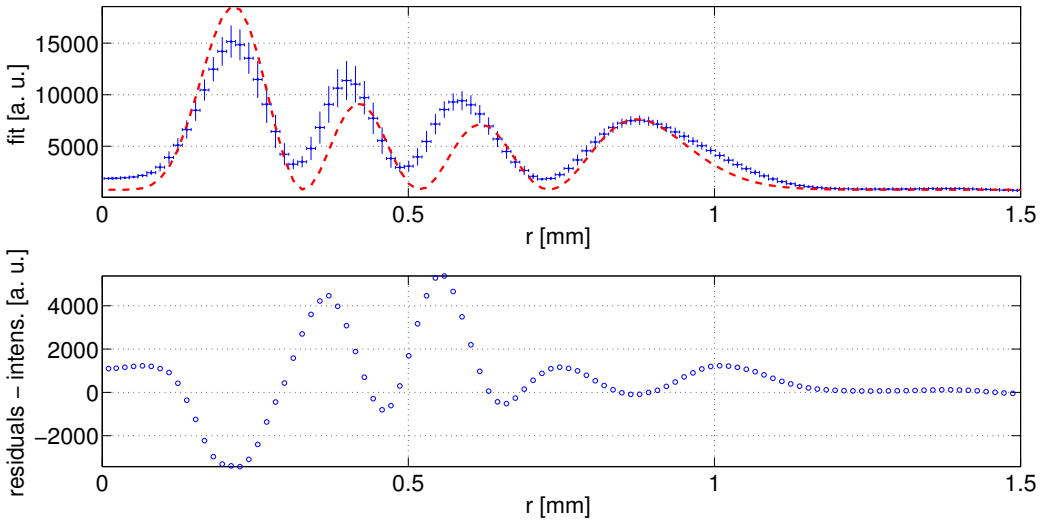

Figure 8.29: Least square fit of the pseudo-LG$_3^3$ mode profile. Top panel: measured (blue dots with errors) and fitted (red dashed curve) profiles in the $r > 0$ plane. Bottom panel: fit residuals, defined as the difference between the data and the model.

2. the intensity associated to each bin is the azimuthal average of $I(r, \theta)$ over 2π, within the single annulus. Due to the spatial defects of the pseudo-LG$_3^3$ mode, the variance of the intensity in each annulus is not null. Its square root is taken as the error σ associated to each azimuthal average.

The error on the radial position (not used in the fit) due to the discretization process is arbitrarily chosen to be half of the pixel size. The fit of $I(r)$ is performed over the $r > 0$ plane, and the fit parameters are calculated by minimizing the function

$$\chi^2(A_3^3, B, w_0) = \sum_{i=1}^{N} \left(\frac{I_3^3(r_i)\big|_{measure} - I_3^3(r_i, A_3^3, B, w_0)\big|_{theory}}{\sigma_i} \right)^2 , \tag{8.28}$$

where $I_3^3(r, A_3^3, B, w_0)\big|_{theory}$ is the square modulus of the LG$_3^3$ mode complex amplitude of eq.(5.13):

$$I_3^3(r, A_3^3, B, w_0)\big|_{theory} = \frac{A_3^3}{w_0^2} \exp\left[\frac{-2r^2}{w_0^2}\right] \left(\frac{2r^2}{w_0^2}\right)^3 \left[L_3^3\left(\frac{2r^2}{w_0^2}\right)\right]^2 + B \ . \tag{8.29}$$

A_3^3 is the normalization factor for the LG$_3^3$ mode, B is the background noise due to the potential presence of residual environmental light collected by the beamscan, w_0 is the beam waist. The fit yields

$$\begin{aligned} A_3^3 &= 7.8 \cdot 10^{-5} \text{ [a. u.]} \\ B &= 780 \text{ [a. u.]} \\ w_0 &= 318 \cdot 10^{-6} \text{ m} \ , \end{aligned} \tag{8.30}$$

with a reduced χ^2 equal to 24.9 (for 255 points and 3 parameters). The position of the innermost and the outermost peaks of the generated pseudo-LG$_3^3$ mode is well fitted by a theoretical mode

with $w_0 = 318$ μm, which is only 10% larger than expected. The relevant difference between the model and the measured profile (stressed by the large fit residuals and reduced χ^2 value) is in the relative amplitude and in the position of the intermediate peaks. This indicates that the difference between the theoretical and the pseudo-LG$_3^3$ modes is not only due to a size mismatch, and that the pseudo mode has spatial defects induced by the plate.

Though the measurement of the intensity distribution of the pseudo-LG$_3^3$ mode has been performed in a dark environment, some background can be also present, since it is not possible to darken the room completely. Nevertheless the environmental background light cannot completely explain all the power left at the radial nodes, which is likely a spatial defects of the mode itself.

8.7 Alignment of the Pseudo-LG$_3^3$ to the Mode-Cleaner

When we tried for the first time to align directly the pseudo-LG$_3^3$ mode to the mode-cleaner, we could not achieve the alignment only by looking at the shape of the mode transmitted through the cavity, as it was possible for some alignment tests with the Gaussian beam. As the input pseudo-LG$_3^3$ mode is misaligned with respect to the cavity optical axis, the shape of the all eigenmodes resonating in the cavity was so distorted that they could not be distinguished from each other. We then realized that we had to pre-align the beam to the cavity with the Gaussian beam, by using a procedure described here below.

The setup we used is sketched in fig.8.30: a mirror installed on a flip mount, two near-field and far-field CCD cameras for the mutual alignment of the LG$_3^3$ and LG$_0^0$ beams, two steering mirrors (SM) mounted on high-precision ultra-stable mounts, a movable beam dump. The procedure for the manual pre-alignment of the pseudo-LG$_3^3$ mode is the following:

1. both the pseudo-LG$_3^3$ beam and the LG$_0^0$ pick-off beam can propagate in the setup. The flip mount mirror is switched up in order to deviate the beams to the path of mutual alignment (sketched with a dashed line in fig.8.30), where the two CCD cameras are installed. The near-field camera is placed at the focal plane of L6, where is the waist of the pseudo-LG$_3^3$ beam. The far-field camera is placed at 1.65 m from the position of the waist, about 7 times farther than the Rayleigh range of the pseudo-LG$_3^3$ beam, equal to 24.5 cm. The LG$_0^0$ beam is superposed to the pseudo-LG$_3^3$ beam by turning the screws of the standard optical mounts of PO1 and M0. The superposition is carried out by observing the interference pattern of the two beams on the cameras, and optimizing the radial symmetry of the pattern. The superposition of the beams on both cameras guarantees that the beams are aligned over a long baseline, which is large enough with respect of the typical lengths of propagation to the mode-cleaner

2. the flip mount is switched down, and the pseudo-LG$_3^3$ beam is blocked with the beam dump. The LG$_0^0$ beam is accurately aligned to the mode-cleaner with the steering mirrors, which are mounted on ultra-stable Thorlabs KS1D mounts. These mounts, whose calibration has been measured before their installation, deliver an angular displacement of the beam of 660 μm per revolution of the tuning screws. The alignment is tuned until the power of HG$_{01}$ and HG$_{10}$ modes that initially resonate in the cavity, due to misalignment, is decreased to a negligible level

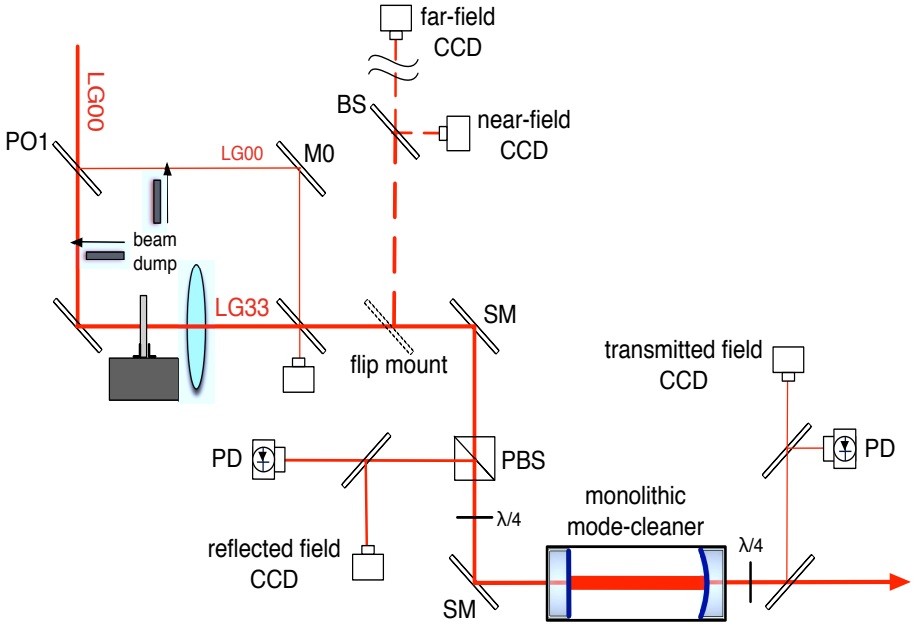

Figure 8.30: Setup for the alignment of the pseudo-LG_3^3 mode.

3. the LG_0^0 beam is blocked with the beam dump and the pseudo-LG_3^3 beam propagates to the mode-cleaner, following the aligned path of the LG_0^0 beam

After this procedure, the pre-alignment of the pseudo-LG_3^3 beam is largely improved, so that it is possible to lock the cavity. The fine tuning of the alignment is performed by optimizing manually the radial symmetry of the reflected mode, monitored by a dedicated CCD camera. Fig. 8.31 shows three images of the field reflected by the mode-cleaner, when the LG_3^3 eigenmode is resonant inside the cavity.

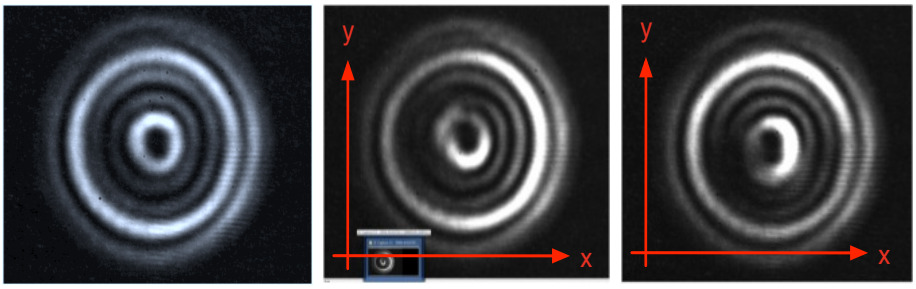

Figure 8.31: Field reflected by the mode-cleaner at the resonance of the LG_3^3 cavity eigenmode: aligned field (left), x misalignment (center), y misalignment (right). The reference frame on the transverse plane is shown by the red axes.

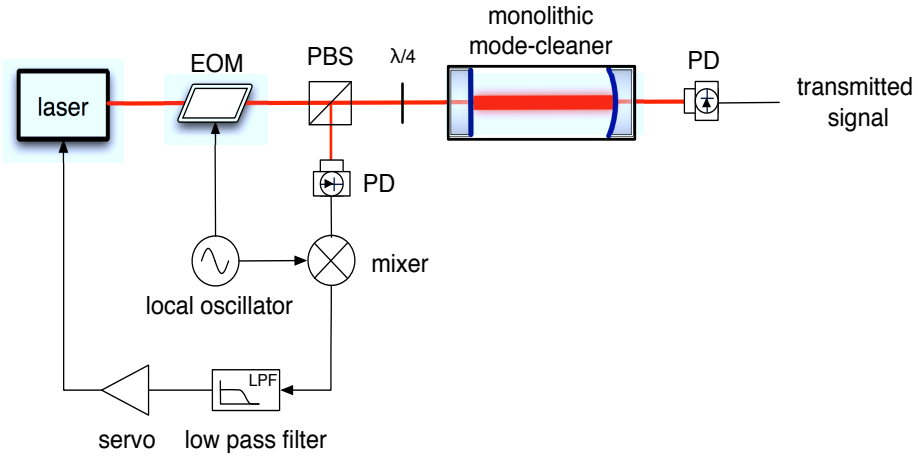

Figure 8.32: Pound-Drever-Hall locking scheme in reflection, for the lock of the LG_3^3 mode resonance.

8.8 Mode-Cleaner Lock

The laser frequency is locked on the frequency of the mode-cleaner LG_3^3 eigenmode through a standard Pound-Drever-Hall scheme [83, 84] in reflection, as sketched in fig.8.32: the laser beam passes through the electro-optic modulator (EOM), where the laser frequency is phase-modulated with a radio-frequency signal used also as local oscillator for demodulation. Thus an upper and a lower sideband fields are generated at the modulation frequency, which propagate with the carrier field to the mode-cleaner. Here the fields are partially reflected, with a phase determined by their frequency. The reflected beam is picked off by a polarizer cube (PBS), and sent to a photodiode (PD). The modulation frequency is chosen large enough (10 MHz) so that the sidebands are poorly transmitted by the cavity (half linewidth $\sim$ 2.5 MHz) when the carrier frequency is resonant, as shown on fig.8.33.

The reflected beat pattern of the carrier and the sidebands depends on the phase of the reflected fields, and contains the error signal which is used to control the laser frequency. The error signal is extracted through demodulation, by mixing the photodiode signal with the local oscillator, and filtering the output with a low-pass filter. The signal is amplified by an analog servo, before it is sent to the laser to control its frequency. Within the cavity linewidth, the error signal is linearly proportional to the deviation from the resonance.

Pound-Drever-Hall error signal

In the following we will compute the theoretical Pound-Drever-Hall error signal, in order to compare it to the measured one. Let the input field of the modulator be

$$E = E_0 e^{i\omega_0 t} \ , \tag{8.31}$$

and let the local oscillator be a sinusoidal function with angular frequency Ω,

$$V_{LO} = V_0 \sin \Omega t \ . \tag{8.32}$$

After the beam has passed through the Pockels cell of the modulator, its electric field has its phase modulated in time, and becomes

$$E = E_0 e^{i(\omega_0 t + m \sin \Omega t)} \ . \tag{8.33}$$

According to the Jacobi-Anger identity, eq.(8.33) can be expanded in series using the Bessel functions of the first kind $J_k(m)$,

$$E = E_0 e^{i\omega_0 t} \sum_{k=-\infty}^{\infty} J_k(m) e^{ik\Omega t} \ . \tag{8.34}$$

The field for $k = 0$, oscillating with the frequency of the input field ω_0, represents the *carrier*. The light fields shifted in frequency by $k\Omega$ are the *sidebands*, which can be divided into upper ($k > 0$) and lower ($k < 0$) sidebands. The upper and lower sidebands with the same absolute value of k are called a pair of sidebands of order k. Eq.(8.34) shows that the carrier is surrounded by an infinite number of sidebands. However, the Bessel functions decrease for large values of k, so for small modulation indices, $m << 1$, the field after the modulator can be approximated by

$$E \simeq E_0 (J_0(m) e^{i\omega_0 t} + J_{-1}(m) e^{i(\omega_0 - \Omega)t} + J_1(m) e^{i(\omega_0 + \Omega)t}) \ . \tag{8.35}$$

Since $J_{-k}(m) = (-1)^k J_k(m)$, the output field of the modulator can be finally written as

$$E \simeq E_0 (J_0(m) e^{i\omega_0 t} - J_1(m) e^{i(\omega_0 - \Omega)t} + J_1(m) e^{i(\omega_0 + \Omega)t}) \ . \tag{8.36}$$

Assuming that the input field is the sum of the carrier and the two first-order sidebands, the total field reflected by the mode-cleaner is

$$E_r = E_0 (R_{MC}(\omega_0) J_0(m) e^{i\omega_0 t} - R_{MC}(\omega_0 - \Omega) J_1(m) e^{i(\omega_0 - \Omega)t} + R_{MC}(\omega_0 + \Omega) J_1(m) e^{i(\omega_0 + \Omega)t}) \ , \tag{8.37}$$

where $R_{MC}(\omega)$ is the frequency-dependent reflectivity of the mode-cleaner cavity from eq.(2.81). The corresponding reflected power is thus $P_r = |E_r|^2$, equal to

$$\begin{aligned} P_r = \ & P_{CARR} |R_{MC}(\omega_0)|^2 + P_{SBs} (|R_{MC}(\omega_0 - \Omega)|^2 + |R_{MC}(\omega_0 + \Omega)|^2) + \\ & + 2\sqrt{P_{CARR} P_{SBs}}\ \mathfrak{Re}\Big[R_{MC}(\omega_0) R^*_{MC}(\omega_+ \Omega) - R^*_{MC}(\omega_0) R_{MC}(\omega_- \Omega) \Big] \cos \Omega t + \\ & + 2\sqrt{P_{CARR} P_{SBs}}\ \mathfrak{Im}\Big[R_{MC}(\omega_0) R^*_{MC}(\omega_+ \Omega) - R^*_{MC}(\omega_0) R_{MC}(\omega_- \Omega) \Big] \sin \Omega t + \\ & - 2P_{SBs}\ \mathfrak{Re}\Big[R^*_{MC}(\omega_+ \Omega) - R_{MC}(\omega_- \Omega) \Big] \cos 2\Omega t + \\ & - 2P_{SBs}\ \mathfrak{Im}\Big[R^*_{MC}(\omega_+ \Omega) - R_{MC}(\omega_- \Omega) \Big] \sin 2\Omega t \ , \end{aligned} \tag{8.38}$$

where $P_{CARR} = J_0^2(m)|E_0|^2$ and $P_{SBs} = J_1^2(m)|E_0|^2$. Eq.(8.38) shows that the total reflected field is a wave with a nominal frequency of ω_0, but with an envelope displaying a beat pattern with two frequencies. The Ω terms arise from the beating between the carrier and the sidebands, and the 2Ω terms come from the sidebands beating with each other. The two terms oscillating at the

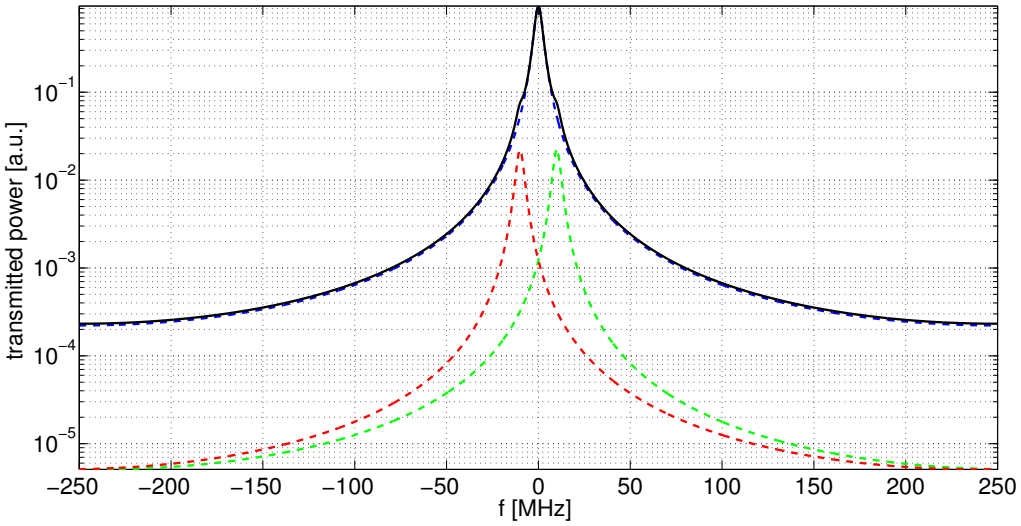

Figure 8.33: Total transmitted field through the LG_3^3 beam mode-cleaner (black solid curve). The carrier field (blue dashed curve), the lower (red dashed curve) and the upper (green dashed curve) radio-frequency sideband fields are shown.

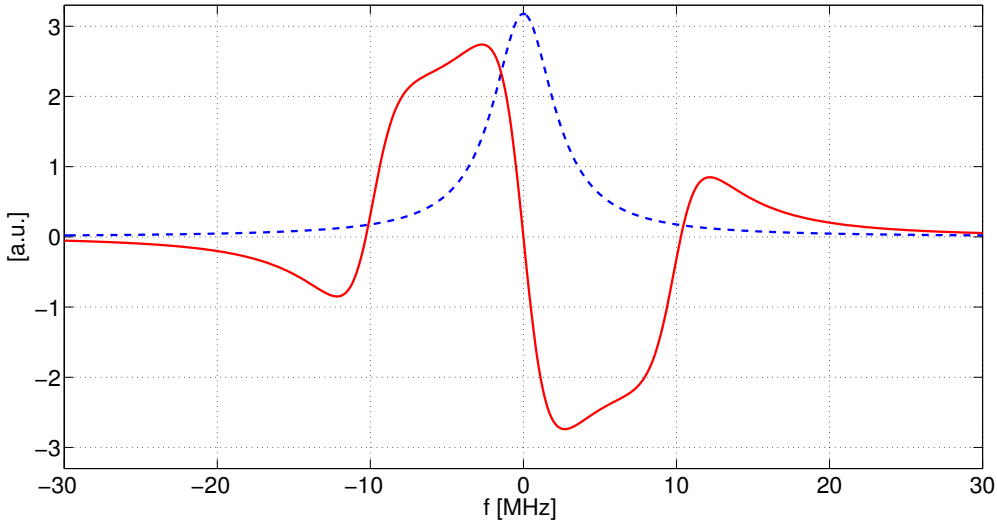

Figure 8.34: Expected shape of the Pound-Drever-Hall signal (red solid curve), superposed to the carrier transmitted signal (blue dashed curve).

modulation frequency Ω sample the phase of the reflected carrier, and must be extracted through demodulation to generate the error signal.

The beam reflected by the mode-cleaner is picked off and measured by a photodiode with gain G_{PD}, so that the signal of the modulated reflected field is $V_r = G_{PD}\ P_r$. The Ω terms of V_r can be isolated by feeding the signal of the photodiode to a mixer and a low-pass filter with cut-off frequency $\Omega_C << \Omega$. The DC and the 2Ω terms of V_r will be instead filtered off, since they will result, after mixing, in a signal at frequencies higher than the cut-off. The only non-null terms are those of frequency Ω.

The phase delay between the modulated signal and the phase oscillator can be adjusted to extract the in-phase (ACp) or the in-quadrature (ACq) demodulated signals:

$$\begin{aligned} ACp &\propto \mathfrak{Im}\Big[R_{MC}(\omega_0)R^*_{MC}(\omega_+\Omega) - R^*_{MC}(\omega_0)R_{MC}(\omega_-\Omega)\Big] \\ ACq &\propto \mathfrak{Re}\Big[R_{MC}(\omega_0)R^*_{MC}(\omega_+\Omega) - R^*_{MC}(\omega_0)R_{MC}(\omega_-\Omega)\Big]\ . \end{aligned} \tag{8.39}$$

Assuming that the the error signal is contained in the in-phase demodulation, the Pound-Drever-Hall signal finally writes

$$\begin{aligned} \varepsilon_{PDH} = \ & 2\sqrt{P_{CARR}P_{SBs}}\ G_{PD}\ G_{MIX}\ G_{LPF} \\ & \times\ \mathfrak{Im}\Big[R_{MC}(\omega_0)R^*_{MC}(\omega_+\Omega) - R^*_{MC}(\omega_0)R_{MC}(\omega_-\Omega)\Big]\ , \end{aligned} \tag{8.40}$$

where G_{MIX} and G_{LPF} are the gains of the mixer and of the low-pass filter, respectively.

The theoretical error signal is shown on fig.8.35, compared to the measured one. We remark the good agreement between the expected and the measured error signals, even if the mode used is not a pure LG^3_3.

Lock of the LG^3_3 eigenmode resonance

The open-loop transfer function of the feedback is:

$$G_{OL} = G_{MC}\ G_{PD}\ G_{mix}\ G_{LPF}\ G_S\ G_{PZT}\ , \tag{8.41}$$

where G_{MC} is the optical gain of the mode-cleaner, measured in W/Hz, and G_S is the gain of the servo. The gains and the bandwidths of the other electronic components of the experimental setup are listed in table 8.3. The resulting global transfer function G_{OL} has a unity gain at 7.75 kHz, with a phase margin of 57 deg. Its frequency dependence is the following:

$$\begin{aligned} &G_{OL} \propto 1/f^5 \quad \mathrm{DC} < f < 72\ \mathrm{Hz} \\ &G_{OL} \propto 1/f^4 \quad 72 < f < 904\ \mathrm{Hz} \\ &G_{OL} \propto 1/f \quad 0.904 < f < 30\ \mathrm{kHz}\ . \end{aligned} \tag{8.42}$$

Initially the laser frequency is tuned manually with the thermal control of the laser crystal, in order to set the resonance condition for the LG^3_3 eigenmode in the mode-cleaner. Then the frequency of

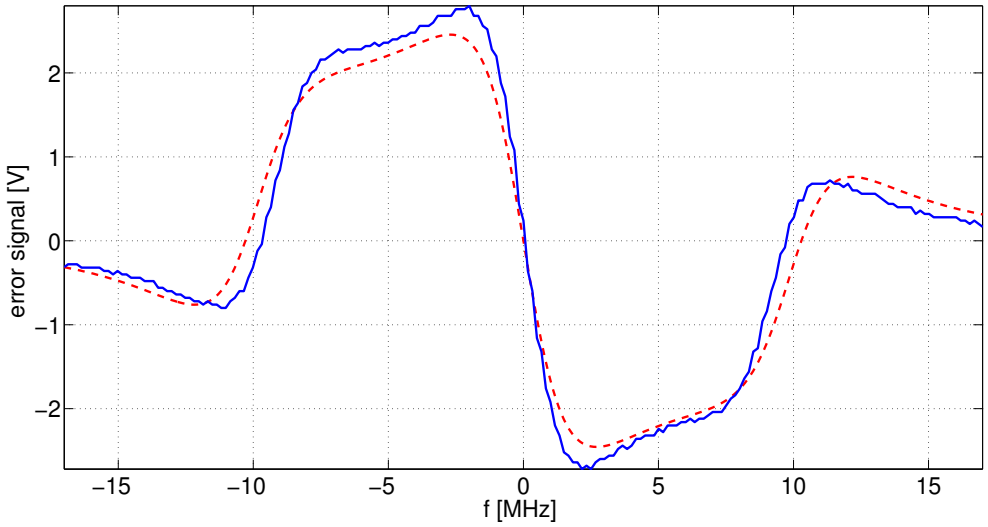

Figure 8.35: Pound-Drever-Hall signal of the pseudo-LG_3^3 mode: measured (blue solid curve) and expected (red dashed curve) signals.

component	gain	bandwidth
photodiode	$G_{PD} = 154$ V/W	22 MHz
mixer	$G_{mix} \simeq 0$ dB	200 MHz
low-pass filter	$G_{LPF} = -5.5$ dB	2.5 MHz
piezo transducer	$G_{PZT} = 1.5$ MHz/V	several tens of kHz

Table 8.3: Gain and bandwidth of electronics used in the servo control of the laser frequency.

resonant eigenmode	transmitted signal [mV]	laser crystal temperature [°C]
LG_3^3	872 ± 40	29.83 ± 0.01
LG_1^ℓ	65 ± 4	29.85 ± 0.01
LG_4^ℓ	42 ± 4	29.90 ± 0.01
LG_5^ℓ	64 ± 4	29.97 ± 0.01
LG_3^3	872 ± 40	29.99 ± 0.01
others (sum)	42 ± 4	–

Table 8.4: Measurement of the pseudo-LG_3^3 mode spectrum.

the laser is swept around the mode resonance with a periodic triangular signal, the *ramp*. The lock acquisition of the LG_3^3 eigenmode resonance is performed manually: the loop is closed by turning off the gain of the dithering ramp, at the same time that the frequency-dependent amplification of the error signal is turned on. Following this procedure, the mode-cleaner has been robustly locked on the resonance of the LG_3^3 eigenmode for several hours.

8.9 Mode-Cleaner spectrum

The pseudo-LG_3^3 mode can be projected on the basis of the mode-cleaner eigenmodes, as the sum of a dominant LG_3^3 mode contribution plus some spurious terms of LG_p^ℓ modes of different order. Each of this terms can resonate in the mode-cleaner, if the frequency of the laser is changed properly. Thus, for the pseudo-LG_3^3 mode, the plot of the power resonant in the mode-cleaner versus the frequency of the laser (or, as it is equivalent, the cavity length) is expected to be a composite spectrum of multiple resonance peaks, as shown on fig.8.11.

The amplitude of the resonance peaks of the spurious terms, if compared to the amplitude of the LG_3^3 eigenmode resonance, is an indirect measure of the purity of the pseudo-LG_3^3 mode: the smaller the amplitude of the spurious peaks, the higher the purity of the mode. A rough measurement of the pseudo-LG_3^3 mode spectrum has been carried out by scanning the free spectral range of the mode-cleaner (500 MHz) with the thermal tuning controller of the laser, the frequency change provided by the piezoelectric actuator (±150 MHz) being too small for this measurement. The smallest temperature change achievable with the controller is ±0.01 K, corresponding to ∓30 MHz (the gain of the Peltier cell of the laser is -3 GHz/K).

As expected, LG_p^ℓ modes of different order are observed in transmission with a CCD camera, as the frequency of the laser is changed. All of them have a radial node of null intensity at $r = 0$. According to eq.(5.13), these modes are supposed to have $\ell \neq 0$ and $p + 1$ radial nodes. Thereby the radial index p of the modes could be identified directly by counting the number of visible rings.

The power of this modes transmitted through the cavity is measured with a photodiode, placed after the mode-cleaner. Table 8.4 shows the result of the characterization of the resonant mode-cleaner eigenmodes, obtained from the measurement of their transmitted signals. Only the modes who could be clearly visible on the CCD camera are reported in the table, whereas some very weak and unidentifiable modes are only considered for their contribution to the total transmitted signal. The uncertainty on the measured signals is equal to the maximum accuracy of the acquisition setup. The images of the observed modes, acquired with the CCD camera, are shown on fig.8.36.

We used the spectrum of the pseudo-LG_3^3 mode of fig.8.11 simulated with OSCAR, together

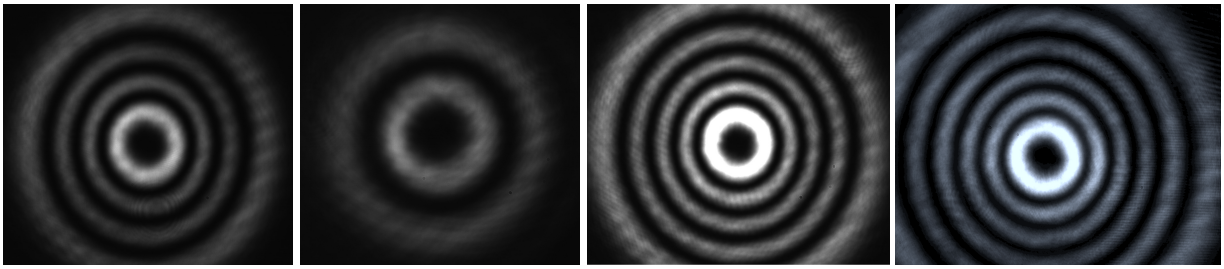

Figure 8.36: Observed mode-cleaner eigenmodes, from the left: LG_3^3, LG_1^ℓ, LG_4^ℓ, LG_5^ℓ. Images have been acquired with different filters before the CCD camera, the grey scale is not indicative of the relative intensities of modes.

resonant eigenmode	ΔN	measured freq. spacing [MHz]	expected freq. spacing [MHz]
$LG_1^\ell \rightarrow LG_1^3$	-4	-60 $\pm$ 30	-64
$LG_4^\ell \rightarrow LG_4^3$	-2	-218 $\pm$ 30	-210
$LG_5^\ell \rightarrow LG_5^3$	+4	-420 $\pm$ 30	-436

Table 8.5: Identification of modes in the pseudo-LG_3^3 mode spectrum.

with eq.(8.12), to identify the azimuthal index of the modes. These are: {LG_1^3, LG_4^3, LG_5^3 }. We do not observe instead the modes identified by $\Delta N = 1$ and $\Delta N = -1$ on the simulated spectrum, though they have an amplitude of the same order of magnitude of the observed modes. Other modes in the simulated spectrum have negligible amplitudes.

The frequency spacings of identified modes have been computed and compared to the measured values, as reported in table 8.5. Reported values are negative, since the frequency increases in the opposite sense of the axis of cavity length tuning in fig.8.11. The comparison shows that the measured values of the frequency spacing are in good agreement with the simulated values. In table 8.6 we show the reconstructed decomposition of the pseudo-LG_3^3 mode in LG_p^ℓ eigenmodes of the mode-cleaner. Three quantities are reported here:

- the fraction of transmitted signal of each mode, computed as the ratio of the single mode signal to the sum of all the transmitted signals. This sum is equal to $V_{tot} = 1083$ mV, including 40 mV of unidentifiable modes.

- the measured relative amplitude of each mode with respect to the LG_3^3 mode, computed as the ratio of the signal of one mode to the signal of the LG_3^3 mode

- the simulated relative amplitude of each mode with respect to the LG_3^3 mode, computed from the spectrum of fig.8.11.

We can observe from this table that there is a partial agreement between the measurement and the simulation: the relative amplitudes of LG_1^3 and LG_5^3 modes are compatible within $\sim 15\%$ error, while the measured amplitude of the LG_4^3 mode is larger than the simulated one by more than a factor of 2.

mode	% of total signal	meas. % of LG_3^3 mode peak	simul. % of LG_3^3 mode peak
LG_3^3	81	100	–
LG_1^3	6	8	7
LG_4^3	4	5	2
LG_5^3	6	7	6

Table 8.6: Characterization of the pseudo-LG_3^3 mode spectrum, compared to simulation.

Since the observed modes are also predicted by simulations where the input LG_0^0 beam of the plate, the matching of the pseudo-LG_3^3 to the cavity and the cavity mirrors are perfect, they are likely due to the phase pattern of the diffractive plate.

8.10 Transmitted LG_3^3 Beam

Mode transmission

When the laser frequency is locked to the resonance of the LG_3^3 eigenmode of the mode-cleaner, it is possible to measure the transmitted power with the powermeter and compare it to the power of the pseudo-LG_3^3 mode measured at the mode-cleaner input, as sketched on fig.8.37a). The ratio between the output and the input power measures the transmission of the LG_3^3 mode content in the pseudo-LG_3^3 input beam, through the mode-cleaner. The measured ratio is:

$$LG_3^3 \text{ transmission} = \frac{P_{out} = 155 \text{ mW}}{P_{in} = 265 \text{ mW}} = 58\% \ .$$

However, this measurement is affected by the optical loss of the mode-cleaner mirrors. To correctly characterize the *throughput* of the cavity, the measurement of the transmitted power has been performed separately by using the LG_0^0 beam of the laser.

The setup used for the measurement is shown in fig.8.37b): the LG_0^0 beam has been deflected after L0 on a parallel path, and the mode-cleaner has been positioned at the beam waist (previously characterized for the mode-matching telescope). The input and the output power of the LG_0^0 beam are measured with the powermeter, and the output beam is also monitored with a CCD camera, placed after a beamsplitter with measured reflectivity $R = 63\%$. The monitoring of the output beam has been used to check the presence of higher-order modes due to a possible mismatch, between the beam waist and the cavity waist. In fact, only an LG_1^0 mode is observed, with an amplitude which is 9% of that of the LG_0^0 beam. With this setup, the transmitted power is computed as the ratio of the power measured by the powermeter and the reflectivity of the beamsplitter. The cavity throughput is then

$$\tau = \frac{(P_{LG_0^0} + P_{LG_1^0})_{out}}{(P_{LG_0^0})_{in}} = \frac{365 \text{ mW} + 33 \text{ mW}}{438 \text{ mW}} = 91\% \ , \tag{8.43}$$

where $(P_{LG_0^0} + P_{LG_1^0})_{out}$ is the total transmitted power and $(P_{LG_0^0})_{in}$ is the measured input power. The measured throughput indicates that the mode-cleaner has a global optical loss of 9%, which

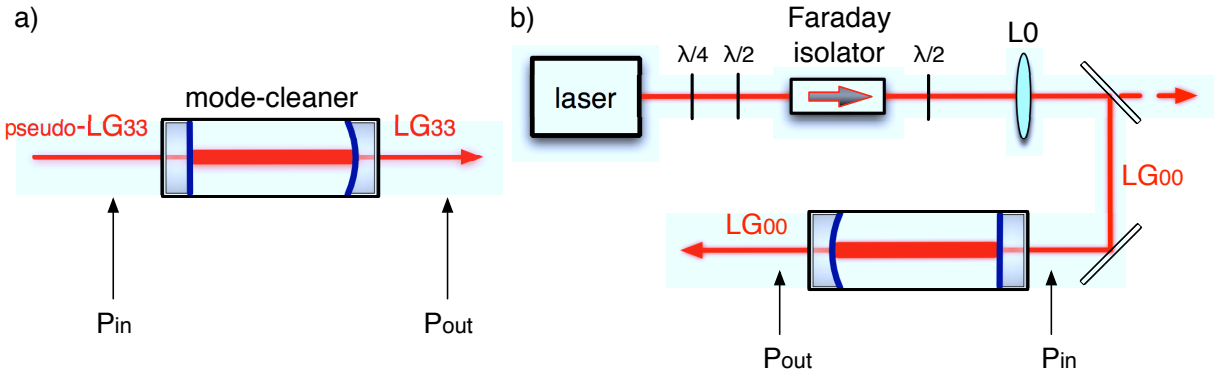

Figure 8.37: Setup for the measurement of the LG_3^3 mode power transmitted by mode-cleaner cavity: a) transmission of the LG_3^3 mode, b) caracterization of the cavity throughput with the LG_0^0 Gaussian beam.

must be taken into account in the measured transmission of the LG_3^3 mode content of the pseudo-LG_3^3 mode. The correct estimation of the LG_3^3 mode transmission is thus

$$LG_3^3 \text{ transmission} = \frac{P_{out}}{\tau P_{in}} = 64\% \ .$$

This result is roughly compatible with the expected coupling upper limit ($\gamma^2 = 77\%$), estimated through the overlap integral of the pseudo-LG_3^3 mode computed in section 8.6. The measured transmission is lower than expected, probably due to the difference between the phase of the pseudo-LG_3^3 mode and the phase of the theoretical LG_3^3 mode, neglected in the computation of the overlap integral. The coupling might be also slightly decreased by some residual mismatch of the beam waist to the cavity.

Analysis of the transmitted LG_3^3 mode

The characterization of the transmitted LG_3^3 mode has been carried out by computing the purity and the least square fit, for an image of the beam acquired after the mode-cleaner. The image is shown on fig.8.38: it has been acquired in far-field regime, with the beamscan at a distance $z = 1.321 \pm 0.003$ m, equal to about 5.4 times the Rayleigh range of the cavity eigenmode. The distance for acquisition is limited in this case by the size of the CCD detector of the beamscan, which cannot detect beams bigger than 15 mm in diameter.

For comparison, fig.8.38 also shows the theoretical LG_3^3 eigenmode transmitted by the mode-cleaner and propagated at the same distance of the measured beam, simulated with an FFT code developed from the core of the code OSCAR. The code simulates the transmission (at resonance) of a pure LG_3^3 mode through the mode-cleaner, and its propagation in free space.

The purity of the transmitted mode is computed as the overlap integral between the square root of the intensities shown on fig.8.38, yielding

$$\gamma = \left\langle LG_3^3|_{simulation} \middle| LG_3^3|_{measure} \right\rangle = 98.3\% \ , \tag{8.44}$$

with $L = 1 - \gamma^2 = 3.4\%$ coupling losses. Thus the beam transmitted by the mode-cleaner is a high-purity LG_3^3 mode, though with a lower purity than the one predicted by simulations ($\gamma = 99.8\%$,

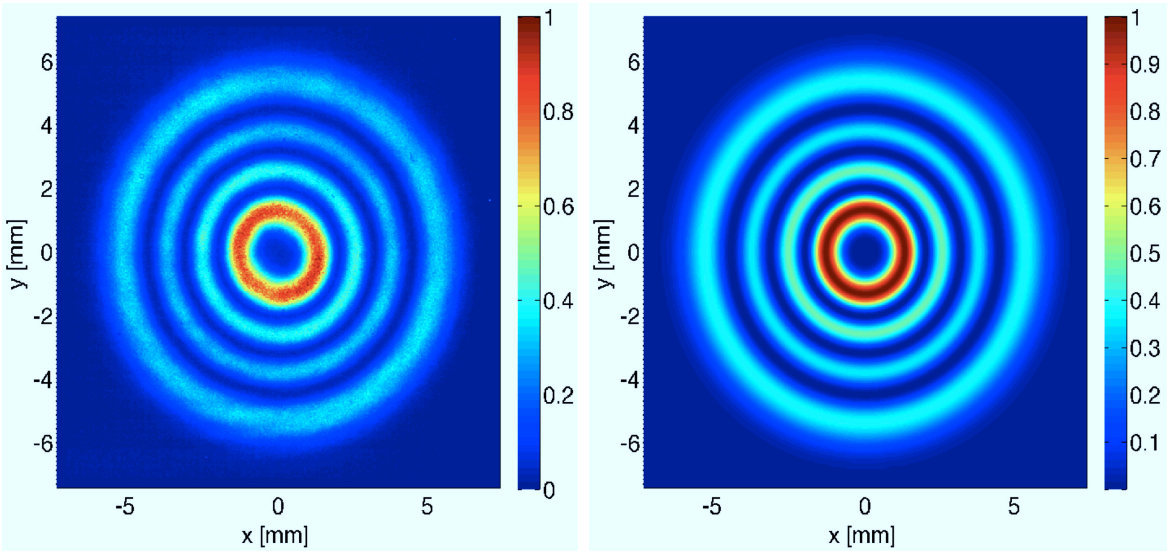

Figure 8.38: Comparison between normalized intensity distributions in far field: measured LG_3^3 mode (left) and simulated theoretical LG_3^3 mode (right).

see section 8.3). These simulations indicate that the cavity should already filter all the spatial defects of the pseudo-LG_3^3 mode with a lower finesse, thus the measured purity might be likely due to the quality of the surface of the cavity mirrors.

The comparison between the cross sectional profiles of the theoretical and measured transmitted beams is shown on fig.8.39. The measured profile presents an overall correspondence with the theoretical one: the position of the peaks and their relative amplitudes are those expected. This also indicates that the divergence of the transmitted LG_3^3 mode is close to that of the theoretical cavity mode. The main difference between the cross sections is the presence of some power left at the radial nodes.

The least square fit of the measured intensity profile, performed with the same method described in section 8.6 for the pseudo-LG_3^3 mode, yields

$$\begin{aligned} A_3^3 &= 1.8 \cdot 10^{-3} \text{ [a. u.]} \\ B &= 479 \text{ [a. u.]} \\ w &= 1.944 \cdot 10^{-3} \text{ m} , \end{aligned} \tag{8.45}$$

where the beam radius w replaced the beam waist w_0. The low residuals and the fit reduced χ^2 equal to 1.1 (for 512 points and 3 parameters) indicate that the model reproduces well the data. This can be seen on fig.8.40: the radial position and the relative amplitudes of the peaks are very well fitted by a theoretical mode with $w = 1.944$ mm, in good agreement with the theoretical propagation of the cavity eigenmode along z and through the (diverging) lens formed by the cavity end mirror. The measured thickness of the end mirror is $d = 6.50 \pm 0.05$ mm, with a curved reflecting surface with $R_1 = 0.5$ m and a flat rear anti-reflective surface with $R_2 = \infty$. Assuming that the refractive index of the fused silica of the mirror is $n = 1.44963$, the lens-maker equation

$$\frac{1}{f_{eq}} = (n-1)\left[\frac{1}{R_1} - \frac{1}{R_2} + \frac{d(n-1)}{nR_1R_2}\right] \tag{8.46}$$

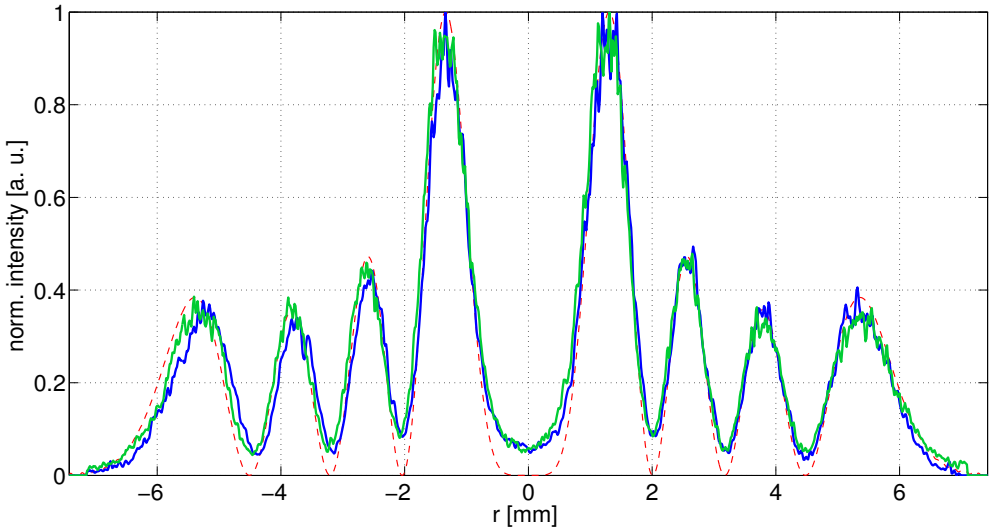

Figure 8.39: Profile comparison: the horizontal (blue solid curve) and the vertical (green solid curve) measured cross sections of the transmitted LG_3^3 mode are shown, together with the cross section of the simulated theoretical LG_3^3 mode (red dashed line). The theoretical mode is not a fit, but it is obtained by propagating the LG_3^3 eigenmode of the mode-cleaner in space.

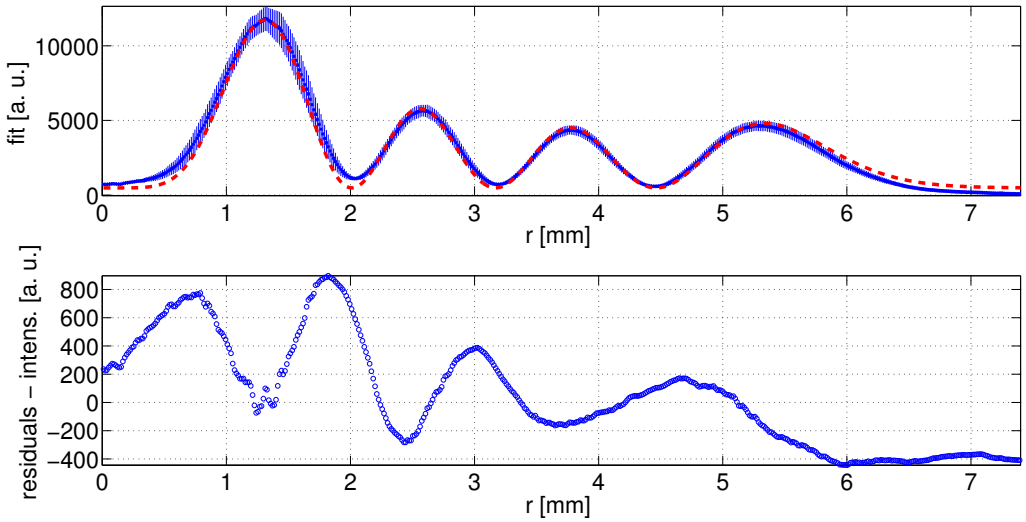

Figure 8.40: Least square fit of the profile of the transmitted LG_3^3 mode. Top panel: measured (blue dots with errors) and fitted (red dashed curve) profiles in the $r > 0$ plane. Bottom panel: fit residuals, defined as the difference between the data and the model.

yields an equivalent focal length for the end mirror equal to $f_{eq} = 1.112$ m. The propagation of the LG_3^3 mode from the cavity waist, computed through ray-matrix formalism, returns $w = 1.957$ mm. Thus the value of the beam radius obtained from the fit is in good agreement with the theoretical expectation.

The power left at the radial nodes is interpreted by the fit as background light, but this is not completely true. Though some low background is present in the acquired picture, by looking at the queue of the outermost peak of the mode in fig.8.40, it is clearly visible that the computed background is overestimated. As mentioned previously, these spatial defects might be due to the surface quality of the mirrors.

8.11 LG_3^3 mode conversion efficiency

The mode conversion efficiency is a fundamental parameter, since it measures the power loss of the LG_3^3 mode generation technique. We define this parameter as follows:

$$\epsilon = \frac{(P_{LG_3^3})_T}{(P_{LG_0^0})_T}\gamma^2 \ , \tag{8.47}$$

where

- $(P_{LG_3^3})_T = 155$ mW is the power of the LG_3^3 beam transmitted by the mode-cleaner at the resonance of the LG_3^3 cavity eigenmode
- $(P_{LG_0^0})_T = \tau\eta P_{PO1}$ is the power of the LG_0^0 mode transmitted through the experimental setup, including the mode-cleaner:
  - $P_{PO1} = 435$ mW is the is the power of the LG_0^0 beam at the input of LG_0^0 pick-off, indicated by an arrow on fig.8.15
  - τ is the cavity throughput measured by eq.(8.43)
  - η is the LG_0^0 beam transmission of the experimental setup **without the diffractive plate**, from the input of PO1 to the mode-cleaner input mirror, as shown on fig.8.41. η is measured as the ratio of the power P_{MCin} before the mode-cleaner input mirror to the power P_{PO1}:
    $$\eta = \frac{P_{MCin} = 339 \text{ mW}}{P_{PO1} = 435 \text{ mW}} = 78\% \ .$$
    The optical loss of the setup are caused by the power fraction that goes into the LG_0^0 pickoff, not used in the LG_3^3 mode generation, and by the optics (mirrors, lens, polarizer cube) placed before the mode-cleaner
- $\gamma^2 = 96\%$ is the LG_3^3 mode power content of the beam transmitted through the mode-cleaner, from eq.(8.44).

Eq.(8.47) defines a global conversion efficiency which takes into account the two steps of the generation technique:

- the LG_0^0-to-LG_3^3 mode conversion through the diffractive plate

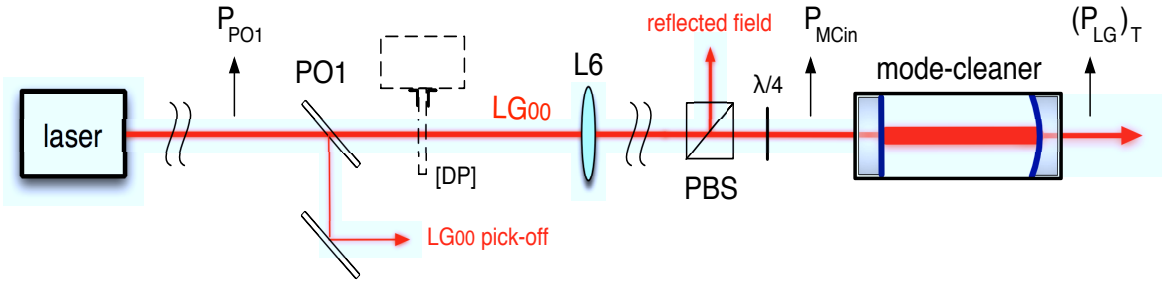

Figure 8.41: Measurement of the LG_0^0 beam through the experimental setup. The usual position of the diffractive plate (DP), removed from the setup for the measurement of the transmission, is shown with a dashed line.

- the spatial filtering of the generated pseudo-LG_3^3 mode.

This definition of efficiency is independent from the optical loss of the experimental setup, and only depends on the design of the diffractive plate and on the transmission through the mode-cleaner. It is equal to

$$\epsilon = 49\% \ .$$

Of the 51% power lost in the conversion, about 20% is lost at the diffractive plate, going in scattered light (due to the absence of the anti-reflective coating) and in higher diffraction orders. The rest of the power is reflected by the cavity when it is locked on the LG_3^3 eigenmode, in the form of modes of different order. A further increase of the efficiency could be achieved by optimizing the plate pattern and by tuning the matching between the beam and the mode-cleaner cavity. The transmission η could be largely improved by replacing PO1 with a movable flip-mount, and by using high quality, low loss optics in the setup.

8.12 LG_3^3 Michelson Interferometer

The scope of the our experiment was initially limited to the test of our generation technique. Nevertheless, as soon as we could generate high purity LG_3^3 beams with our setup, we decided to extend the layout of the experiment to test also high-precision interferometry with the higher-order LG_3^3 mode. As a first step we chose to test a configuration of limited complexity, thus we assembled a Michelson interferometer. The layout of this part of the experimental setup is shown on fig.8.42.

The LG_3^3 beam coming from the mode-cleaner goes through a collimating lens with $f = 1$ m, placed at 42 $\pm$0.5 cm from the cavity end mirror. According to the theoretical propagation of the cavity eigenmode computed in section 8.10, the parameter of the beam after the lens is expected to be $q = (2.16 + i4.98)$ m, corresponding to a beam radius $w = 1.3$ mm. Thus we expect the beam to be collimated over few meters, and this was checked by measuring the beam radius with the beamscan at different positions after the lens. At $\sim$ 65 cm, where the beam encounters the beamsplitter, the beam size does not change appreciably. The beam is collimated also inside the interferometer, which has 16-cm long arms.

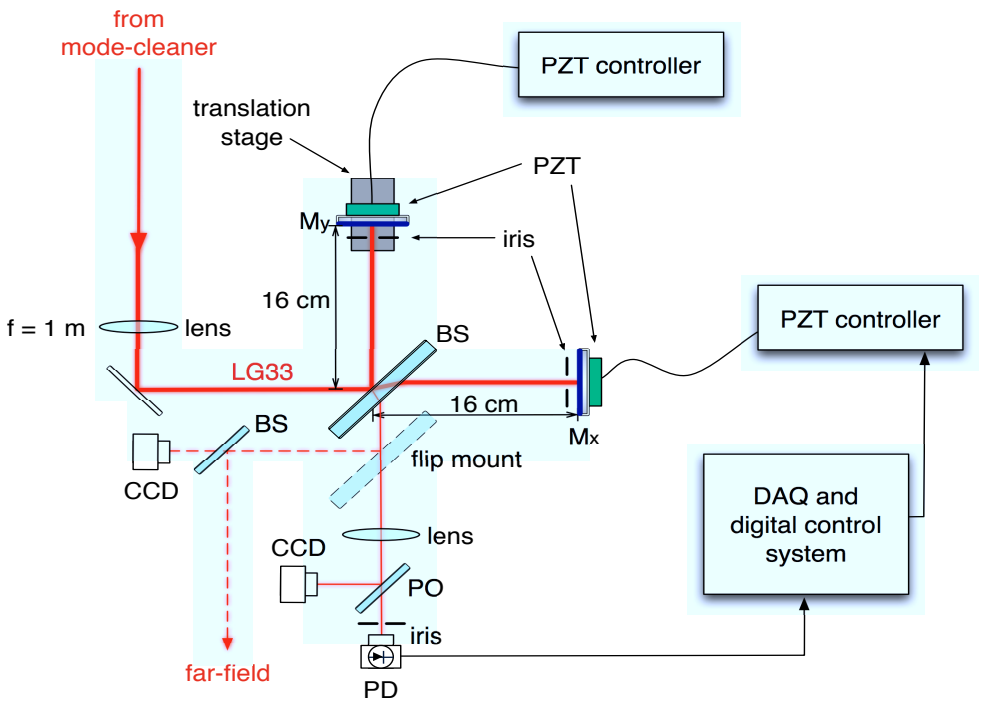

Figure 8.42: Layout of the Michelson interferometer illuminated with LG_3^3 beams.

The beamsplitter, given the large size of the input beam (the diameter, taken at the outer ring of the mode, is of the order of 1 cm) and the non-normal incidence angle of the beam, is a 2-inches optic to avoid the clipping of the beam. The high-reflectivity 1-inch end mirrors are plane. Facing each mirror we put an iris to block the secondary beams, generated by a wedge of 30 arcminutes (according to the datasheet) in the beamsplitter, and also some spurious reflections coming from the other optics of the setup. We put the mirrors into two mounts Thorlabs KC1-PZ with piezoelectric actuators, to remotely control the alignment. Each mount has three independent actuators to realize angular or longitudinal displacements, driven by a controller Thorlabs MDT693A with three channels. The gain specified by the datasheet for each actuator is $G = 6.1 \cdot 10^{-8}$ m/V.

Under the end mirror of the y arm (the arm of the beamsplitter reflection) we put a translation stage Thorlabs PT1, to tune the arm length within ± 250 μm accuracy. We initially set the length of the interferometer arms to (162 ± 2) mm. We then used the translation stage during the operation of the interferometer, as described further below.

At the output, the beam goes through a focusing lens (with $f = 50$ mm) and a pick-off (with $R = 8\%$), then is detected by a photodiode. The pick-off beam is used to monitor the interferometer output interference fringe (*dark fringe*) with a CCD camera. Facing the photodiode, another iris blocks other spurious reflections.

Between the pick-off and the beamsplitter, we put a mirror on a flip-mount, to deviate the beam on a parallel path for the pre-alignment of the beams in the arms. On this path we arranged a setup similar to that used for the relative alignment of the pseudo-LG_3^3 mode and the LG_0^0 pick-off, described in section 8.7. A CCD camera is placed in near field, while we observe the beams in far field against the wall of the room nearby, ~ 10 m far. We pre-align the beams in the arms with

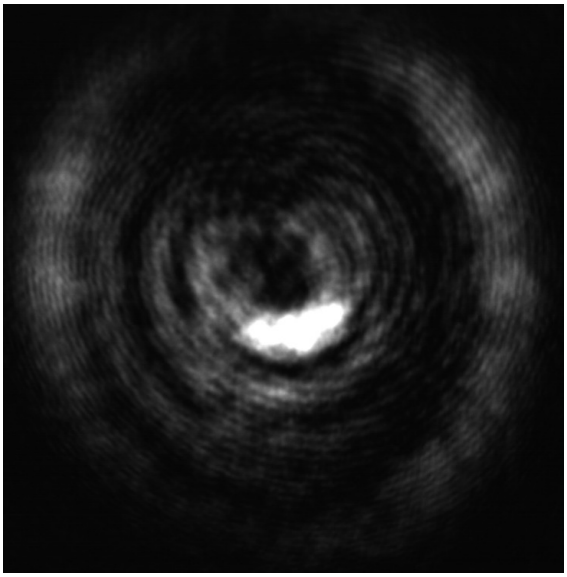

Figure 8.43: Image of the interference fringe at the output of the LG_3^3 Michelson interferometer (the image has been acquired with a long exposition time in order to make it clearly visible).

this setup, following this procedure:

1. we block the beam in the y arm, before the end mirror
2. we align the reflection of the x-arm mirror on the input beam of the interferometer: we put two iris on the path of the input beam, at two distant places, and we center the spot reflected by the end mirror on both the iris
3. we align the beam of the y arm to the other. We make sure that the beams are well superposed, by looking at the shape of the fringe in near and far field, at the same time. The long baseline between the two points of observation ensures that the beams are well aligned also at any point inside the interferometer.

When the pre-alignment is done, we lock the interferometer on the dark fringe, as shown on fig.8.43. The error signal is generated by dithering the x mirror, by sending to the three actuators of the mount the same sinusoidal signal at 1 kHz.

The dithering signal is generated by a digital acquisition and control system (DAQ, the same presently used in Virgo), installed on a computer. The dithering induces a periodic phase modulation of the beam and thus generates sidebands. The beating pattern between the carrier and the sidebands is detected by the photodiode. The signal is sent to the DAQ for demodulation, performed by executing a series of coded commands in a script. To extract the error signal we implemented in the code a standard demodulation scheme with a mixer and a low-pass filter.

Once the lock is acquired, we perform the fine alignment of the beams, using the controllers of the actuators to tune the angular position of mirrors. We optimize the alignment by looking initially at the shape of the dark fringe acquired by the pick-off camera. When the change of the fringe shape cannot be appreciated any longer by eye, we continue the optimization of the alignment by minimizing the output DC signal.

We then compute the contrast of the interferometer from the measurement of the bright fringe signal V_{BF}, initially acquired when the interferometer is unlocked, and the dark fringe signal V_{DF} of the locked interferometer. Since the signals are directly proportional to the detected output power, we can use eq.(2.7) to write

$$C = \frac{V_{BF} - V_{DF}}{V_{BF} + V_{DF}} \ . \tag{8.48}$$

By applying iteratively the procedure of lock and fine alignment described above, we performed a series of measurements of contrast adjusting the macroscopic length of the y arm, tuned with the translation stage. The best contrast achieved is $C = 99.5\%$ ($V_{BF} = 3.1$ V, $V_{DF} = 0.0085$ V). We expect it should be possible to decrease the contrast defect (1-C) of about one order of magnitude in our setup, and this will be the subject of future study.

Conclusions and Perspectives - Part II

Mirror thermal noise will limit the sensitivity of all currently planned terrestrial detectors in the central region of the detection band. In order to decrease this noise, it has been necessary to increase the beam size on the arm cavity mirrors of advanced detectors, and LCGT and Einstein Telescope will implement cryogenics. The investigation is ongoing to find new solutions to the issue of mechanical loss of the coatings.

A relevant reduction of mirror thermal noise could be achieved by using non-Gaussian read-out beams. The use of LG_p^ℓ modes has been proposed, since they are eigenmodes of resonators with spherical mirrors. These modes had never been used before in applications of high-precision interferometry, thus we realized an experiment to study their optical performances.

Conclusions of the Experiment

We designed, assembled and operated a table-top experiment to generate LG_3^3 modes and test basic interferometry [139]. The results of the experiment may be summarized as follows:

- **the upper limit of the pseudo-LG_3^3 mode purity is $\gamma = 88\%$**, which is compatible with the prediction of FFT simulations of the plate ($\gamma = 85\%$). The measured spectrum of the mode features the resonances of three modes $\{LG_1^3, LG_4^3, LG_5^3\}$ which were also predicted by simulations. Other modes predicted by the simulated spectrum, instead, have not been observed

- **the upper limit of the LG_3^3 mode purity** at the output of the mode-cleaner is $\gamma = 98\%$, which is smaller than $\gamma = 99.9\%$ predicted by the FFT simulations of the cavity with perfect optics. Thus this discrepancy is likely due to the surface quality of the mode-cleaner mirrors

- **the global conversion efficiency**, inferred from our direct measurements of LG_3^3/LG_0^0 power ratio (36 %) and setup transmission ($\eta = 78\%$), is $\epsilon = 49\%$. The power budget of the setup is the following:

  - 18.5% of the initial LG_0^0 power is lost at the diffractive plate. The majority of the loss is likely due to the efficiency of the blazed grating, while 4% is lost at each surface because of the lack of an anti-reflective coating. Part of the loss is also due to imperfections of the plate phase pattern, caused by errors in the etching process of the plate surface
  - the FFT simulations of the plate indicate that the coupling of the pseudo-LG_3^3 mode should be $\gamma^2 = (0.85)^2 = 72\%$, but its measured transmission through the mode-cleaner is 64%. Therefore 8% of LG_3^3 power is lost, probably due to the combined effect of astigmatism of the input LG_0^0 beam and of mismatch of the pseudo-LG_3^3 to the cavity

  - at the output of the mode-cleaner, a fraction $L \geq 1 - (0.98)^2 = 4\%$ is lost because of the purity of the transmitted LG_3^3 beam. As mentioned above, this should be due to the surface quality of the mode-cleaner mirrors

- **the long-term stability of the LG_3^3 beam generator is demonstrated** by the robust lock of the laser frequency on the LG_3^3 resonance and by the constant transmission of the mode, during several hours. The lock is realized through a standard Pound-Drever-Hall locking scheme in reflection: the shape and the amplitude of the error signal agree with the theoretical predictions

- **the alignment of the pseudo-LG_3^3 beam** on the mode-cleaner cavity is more difficult than with the LG_0^0 beam, so we developed a pre-alignment procedure using the LG_0^0 beam. The procedure works correctly, and no fundamental obstacles have been encountered in the manual alignment of the pseudo-LG_3^3 beam on the mode cleaner cavity

- we illuminated a **Michelson interferometer with the filtered LG_3^3 beam**. We locked the interferometer on the dark fringe and we achieved a contrast C = 99.5 %.

The measured conversion efficiency is a first acceptable achievement, and some elements of the setup can be optimized to further increase its value. The estimated purity of the filtered LG_3^3 beam is high, and might be likely increased as well. We have also shown that LG_3^3 beams are compatible with the technique for longitudinal error signal extraction used in gravitational-wave interferometers. The alignment and lock of the mode-cleaner cavity and of the simple Michelson interferometer demonstrate experimentally the feasibility of higher-order LG_p^ℓ mode basic interferometry.

LG_3^3 beams of high purity have also been obtained using spatial light modulators [145]. However, the use of spatial light modulators is limited to applications with low-power laser beams, making them unsuitable for the potential implementation in future gravitational-wave detectors. Our technique has been developed to be specifically used in future interferometers, since the diffractive plate can in principle handle high-power laser beams.

Recently, a diffractive plate has been used to generate LG_3^3 beams which have been injected in a 10-m long cavity of finesse $\mathcal{F} = 600$ [146].

Further Developments

Efficiency and mode purity

The global power conversion efficiency could be increased by minimizing the loss of the diffractive plate. In principle it should be possible to increase the efficiency of the blazed grating of the plate [143], then 4% of efficiency might be recovered by coating the plane surface of the diffractive plate with an anti-reflective layer. An additional $\sim 2\%$ could be recovered by coating the etched surface of the plate [147].

Another improvement of the efficiency could come from the increase of the pseudo-LG_3^3 mode purity, in order to maximize its transmission through the mode-cleaner. For this purpose we could optimize the shape of the input LG_0^0 beam, as well as the matching of the pseudo-LG_3^3 mode to the cavity. It should be possible to compensate for the astigmatism of the LG_0^0 beam by adjusting the

lenses of the telescope. The matching of the pseudo-LG_3^3 mode might be improved by optimizing the position of the mode waist on the cavity. Therefore the resulting efficiency could be improved by $\leq 8\%$. To increase much further the purity of the pseudo-LG_3^3 mode, we should rather try to improve the design of the diffractive plate.

There exist in literature some examples of *complex-amplitude* modulation patterns [148], which are numerically computed to encode amplitude and phase modulation on a single phase plate, and might potentially generate modes of very high purity. These patterns have been already tested on spatial light modulators, yielding promising results in terms of achieved beam purity [135]. Also the option of using two diffractive plates could be re-evaluated.

Finally, also the purity of the LG_3^3 mode transmitted through the mode-cleaner might be further increased, as shown by the FFT simulation of the mode-cleaner. By using high-quality cavity mirrors, it should be possible to achieve a purity of the transmitted mode of more than 99%.

LG_3^3 interferometry

In our experiment we operate a Fabry-Perot cavity and a Michelson interferometer with LG_3^3 beams, demonstrating that basic interferometry with LG_3^3 modes does not pose any fundamental obstacle. The next step should be the upgrade the Michelson interferometer to the full optical configuration of a gravitational-wave detector, by implementing Fabry-Perot cavities in the arms and for power recycling.

The setup will be used to study the optical performances of an LG_3^3 detector, to validate a control scheme for longitudinal and angular control, and to characterize the sensitivity of LG_3^3 beams beams to mirror misalignments and figure errors. The setup could be used also to address the issue of degeneracy of higher-order modes, described in the following, from an experimental point of view.

Simulation of a real detector: the issue of mode degeneracy

LG_p^ℓ modes of the same order $N = 2p + |\ell|$ are degenerate, i. e. they can resonate at the same time in a Fabry-Perot cavity. For example, there exist 9 other modes, $\{LG_0^{\pm 9}, LG_1^{\pm 7}, LG_2^{\pm 5}, LG_3^{-3}, LG_4^{\pm 1}\}$, which have $N = 9$ and are degenerate with the LG_3^3 mode.

The potential issue related to mode degeneracy had been already raised at the time LG_p^ℓ modes had been originally proposed [125], though without going into the details of its possible impact. The issue has been successively confirmed by simulating the mode content of a km-long Fabry-Perot cavity with realistic state-of-the-art mirrors, illuminated with an LG_3^3 beam.

The spatial defects of the mirrors transfer energy from the LG_3^3 mode to other modes of the same order. The contamination of non-LG_3^3 modes is large, yielding an important decrease of contrast of the interferometer. For example, with a mirror surface roughness of 0.5 nm rms, the contrast is decreased down to the order of 60% [149]. Especially low-frequency spatial defects, and in particular astigmatism, highly contribute to mode contamination [150, 149, 151].

In order to use LG_p^ℓ beams, the quality of the mirrors should be drastically improved. For example, by using ultra-high quality polishing for cavity mirrors, in order to achieve a surface defect rms amplitude 0.2 nm and a cut-off of low-frequency spatial defects below 100 m^{-1} [149]. In this case the expected mode contamination could be mitigated, and the contrast would be increased up to 99% [149].

The application of a corrective pattern of rings on the surface of cavity mirrors (placed at the position of radial nodes of the LG_3^3 mode) has also been proposed [150, 152]. This would allow to damp resonant degenerate modes.

Beside the encouraging results of the simulations, we believe that mode degeneracy probably remains the main issue with respect to the use of LG_p^ℓ beams, so that a solution to this problem is needed [152].

Bibliography

[1] A. Einstein, *Die Grundlage der allgemeinen Relativitätstheorie*, Annalen der Physik **354**, 769 (1916)

[2] P. R. Saulson, *Fundamentals of Interferometric Gravitational Wave Detectors*, Singapore: World Scientific, 1994

[3] B. S. Sathyaprakash and B. F. Schutz, *Physics, Astrophysics and Cosmology with Gravitational Waves*, Living Rev. Relativity **12** (2009)

[4] W. H. Lee and E. Ramirez-Ruiz, *The progenitors of short gamma-ray bursts*, New J. Phys. **9**, 17 (2007)

[5] J. Abadie et al. (The LIGO Scientific Collaboration and The Virgo Collaboration), *Predictions for the rates of compact binary coalescences observable by ground-based gravitational-wave detectors*, Class. Quantum Grav. **27**, 173001 (2010)

[6] C. D. Ott, *The gravitational-wave signature of core-collapse supernovae*, Class. Quantum Grav. **26**, 063001 (2009)

[7] K. Thorne in *300 Years of Gravitation*, S.W. Hawking and W. Israel editors, Cambridge University Press, Cambridge, 1987, p. 330-458

[8] J. Abadie et al. (The LIGO Scientific Collaboration and The Virgo Collaboration), *Search for gravitational wave bursts from six magnetars*, Astrophys. J. **734**, L35 (2011)

[9] M. Maggiore, *Gravitational wave experiments and early universe cosmology*, Phys. Rep. **331**, 283 (2000)

[10] The LIGO Scientific Collaboration and The Virgo Collaboration, *An upper limit on the stochastic gravitational-wave background of cosmological origin*, Nature **460**, 990 (2009)

[11] S. E. Woosley and J. S. Bloom, *The Supernova Gamma-Ray Burst Connection*, Annual Rev. Astron. Astrophys. **44**, 507 (2006)

[12] D. E. Holz and S. A. Hughes, *Using gravitational-wave standard sirens*, Astrophys. J. **629**, 15 (2005)

[13] R. A. Hulse and J. H. Taylor, *Discovery of a pulsar in a binary system*, Astrophys. J. **195**, L51 (1975)

[14] J. M. Weisberg and J. H. Taylor in *Binary Radio Pulsars*, ASP Conference Series **328**, F. A. Rasio and I. H. Stairs editors, San Francisco, 2005, p. 25

[15] J. H. Taylor, *Pulsar Timing and Relativistic Gravity*, Phil. Trans. R. Soc. Lond. A **341**, 117 (1992)

[16] I. H. Stairs, S. E. Thorsett, J. H. Taylor, J. Henry and A. Wolszczan, *Studies of the relativistic binary pulsar PSR B1534+12. I. Timing analysis*, Astrophys. J. **581**, 501 (2002)

[17] A. J. Faulkner et al., *PSR J1756-2251: a new relativistic double neutron star system*, Astrophys. J. **618**, L119 (2005)

[18] M. Kramer et al., *Tests of General Relativity from Timing the Double Pulsar*, Science **314**, 97 (2006)

[19] A. Abramovici et al., *LIGO: The Laser Interferometer Gravitational-Wave Observatory*, Science **256**, 325 (1992)

[20] C. Bradaschia et al., *The VIRGO Project: A wide band antenna for gravitational wave detection*, Nucl. Instrum. Meth. A **289**, 518 (1990)

[21] F. Acernese et al. (The Virgo Collaboration), *Properties of seismic noise at the Virgo site*, Class. Quantum Grav. **21**, S433 (2004)

[22] S. A. Hughes and K. S. Thorne, *Seismic gravity-gradient noise in interferometric gravitational-wave detectors*, Phys. Rev. D **58**, 122002 (1998)

[23] T. Creighton, *Tumbleweeds and airborne gravitational noise sources for LIGO*, Class. Quantum Grav. **25**, 125011 (2008)

[24] M. Beccaria et al., *Relevance of Newtonian seismic noise for the VIRGO interferometer sensitivity*, Class. Quantum Grav. **15**, 3339 (1998)

[25] M. G. Beker et al., *Improving the sensitivity of future GW observatories in the 110 Hz band: Newtonian and seismic noise*, Gen. Relativ. Gravit. **43**, 623 (2011)

[26] J. Harms, R. DeSalvo, S. Dorsher and V. Mandic, *Simulation of underground gravity gradients from stochastic seismic fields*, Phys. Rev. D **80**, 122001 (2009)

[27] H. B. Callen and R. F. Greene, *On a Theorem of Irreversible Thermodynamics*, Phys. Rev. **86**, 702 (1952)

[28] P. R. Saulson, *Thermal noise in mechanical experiments*, Phys. Rev. D **42**, 2437 (1990)

[29] C. Zener, *Internal Friction in Solids II. General Theory of Thermoelastic Internal Friction*, Phys. Rev. **53**, 90 (1938)

[30] A. M. Gretarsson, G. M. Harry, S. D. Penn, P. R. Saulson, W. J. Startin, S. Rowan, G. Cagnoli and J. Hough, *Pendulum mode thermal noise in advanced interferometers: a comparison of fused silica fibers and ribbons in the presence of surface loss*, Phys. Lett. A **270**, 108 (2000)

[31] P. Amico, L. Bosi, L. Carbone, L. Gammaitoni, F. Marchesoni, M. Punturo, F. Travasso and H. Vocca, *Monolithic fused silica suspension for the Virgo gravitational waves detector*, Rev. Sci. Instrum. **73**, 3318 (2002)

[32] M. Punturo, *The VIRGO sensitivity curve*, Virgo technical note VIR-NOT-PER-1390-51, `https://tds.ego-gw.it/itf/tds/`

[33] Yu. Levin, *Internal thermal noise in the LIGO test masses: A direct approach*, Phys. Rev. D **57**, 659 (1998)

[34] J. Y. Vinet, *On Special Optical Modes and Thermal Issues in Advanced Gravitational Wave Interferometric Detectors*, Living Rev. Relativity **12** (2009)

[35] M. L. Gorodetsky, *Thermal noises and noise compensation in high-reflection multilayer coating*, Phys. Lett. A **372**, 6813 (2008)

[36] M. Cerdonio, L. Conti, A. Heidmann and M. Pinard, *Thermoelastic effects at low temperatures and quantum limits in displacement measurements*, Phys. Rev. D **63**, 082003 (2001)

[37] M. M. Fejer, S. Rowan, G. Cagnoli, D. R. M. Crooks, A. Gretarsson, G. M. Harry, J. Hough, S. D. Penn, P. H. Sneddon and S. P. Vyatchanin, *Thermoelastic dissipation in inhomogeneous media: loss measurements and displacement noise in coated test masses for interferometric gravitational wave detectors*, Phys. Rev. D **70**, 082003 (2004)

[38] V.B. Braginsky, M.L. Gorodetsky and S.P. Vyatchanin, *Thermo-refractive noise in gravitational wave antennae*, Phys. Lett. A **271**, 303 (2000)

[39] M. Evans, S. Ballmer, M. Fejer, P. Fritschel, G. Harry and G. Ogin, *Thermo-optic noise in coated mirrors for high-precision optical measurements*, Phys. Rev. D **78**, 102003 (2008)

[40] R. Nawrodt, S. Rowan, J. Hough, M. Punturo, F. Ricci and J. Y. Vinet, *Challenges in thermal noise for 3rd generation of gravitational wave detectors*, Gen. Relativ. Gravit. **43**, 593 (2011)

[41] B. Willke, N. Uehara, E. K. Gustafson, R. L. Byer, E. L. Ginzton, P. J. King, S. U. Seel and R. L. Savage Jr., *Spatial and temporal filtering of a 10-W Nd:YAG laser with a Fabry-Perot ring-cavity premode cleaner*, Opt. Lett. **23**, 1704 (1998)

[42] T. Accadia et al. (The Virgo Collaboration), *Status of the Virgo project*, Class. Quantum Grav. **28**, 114002 (2011)

[43] Virgo website: `https://wwwcascina.virgo.infn.it/`

[44] EGO website: `http://www.ego-gw.it/`

[45] B. P. Abbott et al. (The LIGO Scientific Collaboration), *LIGO: the Laser Interferometer Gravitational-Wave Observatory*, Rep. Prog. Phys. **72**, 076901 (2009)

[46] LIGO website: `http://www.ligo.caltech.edu/`

[47] H. Grote for the LIGO Scientific Collaboration, *The GEO 600 status*, Class. Quantum Grav. **27**, 084003 (2010)

[48] GEO600 website: `http://www.geo600.org/`

[49] K. Arai for the TAMA Collaboration, *Recent progress of TAMA300*, J. Phys.: Conf. Ser. **120**, 032010 (2008)

[50] TAMA300 website: `http://tamago.mtk.nao.ac.jp/`

[51] S. Fairhurst, *Triangulation of gravitational wave sources with a network of detectors*, New J. Phys. **11**, 123006 (2009)

[52] S. Klimenko, G. Vedovato, M. Drago, G. Mazzolo, G. Mitselmakher, C. Pankow, G. Prodi, V. Re, F. Salemi and I. Yakushin, *Localization of gravitational wave sources with networks of advanced detectors*, Phys. Rev. D **83**, 102001 (2011)

[53] F. Acernese et al. (The Virgo Collaboration), *Measurements of Superattenuator seismic isolation by Virgo interferometer*, Astropart. Phys. **33**, 182 (2010)

[54] M. Lorenzini for The Virgo Collaboration, *The monolithic suspension for the Virgo interferometer*, Class. Quantum Grav. **27**, 084021 (2010)

[55] J. Abadie et al. (The LIGO Scientific Collaboration and The Virgo Collaboration), *Search for gravitational waves from compact binary coalescence in LIGO and Virgo data from S5 and VSR1*, Phys. Rev. D **82**, 102001 (2010)

[56] J. Abadie et al. (The LIGO Scientific Collaboration and The Virgo Collaboration), *Search for gravitational waves from binary black hole inspiral, merger, and ringdown*, Phys. Rev. D **83**, 122005 (2011)

[57] J. Abadie et al. (The LIGO Scientific Collaboration and The Virgo Collaboration), *All-sky search for gravitational-wave bursts in the first joint LIGO-GEO-Virgo run*, Phys. Rev. D **81**, 102001 (2010)

[58] B. P. Abbott et al. (The LIGO Scientific Collaboration and The Virgo Collaboration), *Searches for gravitational waves from known pulsars with Science Run 5 LIGO data*, Astrophys. J. **713**, 671 (2010)

[59] B. P. Abbott et al. (The LIGO Scientific Collaboration and The Virgo Collaboration), *Search For Gravitational-wave Bursts Associated with Gamma-ray Bursts using Data from LIGO Science Run 5 and Virgo Science Run 1*, Astrophys. J. **715**, 1438 (2010)

[60] J. Abadie et al. (The LIGO Scientific Collaboration and The Virgo Collaboration), *Search for gravitational-wave inspiral signals associated with short gamma-ray bursts during LIGO's fifth and Virgo's first science run*, Astrophys. J. **715**, 1453 (2010)

[61] J. Kanner, T. L. Huard, S. Marka, D. C. Murphy, J. Piscionere, M. Reed and P. Shawhan, *LOOC UP: locating and observing optical counterparts to gravitational wave bursts*, Class. Quantum Grav. **25**, 184034 (2008)

[62] J. Abadie et al. (The LIGO Scientific Collaboration and The Virgo Collaboration), *Beating the spin-down limit on gravitational wave emission from the Vela pulsar*, accepted for publication on Astrophys. J. (arXiv:1104.2712v2 [astro-ph-HE])

[63] R. K. Kopparapu, C. Hanna, V. Kalogera, R. O'Shaughnessy, G. Gonzalez, P. R. Brady and S. Fairhurst, *Host Galaxies Catalog Used in LIGO Searches for Compact Binary Coalescence Events*, Astrophys. J. **675**, 1459 (2008)

[64] B. P. Abbott et al. (The LIGO Scientific Collaboration), *Upper limits on gravitational wave emission from 78 radio pulsars*, Phys. Rev. D **76**, 042001 (2007)

[65] R. J. Dupuis and G. Woan, *Bayesian estimation of pulsar parameters from gravitational wave data*, Phys. Rev. D **72**, 102002 (2005)

[66] B. J. Owen, *Maximum Elastic Deformations of Compact Stars with Exotic Equations of State*, Phys. Rev. Lett. **95**, 211101 (2005)

[67] G. M. Harry for The LIGO Scientific Collaboration, *Advanced LIGO: the next generation of gravitational wave detectors*, Class. Quantum Grav. **27**, 084006 (2010)

[68] The LIGO Scientific Collaboration, *Advanced LIGO Reference Design*, LIGO technical note LIGO-M060056-v2, `https://dcc.ligo.org/cgi-bin/DocDB/DocumentDatabase/`

[69] F. Acernese et al. (The Virgo Collaboration), *Advanced Virgo Baseline Design*, Virgo technical note VIR-0027A-09, `https://tds.ego-gw.it/itf/tds/`

[70] K. Kuroda for the LCGT Collaboration, *Status of LCGT*, Class. Quantum Grav. **27**, 084004 (2010)

[71] B. J. Meers, *Recycling in laser-interferometric gravitational-wave detectors*, Phys. Rev. D **38**, 2317 (1988)

[72] S. Sato, S. Miyoki, S. Telada, D. Tatsumi, A. Araya, M. Ohashi, Y. Totsuka, M. Fukushima and M. Fujimoto, *Ultrastable performance of an underground-based laser interferometer observatory for gravitational waves*, Phys. Rev. D **69**, 102005 (2004)

[73] Punturo et al., *The Einstein Telescope: a third-generation gravitational wave observatory*, Class. Quantum Grav. **27**, 194002 (2010)

[74] Einstein Telescope website: `http://www.et-gw.eu/`

[75] M. Abernathy et al., *Einstein gravitational wave Telescope conceptual design study*, Einstein Telescope technical note ET-0106C-10, `https://tds.ego-gw.it/itf/tds/`

[76] ASPERA website: `http://www.aspera-eu.org/`

[77] S. Hild, S. Chelkowski, A. Freise, J. Franc, N. Morgado, R. Flaminio and R. DeSalvo, *A xylophone configuration for a third-generation gravitational wave detector*, Class. Quantum Grav. **27**, 015003 (2010)

[78] Punturo et al., *The third generation of gravitational wave observatories and their science reach*, Class. Quantum Grav. **27**, 084007 (2010)

[79] J. A. Sidles and D. Sigg, *Optical torques in suspended FabryPerot interferometers*, Phys. Lett. A **354**, 167 (2006)

[80] R. Ward, *Advanced Virgo Optical Design Parameters Summary*, Virgo technical note VIR0541B10, `https://tds.ego-gw.it/itf/tds/`

[81] J. Mizuno, K. A. Strain, P. G. Nelson, J. M. Chen, R. Schilling, A. Rdiger, W. Winkler and K. Danzmann, *Resonant sideband extraction: a new configuration for interferometric gravitational wave detectors*, Phys. Lett. A **175**, 273 (1993)

[82] F. Acernese et al. (The Virgo Collaboration), *Lock acquisition of the Virgo gravitational wave detector*, Astropart. Phys. **30**, 29 (2008)

[83] R. W. P. Drever, J. L. Hall, F. V. Kowalski, J. Hough, G. M. Ford, A. J. Munley and H. Ward, *Laser phase and frequency stabilization using an optical resonator*, Appl. Phys. B: Photophys. Laser Chem. **31**, 97 (1983)

[84] E. D. Black, *An introduction to Pound-Drever-Hall laser frequency stabilization*, Am. J. Phys. **69**, 79 (2001)

[85] T. Accadia et al. (The Virgo Collaboration), *A thermal compensation system for the gravitational wave detector Virgo*, Proc. 12th Marcel Grossmann Meeting on General Relativity, ed. T. Damour, R. T. Jantzen and R. Ruffini, Singapore: World Scientific, 2011

[86] K. Goda, D. Ottaway, B. Connelly, R. Adhikari, N. Mavalvala and A. Gretarsson, *Frequency-resolving spatiotemporal wave-front sensor*, Optics Letters **29**, 1452 (2004)

[87] T. L. Kelly, P. J. Veitch, A. F. Brooks and J. Munch, *Accurate and precise optical testing with a differential Hartmann wavefront sensor*, Appl. Opt. **46**, 861 (2007)

[88] V. Fafone, E. Coccia, M. DiPaolo Emilio, V. Malvezzi, Y. Minenkov, A. Rocchi, L. Sperandio, *TCS: R&D progress*, Virgo technical note VIR-0090A-11, `https://tds.ego-gw.it/itf/tds/`

[89] R. Lawrence, M. Zucker, P. Fritschel, P. Marfuta and D. Shoemaker, *Adaptive thermal compensation of test masses in advanced LIGO*, Class. Quantum Grav. **19**, 1803 (2002)

[90] M. Beccaria et al., *Extending the VIRGO gravitational wave detection band down to a few Hz: metal blade springs and magnetic antisprings*, Nucl. Instr. and Meth. A **394**, 397 (1997)

[91] A. Bernardini, E. Majorana, P. Puppo, P. Rapagnani, F. Ricci and G. Testi, *Suspension last stages for the mirrors of the Virgo interferometric gravitational wave antenna*, Rev. Sci. Instrum. **70**, 3463 (1999)

[92] P. Rapagnani, *AdV input and BS payload*, Virgo technical note VIR-0243A-11, `https://tds.ego-gw.it/itf/tds/`

[93] M. A. Arain and G. Mueller, *Design of the Advanced LIGO recycling cavities*, Opt. Express **16**, 10018 (2008)

[94] Y. Pan, *Optimal degeneracy for the signal-recycling cavity in advanced LIGO*, arXiv:gr-qc/0608128v1

[95] H. Kogelnik and T. Li, Appl. Opt. **5**, 1550 (1966)

[96] A. E. Siegman, *Lasers*, University Science Books, Sausalito, California, U.S.A., 1986

[97] Wikipedia, `http://en.wikipedia.org/wiki/Transverse_mode`

[98] L. Allen, M. W. Beijersbergen, R. J. C. Spreeuw and J. P. Woerdman, *Orbital angular momentum of light and the transformation of Laguerre-Gaussian laser modes*, Phys. Rev. A **45**, 8185 (1992)

[99] K. A. Strain, K. Danzmann, J. Mizuno, P. G. Nelson, A. Rudiger, R. Schilling and W. Winkler, Phys. Lett. A **194**, 124 (1994)

[100] A. M. Gretarsson, E. DAmbrosio, V. Frolov, Brian OReilly and P. K. Fritschel, *Effects of mode degeneracy in the LIGO Livingston Observatory recycling cavity*, J. Opt. Soc. Am. B **24**, 2821 (2007)

[101] T. Accadia et al. (The Virgo Collaboration), *Performance of the Virgo interferometer longitudinal control system during the second science run* , Astropart. Phys. **34**, 521 (2011)

[102] R. Bonnand, R. Flaminio, *Simulation of Thermal Effects in Advanced Virgo*, Virgo technical note VIR-0267A-10, `https://tds.ego-gw.it/itf/tds/`

[103] H. Yamamoto, *SIS (Stationary Interferometer Simulation) manual*, LIGO technical note LIGO-T070039-v6, `https://dcc.ligo.org/cgi-bin/DocDB/DocumentDatabase/`

[104] P. Hello and N. Man, *Design of a low-loss beam expander*, Virgo technical note VIR-NOT-LAS-1390-12, `https://tds.ego-gw.it/itf/tds/`

[105] M. Granata, M. Barsuglia, R. Flaminio, A. Freise, S. Hild and J. Marque, *Design of the Advanced Virgo non-degenerate recycling cavities*, J. Phys.: Conf. Ser. **228**, 012016 (2010)

[106] P. Rapagnani, *Design issues on multi-payload systems*, Virgo technical note VIR-0350A-10, `https://tds.ego-gw.it/itf/tds/`

[107] M. Barsuglia, R. Flaminio, M. Granata, B. Mours and R.Ward, *New optical layout for stable recycling cavities*, Virgo technical note VIR-0452A-10, `https://tds.ego-gw.it/itf/tds/`

[108] J. F. J. van den Brand, *NIKHEF PROJECT PLAN: MSAT. Multi-payload suspensions for Advanced Virgo*, Virgo technical note VIR-0553A-10, `https://tds.ego-gw.it/itf/tds/`

[109] J. Marque, *AdV optical layout: Optical aspects in the long recycling cavities*, Virgo technical note VIR-0448A-10, `https://tds.ego-gw.it/itf/tds/`

[110] M. Beker, J. F. J. van den Brand, M. Colombini, M. Doets, E. Hennes, E. Majorana, D. Rabeling, R. Rosing and P. Ruggi,*DOUBLE VERTICAL PAYLOADS On-axis suspension of power and signal recycling mirrors*, Virgo technical note VIR-0145A-11, `https://tds.ego-gw.it/itf/tds/`

[111] M. Granata, M. Barsuglia, J. Marque, R. Ward, *Matching Optimization for the Non-Degenerate Recycling Cavities*, Virgo technical note VIR-0065A-11, `https://tds.ego-gw.it/itf/tds/`

[112] H. Heitmann, *Minutes of AdV design integration meeting 20/01/2011*, Virgo technical note VIR-0036A-11, `https://tds.ego-gw.it/itf/tds/`

[113] H. Heitmann, *Minutes of AdV design integration meeting 03/02/2011*, Virgo technical note VIR-0068B-11, `https://tds.ego-gw.it/itf/tds/`

[114] V. Fafone and A. Rocchi, *Studies on thermal correction of PRM3*, Virgo technical note VIR-0026A-11, `https://tds.ego-gw.it/itf/tds/`

[115] R. Ward, *A study of cold ITF defects in MSRC with SIS*, Virgo technical note VIR-0326A-11, `https://tds.ego-gw.it/itf/tds/`

[116] R. Ward, *MSRC SIS update: compensated cold ITF defects*, Virgo technical note VIR-0391A-11, `https://tds.ego-gw.it/itf/tds/`

[117] E. Coccia, V. Fafone, V. Malvezzi, Y. Minenkov, A. Rocchi, L. Sperandio, *Control of thermal effects on Advanced Virgo*, presentation at the 9th Edoardo Amaldi Conference on Gravitational Waves, Cardiff, 2011. Available online: `http://www.amaldi9.org/abstracts/372/TCS_Rocchi.pdf`

[118] ANSYS website: `http://www.ansys.com/`

[119] R. Ward, *SIS simulations for MSRC with TCS maps: preliminary results*, Virgo technical note VIR-0232A-11, `https://tds.ego-gw.it/itf/tds/`

[120] A. Rocchi and V. Fafone, *AdV TCS: effect of non-uniform absorption - thermal simulations*, Virgo technical note VIR-0207A-11, `https://tds.ego-gw.it/itf/tds/`

[121] K. Yamamoto et al., *Current status of the CLIO project*, J. Phys.: Conf. Ser. **122**, 012002 (2008)

[122] E. D'Ambrosio, *Nonspherical mirrors to reduce thermoelastic noise in advanced gravitational wave interferometers*, Phys. Rev. D **67**, 102004 (2003)

[123] M. Bondarescu, O. Kogan and Y. Chen, *Optimal light beams and mirror shapes for future LIGO interferometers*, Phys. Rev. D **78**, 082002 (2008)

[124] M. G. Tarallo et al., *Generation of a flat-top laser beam for gravitational wave detectors by means of a nonspherical Fabry-Perot resonator*, Appl. Opt. **46**, 6648 (2007)

[125] B. Mours, E. Tournefier and J. Y. Vinet, *Thermal noise reduction in interferometric gravitational wave antennas: using high order TEM modes*, Class. Quantum Grav. **23**, 5777 (2006)

[126] J. Franc, M. Galimberti, R. Flaminio, S. Chelkowski, A. Freise and S. Hild, *Role of high-order Laguerre-Gauss modes on mirror thermal noise in gravitational wave detectors*, Einstein Telescope technical note ET-0002A-10, `https://tds.ego-gw.it/itf/tds/`

[127] A. Mair, A. Vaziri, G. Weihs and A. Zeilinger, *Entanglement of the orbital angular momentum states of photons*, Nature **412**, 313 (2001)

[128] D. G. Grier, *A revolution in optical manipulation*, Nature **424**, 810 (2003)

[129] R. Oron, N. Davidson, A. A. Friesem, E. Hasman, *Efficient formation of pure helical laser beams*, Opt. Comm. **182**, 205 (2000)

[130] S. C. Chu and K. Otsuka, *Doughnut-like beam generation of Laguerre-Gaussian mode with extremely high mode purity*, Opt. Comm. **281**, 1647 (2008)

[131] M. W. Beijersbergen, L. Allen, H. E. L. O. van der Veen and J. P. Woerdman, *Astigmatic laser mode converters and transfer of orbital angular momentum*, Opt. Comm. **96**, 123 (1993)

[132] M. W. Beijersbergen, R. P. C. Coerwinkel, M. Kristensen and J. P. Woerdman, *Helical-wavefront laser beams produced with a spiral phaseplate*, Opt. Comm. **112**, 321 (1994)

[133] S. S. R. Oemrawsingh, J. A. W. van Houwelingen, E. R. Eliel, J. P. Woerdman, E. J. K. Verstegen, J. G. Kloosterboer and G. W. t Hooft, *Production and characterization of spiral phase plates for optical wavelengths*, Appl. Opt. **43**, 688 (2004)

[134] N. Matsumoto, T. Ando, T. Inoue, Y. Ohtake, N. Fukuchi and T. Hara, *Generation of high-quality higher-order Laguerre-Gaussian beams using liquid-crystal-on-silicon spatial light modulators*, J. Opt. Soc. Am. A **25**, 1642 (2008)

[135] T. Ando, Y. Ohtake, N. Matsumoto, T. Inoue and N. Fukuchi, *Mode purities of Laguerre-Gaussian beams generated via complex-amplitude modulation using phase-only spatial light modulators*, Opt. Lett. **34**, 34 (2009)

[136] S. N. Khonina, V. V. Kotlyar, R. V. Skidanov, V. A. Soifer, P. Laakkonen and J. Turunen, *Gauss-Laguerre modes with different indices in prescribed diffraction orders of a diffractive phase element*, Opt. Comm. **175**, 301 (2000)

[137] S. A. Kennedy, M. J. Szabo, H. Teslow, J. Z. Porterfield and E. R. I. Abraham, *Creation of Laguerre-Gaussian laser modes using diffractive optics*, Phys. Rev. A **66**, 043801 (2002)

[138] J. Arlt, K. Dholakia, L. Allen and M. J. Padgett, *The production of multiringed Laguerre Gaussian modes by computer-generated holograms*, J. Mod. Opt. **45**, 1231 (1998)

[139] M. Granata, C. Buy, R. Ward and M. Barsuglia, *Higher-Order Laguerre-Gauss Mode Generation and Interferometry for Gravitational Wave Detectors*, Phys. Rev. Lett. **105**, 231102 (2010)

[140] SILIOS Technologies website: `http://www.silios.com/`

[141] J. Degallaix, *OSCAR a Matlab based optical FFT code*, J. Phys.: Conf. Ser. **228**, 012021 (2010)

[142] OSCAR website: `http://www.mathworks.com/matlabcentral/fileexchange/20607`

[143] D. C. O'Shea, T. J. Suleski, A. D. Kathman, D. W. Prather, *Diffractive optics. Design, fabrication and test*, SPIE Press, Bellingham, Washington, U.S.A., 2004

[144] M. Barsuglia, *Some considerations about HOLM for AdV*, presentation at the Advanced Virgo biweekly meeting, 2008. Available online: `https://wwwcascina.virgo.infn.it/advirgo/biweekly.html`

[145] P. Fulda, K. Kokeyama, S. Chelkowski and A. Freise, Phys. Rev. D **82**, 012002 (2010)

[146] B. Sorazu et al., *Experimental test of higher-order LG modes in the 10m Glasgow prototype interferometer*, presentation at the 9th Edoardo Amaldi Conference on Gravitational Waves, Cardiff, 2011. Available online: `http://www.amaldi9.org/index.php?option=com_fabrik&view=form&fabrik=15&rowid=Monday&usekey=day&dd=1&tt=2&desc=224&no=1&type=abs`

[147] SILIOS Technologies, personal communication

[148] V. Arrizón, U. Ruiz, R. Carrada and L. A. González, *Pixelated phase computer holograms for the accurate encoding of scalar complex fields*, J. Opt. Soc. Am. A **24**, 3500 (2007)

[149] M. Galimberti, *Surface specifications for ET mirrors: state of the art*, presentation at the ET 3rd Annual Workshop, Budapest, 2010. Available online: `http://agenda.infn.it/getFile.py/access?contribId=19&sessionId=4&resId=0&materialId=slides&confId=2701`

[150] R. Adhikari, *Enhancing the 2nd generation interferometers*, presentation at the Gravitational Wave Advanced Detector Workshop, Kyoto, 2010. Available online: `http://gw.icrr.u-tokyo.ac.jp/gwadw2010/program/2010_GWADW_Rana_2.pdf`

[151] C. Bond, P. Fulda, L. Carbone, K. Kokeyama and A. Freise, *Higher order Laguerre-Gauss mode degeneracy in realistic, high finesse cavities*, arXiv:1107.3812v1 [gr-qc]

[152] T. Hong, J. Miller, H. Yamamoto, Y. Chen and R. Adhikari, *Effects of Mirror Aberrations on Laguerre-Gaussian Beams in Interferometric Gravitational-Wave Detectors*, arXiv:1108.3114v3 [gr-qc]